Supported by 日本財団 THE NIPPON FOUNDATION

日中笹川医学奨学金制度(学位取得コース)中間報告書（研究者用）

第 40 期　　研究者番号：G4006　　作成日：2019 年 03 月 01 日

氏名	TANG CHUNHUA	唐春花	性別	F	生年月日　1984.01.22
所属機関(役職)	大坪医院（第三軍医大学附属第三医院）神経内科　（　主治医師　）				
研究先(指導教官)	慶應義塾大学　医学部　内科学教室（神経内科）　（中原　仁　教授　）				
研究テーマ	家族性片麻痺性偏頭痛２型モデルマウスを用いた偏頭痛病態の解明 Deciphering pathological mechanisms of migraine using a mouse model of familial hemiplegic migraine 2				
専攻種別	論文博士　☑		課程博士　□		

1. 研究概要

1）Purpose(目的)

To clarify the pathogenesis of migraine by comparing the susceptibility and responsiveness to cortical spreading depression (CSD) in adult mice harboring the E700K mutation in *Atp1a2* gene mimicking familial hemiplegic migraine 2 and their wild-type littermates.

2）Approach (戦略)

FHM is an autosomal dominant subtype of migraine, and at least one first- or second-degree relative has migraine aura including hemiparesis (one-sided motor weakness). FHM2 is caused by mutations in the *ATP1A2* gene, which encodes the α2 subunit of the Na$^+$,K$^+$-ATPase and is mainly expressed in astrocytes in adult brain. The E700K mutation in *ATP1A2* exon 15, which replaces glutamic acid with lysine, was identified in three migraine patients from one family. Affected individuals showed a stereotypic pattern of migrainous headache associated with hemisesory and hemiparetic attacks as auras. CSD has been hypothesized to be the underlying mechanism of the migraine aura, and we demonstrated enhanced susceptibility to CSD in Atp1a2-deficient mice [1].

3）Materials and methods (材料と方法)

CSD was elicited by application of a gradient KCl over the occipital cortex surface in transgenic mice [2], C57BL/6J-Tg(Atp1a2*E700K)9151Kwk (Fig.1) (Tg, N=30, both males and females) and their wild-type littermates (WT, N=38) under urethane anesthesia and artificially ventilated, and the responsiveness and sensitivity to CSD were examined (Fig.2).

4）Results (実験結果)

In total, Tg mice exhibited faster propagation velocity (Tg, 4.76±0.18mm/min; WT, 3.89±0.18mm/min; P=0.001）and a longer full-width-at-half-maximum (FWHM), reflecting slower recovery from DC deflection, compared to WT mice (Tg, 87.1±6.5s; WT, 61.5±5.1s; P=0.003). Both male and female groups showed the same trend. The threshold for initiating CSD tended to be lower in the Tg group, especially in female mice. The electroencephalogram (EEG) was suppressed immediately after the first CSD wave passed and then gradually recovered, and no difference of maximum EEG suppression was observed between Tg and WT.

The initial decrease of regional cerebral blood flow (rCBF) elicited by the first CSD seemed to be similar in each group, but the subsequent transient increase of rCBF in the Tg group was slightly but significantly larger than that in WT in the case of males. Post-CSD oligemia and the temporal changes of rCBF in response to second and subsequent CSD were quite similar between Tg and WT. Physiological parameters such as systemic arterial pressure, heart rate, respiratory rate and expiratory CO_2 concentration were well maintained during experiments, and were not significantly different among groups.

5）Discussion (考察)

We previously showed that susceptibility and responsiveness to CSD may differ depending upon the knockout strategy for the gene disruption in two types of *Atp1a2*-deficient mice [1]. Although E700K mutant mice showed a similar threshold to WT for KCl-induced CSD, the effect of CSD might be greater, as indicated by rapid propagation and slow recovery.

6）Reference(参考文献)

[1] Unekawa M, Ikeda K, Tomita Y, et al. Enhanced susceptibility to cortical spreading depression in two types of Na^+,K^+-ATPase α2 subunit-deficient mice as a model of familial hemiplegic migraine 2. Cephalalgia. 2018, 38(9):1515-1524

[2] Pierelli F, Grieco GS, Pauri F, et al. A novel *ATP1A2* mutation in a family with FHM type II. Cephalalgia. 2006,26(3):324-328.

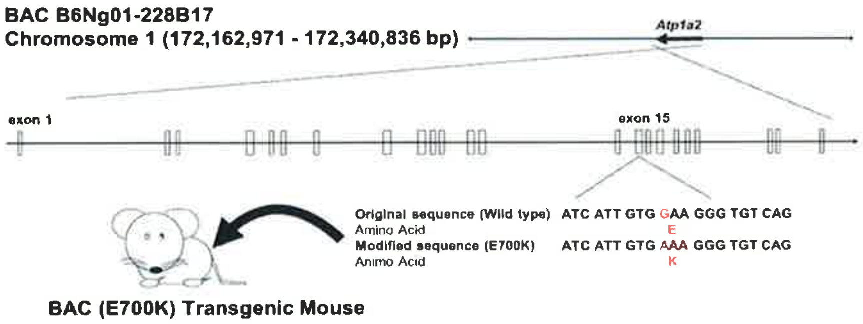
BAC B6Ng01-228B17
Chromosome 1 (172,162,971 - 172,340,836 bp)
Atp1a2
exon 1
exon 15
Original sequence (Wild type) ATC ATT GTG GAA GGG TGT CAG
Amino Acid E
Modified sequence (E700K) ATC ATT GTG AAA GGG TGT CAG
Animo Acid K
BAC (E700K) Transgenic Mouse

Fig.1 Targeting strategy for mutating Na^+,K^+-ATPase α2 subunit gene (*Atp1a2*). The E700K mutation in *Atp1a2* exon 15 replaces glutamic acid (E) for lysine (K).

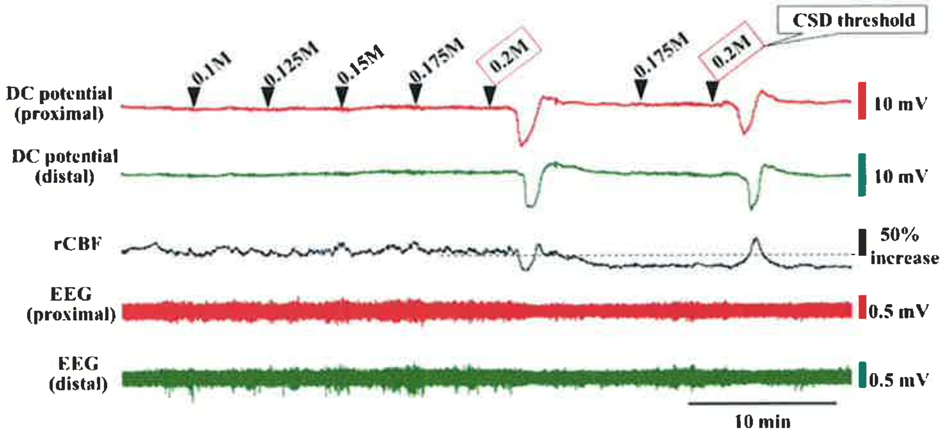

Fig.2 Assess of threshold of CSD by KCl of different concentration. 5 μl of KCL from 0.025M was applied over the occipital cortex, and increased by stepwise concentration. The minimum concentration that can elicit CSD was considered as a threshold of CSD. The properties of electrophysiology and rCBF corresponding to each CSD were evaluated.

3. 学会発表　Conference presentation　※筆頭演者として総会・国際学会を含む主な学会で発表したものを記載してください。

※Describe your presentation as the principal presenter in major academic meetings including general meetings or international meeting

学会名 Conference	第61回日本脳循環代謝学会学術集会		
演 題 Topic	Property of behavior after cortical spreading depression in Na+, K+—ATPase α2subunit-defective mice		
開催日 date	2018 年 10 月 19 日	開催地 venue	盛岡
形式 method	□ 口頭発表 Oral ☑ ポスター発表 Poster	言語 Language	□ 日本語 ☑ 英語 □ 中国語
共同演者名 Co-presenter			
学会名 Conference			
演 題 Topic			
開催日 date	年 月 日	開催地 venue	
形式 method	□ 口頭発表 Oral □ ポスター発表 Poster	言語 Language	□ 日本語 □ 英語 □ 中国語
共同演者名 Co-presenter			
学会名 Conference			
演 題 Topic			
開催日 date	年 月 日	開催地 venue	
形式 method	□ 口頭発表 Oral □ ポスター発表 Poster	言語 Language	□ 日本語 □ 英語 □ 中国語
共同演者名 Co-presenter			
学会名 Conference			
演 題 Topic			
開催日 date	年 月 日	開催地 venue	
形式 method	□ 口頭発表 Oral □ ポスター発表 Poster	言語 Language	□ 日本語 □ 英語 □ 中国語
共同演者名 Co-presenter			

4. 受賞（研究業績）　Award (Research achievement)

名 称 Award name				
	国名 Country		受賞年 Year of award	年 月
名 称 Award name				
	国名 Country		受賞年 Year of award	年 月

5. 本研究テーマに関わる他の研究助成金受給 Other research grants concerned with your resarch theme

受給実績 Receipt record	□ 有　　□ 無
助成機関名称 Funding agency	
助成金名称 Grant name	
受給期間 Supported period	年　月 ～　年　月
受給額 Amount received	円
受給実績 Receipt record	□ 有　　□ 無
助成機関名称 Funding agency	
助成金名称 Grant name	
受給期間 Supported period	年　月 ～　年　月
受給額 Amount received	円

6. 他の奨学金受給 Another awarded scholarship

受給実績 Receipt record	□ 有　　□ 無
助成機関名称 Funding agency	
奨学金名称 Scholarship name	
受給期間 Supported period	年　月 ～　年　月
受給額 Amount received	円

7. 研究活動に関する報道発表 Press release concerned with your research activities

※記載した記事を添付してください。Attach a copy of the article described below

報道発表 Press release	□ 有　　□ 無	発表年月日 Date of release	
発表機関 Released medium			
発表形式 Release method	・新聞　・雑誌　・Web site　・記者発表　・その他（　　）		
発表タイトル Released title			

8. 本研究テーマに関する特許出願予定 Patent application concerned with your research theme

出願予定 Scheduled	□ 有　　□ 無	出願国 Application	
出願内容（概要） Application contents			

9. その他 Others

指導責任者（署名）　㊞

Supported by 日本財団 THE NIPPON FOUNDATION

日中笹川医学奨学金制度（学位取得コース）中間評価書
論文博士：指導教官用

第 40 期　研究者番号：G4006　　作成日：2019 年 2 月 5 日

氏　名	唐 春花	TANG CHUNHUA	性別	F	生年月日　1984. 1 . 22

所属機関（役職）	大坪医院（第三軍医大学附属第三医院）神経内科（　主治医師　）	
研究先（指導教官）	慶應義塾大学医学部　内科学教室（神経）（　中原　仁　教授　）	
研究テーマ	家族性片麻痺性片頭痛 2 型モデルマウスを用いた片頭痛病態の解明	
専攻種別	☑論文博士	□課程博士

研究者評価（指導教官記入欄）

成績状況	[✓ 優]　良　可　不可	取得単位数 ~~取得単位数／取得すべき単位総数~~

学生本人が行った研究の概要	片頭痛の病態解明を目的とし、家族性片麻痺性片頭痛 2 型モデルマウスにおいて、片頭痛の前兆発現との関連性が示唆されている大脳皮質性拡延性抑制（CSD）に対する感受性および反応性を検討した。ウレタン麻酔下で後頭部に作製した小骨窓から濃度の異なる KCl 溶液を滴下することによって CSD を誘発する系を立ち上げ、KCl 濃度（閾値）および同時に測定した大脳皮質表面の DC 電位と局所脳血流の反応性を解析し、本モデルマウスでは CSD の伝播速度が速く、CSD からの回復が遅いという結果が得られた。
総合評価	【良かった点】 マウスを用いた *in vivo* 実験手法をいち早く習得し、自ら工夫しながらばらつきの少ない安定した実験を行えるようになった。根気を要する地道な作業も厭わず取り組み、指示されたことをこなすだけではなく、効率よく作業ができるように創意工夫を怠らない。さらに多くの論文を読みこなし、背景や問題点を理解しながら研究を進められた。 【改善すべき点】 特になし。 【今後の展望】 本モデルマウスにおいて CSD が明所忌避行動、不安行動に及ぼす影響を検討し、患者でみられる症状とモデルマウスの結果を比較することによって片頭痛の病態解明を進める。
学位取得見込	順調に行けば、今後約 1 年程度で実験を終了して論文化することが可能であると推定している。当該論文が学術誌に受理された際には学位審査を請求する予定である。

評価者（指導教官名）　中原 仁 ㊞

日中笹川医学奨学金制度(学位取得コース)中間報告書
研究者用

Supported by
日本財団
THE NIPPON FOUNDATION

第40期　　研究者番号：G4007　　作成日：2019年3月10日

氏名	ZHANG SHUN	張 順	性別	M	生年月日 1985. 1. 17
所属機関(役職)	上海市東方病院（同済大学付属東方病院）胃腸外科 （ 主治医師 ）				
研究先（指導教官）	順天堂大学医学研究科消化器低侵襲外科学 （福永 哲 教授 ）				
研究テーマ	The Relationship between p21 and Carboxylesterase 2 Expression in Human Colorectal Cancer Cells				
専攻種別	論文博士	☑	課程博士	□	

1．研究概要（1）

1）目的（Goal）
Irinotecan (CPT-11) is an anticancer prodrug that is activated by the carboxylesterase CES2 and has been approved for the treatment of many types of solid tumors, including colorectal cancer[1,2]. Maximize the expression of CES2 may upregulate the anti-cancer effect of Irinotecan. Recent studies with cell lines show that CES2 expression is regulated by the tumor suppressor protein p53[3]. However, approximately 50% of colorectal cancer bears missense mutations in TP53, the gene encoding p53[4]. Deregulated p53 signaling may affects CES2 expression in colorectal cancer. In previous study, there was a significant positive correlation between p21 and CES2 expression even in the tumors with nonfunctional p53[5]. However, basic research for the relationship between p21 and CES2 in colon cancer is lacking. In this study, we want to verify the relationship between p21 and CES2 according to different expression of p53 in colorectal cancer cells.

2）戦略（Approach）
In this study, we want to verify the relationship between p21 and CES2 in p53 dependent or independent pathway using colorectal cancer cells. The wild-type p53 (HCT116, LoVo, RKO, and LS174T), p53-null Caco-2 cells and mutant p53 (KM12C and SW480) colon cells lines were treated with Doxorubicin, Suberoylanilide Hydroxamic Acid (SAHA) or p21 Inhibitor, UC2288 for 24 hours according to protocols. Real-Time reverse transcriptase PCR and Western blotting analysis were used for testing the mRNA and protein expression.

3）材料と方法（Materials and methods）
3.1 Cell Culture.
The human colorectal cancer cell lines were cultured at 37°C and 5% CO2 in a 1 : 1 (v/v) mixture of Dulbecco's modified Eagle's medium (Wako) and Ham's F-12 medium (Wako)supplemented with 10% fetal bovine serum and penicillin/streptomycin. Cells expressing wild-type p53 (HCT116, LoVo, RKO, and LS174T), p53-null Caco-2 cells and mutant p53 (KM12C and SW480) were seeded at 2.5×10^5cells/well in 6-well plates and incubated for 24 hours. The cells were then treated with Doxorubicin, Suberoylanilide Hydroxamic Acid (SAHA) or p21 Inhibitor, UC2288 for 24 hours according to protocols.

3.2 Real-Time Reverse Transcriptase PCR.
Total RNA from cell lines and tissues was extracted using the RNeasy Mini Kit (Qiagen) according to the manufacturer's protocol. Semiquantitative real-time PCR was performed using FastStart Essential DNA Green Master (Roche) on a LightCycler 96 (Roche). PCR reactions were performed in duplicate for all genes. The relative expression of each gene was calculated using the $2-\Delta\Delta Ct$ method.

3.3 Western Blotting Analysis.
The colon cell pellet was collected and lysed with lysis buffer (50 mM Tris–HCl pH 8.0, 120 mM NaCl, 0.5% NP-40, 1 mM phenylmethylsulfonyl fluoride). Protein 40ug was loaded onto 10% sodium dodecyl sulfate-polyacrylamide gels and electrophoresed. After electrophoresis, the protein was transferred to a polyvinylidene difluoride (PVDF) membrane (Bio-Rad; Hercules, CA, USA) and the membrane blocked with 5% non-fat dry milk in tris-buffered saline-Tween buffer 7 (0.12 M Tris-base, 1.5 M NaCl, 0.1% Tween 20) at room temperature for 1 hours. The membrane was then incubated with primary mouse antibody against β-actin (1:1000) and primary rabbit antibody against p21(1:1000) overnight at 4°C followed by incubation with horseradish peroxidase-conjugated secondary antibody (1:1,000) for 1.5 hour at room temperature. Protein- antibody complexes were detected by chemiluminescence (ECL System) before autoradiography.

4）実験結果（Results）
4.1 Activation of p53 can upregulation of p21 and CES2 expression
Wild-type p53(HCT116, LS174T, Lovo and RKO) cell lines were treated with Doxorubicin, which can activate p53 expression in p53 wild-type colorectal cancer cells. The expression of p21, a downstream target of p53, increased following doxorubicin treatment in the results of Real-Time Reverse Transcriptase PCR and Western Blotting Analysis. We also found the CES2 expression was upregulated in the result of Reverse Transcriptase PCR. However, after treatment of doxorubicin, p53 mutant (SW480 and KM12C) and p53 null (Caco-2) cell lines didn't show significant upregulation of p21 and CES2 expression.

1．研究概要（2）

4.2 Activation of p21 can upregulate CES-2 expression in p53 dependent or independent pathway
Wild-type p53(HCT116, LS174T, Lovo and RKO), p53 mutant (SW480 and KM12C) and p53 null (Caco-2) were treated with SAHA, which can activate p21 expression. The expression of p21 increased after treatment in the results of Real-Time Reverse Transcriptase PCR and Western Blotting Analysis. The mRNA expression of CES2 was also upregulated after SAHA treatment. The results suggested the CES2 may have relationship with p21 expression.

4.3 p21 inhibitor can decreased the increasing level of CES-2 expression in p53 dependent or independent pathway
A novel p21 inhibitor, UC2288 combined with Doxorubicin were treated in Wild-type p53(HCT116, LS174T, Lovo and RKO), or combined with SAHA in p53 mutant (SW480 and KM12C) and p53 null (Caco-2). We found UC2288 can decreased the increasing level of CES-2 expression in Wild-type p53 cells treated with Doxorubicin and in p53 mutant and null cells treated with SAHA. The results may suggest p21 can regulate CES2 in p53 dependent or independent pathway.

5）考察（Discussion）
Although the liver is the major site for irinotecan metabolism in general, it has been suggested that colon may also serve as a major site for irinotecan activation since CES2 is highly expressed in this tissue[1]. Thus, CES2 expression in colorectal cancer could be a key determinant of the therapeutic efficacy of irinotecan. Recent studies suggest that CES2 expression is regulated by p53 in colorectal cancer cell lines. Mutations in TP53 coding gene are found in approximately 50% of colorectal cancer, which can decrease the drug effectiveness of irinotecan. It has been shown that p21 expression can be induced by various stress signals in a p53-independent fashion[6]. There was a significant positive correlation between p21 and CES2 expression even in the tumors with nonfunctional p53[5]. Our results showed activation of p21 can upregulate CES2 expression in p53 dependent or independent pathway. Similarly, on the contrary p21 inhibitor can decreased the increasing level of CES2 expression in p53 dependent or independent pathway. All these may suggest p21 can regulate CES2 in p53 dependent or independent pathway.

6）参考文献（References）
1. Humerickhouse R, Lohrbach K, Li L, Bosron WF, Dolan ME. Characterization of CPT-11 hydrolysis by human liver carboxylesterase isoforms hCE-1 and hCE-2. Cancer Res 2000;60:1189-92.
2. Sanghani SP, Quinney SK, Fredenburg TB, Sun Z, Davis WI, et al. Carboxylesterases expressed in human colon tumor tissue and their role in CPT-11 hydrolysis. Clin Cancer Res 2003;9:4983-91.
3. Choi W, Cogdell D, Feng Y, Hamilton SR, Zhang W. Transcriptional activation of the carboxylesterase 2 gene by the p53 pathway. Cancer Biol Ther 2006;5:1450-6.
4. Munro AJ, Lain S, Lane DP. P53 abnormalities and outcomes in colorectal cancer: a systematic review. Br J Cancer 2005;92:434-44.
5. Ishimine M, Lee HC, Nakaoka H, Orita H, Kobayashi T, et al. The Relationship between TP53 Gene Status and Carboxylesterase 2 Expression in Human Colorectal Cancer. Dis Markers 2018;2018:5280736.
6. Gartel AL, Tyner AL. Transcriptional regulation of the p21((WAF1/CIP1)) gene. Exp Cell Res 1999;246:280-9.

研究者番号：G4007

2. 執筆論文 Publication of thesis※記載した論文を添付してください。Attach all of the papers listed below

論文名 1 Title	Internet videos and colorectal cancer in mainland China: a content analysis				
掲載誌名 Published journal	BMC Medical Informatics and Decision Making				
	2018 年 12 月	18: 129 巻（号）	1 頁 ～ 6 頁	言語 Language	English
第 1 著者名 First author	Shun Zhang	第 2 著者名 Second author	Yao Yang	第 3 著者名 Third author	Dongyi Yan
その他著者名 Other authors	Biao Yuan, Xiaohua Jiang, Chun Song				
論文名 2 Title	Current status of technique for Billroth-I anastomosis in totally laparoscopic distal gastrectomy for gastric cancer				
掲載誌名 Published journal	Mini-invasive Surgery				
	2019 年 1 月	3（2） 巻（号）	1 頁 ～ 7 頁	言語 Language	English
第 1 著者名 First author	Shun Zhang	第 2 著者名 Second author	Tetsu Fukunaga	第 3 著者名 Third author	
その他著者名 Other authors					
論文名 3 Title					
掲載誌名 Published journal					
	年 月	巻（号）	頁 ～ 頁	言語 Language	
第 1 著者名 First author		第 2 著者名 Second author		第 3 著者名 Third author	
その他著者名 Other authors					
論文名 4 Title					
掲載誌名 Published journal					
	年 月	巻（号）	頁 ～ 頁	言語	
第 1 著者名 First author		第 2 著者名 Second author		第 3 著者名 Third author	
その他著者名 Other authors					
論文名 5 Title					

3. 学会発表 Conference presentation※筆頭演者として総会・国際学会を含む主な学会で発表したものを記載してください。

※Describe your presentation as the principal presenter in major academic meetings including general meetings or international meetings.

学会名 Conference			
演　題 Topic			
開催日 date	年　　月　　日	開催地 venue	
形式 method	口頭発表 Oral　ポスター発表 Poster	言語 Language	日本語　英語　中国語
共同演者名 Co-presenter			
学会名 Conference			
演　題 Topic			
開催日 date	年　　月　　日	開催地 venue	
形式 method	口頭発表 Oral　ポスター発表 Poster	言語 Language	日本語　英語　中国語
共同演者名 Co-presenter			
学会名 Conference			
演　題 Topic			
開催日 date	年　　月　　日	開催地 venue	
形式 method	口頭発表 Oral　ポスター発表 Poster	言語 Language	日本語　英語　中国語
共同演者名 Co-presenter			
学会名 Conference			
演　題 Topic			
開催日 date	年　　月　　日	開催地 venue	
形式 method	口頭発表 Oral　ポスター発表 Poster	言語 Language	日本語　英語　中国語
共同演者名 Co-presenter			

4. 受賞（研究業績Award (Research achievement)

名　称 Award name	国名 Country name		受賞年 Year of award	年　　月
名　称 Award name	国名 Country name		受賞年 Year of award	年　　月

5．本研究テーマに関わる他の研究助成金受給 Other research grants concerned with your resarch then

受給実績 Receipt record	☑ 有　　☐ 無
助成機関名称 Funding agency	中国自然科学基金委員会
助成金名称 Grant name	中国自然科学基金(NO.81700452)
受給期間 Supported period	2018 年 1 月 ～ 2020 年 12 月
受給額 Amount received	3,500,000 円

6．他の奨学金受給 Another awarded scholarship

受給実績 Receipt record	☐ 有　　☐ 無
助成機関名称 Funding agency	
奨学金名称 Scholarship name	
受給期間 Supported period	年 月 ～ 年 月
受給額 Amount received	円

7．研究活動に関する報道発表 Press release concerned with your research activities

※記載した記事を添付してください。 Attach a copy of the article described below

報道発表 Press release	☐ 有　　☐ 無	発表年月日 Date of release	
発表機関 Released medium			
発表形式 Release method	・新聞　・雑誌　・Web site　・記者発表　・その他（		
発表タイトル Released title			

8. 本研究テーマに関する特許出願予定 Patent application concerned with your research theme

出願予定 Scheduled application	☐ 有　　☐ 無	出願国 Application country	
出願内容（概要） Application			

9. その他 Others

指導責任者（署名） 福永

1

Supported by
日本財団
THE NIPPON FOUNDATION

日中笹川医学奨学金制度（学位取得コース）中間評価書

論文博士：指導教官用

第 40 期　研究者番号：G4007　作成日　：2019 年 3 月　日

氏　名	張 順	ZHANG　SHUN	性別	M	生年月日　1985. 01. 17

所属機関（役職）	上海市東方医院（同済大学附属東方医院）胃腸外科　（　主治医師　）
研究先（指導教官）	順天堂大学大学院医学研究科　消化器・低侵襲外科（　福永 哲　教授　）
研究テーマ	The Relationship between p21 and Carboxylesterase 2 Expression in Human Colorectal Cancer Cells
専攻種別	☑論文博士　□課程博士

研究者評価（指導教官記入欄）

成績状況	[✓ 優]　良　可　不可	取得単位数 ~~取得単位数／取得すべき単位総数~~
学生本人が行った研究の概要	Irinotecan (CPT-11) is an anticancer prodrug that is activated by the carboxylesterase CES2. Studies with cell lines show that CES2 expression is regulated by the tumor suppressor protein p53. However, approximately 50% of colorectal cancer bears missense mutations in p53 which may affects CES2 expression in colorectal cancer and then influence the drug effect of Irinotecan. Maximize the expression of CES2 in colon cancer especially in p53 mutation type may upregulate the anti-cancer effect of Irinotecan. In our previous study, there was a significant positive correlation between p21 and CES2 expression even in the tumors with nonfunctional p53. In this study, we are using different p53 type colon cancer cells to analysis the relationship between p21 and CES2 dependent and independent of p53 way. Exact methods are including Real-Time reverse transcriptase PCR, Western blotting analysis and XTT viability assay. We found that activation of p21 can upregulate CES2 expression in p53 dependent or independent pathway. Similarly, on the contrary p21 inhibitor can decreased the increasing level of CES2 expression in p53 dependent or independent pathway. All these may suggest p21 can regulate CES2 in p53 dependent or independent pathway.	
総合評価	【良かった点】 非常に綿密な実験計画を立て、毎週の報告でもそれが着実に進行していることがよくわかった。 この実験により p21 により p53 とは依存的、独立的に CES2 を調整できることが示唆され、臨床的にも非常に意義が深い。 【改善すべき点】 特になし 【今後の展望】 本年中に、現在の実験結果をまとめて英文誌に投稿予定。	
学位取得見込	来年 4 月には、取得できる見込み	

評価者（指導教官名）　福永 哲　福永　印

Zhang et al. BMC Medical Informatics and Decision Making (2018) 18:129
https://doi.org/10.1186/s12911-018-0711-x

BMC Medical Informatics and Decision Making

RESEARCH ARTICLE Open Access

Internet videos and colorectal cancer in mainland China: a content analysis

Shun Zhang*, Yao Yang, Dongyi Yan, Biao Yuan, Xiaohua Jiang* and Chun Song*

Abstract

Background: Colorectal cancer incidence and mortality have been increasing in China and as one of the most important health problems facing the nation. Adequate dissemination of correct information about colorectal cancer could help in reducing cancer-related morbidity and mortality. This study aims to assess the completeness and reliability of colorectal cancer-related information available on the video website of Youku in mainland China.

Methods: Youku (https://www.youku.com/) was searched on September 15, 2016 for the search terms colorectal cancer. Only Chinese videos were included. Two reviewers independently evaluate the videos for characteristics, information source and usefulness. Content was analysed under six categories (aetiology, anatomy, symptoms, preventions, treatments and prognosis). Completeness was evaluated with a checklist developed by the researchers. Any discrepancies were resolved by consensuses. SPSS software was used to analyze data.

Results: There were 242 videos with relevant information about colorectal cancer. The type of source were as follows: independent users, 118 (49%); health information web sites, 60 (25%); medical doctors, 31 (13%); news network, 22 (9%); and hospital/university, 11 (4%). In all, 57% of videos had useful information about colorectal cancer, 21% were misleading. Videos posted by medical doctors ($P = 0.021$) and health information web sites ($p = 0.039$) were less incomplete than videos by independent users. Of the Traditional Chinese medicine (TCM) videos, 97 (76%) had information about treatments of colorectal cancer. 30% TCM videos contain misleading information, whose misleading rate was higher than total's (21%).

Conclusions: The colorectal cancer videos in mainland China represented by Youku varied base on ownership and content and information incompleteness were fairly high. It is necessary that professionals adapt to the advanced technology and think useful methods to solve the variable quality of information of internet video websites in mainland China.

Keywords: Colorectal cancer, Internet, Youku, Mainland China

Background

Cancer incidence and mortality have been increasing in China and have created a significant number of health concerns [1]. Colorectal cancer ranks the fifth most commonly diagnosed cancer among male and female in China [2]. The ratio of estimated new colorectal cancer mortality incidence is 50.8% in China for 2015 [2] compared with 36.3% in the United States for 2016 [3]. This considerably higher ratio means cancer prevention and control in China lags behind some Western countries.

Up to 31 December 2016, it was reported that 731 million Chinese internet users, and more than 695 million people were using mobile devices to quick browse online information. Over 570 million online video users accounted for three-quarters of total internet users [4]. Health and medical treatment has been the most popular science topics in mainland China [5]. Freely available video websites, such as YouTube, are popular sources of information dissemination with more than 100 million viewers every day [6]; however, YouTube is blocked in China because of Chinese internet censorship.

Chinese people prefer online video websites, such as Yoku, iQiyi, Sohu Tv or Tencent Video. Youku is the most popular source of video blogs and short original

---

* Correspondence: v2zs@hotmail.com; jiangxiaohua@163.com; chunsong163@163.com
Department of Gastrointestinal Surgery, Shanghai East Hospital (East Hospital Affiliated to Tongji University), 150 Jimo Road, Shanghai 200120, People's Republic of China

© The Author(s). 2018 **Open Access** This article is distributed under the terms of the Creative Commons Attribution 4.0 International License (http://creativecommons.org/licenses/by/4.0/), which permits unrestricted use, distribution, and reproduction in any medium, provided you give appropriate credit to the original author(s) and the source, provide a link to the Creative Commons license, and indicate if changes were made. The Creative Commons Public Domain Dedication waiver (http://creativecommons.org/publicdomain/zero/1.0/) applies to the data made available in this article, unless otherwise stated.

videos uploaded by individuals in mainland China [7]. Youku initially emphasized user-generated content. The average number of daily video views was 1.18 billion [8]. The number of monthly active users was over 500 million, and 60% of audiences were male [7]. Youku features the same kinds of videos on YouTube and is considered the largest Chinese video broadcast site. Similar to YouTube, the posted videos are not peer control, could be uploaded from different sources and are likely to be of variable quality [9].

Many studies reported that video broadcast sites have positive and negative effects on health information dissemination. Some videos can provide useful resources for knowledge and were used by medical students as a learning resource [10, 11]. Videos may promote misleading information, such as disparaging vaccinations [9] and describing ineffective or potentially dangerous natural therapies for gallstone disease [12]. Not only were audience attempting therapies that may be harmful, but they were not going in for accurate therapy, which can lead to other complications.

The use of video broadcasting sites as a source of information in disease areas, especially in colorectal cancer in mainland China, has not been evaluated. Thus, the present study aimed at evaluating the completeness and reliability of Chinese-language colorectal cancer-related information available on the video website of Youku in mainland China; assess the overall quality of online information on colorectal cancer; and share our thoughts on important future directions for managing information about colorectal cancer on websites of mainland China.

Method

We searched Youku (www.youku.com) on November 15, 2016 to locate video clips containing relevant information about colorectal cancer in human patients. The keyword "colorectal cancer" was used to identify related video clips. Videos that were duplicated, not in Chinese and not directly related to the investigated condition were excluded.

We included all unique videos with Chinese language content that contained any message about human colorectal cancer. All videos were downloaded and saved. We assessed each video according to the following characteristics: duration, ownership, number of views, video quality, and colorectal cancer content. Ownership was classified by medical doctor, hospital/university, news network, health information website or independent user.

All videos were viewed and analysed for content by 2 reviewers, and disagreements were resolved by an arbitrator. All researchers had medical background and specialized in gastrointestinal surgery. All researchers had finished their respective residencies at general hospital and had enough experience in the diagnosis and management of colorectal cancer. The reviewers classified the videos as useful, misleading or useless, as defined by the following: **useful**—containing scientifically correct information about any aspect of the disease: symptoms, treatment, and prevention; **misleading**— containing scientifically unproven information; **useless**—without containing the any aspect of colorectal cancer or addressing personal experience. If the video included trustable and misleading information at the same time, the videos were categorized as "misleading".

We assessed the quality of each video using a completeness score (Table 1). Two reviewers viewed each video in all content areas (aetiology, anatomy, symptoms, preventions, treatments and prognosis). At present, no validated tool for this purpose exists in the literature. Any disagreements were resolved with consensuses.

Traditional Chinese medicine (TCM) has been is deeply embedded in the populations of China and applied to the prevention and treatment of various diseases from ancient times until now. TCM is promoted and institutionalized by the Chinese government, has spread to more than 100 countries and has grown into an international industry [13]. For this reason, we also analysed TCM content regarding colorectal cancer in our study. Inter-observer agreement was evaluated with a kappa coefficient. Differences between groups were compared with a one-way ANOVA. Data analysis was performed with SPSS Version 16 Software. If the p-value is less than 0.05, the result was considered to be significant.

Table 1 Completeness checklist

Content	Description
Aetiology	Precancerous lesion
	Heredity
	Eating habits
Anatomy	–
Symptoms	Stool change
	Altered bowel habits
	Abdominal pain
	Abdominal mass
	Systemic symptoms
Preventions	Screening
	Daily habits
Treatments	Surgery
	Chemotherapy
	Radiotherapy
	Traditional Chinese medicine
Prognosis	TNM stage
	Perioperative treatments
	Others

Result

A Youku search revealed 348 videos for colorectal cancer. Videos were removed for a variety of reasons (Table 2). Video duplication and not being in Chinese were the two main reasons. Of the 348 videos screened, 242 videos met the inclusion criteria.

Ownership

A total of 49% of the videos were posted on the website by independent users. Health information websites were responsible for uploading 25% of the total videos. The videos contributed by medical doctors were only 13% but higher than other owner videos by max viewership and mean viewership (Table 3). This difference among groups was statistically significant ($p < 0.05$).

Information reliability

The 242 included videos were classified as useful (136 [57%]), misleading (51 [21%]), and useless (55 [22%]) according to medical content (Table 4). The kappa coefficient statistics of agreement of these videos was 0.88.

The number of videos containing misleading information was 51. A large part (41 [80%]) were amateur videos about personal experiences and emotions. The mean duration of the videos was 4.0 min with no significant differences between useful and misleading videos or between useful and irrelevant videos ($p < 0.05$).

Content

Useful videos were analysed based on the information they contained. In all of the categories, treatments were the most frequently covered topic (70%), followed in descending order by symptoms (33%), prognosis (26%), anatomy (20%), preventions (15%) and aetiology (11%). Table 5 shows the information completeness scores. Videos by medical doctors ($p = 0.021$) and health information websites ($p = 0.039$) sources were significantly more complete than those posted by independent users.

Traditional Chinese medicine

There were 128 videos containing TCM from diagnosis to treatment. Of the TCM videos, 97 (76%) had information about treatments of colorectal cancer. Among these videos, 10 included TCM and Western medicine at the same time. The information reliability is shown in Table 6. Medical doctors and university provided more reliable information than others ($p < 0.05$). A total of 30% TCM videos contain misleading information, and this misleading rate was higher than the totals (21%). Among the videos containing both TCM and Western medicine, the misleading rate was as high as 90%. Most of the videos exaggerated the actual effect of TCM and understated therapies, except for the health information websites mean viewership (798: 895). The other sources' mean viewership in TCM were higher than those containing both TCM and non-TCM videos.

Table 2 Reasons for excluding videos

Reason for exclusion	No.
No audio	1
No video	2
Not in Chinese	15
Not related to subject	3
Duplicate	85
Total exclusions	106

Discussion

Colorectal cancer ranks as the fifth leading cause of cancer death among both male and female in mainland China. Because the population of China accounts for one fifth of the global world, colorectal cancer cases in China account for 22% of all newly diagnosed cases and 27% of all deaths from worldwide [14]. The effectiveness of prevention, early detection, and management of colorectal cancer is not only important for China but also for the world.

Internet video websites can provide useful diagnostic, treatment and preventative medical services information. Previous research has evaluated YouTube as an important source of information on disease topics [15]. Although YouTube is blocked due to many reasons in mainland China, there are many similar internet video websites delivering the same functionality, such as Youku. To the best of our knowledge, no study has been performed to assess the accuracy and usefulness of internet videos as a source of healthy information for colorectal cancer in mainland China.

In this study, we selected Youku.com as the target video website, which is ranked the largest Chinese video broadcast site. The website of Youku not only focuses on professionally produced videos but also emphasizes user-generated content. The monthly unique visitors of Youku were 2,6376,000,000 according to the data of October in 2016 [7].

Our study demonstrates approximately 242 videos addressing colorectal cancer were provided by different sources. Independents users represent the greatest number of sources. The content was mainly about personal experiences in surgical procedures or hospital stays. Our results also show that Chinese medical doctors and health related institutions comprising 17% of colorectal cancer videos do not pay sufficient attention to the platform for the distribution of information. Doctors in china frequently experience work overload, tend to work overtime and experience energy deficiencies, which seem to be one of reasons for this phenomenon [16]. The videos that were viewed most often were the videos posted

Table 3 Sources and classification of detected videos

Source	Total videos	Max viewership	Min viewership	Mean viewership
Independent user	118	53,455	8	10,621
Health information web site	60	60,234	167	15,390
Medical doctor	31	61,132	12,583	23,893
Hospital/University	11	20,343	670	8783
News network	22	57,890	4791	9321

by doctors followed by health information websites. This indicates that people are more interested in a professionals experience regarding disease rather than their peers.

As the content of most videos often lacks peer or institutional quality review, many may not be subject to quality controls and may not be evidence-based; thus, it is not surprising that a majority of this content is misleading or irrelevant. According to previous studies, the dissemination of inaccurate information by video websites differs from diseases. A total of 56.5% of the video information on cholecystolithiasis [11], 16.2% on H1N1 influenza [17] and 1.6% on acute appendicitis in children [18] on YouTube were misleading. In our study, it was demonstrated that only one-fifth of website videos contain no scientifically oriented information. Only 36% of the independent users videos reviewed were considered to be useful compared with 90% useful doctors' videos.

The most commonly watched videos from independent users were those that contained misleading information, while the lowest number of views were from medical doctors and health information websites. These results also indicated that effective regulatory measures are needed to control scientifically accredited information. If misleading videos were less viewed by audiences, the harm might be reduced.

Regarding videos addressing colorectal cancer, it is highly difficult for laypeople or patients to distinguish between useful videos or those containing no accurate information. Our result indicates that an important element to assess the reliability of videos regarding colorectal cancer may be the ownership. If academic institutions represent the source, such as hospital/university or medical doctors, the videos may be regarded to be trustworthy on the basis of content [19]. The result is similar to those of other studies conducted outside of mainland China [15, 16].

We found that the average completeness scores were only 18% with a combination of aetiology, anatomy, symptoms, preventions, treatments and prognosis. Most of the included website videos only contained one of the above-mentioned categories. In all of the categories, treatments were the most frequently covered topic (70%). It is unlikely to expect all videos to comprehensively cover all aspects of colorectal cancer; therefore, it should be deemed that some videos, whilst incomplete, do contain precise and valuable content. Our results indicated that videos from medical doctors and health related institutions have significantly higher completeness scores than those posted by independent users. This result may suggest that videos posted by layperson mainly aim a more social goal and videos posted by health and medical organizations commonly take a more educational purpose. The study indicated that professionals should utilize their expertise and contribute to more high-quality videos for patients as information sources in mainland China.

When video contents were analyzed, the most universal topic were the treatment aspects of the colorectal cancer. This finding may indicate that most publishers thought that treatment factors are the most important component of colorectal cancer. Surgery, chemotherapy and radiotherapy have been the mainstay of colorectal cancer treatment. Approximately 70% of videos contained one of the above subjects. As the country of origin and application of TCM, China has a unique TCM theoretical system and effective treatment methods. In mainland China, TCM has been recognized as additional

Table 4 Sources and classification of detected videos

Ownership	Total Videos	Useful (Mv)	Misleading (Mv)	Useless (Mv)
Independent users	118	43 (7689)	41 (18123)	34 (5283)
Health information web site	60	48 (17517)	4 (895)	8 (9876)
Medical doctors	31	28 (24588)	1 (12583)	2 (19812)
Hospital/University	11	11 (8783)	0 (–)	0 (–)
News network	22	6 (7302)	6 (4567)	11 (12583)
Mean duration (min ± SD)	4.0 ± 2.3	5.5 ± 3.7	4.3 ± 2.1	3.7 ± 3.1

Abbreviation: *SD*, standard deviation; Mean viewership: *Mv*

Table 5 Completeness score

Completeness score	No	Mean ± SD
Aetiology	15	1.53 ± 0.51
Anatomy	27	–
Symptoms	43	2.77 ± 1.23
preventions	21	1.24 ± 0.44
Treatments	95	2.07 ± 0.83
Prognosis	35	1.77 ± 0.69
Total (max = 17)	136	3.07 ± 1.94

treatment methods for colorectal cancer [20]. Our study shows that approximately 128 videos were about the anticancer properties of traditional Chinese medicine.

In oncology, TCM is believed to have great healing properties such as exerting specific anticancer activity or chemosensitisation to help in the individualization of anticancer treatment [21, 22]. Chinese cancer patients frequently believe that herbs of TCM can help them against suffering from complications and to live well. Doctors trained in Western medicine published fewer videos than doctors trained in Chinese medicine. However, 30% of TCM videos contained misleading information that exaggerated actual effects and propaganda error messages, such as curing colorectal cancer. The highest total and misleading number of videos were posted by independent users. The meanest viewership was also from independent users. The misleading rate was higher than total misleading rate (21%). There have been a large number of controlled clinical studies published in Chinese literature, but high-level evidence for the clinical efficacy of TCM is still lacking [23]. Mistakes were often found in professorial papers and in internet videos.

Colorectal cancer is characterized by high prevalence, a long asymptomatic period and eminently treatable precancerous lesions which, taken together, suggests that screening is a prudent option in mainland China [24]. For this reason, facilitating the earlier diagnosis of colorectal cancer may have a more immediate impact on the existing cancer burden in mainland China. A total of 21 videos contained colorectal cancer screening, which represented only 15% of all useful videos. Almost all screening videos address the importance of a Faecal Occult Blood Test, digital rectal exam, and colorectaloscopy.

Despite the rising colorectal cancer incidence, public awareness is still low in mainland China. Chinese internet websites, such as Youku, provide a different medium to disseminate colorectal cancer information to the public by video instead of written text. The written healthy information is commonly at a considerably higher reading level for Chinese patients. This video-based information source can help them and their caregivers get better understanding. Use of the internet for colorectal cancer information is likely to increase. It is necessary that professional individuals and academic institutions adapt to the advanced technology and think useful methods to solve the variable quality of information uploaded on internet video websites in mainland China. To maximize the potential of video-based information and minimize the quantity misleading or unhelpful information, multilateral efforts between doctors, governments and websites are needed.

Limitations

First, the main bias of our study was the subjectivity of judgement. There were no validated tools for assessing video data. Therefore, our classification method was subjective. However, the kappa statistic indicated quite high agreement between two reviewers. Second, there was no website, such as YouTube, with a clearly dominant position in China. Selecting only one Chinese video website's data may lead to some bias. Youku was the most popular website and had the largest audience in China. Youku in mainland China may still reflect the reliability of information available on video websites. Third, our results comprise a snapshot of information distribution to illustrate the quality of internet video at one point in time in China mainland, and these results may change according to the videos that can be added or removed with time.

Table 6 Treatments of Traditional Chinese medicine

	Total videos	Useful (Mv)	Misleading (Mv)	Useless (Mv)
Independent users	62	23 (13532)	35 (20021)	4 (6577)
Health information web site	24	16 (23122)	3 (798)	5 (1201)
Medical doctors	7	7 (27349)	0 (–)	0 (–)
Hospital/University	1	1 (13653)	0 (–)	0 (–)
News network	3	1 (12021)	0 (–)	2 (13216)

Abbreviation: Mean viewership: *Mv*

Conclusions

Colorectal cancer videos represented by Youku in mainland China varied significantly by ownership and content and information incompleteness were fairly high. It is necessary that professionals adapt to the advanced technology and think useful methods to solve the variable quality of information uploaded on internet video websites in mainland China.

Abbreviation

TCM: Traditional Chinese medicine

Acknowledgements

None.

Funding

The study was supported by National Natural Scientific Foundation of China (No. 81700452) and in part by Japan China Sasakawa Medical Fellowship.

Availability of data and materials

The datasets used and/or analysed during this study are available from the corresponding author upon reasonable request. All the video were from Youku (www.youku.com) on November 15, 2016. Because everyday many new videos can be uploaded in the internet. Maybe now the number of videos have been changed in the website.

Authors' contributions

SZ, CS and XHJ developed the idea for the paper and led the development of the paper. SZ and YY conducted the data searches in Internet. SZ, DYY and BY extracted relevant data and analysis data. XHJ, CS and YY critically reviewed the manuscript for important intellectual content. SZ did the structure and writed the paper. All authors read and approved the final manuscript.

Ethics approval and consent to participate

This study did not require approval by the local Research Ethics Board as it involved publicly available data only.

Consent for publication

Not applicable.

Competing interests

The authors' declare that they have no competing interests.

Publisher's Note

Springer Nature remains neutral with regard to jurisdictional claims in published maps and institutional affiliations.

Received: 24 June 2018 Accepted: 22 November 2018
Published online: 04 December 2018

References

1. China NBoSo. China Statistical Yearbook 2016. Beijing: China Statistics Press; 2016.
2. Chen W, Zheng R, Baade PD, Zhang S, Zeng H, Bray F, Jemal A, Yu XQ, He J. Cancer statistics in China, 2015. CA Cancer J Clin. 2016;66:115–32.
3. Siegel RL, Miller KD, Fedewa SA, Ahnen DJ, Meester RG, Barzi A, Jemal A. Colorectal cancer statistics, 2017. CA Cancer J Clin. 2017;67(3):177–93.
4. China Internet Network Information Center Basic Data [(accessed on 18 June 2017)]. https://cnnic.com.cn/IDR/ReportDownloads/201706/P020170608523740585924.pdf .
5. China Science Communication Report on Chinese Netizens' Need and Search Behaviors of Science Communication, the Four Season [(accessed on 22 January 2017)] (In Chinese) http://index.baidu.com/special/kepu/.
6. Nason K, Donnelly A, Duncan HF. YouTube as a patient-information source for root canal treatment. Int Endod J. 2016;49:1194–200.
7. Chinese Web User Behavior Insight, iResearch PC index. [(accessed on 22 January 2017)] (In Chinese) http://index.iresearch.com.cn/pc/detail?id=8173&kid=78&Tid=57.
8. 20 Interesting Yoku Facts and Statistics [(accessed on 20 October 2018)] https://expandedramblings.com/index.php/youku-facts-statistics.
9. Keelan J, Pavri-Garcia V, Tomlinson G, Wilson K. YouTube as a source of information on immunization: a content analysis. JAMA. 2007;298:2482–4.
10. Azer SA, Algrain HA, AlKhelaif RA, AlEshaiwi SM. Evaluation of the educational value of YouTube videos about physical examination of the cardiovascular and respiratory system. J Med Internet Res. 2013;15:e24.
11. Azer SA, Aleshaiwi SM, Algrain HA, Alkhelaif RA. Nervous system examination on YouTube. BMC Med Educ. 2012;12:126.
12. Lee JS, Seo HS, Hong TH. YouTube as a source of patient information on gallstone disease. World J Gastroenterol. 2014;20:4066–70.
13. WHO. WHO Traditional Medicine Strategy: 2014–2023. Geneva: World Health Organization; 2013.
14. Ferlay JSI, Ervik M, Dikshit R, Eser SM. GLOBOCAN 2012 v1.0, Cancer incidence and mortality worldwide: IARC CancerBase no. 11, vol. 2013. Lyon: International Agency for Research on Cancer; 2017.
15. Hayanga AJ, Kaiser HE. Medical information on YouTube. JAMA. 2008;299:1424–5 author reply 1425.
16. Wu H, Liu L, Wang Y, Gao F, Zhao X, Wang L. Factors associated with burnout among Chinese hospital doctors: a cross-sectional study. BMC Public Health. 2013;13:786.
17. Pandey A, Patni N, Singh M, Sood A, Singh G. YouTube as a source of information on the H1N1 influenza pandemic. Am J Prev Med. 2010;38:e1–3.
18. Adorisio O, Silveri M, De Peppo F, Ceriati E, Marchetti P, De Goyet Jde V. YouTube and pediatric surgery. What is the danger for parents? Eur J Pediatr Surg. 2015;25:203–5.
19. Syed-Abdul S, Fernandez-Luque L, Jian WS, Li YC, Crain S, Hsu MH, Wang YC, Khandregzen D, Chuluunbaatar E, Nguyen PA, Liou DM. Misleading health-related information promoted through video-based social media: anorexia on YouTube. J Med Internet Res. 2013;15:e30.
20. Goss PE, Strasser-Weippl K, Lee-Bychkovsky BL, Fan L, Li J, Chavarri-Guerra Y, Liedke PE, Pramesh CS, Badovinac-Crnjevic T, Sheikine Y, Chen Z, Qiao YL, Shao Z, Wu YL, Fan D, Chow LW, Wang J, Zhang Q, Yu S, Shen G, He J, Purushotham A, Sullivan R, Badwe R, Banavali SD, Nair R, Kumar L, Parikh P, Subramanian S, Chaturvedi P, Iyer S, Shastri SS, Digumarti R, Soto-Perez-de-Celis E, Adilbay D, Semiglazov V, Orlov S, Kaidarova D, Tsimafeyeu I, Tatishchev S, Danishevskiy KD, Hurlbert M, Vail C, St Louis J, Chan A. Challenges to effective cancer control in China, India, and Russia. Lancet Oncol. 2014;15:489–538.
21. Chiu J, Yau T, Epstein RJ. Complications of traditional Chinese/herbal medicines (TCM)--a guide for perplexed oncologists and other cancer caregivers. Support Care Cancer. 2009;17:231–40.
22. Ernst E. Complementary and alternative medicine (CAM) and cancer: the kind face of complementary medicine. Int J Surg. 2009;7:499–500.
23. Ma B, Guo J, Qi G, Li H, Peng J, Zhang Y, Ding Y, Yang K. Epidemiology, quality and reporting characteristics of systematic reviews of traditional Chinese medicine interventions published in Chinese journals. PLoS One. 2011;6:e20185.
24. Huang W, Liu G, Zhang X, Fu W, Zheng S, Wu Q, Liu C, Liu Y, Cai S, Huang Y. Cost-effectiveness of colorectal cancer screening protocols in urban Chinese populations. PLoS One. 2014;9:e109150.

Ready to submit your research? Choose BMC and benefit from:

- fast, convenient online submission
- thorough peer review by experienced researchers in your field
- rapid publication on acceptance
- support for research data, including large and complex data types
- gold Open Access which fosters wider collaboration and increased citations
- maximum visibility for your research: over 100M website views per year

At BMC, research is always in progress.

Learn more biomedcentral.com/submissions

BMC

Zhang *et al. Mini-invasive Surg* 2019;3:2
DOI: 10.20517/2574-1225.2018.64

Mini-invasive Surgery

Review

Open Access

Current status of technique for Billroth-I anastomosis in totally laparoscopic distal gastrectomy for gastric cancer

Shun Zhang[1,2], Tetsu Fukunaga[1]

[1]Department of Gastroenterology and Minimally Invasive Surgery, Juntendo University Hospital, Tokyo 113-8421, Japan.
[2]Department of Gastroenterology Surgery, Shanghai East Hospital, Shanghai 200120, China.

Correspondence to: Dr. Tetsu Fukunaga, Department of Gastroenterology and Minimally Invasive Surgery, Juntendo University Hospital, 3-1-3 Hongo, Bunkyo-ku, Tokyo, Japan. E-mail: t2fukunaga@juntendo.cac.jp

How to cite this article: Zhang S, Fukunaga T. Current status of technique for Billroth-I anastomosis in totally laparoscopic distal gastrectomy for gastric cancer. *Mini-invasive Surg* 2019;3:2. http://dx.doi.org/10.20517/2574-1225.2018.64

Received: 2 Oct 2018 **First Decision:** 23 Oct 2018 **Revised:** 19 Dec 2018 **Accepted:** 24 Dec 2018 **Published:** 14 Jan 2019

Science Editor: Tetsu Fukunaga **Copy Editor:** Cui Yu **Production Editor:** Huan-Liang Wu

Abstract

Several reconstruction techniques are possible after totally laparoscopic distal radical gastrectomy. An optimal technique of digestive tract reconstruction after distal gastrectomy has not yet been established. The ideal reconstruction should be not only for doctors but also for patients. Alimentary intake, satisfactory nutritional status and easy performing should be all considered. The aim of the study was to describe the different Billroth-I reconstruction techniques that can be proposed after totally laparoscopic distal radical gastrectomy.

Keywords: Billroth-I anastomosis, totally laparoscopic distal gastrectomy, gastric cancer

INTRODUCTION

In 1994, Kitano firstly reported the technique for laparoscopy assisted Billroth-I (B-I)[1]. Since then, the use of laparoscopic treatments for gastric cancer is increasing due to the advantages of improving patients' quality of life. The new technologies and improved techniques have allowed laparoscopy gastrectomy to expand its indications and also to use this treatment for more complex cases. Japan Society of Endoscopic Surgery (JSES) conducted national survey every 2 years and indicated the percentage of laparoscopic procedures for gastric cancer was increasing. According to the 12th JSES survey, laparoscopic distal gastrectomy (LDG) was the most commonly performed type of laparoscopic gastrectomy[2].

In initial series for LDG, the majority of anastomoses were performed by laparoscopy assisted procedures.

© The Author(s) 2019. **Open Access** This article is licensed under a Creative Commons Attribution 4.0 International License (https://creativecommons.org/licenses/by/4.0/), which permits unrestricted use, sharing, adaptation, distribution and reproduction in any medium or format, for any purpose, even commercially, as long as you give appropriate credit to the original author(s) and the source, provide a link to the Creative Commons license, and indicate if changes were made.

OAE Publishing Inc.

The assisted procedures needed a mini-laparotomy incision of 60-70 mm in length made on the epigastrium[3]. But this procedure was not always easy to do, especially on patients with a small remnant stomach or obese patients with thick abdominal walls[4]. Anastomosis in such restricted space was usually difficult. With the accumulation of laparoscopic surgery experience and the development of laparoscopic devices, the gastrointestinal reconstruction now can be completed laparoscopically. Furthermore, unnecessary manipulations and the incision made on the epigastrium can be avoided.

The ideal reconstruction should be not only for doctors but also for patients. Alimentary intake, satisfactory nutritional status and easy performing should be all considered[5]. The B-I anastomosis is preferred by many doctors. It is said that the B-I anastomosis is simple and can provide a physiological route for food digestion and absorb without the need for an intestinal bypass or blind loop. Until now, various intracorporeal B-I anastomosis techniques were reported. In this article, we will review theses reconstruction methods.

HAND-SEWN ANASTOMOSIS IN INTRACORPOREAL B-I RECONSTRUCTION

After the accumulation of operative experience, some experienced surgeons had also presented intracorporeal hand-sewn techniques.

Takiguchi *et al.*[6] firstly reported B-I intracorporeal hand-sewn anastomosis in 2003. In his study, the Albert-Lembert method was used for the laparoscopic hand-sewing procedure and the anastomosis time was 90 min. Due to the complexity of the procedure and large amount of time required for anastomosis, it seemed that the hand-sewn anastomosis was not widely performed.

After almost 10 years, Matsuo *et al.*[7] reported another study about hand-sewn B-I anastomosis. They performed hand-sewn gastroduodenal anastomosis in 18 cases. The mean time of B-I anastomosis was 64.6 min. Matsuo *et al.*[7] described that 3-0 absorbing thread was placed in the lesser curvature as a supporting thread. A seromyotomy of the stomach was performed at the posterior wall. Both the remmant stomach and the duodenum's seromuscular layer were discontinuously sutured by extracorporeal knot-typing method. The lumen was opened with the stomach and the duodenum in a fixed status. The thread of the anchor suture was lifted upward to the abdominal wall. After that all layers of the stomach and the duodenum at the posterior wall were continuously sutured. The authors believed that hand-sewn anastomosis had some advantages. Hand-sewn sutures were not affected by the degree of freedom of the duodenum. Because staplers were not used, the anastomosis area was soft and highly flexible. The hand-sewn anastomosis was economical due to that less staplers were used.

CIRCULAR STAPLER USED IN INTRACORPOREAL B-I RECONSTRUCTION

In the open surgery, circular stapler is well applied as a standardized reconstruction method of gastroduodenostomy. However, when it was attempted laparoscopically, the situation was often the opposite.

Uyama *et al.*[8] firstly described intracorporeal B-I reconstruction using a circular stapling device and introduced one case in 1995. The method was defined by the same anatomic parameters as for the open B-I. After that, Moriya *et al.*[9] and Mayers and Orebaugh[10] also reported B-I gastroduodenostomy with a circular stapler device. Both techniques were complicated and difficult to operate, and especially at the left subcostal area where an extended incision was needed. The extra incision spoiled the merit of minimally invasive surgery.

There are 2 major difficulties when circular stapler is applied in laparoscopic gastroduodenostomy: the first is the lack of a safe and fast intracorporeal purse-string suture technique and the second is the difficulty in manipulating the stapler and the stomach in a narrow abdominal cavity. In order to enable the anvil placement into the dudenum, many strategies were applied, such as a triple stapling procedure[8] and the use of the natural pyloric ring with endo-looping of the duodenum[9]. Some techniques usually used in esophagoenteral anastomosis were also reported, such as using specially modified laparoscopic purse-string instrument[11] and opening the lumen and applying manual purse-string suture[12]. However, there are still many difficulties to be overcome.

Kim *et al.*[13] reported a method which seemed to be quick and economical. The atraumatic clamps were used to prevent slippage of the duodenum which was cut with ultrasonic shear instead of linear stapler. After that, a seromuscular suture was done around the duodenal outer layer along the clamp. Omori *el al.*[14] reported a method like reverse puncture technique used in total gastrectomy. The anvil secured with vicryl suture was inserted into the duodenum through semicircumferential duodenotomy. The needle was advanced to the anterior duodenal wall and then the duodenum was staple-transected. Finally, the center rod penetrated the duodenal wall. In this method the need for purse-string suture placement was totally eliminated.

Although the skill inserting anvil head in the duodenal stump can be improved, laparoscopically inserting the circular stapler into the remnant stomach was not always easy. After removing two-thirds to three-quarters of the stomach, the small remnant stomach was usually so small that it was difficult to insert the stapler, even from the epigastric region. Sometime it was very difficult to form a straight line among the duodenum, remnant stomach and the circular stapler from the umbilical wound. Omori *el al.*[15] described a novel method to insert the circular stapler to connect the anvil head. Firstly, the anvil head was passed through the posterior gastric wall with laparoscopic endloop, which can make the duodenum and remnant stomach form a straight line. Secondly anterior gastric suture was used to exteriorize the anvil shaft partly from the gastrotomy. And then the anvil shaft was advanced into the remnant stomach to make the anvil and the stapler join tighter.

LINEAR STAPLER INTRACORPOREAL B-I RECONSTRUCTION

Delta-shaped anastomosis and modified delta-shaped anastomosis

With the development of laparoscopic instruments and the continuous accumulation of surgical experience in recent years, linear stapler intracorporeal gastrointestinal anastomosis techniques have been developed.

Kanaya *et al.*[16] firstly reported a anastomosis method which used only laparoscopic linear staplers in the hope of overcoming the drawbacks of extracorporeal reconstruction. The method named delta-shaped anastomosis (DA) was a modified intracorporeal B-I reconstruction which was soon promoted. The emergence of the DA method made intracorporeal gastroduodenostomy possible, which greatly promoted the development of totally laparoscopic distal gastrectomy (TLDG). Utilization DA method allows gastroduodenal anastomosis with a diameter of at least 30 mm while avoiding stricture. Kanaya *et al.*[17] analyzed the result of initial 100 procedures and showed that the mean time of the anastomosis was 13 min and the rate of anastomosis related complications was rare in 2011.

But some surgeons worry about the blood supply affected during cutting, which would result in leakages ranging from 0.42% to 8.5%[17-20] and anatomical distortion which exist in twisting around the anastomosis[21]. In order to overcome the twisting around the anastomosis, some modified delta-shaped techniques were studied.

Huang *et al.*[22] reported modified DA in 2014. This was different from the conventional DA in closing the common stab incision of stomach and duodenum. In order to avoid the poor blood supply of the duodenum, the duodenal cutting was totally resected. The appearance of the anastomoses was changed from two intersections to only one as an inverted T-shape, which could decrease the anastomotic weak point. They reported comparable postoperative outcomes and showed that modified DA was technically safe and feasible[23] in another study.

After DA, many surgeons develop many other anastomosis methods based on linear stapler.

Triangulating stapling technique

Tanimura *et al.*[24] described the triangulating stapling technique based on a linear stapling device in 2008. The mean anastomotic time was 35 min. In this method, the duodenum can be transected in any direction, and by forming a triangle, the anastomosis lumen is made wide with no ischemic areas. Both stumps of duodenum and remnant stomach were opened fitting their caliber, the gastroduodenostomy linear stapler in the posterior wall and 2 everted sutures in the anterior wall with linear staplers. Before each direction anastomosis, both duodenum and remnant stomach were elevated ventrally with 3 stay sutures. But there are still some problems about this method. There were some differences between the stomach and duodenum in terms of lumen size, wall thickness, and wall extensibility. The first introverted anastomosis, which forms the base of the triangle, was cumbersome once all of the staple lines on the stomach and duodenum had been cut off.

Book-binding technique

Ikeda *el al.*[25] described the book-binding technique using linear stapler in 2012. The mean anastomotic time was 34 min. In their method, the duodenum was transected form the greater curvature side to the lesser curvature side. Small openings are made in the remnant stomach and duodenal stumps just wide enough to insert one of the jaws of the linear stapler. After the first stapling, there were three staple lines including those from the transection of the stomach and duodenum, which ran in parallel to the anterior wall. To prevent the formation of ischemic areas, a large opening was created on the anterior wall by transecting the entire duodenal stump and one-third of the gastric stump together with the anterior wall of the first anastomosis line. The anterior hole was then fired by linear stapler twice to close the large opening. Because a large opening was created on the anterior wall by transecting tissue and anastomosis line, maybe some tension was generated after the anterior hole was closed by the linear stapler. Further studies need to be done.

Linear-shaped gastroduodenostomy

Byun *et al.*[26] developed a linear-shaper gastroduodenostomy method by which the appearance of anastomosis was completed inverted T-shaped in 2009. Duodenum was transected from the greater curvature side to less side. One incision was done in the greater curvature of remnant stomach at the point 60 mm apart from the resected line. The other incision was done on the superior edge of the duodenal transection line. After creating the c anastomosis lumen, the common entry incision was closed by laparoscopic linear staplers. Finally, the greater curvature of stomach and the antero-superior of duodenum were perpendicular. By using this method, the rotation duodenum and remnant stomach was not needed which can reduce the risk of poor vascular supply. In their study, there were less bile reflux, gastritis degree and residual food grade compared to DA anastomosis in 6 months after surgery.

Augmented rectangle technique

In our group, we developed a method named augmented rectangle technique (ART) anastomosis. Three automatic laparoscopic linear staplers were used to create the gastroduodenostomy and the anastomotic opening was wide and less likely to become stenosed or twisted[27]. This method was easy and time-saving. We performed 160 LDG operations using this technique from December 2013 to August 2017. There were no postoperative complications associated with the reconstruction, such as anastomotic leakage, hemorrhage or stenosis. In the ART method, the duodenum was transected form the greater curvature side to less side. Small incisions were made in duodenal stumps and the greater curvature of remnant stomach in order to insert the jaws of the linear stapler. After inserting the stapler, the lesser curvature

Table 1. Summary of different methods applied in intracorporeal Billroth-I reconstruction

Year	Author	No.	Age	Method	Anastomotic time (min)	Operative time (min)	Blood loss	Postoperative stay (d)	Anastomosis-related complations
				Hand-sewn anastomosis in intracorporeal B-I reconstruction					
2003	Takiguchi *et al.*[6]	1	50	Hand-sewn	90	420	NS	7	0
2012	Matsuo *et al.*[7]	18	NS	Hand-sewn	64.6	NS	53.1 ± 91	21.7	0
				Circular stapler used in intracorporeal B-I reconstruction					
1995	Uyama *et al.*[8]	1	56	CS	NS	318	NS	14	0
2012	Kim *et al.*[13]	23	60.3 ± 11.3	CS	43.3 ± 15.4	209.7 ± 49.9	72.6 ± 47.9	7.7 ± 2.3	0
2012	Omori *et al.*[15]	20	NS	CS	NS	279	NS	9	0
				Linear stapler intracorporeal B-I reconstruction					
2011	Kanaya *et al.*[17]	100	65.5 ± 9.3	DA	13.0 ± 3.9	239.2 ± 53.2	92.6 ± 89.7	16.7 ± 13.8	1 (anastomotic leak)
2014	Okabe *et al.*[20]	185	NS	DA	NS	283	NS	NS	5 (anastomotic leak) 3 (delayed gastric emptying)
2011	Noshiro *et al.*[19]	71	70 ± 10	DA	NS	260 ± 56	63 ± 79	NS	6 (anastomotic leak)
2014	Huang *et al.*[22]	102	60 ± 12	Modified DA	12.2 ± 4.2	150.6 ± 30.2	48.2 ± 33.2	12.0 ± 6.5	2 (anastomotic leak)
2008	Tanimura *et al.*[24]	196	NS	TST	28 ± 4	249 ± 38	NS	NS	1 (anastomotic leak)
2013	Ikeda *et al.*[25]	9	59.3	BBT	34 ± 7	255 ± 13	50 ± 66	14.2 ± 2.3	0
2016	Byun *et al.*[26]	190	57.2 ± 12.5	LSGD	NS	147.9 ± 49.4	97.3 ± 95.7	6.8 ± 3.1	2 (anastomotic stenosis)
2018	Fukunaga *et al.*[27]	160	69.5 ± 10	ART	NS	227 ± 75	47.3 ± 50	12 ± 5	0

CS: Circular stapler; DA: delta-shaped anastomosis; TST: triangulating stapling technique; BBT: book-binding technique; LGSD: linear-shaped gastroduodenostomy; ART: augmented rectangle technique; NS: not stated

end of the duodenal stump was rotated externally by 90°. After the initial suturing between the remnant stomach and the duodenum, the two sides (posterior wall and cranial wall), the posterior wall and caudal wall, form a V-shape. A 30 mm linear stapler was applied to close the insertion holes up to the closest side of the duodenal resection margin. After gastric and duodenal resection margins were ensured to be close together, the 60 mm laparoscopic linear stapler was used to transect the duodenal resection margin to create the margin. After the above steps, all the previous linear staplers were removed from duodenal resection margin.

Thanks to the elimination of the stay sutures in the anastomosis site, the risk of leakage of the intestinal contents into the peritoneal cavity can be reduced with a result of reduced incidence of peritoneal abscess[28,29]. Removing the staple line of the duodenal stump without creating a T-shaped anastomotic region can avoid postoperative stenosis. The ART can create larger 4-sided anastomosis diameters than 3-sided ones, without worrying about whether the width of the opening will be reduced by the final stapling.

APPLICATION OF BARBED SUTURE IN INTRACORPOREAL ANASTOMOSES

Intracorporeal suturing and knot typing in some B-I anastomosis were time-consuming and tedious and especially these procedures were the last steps to do in LDG. But various devices have been developed to simplify the placement of intracorporeal sutures, and barbed suture is one such device. Using the barber suture could reduce the number of knot typing, the suturing efficiency and reduce the cost of intracorporeal reconstruction with staplers[30]. Lee *et al.*[30] used barber sutures to close entry hole in 354 patients instead of staplers with a result of minimizing the suturing time. There were no patients who needed to be converted to usual sutures or mechanical closure with staplers and only one patient presented with postoperative anastomotic bleeding.

CONCLUSION

Several reconstruction techniques are possible after TLDG [Table 1]. The best reconstruction is the one, that simplifies the technique, maintains satisfactory nutritional status and quality of life while keeping postoperative morbidity as low as possible. We believe that the new technologies and improved techniques will bring more benefits to patients and doctors.

DECLARATIONS

Authors' contributions

Study's conception and design: Zhang S, Fukunaga T
Writing the paper: Zhang S
Provided administrative, technical, and material support: Fukunaga T

Availability of data and materials

Not applicable.

Financial support and sponsorship

The study was supported part by Japan China Sasakawa Medical Fellowship.

Conflicts of interest

All authors declared that there are no conflicts of interest.

Ethical approval and consent to participate

Not applicable.

Consent for publication

Not applicable.

Copyright

© The Author(s) 2019.

REFERENCES

1. Kitano S, Iso Y, Moriyama M, Sugimachi K. Laparoscopy-assisted Billroth I gastrectomy. Surg Laparosc Endosc 1994;4:146-8.
2. Bandoh T, Shiraishi N, Yamashita Y, Terachi T, Hashizume M, et al. Endoscopic surgery in Japan: the 12th national survey(2012-2013) by the Japan Society for Endoscopic Surgery. Asian J Endosc Surg 2017;10:345-53.
3. Zhang DT, Yan D, Jiang X, Song C. A modified uncut roux-en-y anastomosis in laparoscopic-assisted distal gastrectomy: balance of the cost and minimally invasion. Trans Surg 2018;3:1-5.
4. Kim MG, Kim KC, Kim BS, Kim TH, Kim HS, et al. A totally laparoscopic distal gastrectomy can be an effective way of performing laparoscopic gastrectomy in obese patients (body mass index ≥ 30). World J Surg 2011;35:1327-32.
5. Piessen G, Triboulet JP, Mariette C. Reconstruction after gastrectomy: which technique is best? J Visc Surg 2010;147:e273-83.
6. Takiguchi S, Sekimoto M, Miyake Y, Fujiwara Y, Yasuda T, et al. Totally laparoscopic distal gastrectomy using the hand-sewn Billroth-I anastomotic technique: report of a case. Surg Today 2003;33:371-4.
7. Matsuo K, Shimura H, Tanaka S, Nakano M, Hashimoto T, et al. Laparoscopic distal gastrectomy with intracorporeal handsewn Billroth-I anastomosis (ICHSA). Surg Endosc 2012;26:2981-7.
8. Uyama I, Ogiwara H, Takahara T, Kato Y, Kikuchi K, et al. Laparoscopic Billroth I gastrectomy for gastric ulcer: technique and case report. Surg Laparosc Endosc 1995;5:209-13.
9. Moriya H, Shimizu S, Okano T, Yamaguchi S. Experimental study of laparoscopic gastrectomy: intracorporeal Billroth I gastroduodenostomy. Surg Laparosc Endosc 1997;7:32-7.
10. Mayers TM, Orebaugh MG. Totally laparoscopic Billroth I gastrectomy. J Am Coll Surg 1998;186:100-3.
11. Usui S, Nagai K, Hiranuma S, Takiguchi N, Matsumoto A, et al. Laparoscopy-assisted esophagoenteral anastomosis using endoscopic purse-string suture instrument "Endo-PSI (II)" and circular stapler. Gastric Cancer 2008;11:233-7.
12. Kinoshita T, Oshiro T, Ito K, Shibasaki H, Okazumi S, et al. Intracorporeal circular-stapled esophagojejunostomy using hand-sewn purse-string suture after laparoscopic total gastrectomy. Surg Endosc 2010;24:2908-12.
13. Kim HI, Woo Y, Hyung WJ. Laparoscopic distal gastrectomy with an intracorporeal gastroduodenostomy using a circular stapler. J Am Coll Surg 2012;214:e7-13.
14. Omori T, Nakajima K, Nishida T, Uchikoshi F, Kitagawa T, et al. A simple technique for circular-stapled Billroth I reconstruction in laparoscopic gastrectomy. Surg Endosc 2005;19:734-6.
15. Omori T, Tanaka K, Tori M, Ueshima S, Akamatsu H, et al. Intracorporeal circular-stapled Billroth I anastomosis in single-incision laparoscopic distal gastrectomy. Surg Endosc 2012;26:1490-4.
16. Kanaya S, Gomi T, Momoi H, Tamaki N, Isobe H, et al. Delta-shaped anastomosis in totally laparoscopic Billroth I gastrectomy: new

technique of intraabdominal gastroduodenostomy. J Am Coll Surg 2002;195:284-7.
17. Kanaya S, Kawamura Y, Kawada H, Iwasaki H, Gomi T, et al. The delta-shaped anastomosis in laparoscopic distal gastrectomy: analysis of the initial 100 consecutive procedures of intracorporeal gastroduodenostomy. Gastric Cancer 2011;14:365-71.
18. Kim BS, Yook JH, Choi YB, Kim KC, Kim MG, et al. Comparison of early outcomes of intracorporeal and extracorporeal gastroduodenostomy after laparoscopic distal gastrectomy for gastric cancer. J Laparoendosc Adv Surg Tech A 2011;21:387-91.
19. Noshiro H, Iwasaki H, Miyasaka Y, Kobayashi K, Masatsugu T, et al. An additional suture secures against pitfalls in delta-shaped gastroduodenostomy after laparoscopic distal gastrectomy. Gastric Cancer 2011;14:385-9.
20. Okabe H, Obama K, Tsunoda S, Tanaka E, Sakai Y. Advantage of completely laparoscopic gastrectomy with linear stapled reconstruction: a long-term follow-up study. Ann Surg 2014;259:109-16.
21. Lee Y, Tan CH, Park DJ. Current status of intracorporeal gastroduodenostomy and modified delta-shape anastomosis after distal gastrectomy for gastric cancer. J Vis Surg 2016;2:158.
22. Huang C, Lin M, Chen Q, Lin J, Zheng C, et al. A modified delta-shaped gastroduodenostomy in totally laparoscopic distal gastrectomy for gastric cancer: a safe and feasible technique. PLoS One 2014;9:e102736.
23. Huang CM, Lin M, Lin JX, Zheng CH, Li P, et al. Comparision of modified and conventional delta-shaped gastroduodenostomy in totally laparoscopic surgery. World J Gastroenterol 2014;20:10478-85.
24. Tanimura S, Higashino M, Fukunaga Y, Takemura M, Nishikawa T, et al. Intracorporeal Billroth 1 reconstruction by triangulating stapling technique after laparoscopic distal gastrectomy for gastric cancer. Surg Laparosc Endosc Percutan Tech 2008;18:54-8.
25. Ikeda T, Kawano H, Hisamatsu Y, Ando K, Saeki H, et al. Progression from laparoscopic-assisted to totally laparoscopic distal gastrectomy: comparison of circular stapler (i-DST) and linear stapler (BBT) for intracorporeal anastomosis. Surg Endosc 2013;27:325-32.
26. Byun C, Cui LH, Son SY, Hur H, Cho YK, et al. Linear-shaped gastroduodenostomy (LSGD): safe and feasible technique of intracorporeal Billroth I anastomosis. Surg Endosc 2016;30:4505-14.
27. Fukunaga T, Ishibashi Y, Oka S, Kanda S, Yube Y, et al. Augmented rectangle technique for Billroth I anastomosis in totally laparoscopic distal gastrectomy for gastric cancer. Surg Endosc 2018; doi: 10.1007/s00464-018-6266-1.
28. Jeong O, Jung MR, Park YK, Ryu SY. Safety and feasibility during the initial learning process of intracorporeal Billroth I (delta-shaped) anastomosis for laparoscopic distal gastrectomy. Surg Endosc 2015;29:1522-9.
29. Lin M, Zheng CH, Huang CM, Li P, Xie JW, et al. Totally laparoscopic versus laparoscopy-assisted Billroth-I anastomosis for gastric cancer: a case-control and case-matched study. Surg Endosc 2016;30:5245-54.
30. Lee SW, Kawai M, Tashiro K, Bouras G, Kawashima S, et al. Laparoscopic distal gastrectomy with D2 lymphadenectomy followed by intracorporeal gastroduodenostomy for advanced gastric cancer: technical guide and tips. Transl Gastroenterol Hepatol 2017;2:84.

日中笹川医学奨学金制度(学位取得コース)中間報告書
研究者用

第40期　　研究者番号：　G4008　　作成日：2019年3月　　日

氏名	XU　WENCHENG	許 文成	性別	M	生年月日　1987.08.11	
所属機関(役職)	湖北省中医院　薬事部　（　主管薬師　）					
研究先（指導教官）	東京薬科大学　薬学部　臨床薬理学教室　（　平野 俊彦　教授　）					
研究テーマ	ヒト末梢血リンパ球に対する生薬成分の効果 Immunosuppressive Efficacies of Herbal Compounds on Human Peripheral Blood Lymphocytes					
専攻種別	論文博士	☑	課程博士	□		

1．研究概要（1）

1）目的（Goal）

Sinomenine has been used as an antirheumatic drug in China. Glucocorticoid (GC) combined with sinomenine could be an alternative therapeutic approach. In this study, we evaluated the sinomenine potential effect on GC pharmacodynamics and disclosed the possible action mechanism.

2）戦略（Approach）

The combination pharmacodynamics of sinomenine and GC were examined by a human peripheral blood mononuclear cell (PBMC) culture system. Influences of drugs on P-glycoprotein function and glucocorticoid receptor (GR) translocation into nucleus were investigated to explain the possible mechanisms.

3）材料と方法（Materials and methods）

PBMC proliferation: Twenty milliliters of venous blood were taken from healthy subjects between 9:00 and 11:00 in the morning and heparinized. Then PBMCs were separated and suspended with RPMI 1640 medium to a final density of 1×10^6 cells/mL. After the culture with drugs, 10 μL of WST-8 assay reagent solution were added to each well, and the plate was incubated for another 3 h. The result was calculated by (Test-Blank)/(Control-Blank)×100%.

Functional assays for P-glycoprotein. P-glycoprotein function of PBMCs was measured *in vitro* by Rhodamine 123 efflux assay using flow cytometry.

Evaluation of GR translocation. To explain the additional effects of sinomenine on GC pharmacodynamics, we investigated sinomenine on GR expression levels and GR subcellular localization by Western Blot and immunofluorescence. Comparing with the T-cell mitogen activated PBMCs, human leukemic Jurkat T-cells were easier to obtain with higher established reliability, and thus chosen for this investigation, in addition to PBMCs.

4）実験結果（Results）

The median (range) of methylprednisolone IC_{50} values against the PBMC proliferation was 3.18 (0.45~6.81) ng/mL, whereas the median (range) IC_{50} values of methylprednisolone combined with 0.03, 0.3, 3 and 30 μM sinomenine were 1.85 (0.05~5.15), 0.83 (0.10~3.90), 0.56(0.09~1.62) and 0.59(0.05~1.30) ng/mL, respectively. Sinomenine significantly decreased the IC_{50} values of methylprednisolone and enhanced the immunosuppressive effect of methylprednisolone ($p<0.05$) (**Fig. A-B**). Sinomenine alone regulated the GR translocation in both Jurkat T cells and normal human PBMCs, and the combination of sinomenine and methylprednisolone showed stronger GR-modulatory activity than methylprednisolone alone (**Fig. E-F**). Thus, the additive effect of sinomenine to promote

1．研究概要（2）

the methylprednisolone immunosuppressive efficacy was suggested to be related to nuclear GR-translocation. However, sinomenine did not significantly inhibit the P-glycoprotein function in the activated PBMCs, suggesting that sinomenine's additive effect seemed to be unrelated with the P-glycoprotein inhibition (**Fig. C-D**).

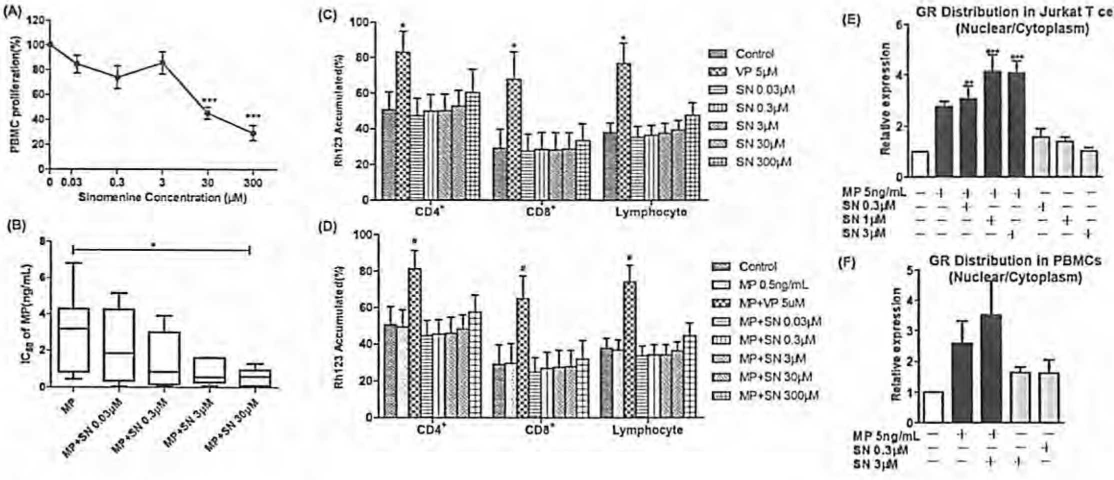

5）考察（Discussion）

The additional function of sinomenine tended to enhance the immunosuppressive efficacy of methylprednisolone to decrease the IC_{50} values (**Fig. B**). Sinomenine at ≥ 30 μM significantly inhibited the PBMC proliferation (**Fig. A**), meanwhile, the agent potentiated the GC pharmacodynamics significantly. Our findings in vitro may partially explain why GC combined with sinomenine has been used for the treatment of rheumatic arthritis patients in China[1,2].

Our data suggested that the additional function of sinomenine to enhance GC immunosuppressive efficacy seemed not to be related with P-glycoprotein target of PBMCs, since we did not observe the inhibitor capacity of SN (<300 μM) on the P-glycoprotein of PBMCs (**Fig. C-D**). 1 or 3 μM sinomenine combined with methylprednisolone exhibited larger efficacy to potentiate the GR translocation in Jurkat T cells, which was in accordance with the tendency of the agents on PBMC pharmacodynamics . Sinomenine was also confirmed to regulate the translocation of GR in PBMC culture system. Sinomenine alone seemed to stimulate the expression of GR in nucleus and sinomenine potentiated methylprednisolone-mediated moving of GR in cytoplasm of PBMC significantly (**Fig. E-F**). In conclusion, our study provided strong evidence that plant-derived alkaloid sinomenine potentiates the GC pharmacodynamics significantly.

6）参考文献（References）

[1] Liu, L, Resch, K, Kaever, V. 1994. *Int. J. Immunopharmacol.* **16**(8): 685-691.

[2] Chen, XM, Huang, RY, Huang, QC, *et al.* 2015. *Evid. Based Complement. Alternat. Med.* **2015**: 910376.

2. 執筆論文 Publication of thesis ※記載した論文を添付してください。Attach all of the papers listed below.

論文名 1 Title	Plant-derived alkaloid sinomenine potentiates glucocorticoid pharmacodynamics in mitogen-activated human peripheral blood mononuclear cells by regulating the translocation of glucocorticoid receptor					
掲載誌名 Published journal	Phytotherapy Research					
	2019 年 1 月	33 巻（号）	187 頁 ～ 196 頁	言語 Language	English	
第1著者名 First author	Wencheng Xu	第2著者名 Second author	Xiaoqin Wang	第3著者名 Third author	Yuanchao Tu	
その他著者名 Other authors	Hiroshi Masaki, Sachiko Tanaka, Kenji Onda, Kentaro Sugiyama, Haruki Yamada, Toshiho Hirano					
論文名 2 Title	Tetrandrine and cepharanthine induce apoptosis through caspase cascade regulation, cell cycle arrest, MAPK activation and PI3K/Akt/mTOR signal modification in glucocorticoid resistant human leukemia Jurkat T cells					
掲載誌名 Published journal	投稿中					
	年 月	巻（号）	頁 ～ 頁	言語 Language	English	
第1著者名 First author	Wencheng Xu	第2著者名 Second author	Xiaoqin Wang	第3著者名 Third author	Yuanchao Tu	
その他著者名 Other authors	Hiroshi Masaki, Sachiko Tanaka, Kenji Onda, Kentaro Sugiyama, Haruki Yamada, Toshiho Hirano					
論文名 3 Title						
掲載誌名 Published journal						
	年 月	巻（号）	頁 ～ 頁	言語 Language		
第1著者名 First author		第2著者名 Second author		第3著者名 Third author		
その他著者名 Other authors						
論文名 4 Title						
掲載誌名 Published journal						
	年 月	巻（号）	頁 ～ 頁	言語 Language		
第1著者名 First author		第2著者名 Second author		第3著者名 Third author		
その他著者名 Other authors						
論文名 5 Title						
掲載誌名 Published journal						
	年 月	巻（号）	頁 ～ 頁	言語 Language		
第1著者名 First author		第2著者名 Second author		第3著者名 Third author		
その他著者名 Other authors						

3. 学会発表 Conference presentation ※筆頭演者として総会・国際学会を含む主な学会で発表したものを記載してください。

※Describe your presentation as the principal presenter in major academic meetings including general meetings or international meetings.

学会名 Conference			
演　題 Topic			
開催日 date	年　月　日	開催地 venue	
形式　method	□ 口頭発表　Oral □ ポスター発表　Post	言語　Language	□ 日本語 □ 英語 □ 中国語
共同演者名 Co-presenter			
学会名 Conference			
演　題 Topic			
開催日 date	年　月　日	開催地 venue	
形式　method	□ 口頭発表　Oral □ ポスター発表　Post	言語　Language	□ 日本語 □ 英語 □ 中国語
共同演者名 Co-presenter			
学会名 Conference			
演　題 Topic			
開催日 date	年　月　日	開催地 venue	
形式　method	□ 口頭発表　Oral □ ポスター発表　Post	言語　Language	□ 日本語 □ 英語 □ 中国語
共同演者名 Co-presenter			
学会名 Conference			
演　題 Topic			
開催日 date	年　月　日	開催地 venue	
形式　method	□ 口頭発表　Oral □ ポスター発表　Post	言語　Language	□ 日本語 □ 英語 □ 中国語
共同演者名 Co-presenter			

4. 受賞（研究業績：Award (Research achievement)

名　称 Award name				
	国名 Country		受賞年 Year of	年　月
名　称 Award name				
	国名 Country		受賞年 Year of	年　月

5．本研究テーマに関わる他の研究助成金受給 Other research grants concerned with your resarch theme

受給実績 Receipt record	□ 有　　■ 無
助成機関名称 Funding agency	
助成金名称 Grant name	
受給期間 Supported	年　　月 ～　　年　　月
受給額 Amount received	円
受給実績 Receipt record	□ 有　　■ 無
助成機関名称 Funding agency	
助成金名称 Grant name	
受給期間 Supported	年　　月 ～　　年　　月
受給額 Amount received	円

6．他の奨学金受給 Another awarded scholarship

受給実績 Receipt record	■ 有　　□ 無
助成機関名称 Funding agency	China Scholarship Council
奨学金名称 Scholarship	State Scholarship Fund
受給期間 Supported	2018　年　12　月 ～　2019　年　11　月
受給額 Amount received	160,000 円

7．研究活動に関する報道発表 Press release concerned with your research activities

※記載した記事を添付してください。 Attach a copy of the article described below

報道発表 Press release	□ 有　　■ 無	発表年月日 Date of release	
発表機関 Released medium			
発表形式 Release method	・新聞　・雑誌　・Web site　・記者発表　・その他（　　　　）		
発表タイトル Released title			

8．本研究テーマに関する特許出願予定 Patent application concerned with your research theme

出願予定 Scheduled	□ 有　　■ 無	出願国 Application	
出願内容（概要） Application contents			

9．その他 Others

指導責任者（署名）平野俊彦 ㊞

日中笹川医学奨学金制度（学位取得コース）中間評価書
論文博士：指導教官用

Supported by 日本財団 THE NIPPON FOUNDATION

第 40 期　**研究者番号**：G4008　**作成日**：2019 年 3 月25日

氏　名	許　文成	XU　WENCHENG	性別	M	**生年月日** 1987.08.11
所属機関（役職）	湖北省中医院　薬事部（　主管薬師　）				
研究先（指導教官）	東京薬科大学　薬学部　臨床薬理学教室（　平野 俊彦　教授　）				
研究テーマ	ヒト末梢血リンパ球に対する生薬成分の効果 Immunosuppressive Efficacies of Herbal Compounds on Human Peripheral Blood Lymphocytes				
専攻種別	☑ 論文博士		☐課程博士		

研究者評価（指導教官記入欄）

成績状況	[✓ 優] 良　可　不可	取得単位数 取得単位数／取得すべき単位総数
学生本人が行った研究の概要	ヒト末梢血リンパ球のＴ細胞マイトゲン応答性増殖に対する、中国防已成分のテトランドリンと本邦防已成分のシノメニンの作用を in vitro にて検討した。これらの化合物はいずれも、上記リンパ球増殖を用量依存的に抑制することを明らかとした。またテトランドリンは、Ｔ細胞マイトゲンで刺激したヒト末梢血リンパ球からの炎症性サイトカインの産生を抑制し、末梢リンパ球中の制御性Ｔ細胞の比率を減少させることを示した。一方シノメニンは、副腎皮質ステロイドと併用することにより、Ｔ細胞マイトゲンで刺激したヒト末梢血リンパ球の増殖を相乗的に抑制することを初めて明らかとした。	
総合評価	【良かった点】 実験研究に前向きに取り組み、幾多の成果をあげるとともに、これらの成果を英論文としてまとめ、投稿にまで至っている。実験計画、実験の実施、データ解析、論文作成およびその投稿に関し、自身で遂行する能力を修得している。また、生薬成分がヒト免疫系に及ぼす作用の機序について、分子生物学的に検討するための新しい実験手法も修得しつつある。以上、博士論文を作成するにあたり、十分な能力を取得できたものと考える。 【改善すべき点】 今後は、本研究内容を臨床に応用していく必要がある。免疫関連疾患や腎疾患など、本研究に関連した臨床の知識はある程度身につけているが、これらの疾患の病態や薬物治療に関するより詳細かつ専門的な知識を修得し、現在の研究内容との関連を意識した臨床研究を行っていけるよう、一層の努力を期待したい。 【今後の展望】 現在は、与えられた研究テーマを確実にこなし、それらを論文としてまとめるのに余念がない。今後は、新しく魅力的な研究テーマを自ら発案できるよう、他分野の研究にも興味を持ち、種々の自然科学領域の知識を修得していってほしい。	
学位取得見込	現在までに、本人が筆頭著者となっている英文論文を３報発表している。また研究成果も、臨床応用も可能な極めて有用かつ斬新な内容を含んでいる。これらの観点から、博士論文作成が可能であるとみなし、現在当該論文の執筆にあたらせている。本年 10 月に本学大学院論文博士の予備審査を受け、来年２月に本審査、そして３月には博士号を取得できるよう指導している。	

評価者（指導教官名）平野俊彦　印

Received: 8 May 2018 | Revised: 5 September 2018 | Accepted: 26 September 2018
DOI: 10.1002/ptr.6215

RESEARCH ARTICLE

WILEY

Plant-derived alkaloid sinomenine potentiates glucocorticoid pharmacodynamics in mitogen-activated human peripheral blood mononuclear cells by regulating the translocation of glucocorticoid receptor

Wencheng Xu[1,2,4] | Xiaoqin Wang[2,3] | Yuanchao Tu[2,3] | Hiroshi Masaki[4] | Sachiko Tanaka[4] | Kenji Onda[4] | Kentaro Sugiyama[4] | Haruki Yamada[4] | Toshihiko Hirano[4]

[1] Department of Pharmacy, Hubei Provincial Hospital of Traditional Chinese Medicine, Wuhan, China

[2] Institute of Traditional Chinese Medicine, Hubei Province Academy of Traditional Chinese Medicine, Wuhan, China

[3] Department of Nephrology, Hubei Provincial Hospital of Traditional Chinese Medicine, Wuhan, China

[4] Department of Clinical Pharmacology, School of Pharmacy, Tokyo University of Pharmacy and Life Sciences, Hachioji, Japan

Correspondence
Toshihiko Hirano, PhD, Department of Clinical Pharmacology, School of Pharmacy, Tokyo University of Pharmacy and Life Sciences, 1432-1 Horinouchi, Hachioji, Tokyo 192-0392, Japan.
Email: hiranot@toyaku.ac.jp

Funding information
Grant-in-Aid for Scientific Research from the Ministry of Education, Science and Culture, Japan, Grant/Award Numbers: 15K08081 and 15 K08081; State Scholarship Fund of China Scholarship Council, Grant/Award Number: 201808420024; Japan China Sasakawa Medical Fellowship, Grant/Award Number: 2017816; Research Project for Practice Development of National TCM Clinical Research Bases, Grant/Award Number: JDZX2015194

Sinomenine has been used as an antirheumatic drug in China. Glucocorticoid combined with sinomenine could be an alternative therapeutic approach. In this study, we evaluated the sinomenine potential effect on glucocorticoid pharmacodynamics in vitro using a human peripheral blood mononuclear cell (PBMC) culture system. We also disclosed the possible action mechanism of sinomenine with a focus on P-glycoprotein function and glucocorticoid receptor (GR) translocation into nucleus. The median (range) of methylprednisolone IC_{50} values against the PBMC proliferation was 3.18 (0.45–6.81) ng/mL, whereas the median (range) IC_{50} values of methylprednisolone combined with 0.03, 0.3, 3, and 30 μM sinomenine were 1.85 (0.05–5.15), 0.83 (0.10–3.90), 0.56(0.09–1.62), and 0.59(0.05–1.30) ng/mL, respectively. Sinomenine significantly decreased the IC_{50} values of methylprednisolone and enhanced the immunosuppressive effect of methylprednisolone ($p < 0.05$). Sinomenine alone regulated the GR translocation in both Jurkat T cells and normal human PBMCs, and the combination of sinomenine and methylprednisolone showed stronger GR-modulatory activity than methylprednisolone alone. Thus, the additive effect of sinomenine to promote the methylprednisolone immunosuppressive efficacy was suggested to be related to nuclear GR-translocation. However, sinomenine did not significantly inhibit the P-glycoprotein function in the activated PBMCs, suggesting that sinomenine's additive effect seemed to be unrelated with the P-glycoprotein inhibition.

KEYWORDS
glucocorticoid receptor, immunosuppressive effect, methylprednisolone, peripheral blood mononuclear cells, P-glycoprotein, sinomenine

1 | INTRODUCTION

Sinomenine (SN), the main active alkaloid of herbal plant *Sinomenium acutum* (Thunb.), has been used to treat patients with rheumatoid arthritis (RA) in China since 1980s (Liu, Resch, & Kaever, 1994; Yamasaki, 1976). Synergistic effects of SN in combination with the immunosuppressive drugs tacrolimus and mycophenolic acid were confirmed in vitro (Vieregge, Resch, & Kaever, 1999). Therefore, immunosuppressive drugs combined with SN became to be an alternative therapeutic approach for RA patients in China.

P-glycoprotein (P-gp) is known to be localized on the immune cell membrane and acts as "efflux pumps," lowing the intracellular

© 2018 John Wiley & Sons, Ltd.

concentration of many lipophilic drugs and thus leading to glucocorticoid (GC) resistant (Garcia-Carrasco et al., 2015). Persistent expression of P-gp was identified on human peripheral blood lymphocytes (PBMCs) of GC resistant patients with systemic lupus erythematosus (Kansal, Tripathi, Rai, & Agarwal, 2016). GC resistant RA patients also companied with higher percentage of P-gp expression (Maillefert et al., 1996). SN was reported to down-regulate P-gp expression and inhibit the efflux function of P-gp in multidrug resistant bladder cancer cell model 253 J/DOX (Chen et al., 2014). Whether therapeutic dose of SN can suppress the function of P-gp in PBMCs, to potentiate immunosuppressive effect of GC is essential to be clarified.

An immune-cell culture system in vitro using the mitogen-activated PBMCs appeared to be able to simulate the immune network in vivo (Xu, Meng, Kusano, et al., 2017; Xu, Meng, Tu, et al., 2017). Hence, in the present study, we evaluated the potential additive effect of SN on GC pharmacodynamics in vitro to suppress the proliferation of T-cell mitogen activated PBMCs with a focus on P-gp function.

GCs mediate their effects by binding on the glucocorticoid receptor (GR), an intracellular hormone receptor, which in absence of a stimulus remain inactive in the cytoplasm. After GC binding, GRs undergo conformational change and translocate into nucleus where they homodimerize and act as a transcriptional regulator of many target genes by binding on GC response elements. Consequently, the GC-GR homodimer shows strong anti-inflammatory and immunosuppressive potencies (Onda et al., 2006; Panagiotou, Mihailidou, Brauhli, Katsarou, & Moutsatsou, 2018). To explain the additional effects of SN on GC pharmacodynamics, we investigated SN on GR expression levels and GR subcellular localization. Comparing with the T-cell mitogen activated PBMCs, human leukemic Jurkat T-cells were easier to obtain with higher established reliability and thus chosen for this investigation (Panagiotou et al., 2018), in addition to PBMCs.

2 | MATERIALS AND METHODS

2.1 | Reagents

Roswell Park Memorial Institute (RPMI) 1640 and fetal bovine serum (FBS) were purchased from Gibco BRL (Grand Island, NY, United States). Concanavalin A was purchased from Seikagaku Kogyo Co., Tokyo, Japan. SN (purity: more than 98%, biological source: *S. acutum*) and verapamil were purchased from Sigma Aldrich (St. Louis, MO, United States). SN was dissolved in ethanol (Wako Pure Chemical Industries, Ltd., Japan) at a concentration of 15 mM, filtered through a 0.2 μm membrane filter (Advantec Co., Japan) then stored at 4°C until use. The working concentrations were prepared by dilution with ethanol. Methylprednisolone (MP) was provided from Sigma Aldrich (St. Louis, MO, United States), dissolved in ethanol, and then stored at 4°C until use. The cell proliferation WST-8 assay kits were obtained from Dojindo Molecular Technologies, Inc., Japan. FITC mouse antihuman CD4 and APC Mouse Anti-Human CD8 were obtained from BD Biosciences, San Jose, CA, United States. GR antibody (G-5) was provided by Santa Cruz Biotechnology, INC (dilution 1:1000, # sc-393232). β-actin was purchased from Proteintech Group (dilution 1:5000, # 66009–1-Ig). Anti-TATA binding p antibody was obtained from Abcam (dilution 1:1000, # ab818). All other reagents were of the highest quality available from commercial vendors.

2.2 | Subjects

The present study was carried out in accordance with The Code of Ethics of the World Medical Association (Declaration of Helsinki). The study was approved by the Ethical Committee of Tokyo University of Pharmacy and Life Sciences, and written informed consent was obtained from all healthy subjects included in the study. The study included seven healthy subjects (four males and three females with a mean age of 26.8 years). These subjects had neither a history of immunological disorders nor a history of taking immunosuppressive drugs including GC.

2.3 | Isolation and culture of PBMCs and evaluation of drug effects in vitro

Twenty milliliters of venous blood were taken from healthy subjects between 9:00 and 11:00 in the morning and heparinized. This 20 mL sample size was the smallest possible to examine the effects of MP in the presence or absence of SN. The heparinized blood was loaded on 4 mL of Ficoll–Hypaque (Nakarai Co., Japan), and centrifuged at 1,300 g for 20 min. PBMCs were separated and suspended with RPMI 1640 medium containing 10% FBS, 100,000 IU/L penicillin, and 100 mg/L streptomycin to a final density of 1×10^6 cells/mL as we described previously (Xu, Meng, Kusano, et al., 2017).

One hundred ninety-four microliters of this cell suspension were loaded into wells of a 96-well plate. Concanavalin A, as a T-cell mitogen, was added to each well to a final concentration of 5 μg/mL. Subsequently, 2 μL of an ethanol solution containing MP were added to give final concentrations of 0.05, 0.5, 5, and 50 ng/mL. To examine the additional effect of SN combined with MP, 4 μL of an ethanol solution containing SN were subsequently added to give final concentrations of 0.03, 0.3, 3, 30, and 300 μM, respectively. Six microliters of ethanol were added to the control wells. The plate was incubated for 96 h in 5% CO_2 at 37°C. After the culture, 10 μL of WST-8 assay reagent solution were added to each well, and the plate was incubated for another 3 h. The PBMC proliferation was determined by measuring the optical density at 450 nm absorbance (ref. 650 nm). PBMCs proliferation was calculated by (Test-Blank)/(Control-Blank) × 100%. IC_{50} values of MP were obtained by GraphPad Prism 5. The culture wells of blank group included RPMI 1640 only. The culture system of test group included concanavalin A, SN, MP, or their combination and PBMC suspension. The culture wells of control group included concanavalin A, ethanol, and PBMC suspension (Xu, Meng, Tu, et al., 2017).

2.4 | Functional assays for P-glycoprotein in PBMCs

PBMCs were loaded with a final concentration of 2 μM of Rhodamine 123 (Rh123) and incubated for 10 min in 5% CO_2 at 37°C. Verapamil was used as a P-gp specific competitive inhibitor. Then, Rh123-treated cells were resuspended in a Rh123-free complete media with or without 0.03, 0.3, 3, 30, or 300 μM SN, combining with or without 0.5 ng/mL MP, 0.5 ng/mL MP, and 5 μM verapamil at 37°C for 180 min. After the efflux period, cells were washed twice with ice-cold PBS/10%FBS and were then stained with FITC mouse anti-human CD4 and APC Mouse Anti-Human CD8. After staining, the cells were washed twice and then resuspended in PBS and kept on ice in the dark until analysis by FACSCanto™ II as we described before (BD Biosciences, San Jose, CA) (Xu, Meng, Tu, et al., 2017).

2.5 | Jurkat cell culture

Human leukemic Jurkat T-cells were purchased from ATCC and cultured in RPMI 1640 medium containing 10% FBS, 100,000 IU/L penicillin and 100 mg/L streptomycin, at 37°C in a humidified atmosphere of 5% CO_2. In order to prepare cells for Western blot analysis and immunofluorescence, cells were cultured with different concentrations of SN (0.03, 0.1, 0.3, 1, and 3 μM) and/or MP (5 ng/mL).

2.6 | Western blot analysis

PBMCs and Jurkat cells were pre-treated with SN for 24 h and harvested in 2 h after MP treatment. Cytoplasmic and nuclear proteins were extracted using the Thermo Scientific NE-PER Nuclear and Cytoplasmic Extraction Reagents (Pierce Biotechnology, Rockford, IL, United States) according to the manufacturer's instruction. Protein concentration was quantified by Pierce BCA Protein Assay Kit (Thermo Scientific). Cytoplasmic and nuclear extractions were subsequently separated by SDS-polyacrylamide gel electrophoresis and then electrotransferred to hydrophobic polyvinylidene fluoride membrane (Immobilon-P; Merk Millipore, Darmstadt, Germany). Membranes were blocked with 5% skimmed milk for 1 h and washed with Tris-buffered saline/0.1% Tween-20 subsequently. Then, the membranes were incubated with primary antibodies against individual proteins overnight at 4°C. After triple washing with TBST, the membranes were continued to incubate with secondary antibody (Anti-mouse IgG, HRP-linked, #7076, Cell Signaling Technology, Inc.) at a dilution of 1:1000 for 1 h at room temperature. After triple washing with TBST, the signals were detected with an ECL or ECL Prime Western Blotting detection kit (GE Healthcare) in a luminescent image analyzer (Fujifilm; LAS-3000; Fujifilm, Tokyo, Japan). The images were subsequently quantitatively analyzed by ImageJ software (version 1.52e, National Institutes of Health, United States; http://imagej.nih.gov/ij).

2.7 | Immunofluorescence

In order to confirm the effect of SN on GR subcellular compartmentalization, Jurkat cells were subjected to immunofluorescence after treatment with SN and/or MP. Briefly, Jurkat cells were treated with SN for 24 h and then cultured with MP for another 2 h. Cells were harvested and fixed with 4% paraformaldehyde. After washing with PBS, cells were blocked for 1 h in PBS/3% BSA/0.5% triton-X at room temperature and incubated with primary GR antibody (1:100; G-5, sc-393232, Santa Cruz, CA, United States) overnight at 4°C. After washing with PBS, cells were continued to incubate with second goat anti-mouse antibody (1:500; Alexa Fluor 488 goat anti-mouse IgG/IgM, # A-10680, Invitrogen) for 1 h at room temperature, followed by 10 min nuclear staining with Hoechst 33342 (#17535, AAT Bioquest, Inc, CA, United States). Images were captured with a fluorescence microscope (Biozero BZ-8000 Series, Keyence, Japan). Signals were quantified using ImageJ program as mentioned above. A same size area was selected and the signal was measured in each nucleus, giving the intensity in arbitrary unit.

2.8 | Statistical analysis

Differences in the percentages of PBMC-proliferation, IC_{50} values of drugs, Rh123 accumulated amounts between controls and the cell fractions treated with serial concentrations of drugs, and protein expression levels were analyzed with Bonferroni tests. Expression and subcellular localization of GR in Jurkat cells after treatment with MP and/or SN were also analyzed with Bonferroni tests. Subcellular localization of GR in Jurkat cells following treatment with MP and/or SN and expression and subcellular localization of GR in PBMCs after treatment with MP and/or SN were performed using Dunnett's Multiple Comparison Test. These analyses were performed with GraphPad PRISM 5.0 (GraphPad Software Inc., San Diego, CA). In each case, two-sided p values (<0.05) were considered to be significant.

3 | RESULTS

3.1 | Effects of sinomenine in the presence or absence of methylprednisolone on mitogen-activated proliferation of PBMCs

The effects of SN on cell proliferation of PBMCs activated with a T-cell mitogen, concanavalin A, were examined in vitro. The results were presented in Figure 1A. SN at concentrations of 0.03–3 μM showed a little inhibitory effects, but SN at concentrations ≥30 μM exhibited strong suppressive effects on the activated proliferation of PBMCs ($p < 0.001$). The median (range) of SN IC_{50} values against the proliferation of PBMCs was 38.4 (2.51–187.00) μM.

Then, we continued to examine the additive efficacy of SN with MP to suppress the proliferation of mitogen-activated PBMCs of healthy subjects. The median (range) of MP IC_{50} values was 3.18 (0.45–6.81) ng/mL, whereas the median (range) IC_{50} values of the drug combined with 0.03, 0.3, 3, and 30 μM of SN decreased dose dependently to 1.85 (0.05–5.15), 0.83 (0.10–3.90), 0.56 (0.09–1.62), and 0.59 (0.05–1.30) ng/mL, respectively (Figure 1b). The additive effect of 30 μM SN compared with the suppressive effect of MP alone was statistically significant ($p < 0.05$) (Figure 1b).

3.2 | Effects of sinomenine in the presence or absence of methylprednisolone on P-glycoprotein function of PBMCs

Next, we investigated whether SN suppressed the function of P-gp in PBMCs to enhance the GC immunosuppressive effect. SN at 0.03 to 30 μM did not show any inhibitory ability on the efflux function of $CD4^+$, $CD8^+$ T cells, or lymphocytes. Three hundred micrometer of SN tended to suppress the P-gp function of these immune cells, but the effect was not significant (Figure 2a). Similar tendency was observed on the combination of MP and SN (Figure 2b). In contrast, verapamil at 5 μM significantly inhibited the efflux potencies of these cells ($p < 0.05$) (Figures 2a and b).

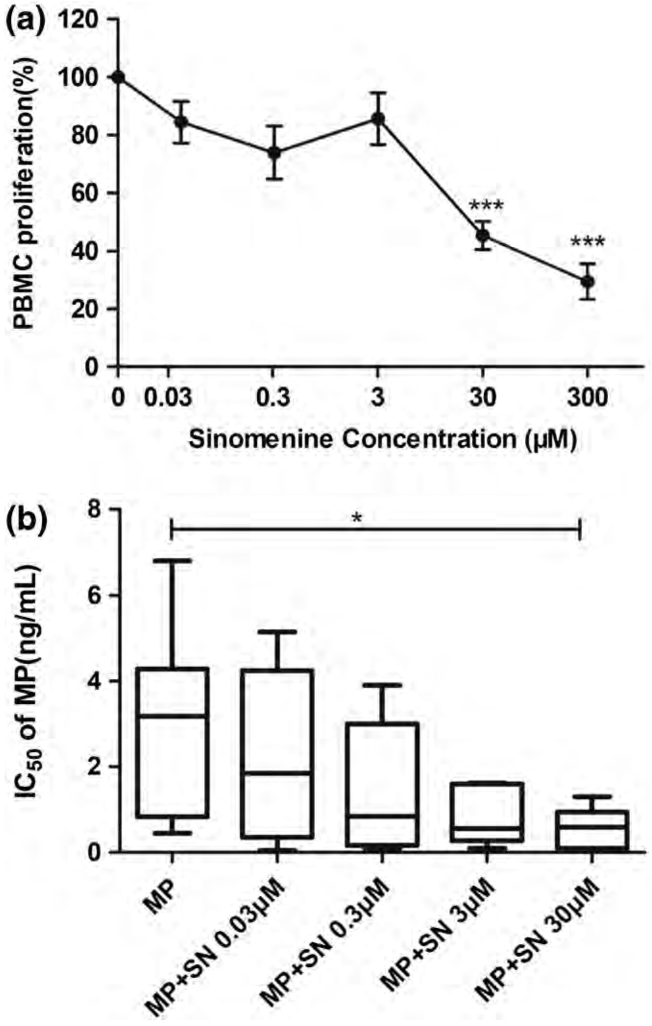

FIGURE 1 Effects of methylprednisolone (MP) in the presence or absence of sinomenine (SN) on proliferation of human peripheral blood mononuclear cells (PBMCs) activated with concanavalin A. Cell proliferation was determined by WST-8 assay. PBMC proliferation was estimated from the formula (Test-Blank)/(Control-Blank) × 100% (PBMC proliferation%). The IC_{50} values were calculated by GraphPad Prism 5. (a) Effects of SN on the proliferation of PBMCs. (b) IC_{50} values of methylprednisolone in the presence or absence of SN on the PBMC proliferation. The data were expressed as means ± S.E.M. Statistical analyses were performed using Bonferroni's multiple comparison tests, *$p<0.05$ and ***$p<0.001$. ($n = 6$)

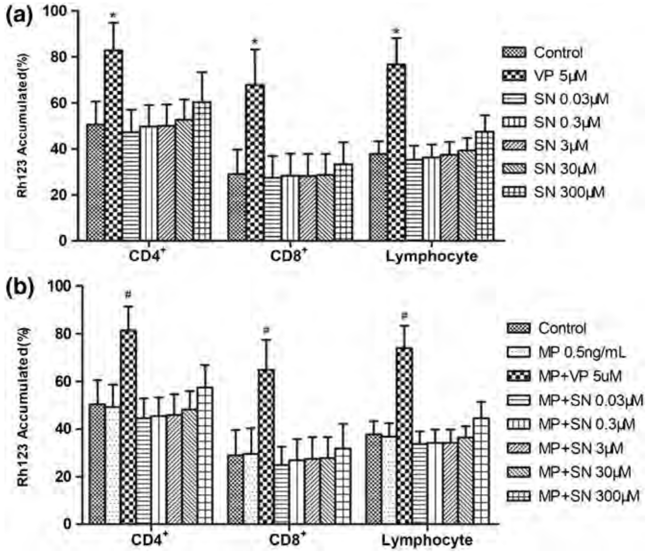

FIGURE 2 Rhodamine 123 (Rh123) accumulation in the human peripheral blood mononuclear cells (PBMCs) in the presence of sinomenine (SN). PBMCs were incubated with 2 μM Rh123 to uptake the fluorescent dye for 10 min. Subsequently, the cells were washed and cultured with or without drugs to efflux intracellular dye for 180 min. (a) Effects of SN, as compared with verapamil (VP), the prototype P-glycoprotein blocker, on P-glycoprotein function of PBMCs. PBMCs were incubated with 0.03–300 μM of SN for the efflux period, and the Rh123 accumulation was measured by flow cytometry. (b) P-glycoprotein inhibitory effect of SN in the presence of methylprednisolone (MP). Rh123 mean fluorescence intensities were detected by flow cytometry analysis, and Rh123 accumulated (%) was calculated by the formula: Dye accumulated/Dye uptaken × 100 (%). The results were expressed as means ± S.E.M. Statistical analyses were performed using Bonferroni's multiple comparison tests. $^{*}p<0.05$ as compared with the group without drugs. $^{\#}p<0.05$ as compared with the group treated with methylprednisolone alone. ($n = 3$)

3.3 | Effects of sinomenine in the presence methylprednisolone on GR expression level and GR subcellular localization of Jurkat cells

To further investigate the underlying mechanism of the additional effect of SN on GC, the GR expression levels and GR subcellular localization were evaluated. Nuclear and cytoplasmic extractions were subjected to Western blot analysis, respectively. As shown in Figure 3a, the levels of GR expression in nucleus was upregulated by 5 ng/mL of MP in Jurkat cells, and this GR upregulation effect of MP was significantly potentiated by 0.3 ($p < 0.05$), 1 ($p < 0.001$), and 3 μM ($p < 0.001$) of SN in a dose-dependent manner. Meanwhile, SN itself also seemed to increase the GR expression in the nucleus of Jurkat cells clearly, although these effects were negatively correlated to the dose of SN (dose range 0.3–3 μM) and the data were not significant. However, the levels of GR expression in cytoplasm were not dramatically changed by MP and/or SN (Figure 3b).

Subsequently, GR subcellular localization of Jurkat cells was analyzed by using the data of Figure 3a and 3b. As shown in Figure 3c, after 2 h treatment by MP, GR was translocated into nucleus, and thus, the ratio of GR distribution in nucleus and cytoplasm was changed by MP treatment. However the influences of SN in combination with MP on GR distribution were obvious, comparing with the MP alone. Therefore, the combination of MP and SN changed the ratio of GR distribution in nucleus and cytoplasm more strongly ($p < 0.01$).

3.4 | Effects of sinomenine alone on GR expression level and GR subcellular localization of Jurkat cells

As mentioned above, SN alone (0.3–3 μM) showed a tendency to upregulate GR expression levels in the nucleus of Jurkat cells, while in a negative dose-dependent manner. To confirm the effect of SN itself on GR translocation, enlarged range doses of SN (0.03–3 μM) were chosen to investigate (Figure 4). SN increased the GR expression in the nucleus dose-dependently. Among the five experimental doses of SN, 0.3 μM of SN showed the strongest effect to upregulate the

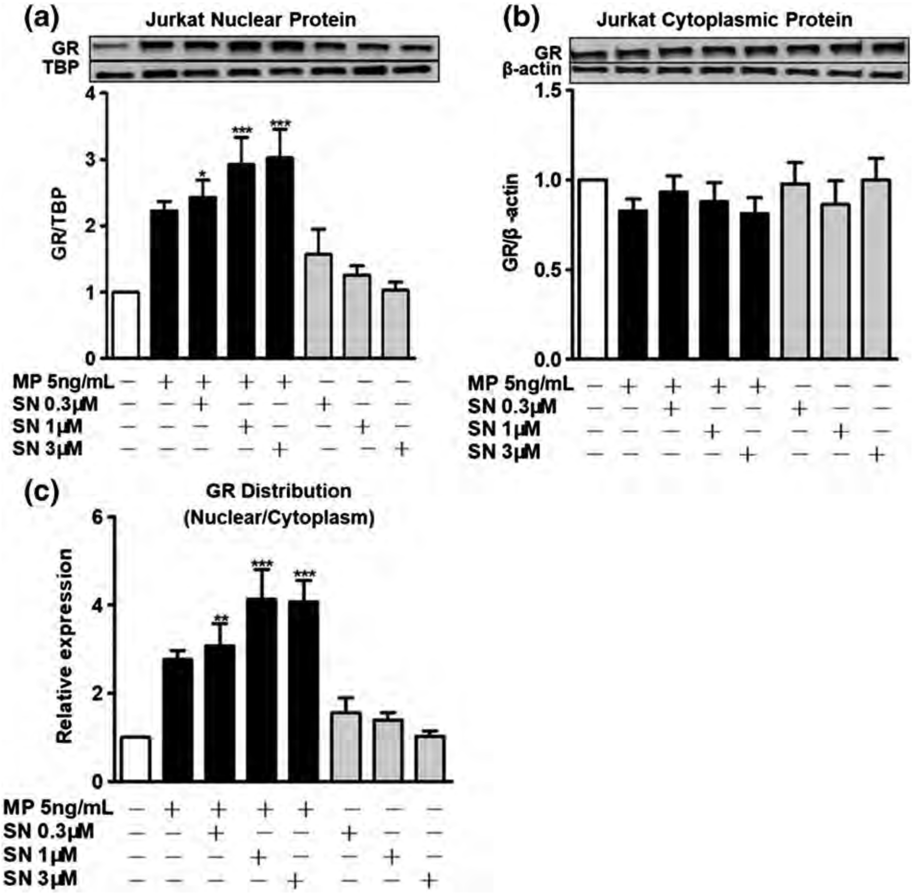

FIGURE 3 Expression and subcellular localization of glucocorticoid receptor (GR) in Jurkat cells after treatment with methylprednisolone (MP) and/or sinomenine (SN). Western blot analysis and densitometric quantification of total GR in nuclear (a) and cytoplasmic (b) extracts of Jurkat cells. Distribution of GR in nuclear/cytoplasmic fractions (c). Cells were pretreated with sinomenine for 24 h and harvested in 2 h after methylprednisolone treatment. Nuclear protein extracts were normalized to TATA-binding protein (TBP) and cytoplasmic extracts to β-actin. Data represented the mean ± S.E.M. of seven independent experiments. Statistical analyses were performed using Bonferroni's multiple comparison tests, $^{*}p < 0.05$, $^{**}p < 0.01$, and $^{***}p < 0.001$, as compared with the control group, respectively

nuclear GR expression level ($p < 0.01$, Figure 4a). All the experimental doses of SN had little effects on the cytoplasmic GR expression, although larger doses (≥1 μM) showed tendency to increase GR expression in cytoplasm (Figure 4b). Thus, the ratio of GR distribution in nucleus and cytoplasm changed by SN in a dose-dependent manner (Figure 4c).

3.5 | Effects of sinomenine in the presence or absence of methylprednisolone on GR subcellular compartmentalization using immunofluorescence in Jurkat cells

To provide morphologic evidence of cells, we further checked the subcellular distribution of GR in Jurkat cells after treatment with SN and/or MP by immunofluorescence. As shown in Figure 5a, treatment with MP (5 ng/mL) facilitated the nuclear translocation of GR. Similar results were observed after incubation of Jurkat cells with SN (0.03–3 μM, Figure 5a). Moreover, SN at 0.3 ($p < 0.05$), 1 ($p < 0.05$), and 3 μM ($p < 0.01$) significantly enhanced the translocation of GR in nucleus caused by MP in Jurkat cells (Figure 5b). These observations were in agreement with the results from Western blot (Figures 3 and 4).

3.6 | Effects of sinomenine in the presence or absence of methylprednisolone on GR expression level and GR subcellular localization of PBMCs

To confirm the modulation effects of SN and MP on the GR translocation, PBMCs obtained from three healthy subjects were fractionated, and GR expression levels were detected by Western blot. Figure 6a showed GR protein in the nucleus of PBMCs treated by the agents. 0.3 and 3 μM of SN tended to stimulate the GR expression in nucleus. Meanwhile, 3 μM of SN influenced the effect of MP (5 ng/mL) on nuclear GR expression slightly. However, in Figure 6b, the level of GR expression decreased by the combination of SN (3 μM) and MP (5 ng/mL) significantly ($p < 0.05$). The combination of MP and SN tended to change the distribution more largely (Figure 6c), which meant that SN could affect the GR subcellular localization of PBMCs.

4 | DISCUSSION

Comparing with isolated T cells, mitogen-activated PBMCs were much closer to the human immune network in vivo. Thus, PBMC culture

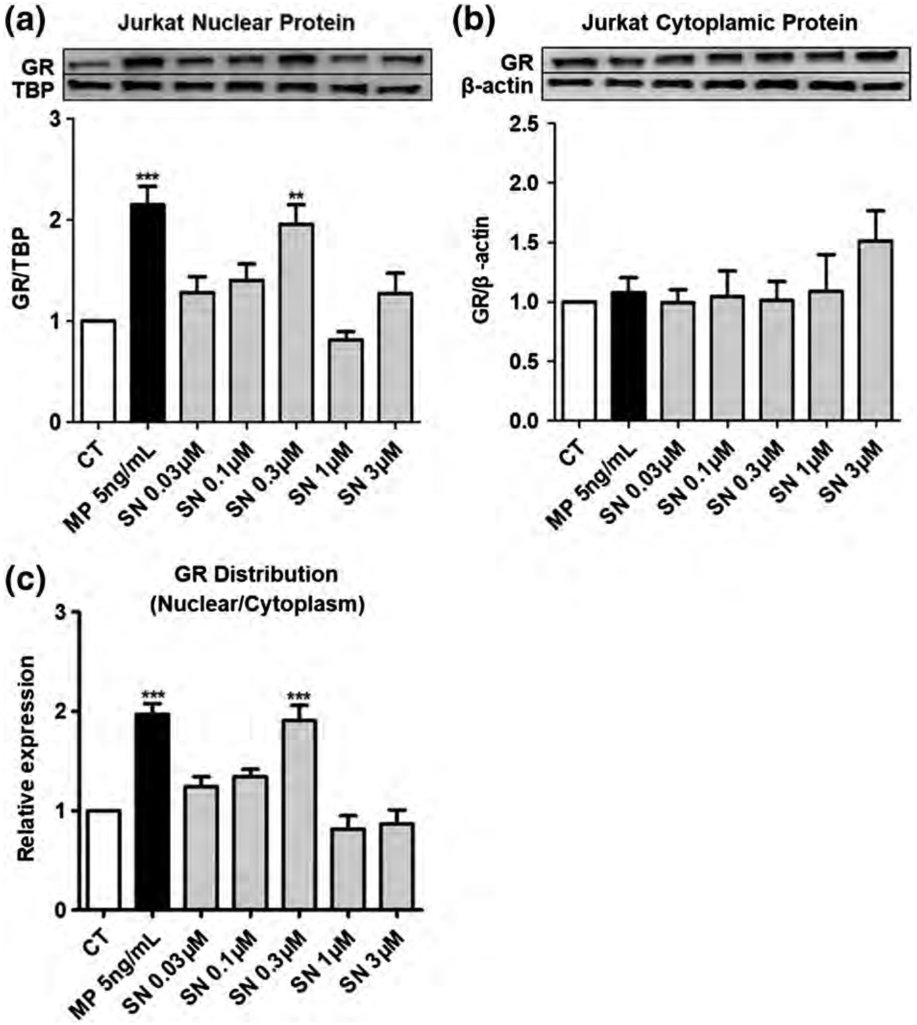

FIGURE 4 Expression and subcellular localization of glucocorticoid receptor (GR) in Jurkat cells after treatment with sinomenine (SN) alone. Western blot analysis and densitometric quantification of total GR in nuclear (a) and cytoplasmic (b) extracts of Jurkat cells. Distribution of GR in nuclear/cytoplasmic fractions (c). Cells were pretreated with sinomenine for 24 h and methylprednisolone (MP) for 2 h. Nuclear protein extracts were normalized to TATA-binding protein (TBP) and cytoplasmic extracts to β-actin. Data represented the mean ± S.E.M. of seven independent experiments. Statistical analyses were performed using Bonferroni's multiple comparison tests, $^{**}p < 0.01$ and $^{***}p < 0.001$, as compared with the control group, respectively

procedure was chosen to examine the SN potential effect on GC immunosuppressive efficacy (Xu, Meng, Tu, et al., 2017). SN at 0.03–3 μM tended to suppress the proliferation of PBMCs. The additional function of these concentrations of SN also tended to enhance the immunosuppressive efficacy of MP to decrease the IC_{50} values (Figures 1a and b). SN at ≥30 μM significantly inhibited the PBMC proliferation (Figure 1a); meanwhile, the agent potentiated the GC pharmacodynamics significantly (Figure 1b). Our findings in vitro may partially explain why GC combined with SN has been used for the treatment of RA patients in China, especially for those who were suffering from refractory RA.

A lot of studies reported that SN had anticancer function in breast and many other cancers due to its suppressive effects on cell proliferation and apoptosis promotion effects (Lu et al., 2013; Song et al., 2015; Song et al., 2018). To exclude a related cytotoxic effect of SN on human T cells, the SN effects on Jurkat T cells were examined by the WST-8 procedures in vitro. All the experimental concentrations of SN, including the highest one 300 μM, did not show any cytotoxic function in Jurkat T cells (data not shown).

Some GC-resistant refractory RA patients were known to be accompanied with higher P-gp expression on peripheral lymphocytes (Maillefert et al., 1996). Our data suggested that the additional function of SN to enhance GC immunosuppressive efficacy seemed not to be related with P-gp target of PBMCs because we did not observe the inhibitor capacity of SN (<300 μM) on the P-gp of PBMCs. Although SN (≥300 μM) tended to suppress the efflux function of P-gp on $CD4^+$, $CD8^+$ T cells, and lymphocytes (Figure 2), the pharmacokinetic parameters of SN tablet in PBMCs of healthy volunteers suggested that the serum concentration of SN could not accumulate with such higher concentration because the C_{max} of SN was 246.604 ± 71.165 ng/mL after taking 80 mg SN tablet once (Yan et al., 1997). Chen et al. reported that SN at 100 or 200 μg/mL exerted significant suppressive effects on P-gp of human bladder cancer 253 J/DOX cells (Chen et al., 2014). However, we did not

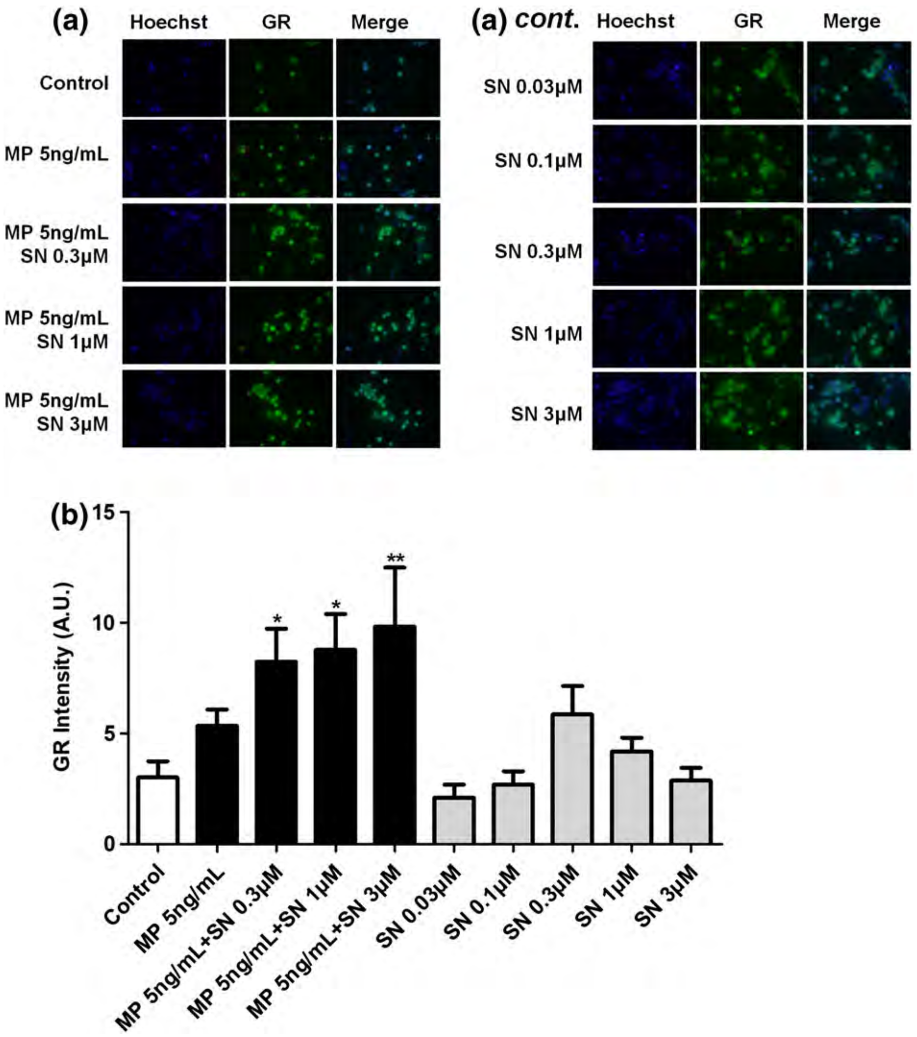

FIGURE 5 Subcellular localization of glucocorticoid receptor (GR) in Jurkat cells following treatment with methylprednisolone (MP) and/or sinomenine (SN). Cells were pretreated with sinomenine for 24 h and harvested in 2 h after methylprednisolone treatment. After washing, the cells were fixed and incubated with GR antibody, following with Alexa Fluor 488 goat anti-mouse IgG/IgM. Images were examined by a fluorescence microscope and the representative result of three independent experiments was shown as in Figure (a). Signals were quantified using ImageJ program, giving the intensity in arbitrary unit (b). GR intensity was expressed as means ± S.E.M. of three independent experiments and analyzed by using Dunnett's Multiple Comparison Test, *$p < 0.05$ and **$p < 0.01$ as compared with the control group, respectively [Colour figure can be viewed at wileyonlinelibrary.com]

obtain the similar results when using the human PBMC culture system, which suggested that P-gp inhibitory function of SN was a cell-type specific effect.

To elucidate the mechanism of the additional function of SN on MP pharmacodynamics, we continued to examine the effects of SN in the presence or absence of MP on GR expression level and GR subcellular localization by using Jurkat cells. SN alone at 0.03–3 μM increased the GR expression in nucleus, showing the maximum efficacy of the agent at these concentrations (Figure 4). In a recent study, Li et al. reported that 1 μM of SN was enough to stimulate the phosphorylation of the mitogen-activated protein kinase p-38, JNK, and ERK on human breast cancer cell lines MDA-MB-231 and MCF-7 (Li et al., 2014). However, lots of researches disclosed that GRs might be phosphorylated by these kinases that alter their binding affinity for GC, stability, translocation to the nucleus, binding to DNA, and interaction with other proteins, such as transcription factors and molecular chaperones (Barnes & Adcock, 2009; Hirano, 2007; Weige & Moore, 2007). The above information may partially explain the phenomenon that SN at concentrations more than 1 μM showed even lower efficacy on the GR translocation.

However, 1 or 3 μM SN combined with MP exhibited larger efficacy to potentiate the GR translocation (Figure 3), which was in accordance with the tendency of the agents on PBMC pharmacodynamics (Figure 1b). The information hinted that some other mechanisms were existed in the additional effect of SN at concentrations of 1–3 μM. One of the possible reasons was that higher doses of SN showed mild effect to increase the amount of GR, resulting in enhanced ability of GR translocation in Jurkat cytoplasm (Figure 4b), and thus the GR expression in nucleus increased. On the other hand, 1 μM SN was reported to prevent IL-1β-induced p-NF-κB p65 expression in human fibroblast-like synoviocytes (Yao, Zhao, Zhao, & Cai, 2017). SN significantly decreased the expression of p-NF-κB p65 in the cardiac tissue of diabetic rats in vivo (Jiang, Tong, Zhang, Liu, & Wang, 2017). Activation and/or increase in number of NF-κB might result in attenuation

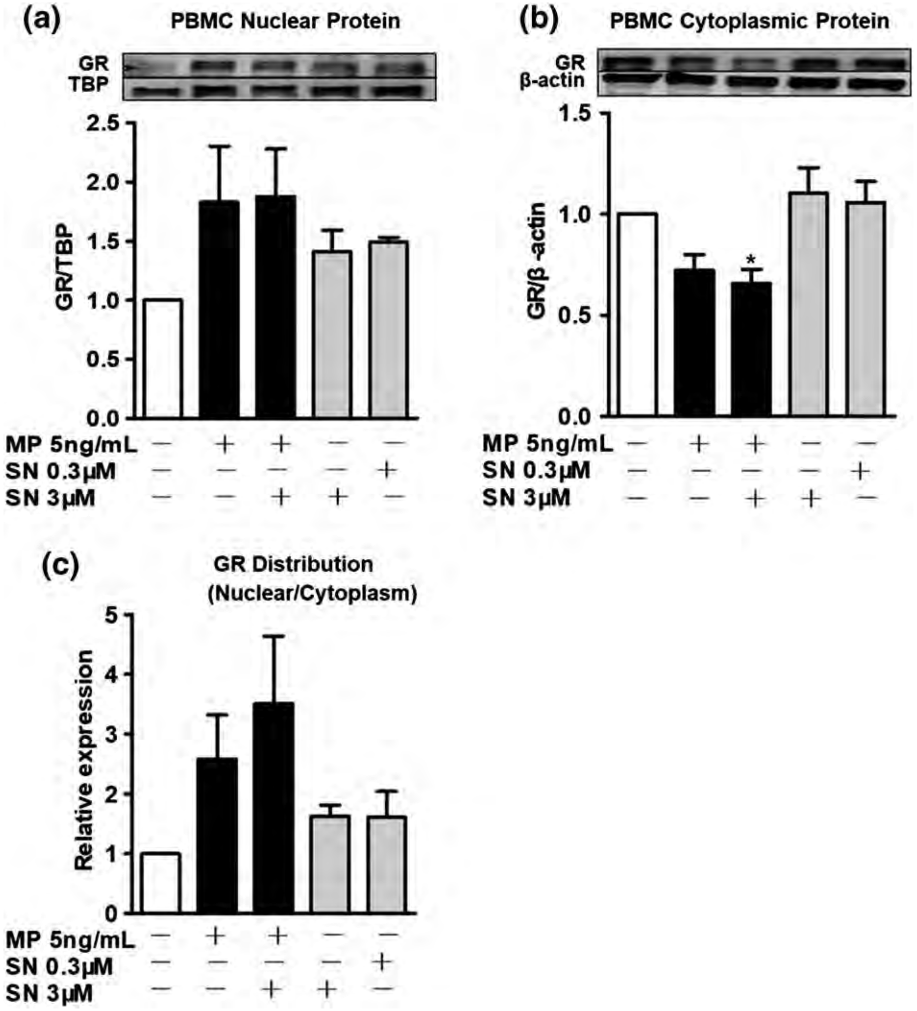

FIGURE 6 Expression and subcellular localization of glucocorticoid receptor (GR) in peripheral blood mononuclear cells (PBMCs) after treatment with methylprednisolone (MP) and/or sinomenine (SN). Western blot analysis and densitometric quantification of total GR in nuclear (a) and cytoplasmic (b) extracts of PBMCs. Distribution of GR in nuclear/cytoplasmic fractions (c). Cells were pretreated with sinomenine for 24 h and harvested in 2 h after methylprednisolone treatment. Nuclear protein extracts were normalized to TATA-binding protein (TBP) and cytoplasmic extracts to β-actin. Data represented the mean ± S.E.M. of more than three experiments. Statistical analyses were performed using Dunnett's Multiple Comparison Test, $^*p < 0.05$ as compared with the control group

of GC efficacy because proinflammatory transcription factors could interact with activated GC-GR complex in nucleus (Barnes & Adcock, 2009; Hirano, 2007). Therefore, the additional effect of SN on GR translocation might be related to the regulatory activity of SN on NF-κB signaling pathway. In agreement with our result of Western blot, morphologic evidences of immunofluorescence provided visual images, as shown in Figure 5.

Considering the differences of Jurkat T cells and PBMCs, we further investigated the GR-mediated effects of SN by using PBMCs. SN was confirmed to regulate the translocation of GR in PBMC culture system. SN alone seemed to stimulate the expression of GR in nucleus (Figure 6a) and SN potentiated MP-mediated moving of GR in cytoplasm of PBMC significantly (Figure 6b). All these findings in PBMCs were consistent with the results obtained from Jurkat cells. According to our best knowledge, it was the first time to report that *N*-Me morphinan alkaloid SN regulated GC receptor translocation in PBMCs and Jurkat T cells. In our experiment, we also certified that GR amounts in the nucleus of PBMCs was less abundant than that in Jurkat T cells because the signals of GR bands in Figure 6a were much weaker than those in Figure 3a and Figure 4a.

Low- to medium-dose GC had been shown to have not only anti-inflammatory but also modifying properties in RA. However, numerous fears about GC adverse events such as osteoporosis, glucose intolerance, and cardiovascular disease had arisen in RA. In fact, these serious side effects might be largely related to high-dose GC treatment (Santiago & da Silva, 2014). In contrast, two meta-analysis reports showed that SN alone or in combination with methotrexate was widely used for treating RA in China with better clinical efficiency and fewer adverse events (Chen, Huang, Huang, Chu, & Yan, 2015; Liu et al., 2016). Due to the higher tolerability and safety combined with the results of the present research, SN might be a proper agent to maintain the low-dose GC immunosuppressive efficacy and thus decrease the incidence rate of GC adverse events.

In conclusion, our study provided strong evidence that plant-derived alkaloid SN potentiates the GC pharmacodynamics significantly. However, the additional effect of SN had no relation to the

P-gp mediated efflux function because P-gp inhibitory function of SN was not observed in PBMC culture system. To disclose the underlying mechanism of SN actions, we found that SN itself regulates the GR translocation in both Jurkat T cells and normal human PBMCs, and the combination of SN and MP showed stronger GR-modulatory activity. These effects of SN were suggested to be beneficial for treatment of RA patients, and thus GC combined with SN would be an alternative and reasonable therapeutic approach for RA.

ACKNOWLEDGEMENTS

This work was supported in part by a Grant-in-Aid for Scientific Research from the Ministry of Education, Science and Culture, Japan (15 K08081), Research Project for Practice Development of National TCM Clinical Research Bases (JDZX2015194), Japan China Sasakawa Medical Fellowship (2017816), and State Scholarship Fund of China Scholarship Council (201808420024).

CONFLICT OF INTERESTS

None.

ORCID

Wencheng Xu http://orcid.org/0000-0003-4065-1548

REFERENCES

Barnes, P. J., & Adcock, I. M. (2009). Glucocorticoid resistance in inflammatory diseases. *The Lancet*, *373*(9678), 1905–1917. https://doi.org/10.1016/S0140-6736(09)60326-3

Chen, X. M., Huang, R. Y., Huang, Q. C., Chu, Y. L., & Yan, J. Y. (2015). Systemic review and meta-analysis of the clinical efficacy and adverse effects of Zhengqing Fengtongning combined with methotrexate in rheumatoid arthritis. *Evidence-Based Complementary and Alternative Medicine*, *2015*, 910376.

Chen, Y., Zhang, L., Lu, X., Wu, K., Zeng, J., Gao, Y., … He, D. (2014). Sinomenine reverses multidrug resistance in bladder cancer cells via P-glycoprotein-dependent and independent manners. *Pharmazie*, *69*(1), 48–54.

Garcia-Carrasco, M., Mendoza-Pinto, C., Macias Diaz, S., Vera-Recabarren, M., Vazquez de Lara, L., Mendez Martinez, S., et al. (2015). P-glycoprotein in autoimmune rheumatic diseases. *Autoimmunity Reviews*, *14*(7), 594–600.

Hirano, T. (2007). Cellular pharmacodynamics of immunosuppressive drugs for individualized medicine. *International Immunopharmacology*, *7*(1), 3–22. https://doi.org/10.1016/j.intimp.2006.09.020

Jiang, C., Tong, Y. L., Zhang, D., Liu, L. Z., & Wang, J. F. (2017). Sinomenine prevents the development of cardiomyopathy in diabetic rats by inhibiting inflammatory responses and blocking activation of NF-kappaB. *General Physiology and Biophysics*, *36*(1), 65–74. https://doi.org/10.4149/gpb_2016033

Kansal, A., Tripathi, D., Rai, M. K., & Agarwal, V. (2016). Persistent expression and function of P-glycoprotein on peripheral blood lymphocytes identifies corticosteroid resistance in patients with systemic lupus erythematosus. *Clinical Rheumatology*, *35*(2), 341–349. https://doi.org/10.1007/s10067-015-3079-7

Li, X., Wang, K., Ren, Y., Zhang, L., Tang, X. J., Zhang, H. M., et al. (2014). MAPK signaling mediates sinomenine hydrochloride-induced human breast cancer cell death via both reactive oxygen species-dependent and -independent pathways: An in vitro and in vivo study. *Cell Death & Disease*, *e1356*, 5.

Liu, L., Resch, K., & Kaever, V. (1994). Inhibition of lymphocyte proliferation by the anti-arthritic drug sinomenine. *International Journal of Immunopharmacology*, *16*(8), 685–691. https://doi.org/10.1016/0192-0561(94)90142-2

Liu, W., Qian, X., Ji, W., Lu, Y., Wei, G., & Wang, Y. (2016). Effects and safety of Sinomenine in treatment of rheumatoid arthritis contrast to methotrexate: A systematic review and Meta-analysis. *Journal of Traditional Chinese Medicine*, *36*(5), 564–577.

Lu, X. L., Zeng, J., Chen, Y. L., He, P. M., Wen, M. X., Ren, M. D., et al. (2013). Sinomenine hydrochloride inhibits human hepatocellular carcinoma cell growth in vitro and in vivo: Involvement of cell cycle arrest and apoptosis induction. *International Journal of Oncology*, *42*(1), 229–238. https://doi.org/10.3892/ijo.2012.1704

Maillefert, J. F., Maynadie, M., Tebib, J. G., Aho, S., Walker, P., Chatard, C., et al. (1996). Expression of the multidrug resistance glycoprotein 170 in the peripheral blood lymphocytes of rheumatoid arthritis patients. The percentage of lymphocytes expressing glycoprotein 170 is increased in patients treated with prednisolone. *British Journal of Rheumatology*, *35*(5), 430–435. https://doi.org/10.1093/rheumatology/35.5.430

Onda, K., Nagashima, M., Kawakubo, Y., Inoue, S., Hirano, T., & Oka, K. (2006). Mitogen-activated protein kinase kinase 1/extracellular signal-regulated kinase (MEK-1/ERK) inhibitors sensitize reduced glucocorticoid response mediated by TNFα in human epidermal keratinocytes (HaCaT). *Biochemical and Biophysical Research Communications*, *351*(1), 266–272. https://doi.org/10.1016/j.bbrc.2006.10.032

Panagiotou, C., Mihailidou, C., Brauhli, G., Katsarou, O., & Moutsatsou, P. (2018). Effect of steviol, steviol glycosides and stevia extract on glucocorticoid receptor signaling in normal and cancer blood cells. *Molecular and Cellular Endocrinology*, *460*, 189–199. https://doi.org/10.1016/j.mce.2017.07.023

Santiago, T., & da Silva, J. A. (2014). Safety of low- to medium-dose glucocorticoid treatment in rheumatoid arthritis: Myths and reality over the years. *Annals of the New York Academy of Sciences*, *1318*, 41–49. https://doi.org/10.1111/nyas.12428

Song, L., Liu, D., Zhao, Y., He, J., Kang, H., Dai, Z., … Zan, Y. (2015). Sinomenine inhibits breast cancer cell invasion and migration by suppressing NF-κB activation mediated by IL-4/miR-324-5p/CUEDC2 axis. *Biochemical and Biophysical Research Communications*, *464*(3), 705–710. https://doi.org/10.1016/j.bbrc.2015.07.004

Song, L., Liu, D., Zhao, Y., He, J., Kang, H., Dai, Z., … Xue, X. (2018). Sinomenine reduces growth and metastasis of breast cancer cells and improves the survival of tumor-bearing mice through suppressing the SHh pathway. *Biomed Pharmacotherapy*, *98*, 687–693. https://doi.org/10.1016/j.biopha.2017.12.065

Vieregge, B., Resch, K., & Kaever, V. (1999). Synergistic effects of the alkaloid sinomenine in combination with the immunosuppressive drugs tacrolimus and mycophenolic acid. *Planta Medica*, *65*(1), 80–82. https://doi.org/10.1055/s-2006-960446

Weigel, N. L., & Moore, N. L. (2007). Steroid receptor phosphorylation: A key modulator of multiple receptor functions. *Molecular Endocrinology*, *21*(10), 2311–2319. https://doi.org/10.1210/me.2007-0101

Xu, W., Meng, K., Kusano, J., Matsuda, H., Hara, Y., Fujii, Y., … Hirano, T. (2017). Immunosuppressive efficacy of tetrandrine combined with methylprednisolone against mitogen-activated peripheral blood mononuclear cells of haemodialysis patients. *Clinical and Experimental Pharmacology & Physiology*, *44*(9), 924–931. https://doi.org/10.1111/1440-1681.12797

Xu, W., Meng, K., Tu, Y., Tanaka, S., Onda, K., Sugiyama, K., … Yamada, H. (2017). Tetrandrine potentiates the glucocorticoid pharmacodynamics via inhibiting P-glycoprotein and mitogen-activated protein kinase in mitogen-activated human peripheral blood mononuclear cells. *European Journal of Pharmacology*, *807*, 102–108. https://doi.org/10.1016/j.ejphar.2017.04.007

Yamasaki, H. (1976). Pharmacology of sinomenine, an anti-rheumatic alkaloid from Sinomenium acutum. *Acta Medica Okayama*, *30*(1), 1–20.

Yan, X. H., Li, H. D., Peng, W. X., Liu, F. Q., Shao, Y., & He, Y. Q. (1997). Determination of sinomenine HCl in serum and urine by HPLC and its pharmacokinetics in normal volunteers. *Acta Pharmaceutica Sinica*, *32*(8), 620–624.

Yao, R. B., Zhao, Z. M., Zhao, L. J., & Cai, H. (2017). Sinomenine inhibits the inflammatory responses of human fibroblast-like synoviocytes via the TLR4/MyD88/NF-kappaB signaling pathway in rheumatoid arthritis. *Pharmazie*, *72*(6), 355–360. https://doi.org/10.1691/ph.2017.6946

How to cite this article: Xu W, Wang X, Tu Y, et al. Plant-derived alkaloid sinomenine potentiates glucocorticoid pharmacodynamics in mitogen-activated human peripheral blood mononuclear cells by regulating the translocation of glucocorticoid receptor. *Phytotherapy Research*. 2019;33:187–196. https://doi.org/10.1002/ptr.6215

日中笹川医学奨学金制度(学位取得コース)中間報告書
研究者用

Supported by 日本財団 THE NIPPON FOUNDATION

第40期　研究者番号: G4009　作成日:2019年3月08日

氏名	LI HONGYANG	李 弘揚	性別	F	生年月日 1993.04.19
所属機関(役職)	天津中医薬大学 鍼灸推拿学院 (医師)				
研究先(指導教官)	金沢大学附属病院 漢方医学科 (小川 恵子 臨床教授・特任准教授)				
研究テーマ	画像解析技術を用いた人体における漢方薬の評価				
専攻種別	論文博士	□	課程博士	☑	

1. 研究概要(1)

1)目的(Goal)

本研究では、主観的な尺度と客観的な測定方法を用いて、漢方治療による治療効果と望診上の改善を評価することを目的とする。

2)戦略(Approach)

漢方医学は、約1500年の長きにわたって日本人の健康を支えてきた日本の伝統医学である。[1]現在、日本では漢方医学(湯液・鍼灸)が広く用いられている。特に漢方薬は医療保険制度の中で医師が処方しており、漢方医学科でも年々患者数は増加している。

漢方医学は、患者の病状(訴え)や体質を重視し、その結果から処方する。湯液は1剤に複数の有効成分が含まれているため、多様な症状に効くのが大きな特徴である。また、鍼灸は人体の気の流れを整えることができる。湯液と鍼灸を併用すると、湯液と鍼灸それぞれの特徴を合わせて治療をすることで効率が上がり、相乗効果が得られる。しかも、我々が以前行った研究では、入院中の患者を対象に漢方治療(湯液・鍼灸)による治療を行い、高い効果を実感している。[2-4]

漢方の診察は望診・聞診・問診・切診の「四診」を用いて行う。その中の望診は視覚により、患者の全身状態、顔色、舌色、舌質、分泌物等を見て患者の状態を判断する主観的な診察法である。漢方の理論では、人体の気血の盛衰が顔面に現れる、したがって、顔面を望診することは全身の気血の状態を知ることにつながる。望診は医師の主観的な感覚に基づいて判断することである、客観化させる必要があると思う。そして、本研究では、当科における患者への漢方治療前後に皮膚の微小循環の変化と肌のキメの変化、Numerical Rating Scale(NRS)(NRS:痛みの程度を数字で選択する方法)による改善度を評価検討する事で、漢方治療法の有効性を数値化し、望診の概念を発展させ、客観化させる。

3)材料と方法(Materials and methods)

①研究方法

金沢大学附属病院漢方医学科を受診した患者カルテの内容(・診療記録・診療経過・使用薬剤名(処方内容)など)を使用し、患者への漢方医学(鍼灸及び湯液)併用治療の使用頻度や、どのような主訴に対して使用しているかの調査、通常の診察に伴って撮影する皮膚画像を用いて、MATLABを使って、短直線マッチング法(皮膚の凹凸を線上に画像修正することでキメを評価する方法)[5, 6]で解析し、皮膚微小循環の改善[7]とNRSによる改善度の評価による評価を行う。

②研究対象者の選定方針

(1)適格基準

金沢大学漢方医学科を受診した患者

(2)除外基準

特記事項なし

(3)目標数:1500名

金沢大学漢方医学科の診療を受ける患者は年間約1000名であり、2021年までに1500名の患者数が見込まれる。

1．研究概要(2)

③研究実施期間

研究実施期間:倫理承認日～2021年5月31日(西暦)
研究対象期間:倫理承認日～2021年3月31日
解析期間　:2020年4月1日～2021年5月31日

④観察・検査・報告項目

・カルテの内容:診療記録(視診、聴診、嗅い、問診、触診、腹診、舌診、脈診、疼痛NRS、倦怠感NRS、唾液アミラーゼ活性・診療経過・使用薬剤名(処方内容)など)
・患者への漢方医学(鍼灸及び湯液)併用治療の使用頻度や、どのような主訴に対して使用しているか
・経過中の血液検査の結果
・LEA.O2Cで測定する皮膚表層約2㎜と8㎜の血流量、血流速度、酸素とヘモグロビン値
・カメラで皮膚を撮影、得た画像を短直線マッチング法で解析した結果

⑤統計的事項

解析項目
患者カルテの内容(・診療記録・診療経過・使用薬剤名(処方内容)など)
LEA.O2Cで測定する皮膚表層約2㎜と8㎜の血流量、血流速度、酸素とヘモグロビン値
短直線マッチング法で解析した皮溝の面積率、皮溝の平均太さ、短直線の傾きの標準偏差
解析方法
主に観察研究であるため、同一個体の前後比較、もしくは、多変量解析を行う。

4)実験結果(Results)

現在、臨床研究倫理審査中である。

5)考察(Discussion)

現在、臨床研究倫理審査中である。

6)参考文献(References)

[1]安井廣迪, 医学生のための漢方医学.千葉.東洋学術出版社.2008:2-7.
[2] Keiko Ogawa, et al. ″Optical examination of the efficacy of contact needle therapy for chemotherapy-induced peripheral neuropathy: intergration of inspection in Kampo therapy with color spectrum information,″ Artificial Life and Robotics, pp. 1-5.
[3] Keiko Ogawa, et al. ″ Optical Examination of the Efficacy of Contact Needle Therapy for Chemotherapy-Induced Peripheral Neuropathy: Integration of the Inspection of Kampo Therapy and the Color Spectrum Information ″ The Journal of Alternative and Complementary Medicine, vol. 20, no. 5, pp. 45-46.
[4] Keiko Ogawa, et al. ″A case of extensive pharyngeal vascular malformation successfully treated with Kampo medicine.″ Auris Nasus Larynx,vol.45,no.1,pp.190-193.
[5] Hiroshi Kobayashi, et al. ″Proposal of Quantitative Index of Skin Texture by the Image Processing and Its Practical Application″ Transactions of the JSME, vol. 76, no. 764, pp. 138-145.
[6] Mihiro Uchida, Rina Akaho, et al. ″Image-based Non-contact Monitoring of Skin Texture Changed by P5loerection for Emotion Estimation″ February 15, 2018, 5th Symposium of the color of Digital Imaging in Biomedicine.
[7]Stefan Beckert, DRMED, MD, Maria B. Witte, MD, et al.″The Impact of the Micro-Lightguide O2C for the Quantification of Tissue Ischemia in Diabetic Foot Ulcers″Diabetes Care, vol. 27, no. 12, pp. 2863-2867.

2. 執筆論文　Publication of thesis　※記載した論文を添付してください。Attach all of the papers listed below.

論文名 1 Title							
掲載誌名 Published journal							
	年	月	巻(号)	頁 ～	頁	言語 Language	
第1著者名 First author		第2著者名 Second author		第3著者名 Third author			
その他著者名 Other authors							
論文名 2 Title							
掲載誌名 Published journal							
	年	月	巻(号)	頁 ～	頁	言語 Language	
第1著者名 First author		第2著者名 Second author		第3著者名 Third author			
その他著者名 Other authors							
論文名 3 Title							
掲載誌名 Published journal							
	年	月	巻(号)	頁 ～	頁	言語 Language	
第1著者名 First author		第2著者名 Second author		第3著者名 Third author			
その他著者名 Other authors							
論文名 4 Title							
掲載誌名 Published journal							
	年	月	巻(号)	頁 ～	頁	言語 Language	
第1著者名 First author		第2著者名 Second author		第3著者名 Third author			
その他著者名 Other authors							
論文名 5 Title							
掲載誌名 Published journal							
	年	月	巻(号)	頁 ～	頁	言語 Language	
第1著者名 First author		第2著者名 Second author		第3著者名 Third author			
その他著者名 Other authors							

3. 学会発表 Conference presentation ※筆頭演者として総会・国際学会を含む主な学会で発表したものを記載してください,

※Describe your presentation as the principal presenter in major academic meetings including general meetings or international meeting

学会名 Conference	The 24th International Symposium on Artificial life and Robotics			
演題 Topic	The effect of different types of acupuncture manipulations on shoulder pain and cardiovascular dynamics			
開催日 date	2019 年 1 月 24 日	開催地 venue	日本 別府	
形式 method	☑ 口頭発表 Oral	□ ポスター発表 Poster	言語 Language	□ 日本語 ☑ 英語 □ 中国語
共同演者名 Co-presenter	Norio Tomita, Mako Iwahashi, Kanji Kawasaki, Akiko Shirai, Keiko Ogawa			
学会名 Conference				
演題 Topic				
開催日 date	年 月 日	開催地 venue		
形式 method	□ 口頭発表 Oral	□ ポスター発表 Poster	言語 Language	□ 日本語 □ 英語 □ 中国語
共同演者名 Co-presenter				
学会名 Conference				
演題 Topic				
開催日 date	年 月 日	開催地 venue		
形式 method	□ 口頭発表 Oral	□ ポスター発表 Poster	言語 Language	□ 日本語 □ 英語 □ 中国語
共同演者名 Co-presenter				
学会名 Conference				
演題 Topic				
開催日 date	年 月 日	開催地 venue		
形式 method	□ 口頭発表 Oral	□ ポスター発表 Poster	言語 Language	□ 日本語 □ 英語 □ 中国語
共同演者名 Co-presenter				

4. 受賞（研究業績） Award (Research achievement)

名称 Award name				
	国名 Country		受賞年 Year of award	年 月
名称 Award name				
	国名 Country		受賞年 Year of award	年 月

5. 本研究テーマに関わる他の研究助成金受給 Other research grants concerned with your resarch theme

受給実績 Receipt record	□ 有　■ 無
助成機関名称 Funding agency	
助成金名称 Grant name	
受給期間 Supported period	年　月 ～　年　月
受給額 Amount received	円
受給実績 Receipt record	□ 有　□ 無
助成機関名称 Funding agency	
助成金名称 Grant name	
受給期間 Supported period	年　月 ～　年　月
受給額 Amount received	円

6. 他の奨学金受給 Another awarded scholarship

受給実績 Receipt record	□ 有　■ 無
助成機関名称 Funding agency	
奨学金名称 Scholarship name	
受給期間 Supported period	年　月 ～　年　月
受給額 Amount received	円

7. 研究活動に関する報道発表 Press release concerned with your research activities

※記載した記事を添付してください。Attach a copy of the article described below

報道発表 Press release	□ 有　■ 無	発表年月日 Date of release	
発表機関 Released medium			
発表形式 Release method	・新聞　・雑誌　・Web site　・記者発表　・その他（　　　　　）		
発表タイトル Released title			

8. 本研究テーマに関する特許出願予定 Patent application concerned with your research theme

出願予定 Scheduled	□ 有　■ 無	出願国 Application	
出願内容（概要） Application contents			

9. その他 Others

一篇論文を投稿する予定です。
テーマは「The effect of different types of acupuncture manipulations on shoulder pain and cardiovascular dynamics」
論文の原文を添付いたします。

指導責任者（署名）　小川恵子　印

Supported by 日本財団 THE NIPPON FOUNDATION

日中笹川医学奨学金制度(学位取得コース)中間評価書

課程博士：指導教官用

第 40 期　　研究者番号：　G4009　　　　作成日　：2019 年 3 月　日

氏　名	李　弘揚	LI　HONGYANG	性別	F	生年月日　1993.04.19
所属機関（役職）	天津中医薬大学　　鍼灸推拿学院（　医師　　　　）				
研究先（指導教官）	金沢大学附属病院　漢方医学科（　小川 恵子　臨床教授・特任准教授）				
研究テーマ	画像解析技術を用いた人体における漢方薬の評価				
専攻種別	□論文博士	☑課程博士			

研究者評価（指導教官記入欄）

成績状況	[✓ 優]　良　可　不可 学業成績係数=	取得単位数 取得単位　5／取得すべき単位総数　30
学生本人が行った研究の概要	1.　画像解析技術を用いた人体における漢方治療の評価（倫理審査前） 漢方の診察は望診・聞診・問診・切診の「四診」を用いて行う。その中の望診は視覚により、患者の全身状態、顔色、舌色、舌質、分泌物等を見て患者の状態を判断する主観的な診察法である。漢方の理論では、人体の気血の盛衰が顔面に現れる、したがって、顔面を望診することは全身の気血の状態を知ることにつながる。望診は医師の主観的な感覚に基づいて判断することである、客観化させる必要がある。本研究では、当科における患者への漢方治療前後に皮膚の微小循環の変化と肌のキメの変化、Numerical Rating Scale (NRS)（NRS：痛みなど症状の程度を数字で選択する方法）による改善度を評価検討する事で、漢方治療法の有効性を数値化し、望診の概念を発展させ、客観化させる。臨床観察研究となるため、現在倫理委員会審査中である。 2.　The effect of different types of acupuncture manipulations on shoulder pain and cardiovascular dynamics（鍼灸の異なった手技による肩こり治療と心血管動態の検討） 刺入鍼と接触鍼による肩こりの治療において、心血管動態に与える影響を測定し、解析した。	
総合評価	【良かった点】 過去の先行研究から、自分の研究デザインを考察することができた。また、予備研究における統計解析についても自主的に勉強して行うことができた。 国際学会での発表準備も自主的に遅延なく行うことができ、座長推薦にて論文投稿権を取得した。 【改善すべき点】 統計解析方法や撮影技術につきさらなる改善が期待できる。 【今後の展望】 倫理委員会承認後、実際の画像情報解析を開始する予定である。	
学位取得見込	李さんは大変勤勉で優秀であり、期間内の学位取得はほぼ確実である。	
	評価者（指導教官名）　　小川恵子	

The effect of different types of acupuncture manipulations on shoulder pain and cardiovascular circulation dynamics

Hongyang Li[1], Norio Tomita[1], Mako Iwahashi[2], Junsuke Arimitsu[2], Kanji Kawasaki[1], Akiko Shirai[2],
Keiko Ogawa-Ochiai[1,2]

[1]Kanazawa University, Japan
[2]Kanazawa University Hospital, Japan
(Tel：81-076-265-2918, Fax：81-076-234-4349)

ikkandoo@gmail.com

ABSTRACT: This study is to compare the effect of ContactingNeedle Technique (CNT) and InsertionNeedle Technique (INT) on cardiovascular dynamics and Visual analogue scale (VAS) in patients with shoulder pain.A total of 11 patients (9 females, 2males, average age 32.27) were recruited and divided into two groups (CNT group and INT group). The treatment was performed once a week and total of 4 weeks. The changes of cardiovascular circulation dynamics were detected at baseline, during the treatment and after the treatment. Pain was assessed before and after acupuncture therapy.There was significant difference on VAS within each group.There was not significant difference between the two groups on CO, SV, BPs, BPd and VAS, and had significant difference on PR ($P<0.05$). PR significantly decreased in both group, the rate of decrease was significantly higher in CNT group than that in INT group.

Keywords: shoulder pain; acupuncture; ContactingNeedle Technique.

1 INTRODUCTION

Shoulder pain is the third most common musculoskeletal pain.[1]The annual prevalence of shoulder complain is reported to be between 41.2 and 48.4, and women are higher than that on men.[2]Shoulder pain is caused by several factors , including physical, psychological, lifestyle and cognitive factors. [3]The patients with shoulder pain may show the chronic pain in shoulders and sometimes show the limited activity , and their daily life, spirituality and ability to work can also be affected, so their quality of life can substantially decrease .

Treatment of shoulder pain generally involves life style changes, medications and surgery.In recent years, acupuncture is frequently used as complementary and alternative medicine in the world. In 1996, World Health Organization (WHO) gave 64 suitable diseases for acupuncture, chronic pain in the musculoskeletal system (neck, shoulder, spine, knee, etc.) was included[4].And both basic and clinical researches showed that acupuncture therapy was useful for many painful diseases, and also has been used more often to treat pain in clinical practice. The mechanism of acupuncture analgesia still not clear, however there were many researches demonstrated that acupuncture can increase the blood circulation[5], stimulate the nervous system and release neuropeptides[6].

But what we always mentioned about the acupuncture was InsertionNeedle Technique (INT) using stainless steel filiform needles. ContactingNeedle Technique (CNT) is one of the traditional Japanese acupuncture methods, which was developed by Bunkei Ono. It is considered to be much safer and well-tolerated than INT because the needles were not inserted but only settled on the acupuncture points. It focuses on the flow of Qi and entire condition of patients. The stimulation of CNT is not too strong but the curative effect is accurate.[7,8]

Result from Chiu YJ‘s research suggested that acupuncture is effective in treating hypertension patients.[9] In healthy adults, acupuncture can also reduce the systolic blood pressure (SBP), heart rate (HR), and rate pressure products (RPP). Therefore acupuncture therapy can be effective in treating cardiovascular disorders[10].Thus it can be seen that numerous studies have shown that acupuncture may affect cardiovascular circulation dynamics[9], while INT is used in all of the studies. To our knowledge, there were no researches on the differences of the two methods(INT and CNT) on cardiovascular change.

In this study, we tried to observe the different change of Visual Analogue Scale (VAS) and cardiovascular circulation dynamics between INT and CNT on patients with shoulder pain.

2 MATERIALS AND METHODS

2.1 Subjects

A total of 11 patients who had shoulder pain without cardiovascular diseases were recruited in this study. All patients agreed to receive acupuncture treatment in the form of INT or CNT. The patients were divided into two groups (CNT group and INT group) according to the Kampo diagnosis. Five patients (four females, one male, mean age 35) received INT, and six patients(five females, one male, mean age 30) received CNT.

The study was approved by the ethical committee of Kanazawa University Hospital, and all patients gave informed consent. The study was started in January 2017 and completed in May 2017.

2.2 Acupuncture therapy(INT)

Acupuncture manipulations of CNT and INT were applied to LI 14,LI10,GB34,BL60（both sides), and acupuncture points are determined based on "WHO Standard Acupuncture Point Location in the Western Pacific Regions.

After the patients had rested for 15minutes in both groups, they received acupuncture treatment for 3minutes. In CNT group, disposable sterile silver needles(0.16*24mm, Asahi JAPAN) were used and it was 20seconds stimulation at per acupuncture points without insertion.In INT group,disposable stainless steel needles(0.18*40mm, Seirin JAPAN) were used. The needles were inserted into the skin and muscles to the depth of 10~15mm and retained for 3mins at per acupuncture points.

The acupuncture therapy was once a week and for 4 weeks (total of 4 treatments). Acupuncture was performed in all cases by the same acupuncturist.

2.3 Outcome measurement

The primary outcome was the change in the Visual Analogue Scale (VAS) score and cardiovascular circulation dynamics.

Cardiovascular circulation dynamics were performed using the ClearSight system (Edwards Lifesciences Corp, Irvine, CA, USA) .The ClearSight system is a device comprised of the EV1000 clinical platform and the ClearSight finger cuff[11], and used for measuring arterial blood pressure and cardiac output continuously and noninvasively through finger-cuffed technology.[12,13]The figure cuff of the ClearSight system was placed on the patient's middle finger of right hand , and diastolic blood pressure(BPd) , systolic blood pressure(BPs) , cardiac output(CO) , pulse rate(PR) and stroke volume(SV) were measured.

With the patient in the supine position for 15mins baseline measurement of Cardiovascular circulation dynamics was continued for 2mins period before acupuncture treatment, after that measurement continued for 3mins during treatment, and then measurement continued for 2mins after treatment.

The shoulder pain was assessed before and after acupuncture therapy, using a Visual analogue scale (VAS) score.

2.4 Statistical Analysis.

Statistical analyses were performed using EZR(Easy R)[14] software (version 3.5.1) by a statistician blinded to the participant allocation. Demographic variables of the age, weight, height and body surface area (BSA) in each group were compared using two-sample independent t-test and for categorical variables(the sex) Chi-Square was used. Means ± standard deviation (SD) were used to represent data. Changes in BPd, BPs, CO, PR, SV in the two groups overtime were analyzed with a two factor repeated-measures analysis of variance (ANOVA) with "treatment" (between INT and CNT) and "time" (before, during and after treatment). And a two-sample independent t-test was performed to compare the changes of VAS scores between the two groups.Then, a paired-samples t-test was performed to compare the changes of VAS scores within each group. The level of significance was set at $P < 0.05$.

3 RESULT

3.1Demographic variables

Participants' demographic variables are presented in Table1. Eleven participants were involved in the study, two(18.18%) of the participants were male and nine(81.82%) were female. Age, height, weight, BSA and sex did not show significant differences among the two groups($P>0.05$).

Table 1. Characteristics of the participants(mean±SD)

		n	mean±SD	F	p-value
Age(y)	INT	5	35±10		
	CNT	6	30±8.36	0.267	0.618
Height(cm)	INT	5	162.8±6.53		
	CNT	6	158.83±7.52	0.274	0.614
Weight(kg)	INT	5	63.6±7.86		
	CNT	6	52.17±7.13	0.094	0.766
BSA(m^2)	INT	5	1.68±0.13		
	CNT	6	1.52±0.12	0.07	0.798
Sex	INT	5	1M/4F		
	CNT	6	1M/5F		0.887

INT: Insert needle therapy
CNT: Contact needle therapy
BSA: Body surface area

3.2 The effect of INT and CNT on VAS

VAS scores were all declined after treatment. In the INT group, VAS scores were significantly decreased after the third time and the fourth time treatment($P<0.05$). In the

CNT group, VAS scores were significantly decreased after each time treatment(P<0.05). But there was not significant difference on the change of VAS scores among the two groups(P>0.05). The results are shown in Table 2. and Fig.1.

Table 2. Mean VAS scores of the two groups before and after each treatment(mean±SD)

		Therapy1	Therapy2	Therapy3	Therapy4
INT	pre-stim	66.8±10.62	73.6±13.58	68.8±19.74	70.0±18.07
	post-stim	57.6±16.06	51.4±26.32	52.6±26.67*	49.6±27.91*
	change	9.2±9.18	22.2±24.06	16.2±12.91	22.2±24.07
CNT	pre-stim	62.83±12.78	55.67±27.23	50.67±28.15	56.67±22.61
	post-stim	38.67±24.36*	34.5±20.77*	31.83±19.74*	32.83±20.93*
	change	24.17±13.92	21.17±18.56	18.83±12.86	23.83±7.88

Pre-stim: At the end of pre-stimulation period of 15min rest(for 2mins).
Post-stim: 5 min after the stimulation period(for 2mins).
Change=pre-post
*:P<0.05, compare with pre-stim

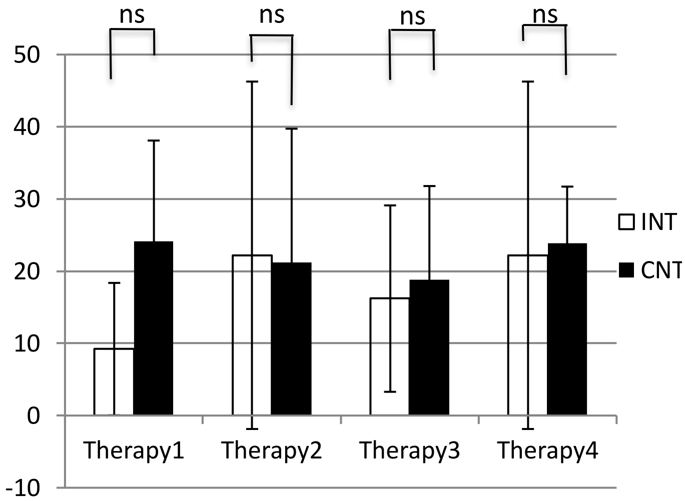

Fig.1. The change of Visual Analogue Scale (VAS) before and after acupuncture treatment. D-value of pre-stim and Post-stim were used to represent data

3.3 The effect of INT and CNT on cardiovascular circulation dynamics.

Cardiovascular circulation dynamics parameters generated by the EV1000 before, during and after treatment are shown in Table3.

There was not significant difference between CNT group and INT group on CO, SV, BPs and BPd, and had significant difference on PR (P<0.05).

The result of CO was presented in Fig.2 and Table 3.The CO decreased during the treatment and then slightly rise after treatment in both group, but there was not statistically significant among the two groups(P>0.05).

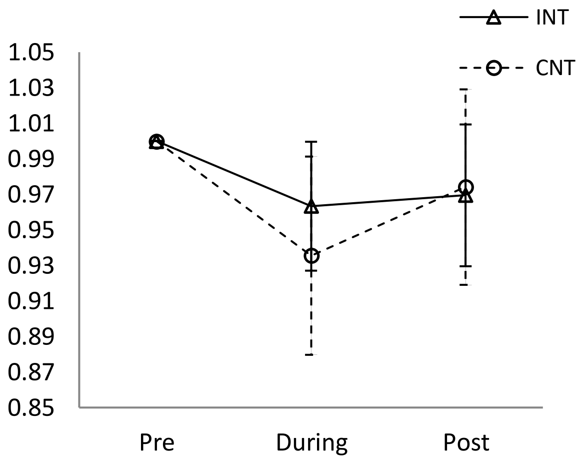

Fig.2. The change of CO before, during and after the two kinds of manipulations. Let the baseline(before) equal 1, during/baseline, and after/baseline were used to represent data

The result of SV was presented in Fig.3. and Table 3.The SV slightly decreased after treatment in both group, and also showed no significant difference between the two groups(P>0.05).

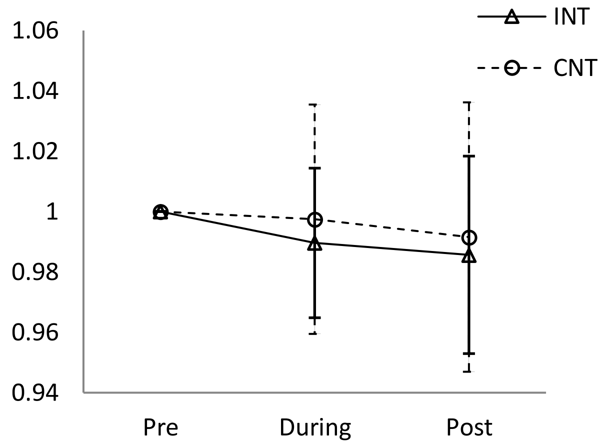

Fig.3. The change of SV before, during and after the two kinds of manipulations. Let the baseline(before) equal 1, during/baseline, and after/baseline were used to represent data

The result of PR was presented in Fig. 4 and Table 3.The PR significantly decreased in both group, the rate of decrease was significantly higher in CNT group(from 63.29+/-7.7 to 59.25+/-6.29) than that in INT group(from 70.10+/-13.95 to 68.20+/-11.65)(P<0.05), and the rate of decrease during treatment was significantly higher than that of after treatment in CNT group than that in INT group.

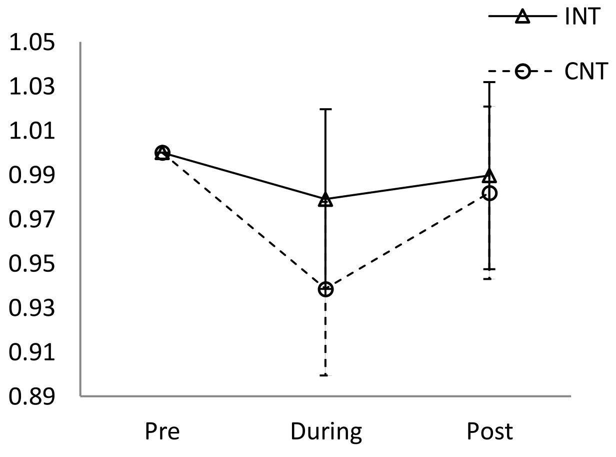

Fig.4. The change of PR before, during and after the two kinds of manipulations. Let the baseline(before)equal 1, during/baseline, and after/baseline were used to represent data

The BPs and BPd slightly changed during treatment and then increased. But no statistically significant differences in BPs and BPd during and after treatment between the two groups were observed(Fig.5.6, Table 3).

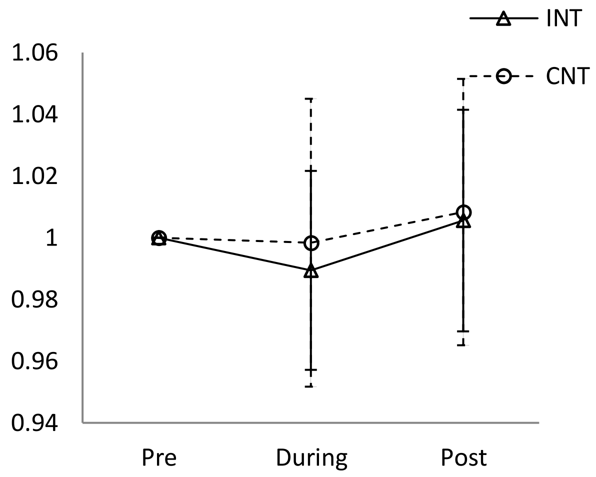

Fig.5. The change of BPs before, during and after the two kinds of manipulations. Let the baseline(before) equal 1, during/baseline, and after/baseline were used to represent data

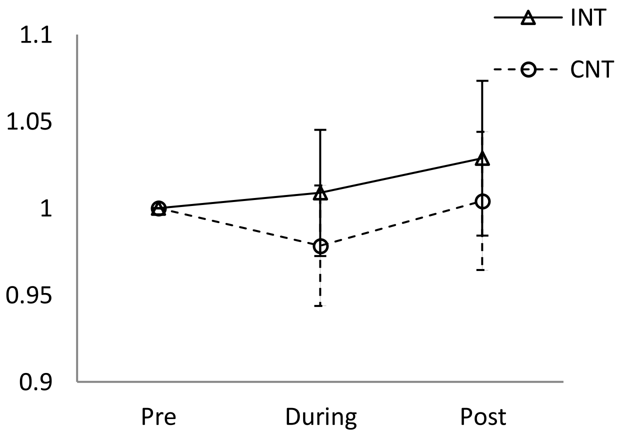

Fig.6. The change of BPd before, during and after the two kinds of manipulations. Let the baseline(before) equal 1, during/baseline, and after/baseline were used to represent data

Table 3. Mean values of CO, SV, PR, BPs and BPd throughout the treatment(mean±SD)

		Pre-stim	During-stim	Post-stim
CO(L/min)	INT	6.81±0.80	6.45±0.65	6.51±0.65
	CNT	5.82±1.04	5.43±0.85	5.65±0.88
SV(ml/b)	INT	98.85±13.03	97.45±12.89	97.30±13.32

	CNT	92.08±9.71	91.79±9.69	91.08±8.23
PR(bpm)	INT	70.10±13.95	68.20±11.65	69.00±12.10
	CNT	63.29±7.70	59.25±6.29	62.04±7.09
BPs(mmHg)	INT	112.55±14.46	111.2±13.16	112.95±12.81
	CNT	107.70±7.40	107.46±7.74	108.50±7.31
BPd(mmHg)	INT	62.75±6.53	62.75±5.97	63.60±5.56
	CNT	59.79±4.75	58.46±4.51	59.96±4.16

Pre-stim: At the end of pre-stimulation period of 15min rest(for 2mins).
During-stim: The whole stimulation period(for 3mins).
Post-stim: 5 min after the stimulation period(for 2mins).

4DISCUSSION

In this study, significantly improvement of pain was found in both group after acupuncture treatment. The acupuncture analgesic effect towards shoulder pain subjects has been confirmed by many previous researches[15,16]. Although the mechanism of acupuncture analgesic has not been schematized, it is clear that it comes with the stimulation of nervous system, immune system, the release of neurotransmitters and hormones. The acupuncture analgesic effect is an explaination for “acupuncture is a small stimulation can induce large response”[17]. As for the theory of traditional Japanese medicine, Qi and blood are two vital materials of life, Qi flowing throughout the body day and night, when the Qi is blocked diseases will appear.Acupuncture is a treatment method that can regulate the flow of Qi, and the Qi will circulate the blood, which is known as ”Qi promoting blood circulation”,

In this research, we found that VAS score of CNT group significantly decreased from the first time treatment, but in INT group it was significantly decreased from the third time, it seems that the analgesic effect of CNT is faster than the INT. In our opinions, when those patients who never or rarely received acupuncture treatment receive INT for the first time they may feel nervous, on the contrary, they may be relaxed about CNT.It is emphasized in The Yellow Emperor's Inner Classic（Huangdineijing） “When treat with acupuncture, the acupuncturists should take care of the patients’ spirit first”.

Analyses of PR, significantly decreased in both group. Similar results were reported by many previous researches(involving both healthy subjects and patients), shown that acupuncture may be able to change the balance of autonomic nervous system, reduce PR[18-22]. At the same time, there are also various views concerning the mechanism of the PR reduction by acupuncture treatment. Some researches indicated that the accentuation of parasympathetic activity playing a role in acupuncture treatment[18]; while other researches indicated that both accentuation of parasympathetic activity and suppression of sympathetic activity playing a role in acupuncturetreatment[19,20]. According to the report of Kazushi Nishijo et al[19] the decreased response of heart rate following acupuncture was blocked by administration of atropine and propranolol, indicating that the increase in cardiac vagal activity and decrease in cardiac sympathetic activity contributed to the response of decrease in heart rate during acupuncture[18]. So it is already known that acupuncture treatment may induce transitory induction in pulse/heart rate. And the change of sympathetic nerve and parasympathetic nerve(cardiac vagal) are also aroused by the acupuncture treatment.

However, the above findings are based on observations in INT subjects. This study also investigated a larger reduction in PR in the CNT group during treatment. The mechanism of CNT has not been clarified, but it does have definite effect[7,8], in our previous research we found that CNT can improve peripheral blood flow[8], and it is an effective method to treat CIPN. For clarify the mechanism of the PR reduction of CNT, in future study we should focus on the change of nervous system of CNT using participants.

In this research, the CO, SV and BP has slightly changed in both groups, and did not show significant changes among the two groups, which shows the influence of the two manipulations in subjects without cardiovascular diseases is extremely slight,therefore the two kinds of manipulations are similarly safe. And we also found that the analgesic effect of CNT is faster than INT. The CNT, using the acupuncture needles without inserting into the skin, patients will feel relaxed and acceptable, also can reduce the risk of infection, so CNT might be considered to be one of the effective treatment methods and may be safer and well-tolerated than INT.

We think that there are also three main limitations of this study : no randomised methods, small sample size and no blank control group .For the sake of patients’ health, we did not use the random methods, the division of participants was according to the Kampo diagnosis, it must have clear limitations. And we recruited 11 subjects into two groups in this study, the sample size in each group was small, the results might change if we recruited more subjects. Furthermore, we did not use a blank control group, so we do not know if these changes will also be seen when we do nothing in participants. However, the results of this study are similar with the results of the previous studies. In addition, this study shows that the CNT is an effective and safe therapeutic method in the treatment of shoulder pain, and may be useful for the future study in patients with cardiovascular diseases.

5 CONCLUSION

In conclusion, the main findings from this study were that INT and CNT both can relieve the pain of shoulder pain patients, and the analgesic effect of CNT maybe faster than INT; the two methods can induce transitory reduction in heart/pulse rate, and the change of CNT during the treatment is significantly higher than that of INT. CNT is one of the effective treatment methods and may be safer than INT.

6ACKNOWLEDGEMENT

The acupuncture therapy of this work was technically supported by Mr. Masaki Tsuda. And we would like to thank Ms. Rei Mishima and Ms. Chie Ogasawara for their data measurement and Ms. Mie Morikawa for her affair assistance.

REFERENCES

[1]Herin F, Vézina M, Thaon I, et al. Predictors of chronic shoulder pain after 5 years in a working population. Pain. 2012;153(11):2253-2259.

[2]Greving K, Dorrestijn O, Winters JC, et al. Incidence, prevalence, and consultation rates of shoulder complaints in general practice. Scandinavian journal of rheumatology. 2012;41(2):150-155.

[3] Barrett E. Examining the Role of Thoracic Kyphosis in Shoulder Pain. Phd Thesis. Limerick: University of Limerick;2016.

[4] World Health Organization. Acupuncture: Review and Analysis of Reports on Controlled Clinical Trials. Geneva: World Health Organization; 2003.

[5] Sandberg M, Lundeberg T, Lindberg LG, et al. Effects of acupuncture on skin and muscle blood flow in healthy subjects. Eur J Appl Physiol2003;90:114–119.

[6] Dawidson I, Angmar-Mansson B, Blom M, et al. The influence of sensory stimulation (acupuncture) on the release of neuropeptides in the saliva of healthy subjects. Life Sci 1998;63:659-674.

[7] Ogawa K, Ogawa M, Nishijima K, et al. Efficacy of contact needle therapy for chemotherapy-induced peripheral neuropathy. Evid Based Complement Alternat Med. 2013; 2013: 928129.

[8] Ogawa K, Shilai A, Tsuda M, et al. Optical examination of the efficacy of contact needle therapy for chemotherapy-induced peripheral neuropathy: integration of inspection in Kampo therapy with color spectrum information .Artificial Life and Roborics.2018;

https://doi.org/10.1007/s10015-018-0447-9

[9] Chiu YJ, Chi A, Reid IA. Cardiovascular and endocrine effects of acupuncture in hypertensive patients. Clin Exp Hypertens. 1997;19:1047-1063.

[10] Ganiyu S, Stanley M, Olabode J, et al.Cardiovascular Response to Manual Acupuncture Needle Stimulation among Apparently Healthy Nigerian Adults. Journal of Acupuncture and Meridian Studies.2016;9(3):143-150

[11] Edwards Lifesciences. The ClearSight system technology overview. Edwards Lifesciences Corporation;2013.

[12]Ameloot K, Palmers PJ, Malbrain MK et al.The accuracy of noninvasive cardiac output and pressure measurements with finger cuff : a concise review. Current Opinion in Critical Care.2015;21(3):232-239.

[13]SaikaiY,Yasuo M, Oyama T, et al.Noninvasive continuous blood pressure monitoring by the ClearSight system during robot-assisted laparoscopic radical prostatectomy.The Journal of Medical Investigation.2018;65:69-73.

[14] KandaY. Investigation of the freely available easy-to-use software 'EZR' for medical statistics. Bone marrow transplantation. 2013;48:452-458.

[15] Shi GX, Liu BZ, Wang J, et al.Motion style acupuncture therapy for shoulder pain: a randomized controlled trial. Journal of Pain Research.2018;11:2039-2050.

[16] Zhang S,Wang X, Yan CQ, et al.Different mechanisms of contralateral- or ipsilateral-acupuncture to modulate the brain activity in patients with unilateral chronic shoulder pain: a pilot fMRI study.Journal of Pain Research.2018;11:505-514.

[17] Yang JM, Shen XY, Zhang L, et al.The Effect of Acupuncture to SP6 on Skin Temperature Changes of SP6 and SP10: An Observation of "Deqi".Evid Based Complement Alternat Med. 2014; 2014: 595963.

[18]YazawaK.Mechanism of the Autonomic Nervous System in Acupuncture-stimulated Bradycardia.JJpn Assoc Phys Med Baln Clim1985;48:183-189.(in Japanese)

[19]Nishijo K, Mori H, Yoshikawa K, et al.Decreased heart rate by acupuncture simulation in humans via facilitation of cardiac vagal activities and suppression of cardiac sympathetic nerve.Neuroscience Letters.1997;227(3):165-168.

[20]Haker E, Egekvist H, Bjerring P. Effect of sensory stimulation (acupuncture) on sympathetic and parasympathetic activities in healthy subjects. J AutonNerv Syst 2000;79(1):52-59.

[21] Imai K, Kitakoji H.Comparison of Transient Heart Rate reduction associated with acupuncture stimulation in supine and sitting subject.Acupunct Med. 2003 Dec;21(4):133-7.

[22] Okada M, Taniguchi H, Kato S, et al.Effect of acupuncture on the hemodynamic system. Correlation between heart rate, cardiac output and blood pressure.Autonomic Neuroscience: basic&clinical.2016;201:74.(in Japanese)

日中笹川医学奨学金制度(学位取得コース)中間報告書（研究者用）

Supported by 日本財団 THE NIPPON FOUNDATION

第 40 期　　研究者番号：G4010　　作成日：2019 年 1 月 28 日

氏名	XU YANYAN	徐妍妍	性別	F	生年月日 1984.02.01
所属機関(役職)	中日友好医院　放射科　（　住院医師　）				
研究先（指導教官）	琉球大学大学院医学研究科　放射線診断治療学　（村山 貞之　教授） 琉球大学大学院医学研究科　放射線診断治療学　（山城　恒雄 講師）				
研究テーマ	超多列 CT，超高精細 CT 等を用いた胸部疾患の研究				
専攻種別	論文博士 ☑		課程博士 □		

研究概要

Strain measurement on four-dimensional dynamic-ventilation CT: quantitative analysis of abnormal respiratory deformation of the lung in COPD

Purpose(目的)

Strain measurement is frequently used to assess myocardial motion in cardiac imaging[1-3]. This study aimed to apply strain measurement to pulmonary motion observed by four-dimensional dynamic-ventilation computed tomography (CT) and to clarify motion abnormality in COPD.

Approach (戦略)

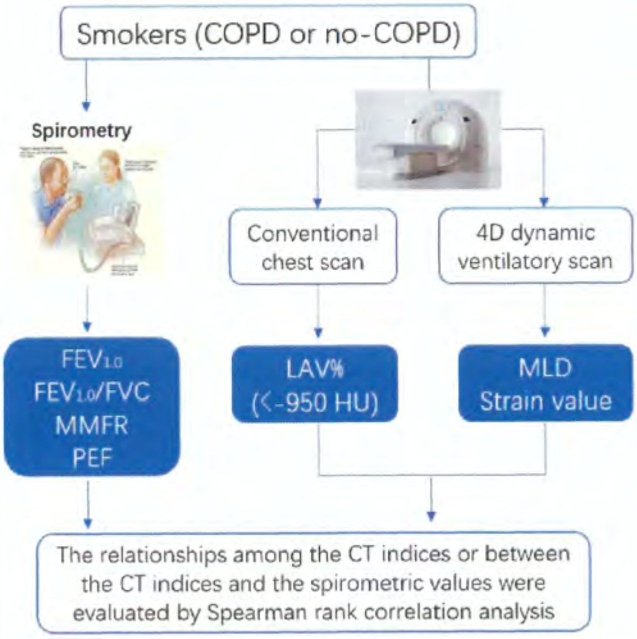
Smokers (COPD or no-COPD)
Spirometry
Conventional chest scan
4D dynamic ventilatory scan
FEV1.0
FEV1.0/FVC
MMFR
PEF
LAV%
(<-950 HU)
MLD
Strain value
The relationships among the CT indices or between the CT indices and the spirometric values were evaluated by Spearman rank correlation analysis

Abbreviations:
COPD, chronic obstructive pulmonary disease;
FEV$_{1.0}$, forced expiratory volume in the first second;
FVC, forced vital capacity;
MMFR, maximum mid-expiratory flow rate;
PEF, peak expiratory flow;
LAV,low attenuation volume;
MLD, mean lung density.

Materials and methods (材料と方法)

Thirty-two smokers, including ten with COPD, underwent dynamic-ventilation CT during spontaneous breathing. CT data were continuously reconstructed every 0.5 seconds. In the series of images obtained by dynamic-ventilation CT, five expiratory frames were identified starting from the peak inspiratory frame (first expiratory frame) and ending with the fifth expiratory frame. Strain measurement of the scanned lung was performed using research software that was originally developed for cardiac strain measurement and modified for assessing deformation of the lung. The measured strain values were divided by the change in mean lung density to adjust for the degree of expiration. Spearman's rank correlation analysis was used to evaluate associations between the adjusted strain measurements and various spirometric values.

Results (実験結果)

The adjusted strain measurement was negatively correlated with FEV1/FVC ($\rho=-0.52$, $P<0.01$), maximum mid-expiratory flow ($\rho=-0.59$, $P<0.001$), and peak expiratory flow ($\rho=-0.48$, $P<0.01$), suggesting that abnormal deformation of lung motion is related to various patterns of expiratory airflow limitation.

Discussion (考察)

In this study, we applied quantitative strain measurement to 4D dynamic-ventilation CT images and found the following: 1) the strain measurement adjusted by the degree of expiration can be used for assessment of abnormal lung deformation during ventilation and 2) the adjusted strain measurement demonstrates negative correlations with several spirometric values. These observations suggest that abnormal pulmonary deformation by ventilation can be expressed by abnormally high strain values, and strain analysis can provide quantitative information that may reflect uneven, heterogeneous lung movement in various pulmonary and airway diseases. We currently believe that early heterogeneous changes in lung motion can be detected by abnormally high strain values in patients with various diseases, such as bronchiectasis, non-tuberculosis mycobacteria, and interstitial lung diseases, which may precede clinical symptoms or abnormalities found by other conventional lung function tests.

As strain values express deformation of targeted structures, we expected that two different types of deformation must have existed in the lung: normal deformation of the lung due to inhalation/exhalation and abnormal regional deformation caused by heterogeneous ventilation due to COPD (emphysema and airway disease)[4-7]. Normal deformation of the lung would appear at lung areas with large respiratory movements, such as the lung bottom adjacent to the diaphragm and the dorsal part of the lung in the supine position. In contrast, abnormal deformation may be observed throughout the lung without any specific locations, because this abnormal deformation is caused by heterogeneous ventilation or partial air-trapping due to emphysema and airway disease of COPD[5-8]. To distinguish these two different deformation patterns, we adjusted measured strain values by the degree of expiration in this study. The changes in MLD between the first and the second to fifth respiratory frames indicate the magnitude of exhalation during the expiratory phase. Even if the value of strain itself may be intermediate in patients with severe COPD without large expiratory movements, but the adjusted strain value may be quite large because of small changes in MLD (insufficient expiration) due to limited airflow. Using this method, we successfully extracted "abnormal" deformation of the lung, which was expressed as the adjusted strain value, and this should be closely associated with heterogeneous lung movements.

Normally, the stresses under constant ventilation are homogeneously transmitted throughout the entire lung[9]. However, in COPD patients, in addition to loss of pulmonary elastic recoil, heterogeneous distribution of pulmonary emphysema and abnormalities of thoracic structures (such as narrowed/collapsed airways) must result in asynchronous transmission of physical stress in the lung during ventilation, which causes heterogeneous pulmonary movement[8,10]. Interestingly, adjusted strain was negatively correlated with the spirometric values. Although the strength of the correlations was intermediate, these correlations suggest that pulmonary motion heterogeneity may be caused by various patterns, such as proximal airway disease, small airway disease, and lung parenchymal abnormalities. Thus, it should be possible to expand strain measurement by dynamic-ventilation CT to other lung/airway diseases, such as asthma, cystic fibrosis, or even diffuse lung disease, which have not been a target of quantitative motion analysis of the lung and airways.

In conclusion, strain analysis using 4D dynamic- ventilation CT is feasible to quantify the abnormal deformation of lung motion in patients with COPD. This technique can be expanded to various lung and airways diseases, in a manner that is similar to cardiac imaging.

Reference(参考文献)

1. Tanabe Y, Kido T, Kurata A, et al. Three-dimensional maximum principal strain using cardiac computed tomography for identification of myocardial infarction. Eur Radiol. 2017; 27(4): 1667–1675
2. Buckert D, Tibi R, Cieslik M, et al. Myocardial strain characteristics and outcomes after transcatheter aortic valve replacement. Cardiol J. 2018;25(2):203–212.
3. Di Franco A, Kim J, Rodriguez-Diego S, et al. Multiplanar strain quantification for assessment of right ventricular dysfunction and non-ischemic fibrosis among patients with ischemic mitral regurgitation. PLoS One. 2017;12(9):e0185657.
4. Yamashiro T, Matsuoka S, Bartholmai BJ, et al. Collapsibility of lung volume by paired inspiratory and expiratory CT scans: correlations with lung function and mean lung density. Acad Radiol. 2010;17(4):489–495.
5. Estrada L, Torres A, Sarlabous L, et al. Estimation of bilateral asynchrony between diaphragm mechanomyographic signals in patients with chronic obstructive pulmonary disease. Conf Proc IEEE Eng Med Biol Soc. 2014;2014:3813–3816.
6. Yamashiro T, Moriya H, Tsubakimoto M, Matsuoka S, Murayama S. Continuous quantitative measurement of the proximal airway dimensions and lung density on four-dimensional dynamic-ventilation CT in smokers. Int J Chron Obstruct Pulmon Dis. 2016;11(1):755–764.
7. Yamashiro T, Moriya H, Matsuoka S, et al. Asynchrony in respiratory movements between the pulmonary lobes in patients with COPD: continuous measurement of lung density by 4-dimensional dynamic-ventilation CT. Int J Chron Obstruct Pulmon Dis. 2017;12(1):2101–2109.
8. Vestbo J, Hurd SS, Agustí AG, et al. Global strategy for the diagnosis, management, and prevention of chronic obstructive pulmonary disease: GOLD executive summary. Am J Respir Crit Care Med. 2013;187(4):347–365.
9. Cai J, Altes TA, Miller GW, et al. MR grid-tagging using hyperpolarized helium-3 for regional quantitative assessment of pulmonary biomechanics and ventilation. Magn Reson Med. 2007; 58(2):373–380.
10. Ley-Zaporozhan J, Ley S, Mews J, Weinheimer O, Kandel S, Rogalla P. Changes of emphysema parameters over the respiratory cycle during free breathing: preliminary results using respiratory gated 4D-CT. COPD. 2017;14(6):597–602.

注:本研究は 2018 年 12 月 18 日「International Journal of Chronic Obstructive Pulmonary Disease」という雑誌より発表しました。

2. 執筆論文　Publication of thesis　※記載した論文を添付してください。Attach all of the papers listed below.

論文名 1	Strain measurement on four-dimensional dynamic-ventilation CT: quantitative analysis of abnormal respiratory deformation of the lung in COPD					
掲載誌名	International Journal of Chronic Obstructive Pulmonary Disease					
	2018 年 12 月	14 巻（号）	65 頁 ～	72 頁	言語	English
第 1 著者名	**Yanyan Xu**	第 2 著者名	Tsuneo Yamashiro	第 3 著者名	Hiroshi Moriya	
その他著者名	Maho Tsubakimoto, Yukihiro Nagatani, Shin Matsuoka, Sadayuki Murayama, ACTIve Study Group					
論文名 2	Correlation Between Intravoxel Incoherent Motion and Dynamic Contrast-Enhanced Magnetic Resonance Imaging Parameters in Rectal Cancer					
掲載誌名	Academic Radiology					
	2018 年 9 月	Epub ahead 巻（号）	頁 ～	頁	言語	English
第 1 著者名	Hongliang Sun	第 2 著者名	**Yanyan Xu**	第 3 著者名	Qiaoyu Xu	
その他著者名	Jianghui Duan, Haibo Zhang, Tongxi Liu, Lu Li, Queenie Chan, Sheng Xie, Wu Wang					
論文名 3	Relationship between CT activity score with lung function and the serum angiotensin converting enzyme in pulmonary sarcoidosis on chest HRCT					
掲載誌名	Medicine (Baltimore)					
	2018 年 9 月	97(36) 巻（号）	e12205 頁 ～	頁	言語	English
第 1 著者名	Jianghui Duan	第 2 著者名	**Yanyan Xu**	第 3 著者名	Haixu Zhu	
その他著者名	Haibo Zhang, Shilong Sun, Hongliang Sun, Wu Wang, Sheng Xie					
論文名 4	Could IVIM and ADC help in predicting the KRAS status in patients with rectal cancer?					
掲載誌名	European Radiology					
	2018 年 7 月	28(7) 巻（号）	3059 頁 ～	3065 頁	言語	English
第 1 著者名	**Yanyan Xu**	第 2 著者名	Qiaoyu Xu	第 3 著者名	Hongliang Sun	
その他著者名	Tongxi Liu, Kaining Shi, Wu Wang					
論文名 5	Quantitative intravoxel incoherent motion parameters derived from whole-tumor volume for assessing pathological complete response to neoadjuvant chemotherapy in locally advanced rectal cancer					
掲載誌名	Journal of Magnetic Resonance Imaging:JMRI					
	2018 年 7 月	48(1) 巻（号）	248 頁 ～	258 頁	言語	English
第 1 著者名	Qiaoyu Xu	第 2 著者名	**Yanyan Xu**	第 3 著者名	Hongliang Sun	
その他著者名	Queenie Chan, Kaining Shi, Aiping Song, Wu Wang					
論文名 6	Intravoxel Incoherent Motion MRI of Rectal Cancer: Correlation of Diffusion and Perfusion Characteristics With Prognostic Tumor Markers					
掲載誌名	American Journal of Roentgenology					
	2018 年 4 月	210(4) 巻（号）	W139 頁 ～	W147 頁	言語	English
第 1 著者名	Hongliang Sun	第 2 著者名	**Yanyan Xu**	第 3 著者名	Aiping Song	
その他著者名	Kaining Shi, Wu Wang					

3. 学会発表　Conference presentation　※筆頭演者として総会・国際学会を含む主な学会で発表したものを記載し

※Describe your presentation as the principal presenter in major academic meetings including general meetings or

学会名 Conference	第11回呼吸機能イメージング研究会学術集会
演　題 Topic	慢性閉塞性肺疾患における肺運動の不均一性：呼吸ダイナミックCTにおけるストレイン値解析
開催日 date	2019 年 1 月 25 日　開催地 venue 東京都千代田区　一橋講堂
形式 method	□ 口頭発表 Oral ☑ ポスター発表 Poste 言語 Language ☑ 日本語 □ 英語 □ 中国語
共同演者名 Co-presenter	山城 恒雄、森谷 浩史、椿本 真穂、村山 貞之
学会名 Conference	the 26th annual meeting ISMRM-ESMRMB
演　題 Topic	Rectal Cancer: Comparison of MRI Characteristics and Texture Analysis Between Different Tumor KRAS Status
開催日 date	2018 年 6 月 16 日　開催地 venue Paris Expo Porte de Versailles, Paris, France
形式 method	□ 口頭発表 Oral ☑ ポスター発表 Poste 言語 Language □ 日本語 ☑ 英語 □ 中国語
共同演者名 Co-presenter	Hongliang Sun, Kaining Shi, Wu Wang
学会名 Conference	
演　題 Topic	
開催日 date	年 月 日　開催地 venue
形式 method	□ 口頭発表 Oral □ ポスター発表 Poste 言語 Language □ 日本語 □ 英語 □ 中国語
共同演者名 Co-presenter	
学会名 Conference	
演　題 Topic	
開催日 date	年 月 日　開催地 venue
形式 method	□ 口頭発表 Oral □ ポスター発表 Poste 言語 Language □ 日本語 □ 英語 □ 中国語
共同演者名 Co-presenter	

4. 受賞（研究業績 Award (Research achievement)

名　称 Award name	Educational Stipend		
	国名 Country　France	受賞年 Year of	2018 年 6 月
名　称 Award name			
	国名 Country	受賞年 Year of	年 月

5．本研究テーマに関わる他の研究助成金受給 Other research grants concerned with your resarch

受給実績 Receipt record	□ 有　■ 無
助成機関名称 Funding agency	
助成金名称 Grant name	
受給期間 Supported period	年　月 ～　年　月
受給額 Amount received	円
受給実績 Receipt record	□ 有　□ 無
助成機関名称 Funding agency	
助成金名称 Grant name	
受給期間 Supported period	年　月 ～　年　月
受給額 Amount received	円

6．他の奨学金受給 Another awarded scholarship

受給実績 Receipt record	□ 有　■ 無
助成機関名称 Funding agency	
奨学金名称 Scholarship name	
受給期間 Supported period	年　月 ～　年　月
受給額 Amount received	円

7．研究活動に関する報道発表 Press release concerned with your research activities

※記載した記事を添付してください。 Attach a copy of the article described below

報道発表 Press release	■ 有　□ 無	発表年月日 Date of release	2018/10/1
発表機関 Released medium	好医生国际教育		
発表形式 Release method	・新聞　・雑誌　[✓ Web site]　・記者発表　・その他（　）		
発表タイトル Released title	协和医生访学日本，同样拼命工作的日本医生，待遇和我们有何不同? https://mp.weixin.qq.com/s/0D6AFDgK2r_0ehrDUxZAag		

8．本研究テーマに関する特許出願予定 Patent application concerned with your research theme

出願予定 Scheduled	□ 有　■ 無	出願国 Application	
出願内容（概要） Application contents			

9．その他 Others

特にありません。

指導責任者（署名） 山城 極雄 ㊞

Supported by 日本財団 THE NIPPON

日中笹川医学奨学金制度（学位取得コース）中間評価書
論文博士：指導教官用

第 40 期　研究者番号：G4010　　作成日　：2019 年 2 月 1 日

氏　名	徐 妍妍	XU　YANYAN	性別	F	生年月日　1984. 02. 01
所属機関（役職）	中日友好医院　放射科（　住院医師　）				
研究先（指導教官）	琉球大学大学院医学研究科　放射線診断治療学（　村山 貞之　教授　） 琉球大学大学院医学研究科　放射線診断治療学（　山城 恒雄　講師　）				
研究テーマ	超多列 CT，超高精細 CT 等を用いた胸部疾患の研究				
専攻種別	☑論文博士	□課程博士			

研究者評価（指導教官記入欄）

成績状況	[✓ 優]　良　可　不可	取得単位数 取得単位数／取得すべき単位総数
学生本人が行った研究の概要	2018 年度においては、徐医師は琉球大学放射線診断治療学講座が主宰する 320 列 CT スキャナーを用いた他施設共同研究「ACTIve Study Group」にて、大原綜合病院（福島市）が収集した 4 次元胸部 CT「呼吸ダイナミック CT」を用いた研究に従事した。ザイオソフト社より研究用として貸与を受けている先進性の極めて高いワークステーションを用い、呼吸ダイナミック CT での「ストレイン（最大主歪み）値測定」を試み、COPD 患者では異常に高いストレイン値が観察されることを確認し、国際的な学術雑誌より徐医師が筆頭著者となって同内容の論文を出版した（Xu Y, Yamashiro T, et al. Strain measurement on four-dimensional dynamic-ventilation CT: quantitative analysis of abnormal respiratory deformation of the lung in COPD. Int J Chron Obstruct Pulmon Dis. 2019; 14(1): 65- 72)。同内容は 2019 年 1 月に東京で開催された第 11 回呼吸機能イメージング研究会でも徐医師が筆頭演者となって発表している。	
総合評価	【良かった点】 研究に主体的に取り組み、山城講師などのサポートを受けながらインパクトファクター付きの医学雑誌に論文を発表できたこと。	
	【改善すべき点】 特になし	
	【今後の展望】 2019 年度では超高精細 CT を使用した肺気腫・COPD の研究で、インパクトファクター付きの医学雑誌に論文を発表できるように研究を遂行する。	
学位取得見込	上記【今後の展望】でも記載の通り、徐医師はすでに超高精細 CT を用いた肺気腫の定量解析の研究に乗り出しており、すでに大半のデータ測定は終了している。2019 年 4 月までには論文の完成を見る予定で、2019 年末までにはアクセプトになる可能性が高い。2019 年度内に琉球大学での論文博士（医学）の取得はまず確実と予想している。	
評価者（指導教官名）	村山 貞之　印	

山城 恒雄

International Journal of COPD

Dovepress
open access to scientific and medical research

Open Access Full Text Article

ORIGINAL RESEARCH

Strain measurement on four-dimensional dynamic-ventilation CT: quantitative analysis of abnormal respiratory deformation of the lung in COPD

This article was published in the following Dove Medical Press journal:
International Journal of COPD

Yanyan Xu[1,2]
Tsuneo Yamashiro[1]
Hiroshi Moriya[3]
Maho Tsubakimoto[1]
Yukihiro Nagatani[4]
Shin Matsuoka[5]
Sadayuki Murayama[1]

On behalf of ACTIve Study Group

[1]Department of Radiology, Graduate School of Medical Science, University of the Ryukyus, Nishihara, Okinawa, Japan; [2]Department of Radiology, China-Japan Friendship Hospital, Beijing, Republic of China; [3]Department of Radiology, Ohara General Hospital, Fukushima-City, Fukushima, Japan; [4]Department of Radiology, Shiga University of Medical Science, Otsu, Shiga, Japan; [5]Department of Radiology, St Marianna University School of Medicine, Kawasaki, Kanagawa, Japan

Purpose: Strain measurement is frequently used to assess myocardial motion in cardiac imaging. This study aimed to apply strain measurement to pulmonary motion observed by four-dimensional dynamic-ventilation computed tomography (CT) and to clarify motion abnormality in COPD.

Materials and methods: Thirty-two smokers, including ten with COPD, underwent dynamic-ventilation CT during spontaneous breathing. CT data were continuously reconstructed every 0.5 seconds. In the series of images obtained by dynamic-ventilation CT, five expiratory frames were identified starting from the peak inspiratory frame (first expiratory frame) and ending with the fifth expiratory frame. Strain measurement of the scanned lung was performed using research software that was originally developed for cardiac strain measurement and modified for assessing deformation of the lung. The measured strain values were divided by the change in mean lung density to adjust for the degree of expiration. Spearman's rank correlation analysis was used to evaluate associations between the adjusted strain measurements and various spirometric values.

Results: The adjusted strain measurement was negatively correlated with FEV_1/FVC ($\rho=-0.52$, $P<0.01$), maximum mid-expiratory flow ($\rho=-0.59$, $P<0.001$), and peak expiratory flow ($\rho=-0.48$, $P<0.01$), suggesting that abnormal deformation of lung motion is related to various patterns of expiratory airflow limitation.

Conclusion: Abnormal deformation of lung motion exists in COPD patients and can be quantitatively assessed by strain measurement using dynamic-ventilation CT. This technique can be expanded to dynamic-ventilation CT in patients with various lung and airway diseases that cause abnormal pulmonary motion.

Keywords: COPD, computed tomography, CT, dynamic-ventilation CT, strain measurement, emphysema

Introduction

Strain analysis, which can express deformation of a tissue or organ in the human body, has been mainly used to assess myocardial motion using various four-dimensional (4D) imaging modalities, including echocardiography, magnetic resonance imaging (MRI), and computed tomography (CT).[1–11] Although various parameters based on strain measurements have been advocated by different software vendors, it is commonly accepted in the field of cardiology that strain is a sensitive parameter to assess regional function of the myocardium.[4–11] It has also been reported that strain measurements reveal minor left ventricular modifications in athletes with common anomalies (ie, bicuspid aortic valve),[3] which might be masked by apparently normal values of

Correspondence: Tsuneo Yamashiro
Department of Radiology, Graduate School of Medical Science, University of the Ryukyus, 207 Uehara, Nishihara, Okinawa 903-0215, Japan
Tel +81 98 895 1162
Fax +81 98 895 1420
Email clatsune@yahoo.co.jp

http://dx.doi.org/10.2147/COPD.S183740

© 2019 Xu et al. This work is published and licensed by Dove Medical Press Limited. The full terms of this license are available at https://www.dovepress.com/terms.php and incorporate the Creative Commons Attribution – Non Commercial (unported, v3.0) License (http://creativecommons.org/licenses/by-nc/3.0/). By accessing the work you hereby accept the Terms. Non-commercial uses of the work are permitted without any further permission from Dove Medical Press Limited, provided the work is properly attributed. For permission for commercial use of this work, please see paragraphs 4.2 and 5 of our Terms (https://www.dovepress.com/terms.php).

global cardiac function parameters, such as ejection fraction and stroke volume.[12,13]

In cardiology, a higher value of myocardial strain observed on MRI or echocardiography usually indicates better myocardial movement, because strong systolic–diastolic movements result in large deformation of the measured myocardium. However, it has also been shown that myocardial strain is heterogeneous in patients with dilated cardiomyopathy, suggesting heterogeneity of myocardial contractile function.[5] Joseph et al presented color contour maps based on MRI strain measurements in patients with dilated cardiomyopathy and concluded that myocardial systolic strain has a heterogeneous regional distribution.[5]

In patients with COPD, the destruction of normal "mesh-like" structures of pulmonary tissue results in pulmonary emphysema and leads to a reduction of lung compliance, causing inhomogeneous transmission of lung motion during the respiratory cycle.[14] Furthermore, the heterogeneous distribution of emphysematous changes and airway diseases also intensify the heterogeneity of lung movement during ventilation,[15–17] which has been clearly confirmed in recent studies using 4D dynamic-ventilation CT and other imaging techniques.[18–20] These recent studies have demonstrated the existence of asynchrony between the right and left lungs, between the proximal airways and lung, and among different lung lobes. However, to the best of our knowledge, there is no published information on motion abnormality of the entire scanned lung. Considering the similar physiologic characteristics of the lungs and heart (both show cyclic movements and changes in volume), we hypothesized that the quantitative strain measurement used in cardiology could be transferred to pulmonary 4D-CT imaging and generate new knowledge on normal and abnormal respiratory movements of the lungs. Also, we predicted that heterogeneity of lung motion, which would be similar to strain heterogeneity in dilated cardiomyopathy, can be demonstrated as abnormal deformation, or a high strain value in the targeted portion of the lungs.

Thus, the goals of this study were the following: 1) to first measure lung strain using 4D dynamic-ventilation CT, 2) to clarify abnormal deformation of lung motion by strain measurement, and 3) to assess correlations between strain and COPD severity.

Materials and methods

The Institutional Review Board at Ohara General Hospital approved this retrospective study. Based on the national guideline of the Japanese Government, the Institutional Review Board at Ohara General Hospital waived written informed consent from enrolled patients for this study. Dynamic-ventilation CT and spirometry were performed as part of routine clinical care at Ohara Medical Center (part of Ohara General Hospital). This study was also part of the Area-detector Computed Tomography for the Investigation of Thoracic Diseases (ACTIve) Study, a multicenter research alliance in Japan. Also, the subjects' data utilized in this study were previously analyzed with a different objective for other research.[20]

Subjects

Thirty-two smokers (4 females and 28 males; mean age 70±12 years) underwent both spirometry and chest CT (conventional and dynamic-ventilatory scans) at Ohara Medical Center. As the same patients were previously analyzed with a different objective,[20] the detailed information regarding the study population is described in the Supplementary material. Patient data analyzed in this study, such as CT scans and clinical information, were anonymized and maintained with strict confidentiality.

CT scanning

All patients were scanned with a 320-row MDCT scanner (Aquilion *ONE*, Canon Medical Systems, Otawara, Tochigi, Japan) for both conventional (static) and dynamic-ventilatory scans. The detailed information regarding the CT scanning is described in the Supplementary material.

Image analysis – lung density measurement on dynamic-ventilation CT

Using commercially available software (Lung Volume Measurement, Canon Medical Systems), the mean lung density (MLD) of the scanned lung ($<$160 mm in the Z-axis) was measured automatically in each frame. On the time curve of MLD, the peak inspiratory frame (= first expiratory frame) was defined as the lowest MLD on the curve. The expiratory phase was defined as the frames starting from the peak inspiratory frame (first expiratory frame), and the MLD values for the first to fifth expiratory frames were obtained for this study.

Image analysis – strain measurement on dynamic-ventilation CT

Strain measurement on the dynamic-ventilation CT was performed using in-house research software installed in a commercially available workstation for 4D-CT analysis (PhyZiodynamics, Ziosoft, Tokyo, Japan). In brief, the software measured the "maximum principal strain" values (Figure 1), which were originally used in cardiac imaging

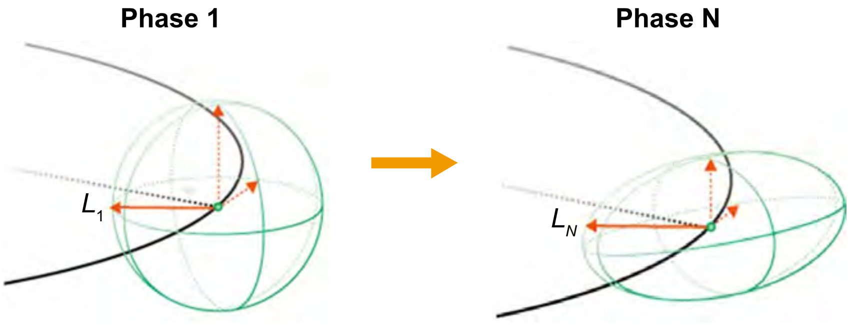

$$\text{Maximum principal strain} \cong \frac{L_N - L_1}{L_1}$$

Figure 1 Illustrations for the concept of "principal strain".

Notes: The maximum principal strain is calculated based on expansion of the principal direction (*L*) from the starting (standard) point (phase 1) to the measured point (phase *N*). L_N at phase *N* becomes large when the original sphere changes its shape strongly at phase *N*.

but newly modified to assess lung motion. Using the motion coherence algorithm, dynamic-ventilation CT data could be analyzed at any given point in the imaging space using image matching and model matching algorithms that produce the matrix of the motion vectors. Maximum principal strain was calculated directly at the composition/interpolation stage, based on the motion vector at any point in the space. The maximum principal strain was calculated at the points in the space during ventilation, based on expansion of the principal direction from the starting (standard) frame (first expiratory frame = peak inspiratory frame) to the second to fifth expiratory frames. Figure 2 shows an example of a serial change in the maximum principal strain in each frame of the expiratory phase. The software automatically excluded the upper and lower marginal zones that were not included in the scanning field during inspiration, even if they were included during expiration.

Strain values for the second to fifth expiratory frames were divided by the changes in MLD between the first and second to fifth frames to adjust each strain value by the degree of expiration. Finally, adjusted strain values for the second to fifth frames were summed to express the total strain measurement during expiration. The sum of the adjusted strain values could be considered to express abnormal deformation of lung motion, which was discriminated from physiologic deformation in lung areas with normal exhalation.

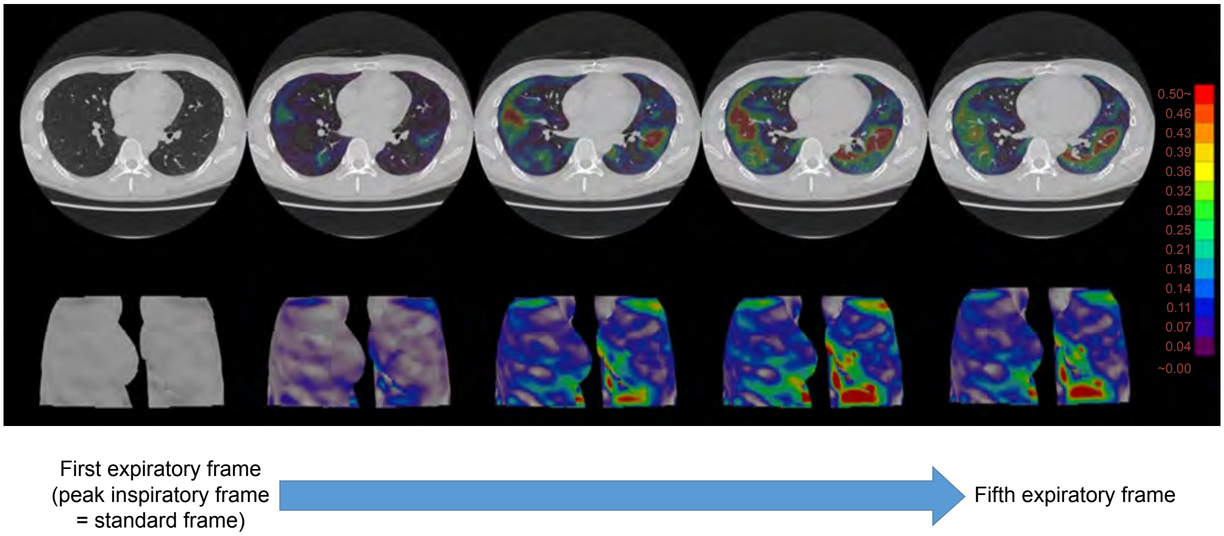

Figure 2 Example of serial changes in strain maps in a patient with COPD.

Note: From the first expiratory frame (left, the peak inspiratory frame) to the fifth expiratory frame, high strain values are observed as red areas, which are different from the gravity-dependent dorsal areas.

Table 1 Clinical characteristics of 32 subjects

Characteristics	Mean ± SD	(Range)
Gender (female:male)	(4:28)	–
Age (years)	70±12	(36–84)
Smoking index (pack-years)	46±21	(2–100)
Smoking status (ex-smoker: current smoker)	(16:16)	–
FEV_1 (L)	2.20±0.93	(0.54–4.07)
FEV_1/FVC	0.73±0.12	(0.41–0.92)
MMFR (L/s)	1.84±1.21	(0.28–4.97)
PEF (L)	5.23±2.67	(1.35–10.5)

Abbreviations: MMFR, maximum mid-expiratory flow rate; PEF, peak expiratory flow.

Image analysis – emphysema measurement by conventional chest CT

Based on the data of the helical CT scans, an emphysema measurement was performed using the same software for the MLD measurement (Lung Volume Measurement, Canon Medical Systems). The percent low attenuation volume (LAV%, < –950 Hounsfield units [HU]) of the whole lung was automatically measured.

Spirometry

All subjects performed spirometry, including FEV_1 and FVC, maximum mid-expiratory flow rate (MMFR), and peak expiratory flow (PEF), according to American Thoracic Society standards.[21] The spirometric values from the study participants are shown in Table 1. Spirometry was performed within 2 weeks of the chest CT.

Statistical analysis

Data are expressed as mean ± SD. Spearman's rank correlation analysis was used to evaluate the associations among the CT indices or between the CT indices and the spirometric values. A *P*-value of <0.05 was considered significant. All statistical analyses were performed using JMP 12.0 software (SAS Institute Inc., Cary, NC, USA).

Results

MLD measurement on dynamic-ventilation CT and emphysema index on conventional CT

Based on dynamic-ventilation CT, the mean MLD values were –871.0±37.3 and –821.5±55.8 HU for the first and fifth expiratory frames, respectively. The MLD values for the first and fifth expiratory frame demonstrated positive correlations with all spirometric values; the MLD at the fifth expiratory frame demonstrated a stronger correlation with FEV_1/FVC (ρ=0.75, $P<0.0001$) compared to the MLD at the first expiratory frame (Table 2). Based on helical CT for the whole lung, the mean LAV% (emphysema index) was 10.8%±14.8% and correlated with multiple spirometric values except for FEV_1 (Table 2).

Strain measurement on dynamic-ventilation CT

The mean adjusted strain for expiration was 24.7±18.0 (range, 5.9–72.6). Generally, higher strain values were observed in patients with lower spirometric values, and negative correlations were found between strain and all spirometric values (ρ=–0.48 to –0.59, $P<0.01$) (Table 2) (Figures 3 and 4, Movies S1 and S2). This implies that homogeneous lung motion would be limited and lost in patients with more severe COPD. Particularly, the correlation coefficient between adjusted strain and the maximum mid-expiratory

Table 2 Correlations between CT measurements and spirometric values

CT measurement	Mean ± SD (range)	Correlation coefficients (ρ)			
		FEV_1	FEV_1/FVC	MMFR	PEF
Dynamic-ventilation CT					
MLD at the first expiratory frame	–871.0±37.3 (–949.6 to –812.9)	0.45 (*P*<0.01)	0.59 (*P*<0.001)	0.57 (*P*<0.001)	0.53 (*P*<0.01)
MLD at the fifth expiratory frame	–821.5±55.8 (–938.7 to –729.8)	0.48 (*P*<0.01)	0.75 (*P*<0.0001)	0.67 (*P*<0.001)	0.57 (*P*<0.001)
Adjusted strain measurement	24.7±18.0 (5.9 to 72.6)	–0.55 (*P*<0.01)	–0.52 (*P*<0.01)	–0.59 (*P*<0.001)	–0.48 (*P*<0.01)
Helical CT					
LAV%	10.8±14.8 (0 to 52.0)	–0.33 (NS)	–0.73 (*P*<0.0001)	–0.57 (*P*<0.001)	–0.38 (*P*<0.05)

Note: The first expiratory frame is the same as the peak inspiratory frame.
Abbreviations: LAV%, percent low attenuation volume (< –950 Hounsfield units); MLD, mean lung density; MMFR, maximum mid-expiratory flow rate; NS, not significant; PEF, peak expiratory flow.

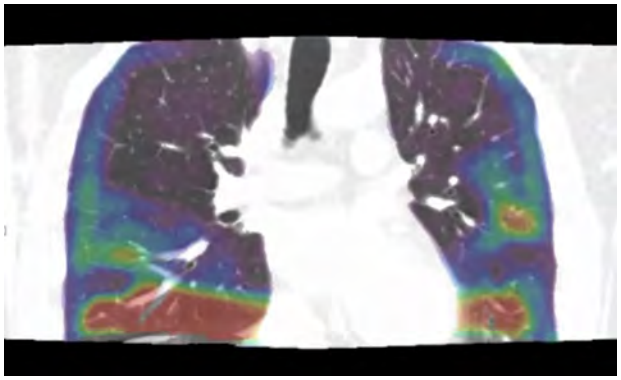

Figure 3 Strain mapping of a non-COPD smoker (during expiration, 39-year-old male, $FEV_1/FVC = 0.92$).

Note: During expiration, high strain values (red areas) are observed just above the diaphragm and around interlobar fissures, suggesting that deformation of the lung would be physiologic due to normal expiration.

airflow was slightly higher ($\rho = -0.59$, $P < 0.001$) than those with other spirometric values.

Discussion

In this study, we applied quantitative strain measurement to 4D dynamic-ventilation CT images and found the following: 1) the strain measurement adjusted by the degree of expiration can be used for assessment of abnormal lung deformation during ventilation and 2) the adjusted strain measurement demonstrates negative correlations with several spirometric values. These observations suggest that abnormal pulmonary deformation by ventilation can be expressed by abnormally high strain values, and strain analysis can provide quantitative information that may reflect uneven, heterogeneous lung movement in various pulmonary and airway diseases. We currently believe that early heterogeneous changes in lung motion can be detected by abnormally high strain values in patients with various diseases, such as bronchiectasis, non-tuberculosis mycobacteria, and interstitial lung diseases, which may precede clinical symptoms or abnormalities found by other conventional lung function tests.

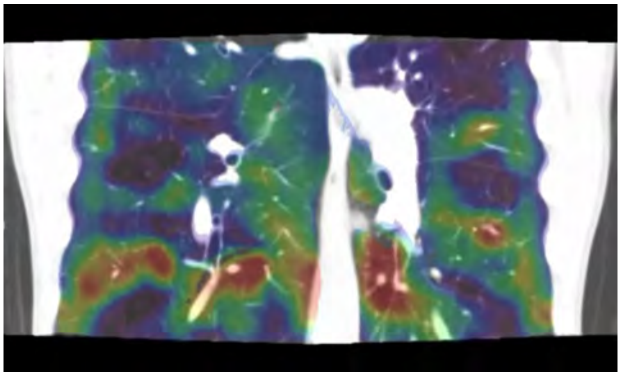

Figure 4 Strain mapping of a severe COPD patient (during expiration, 70-year-old male, $FEV_1/FVC = 0.41$).

Note: Compared with a non-COPD smoker (Figure 3), high strain areas (red areas) are scattered in the lungs, suggesting that these deformations are abnormal and caused by COPD.

Strain measurement has been widely used in cardiology for describing multidimensional deformations or underlying structural changes of muscular fibers, observed by various modalities (such as MRI, CT, and echocardiography).[1–13] Generally, as the normal myocardium contracts in systole and expands in diastole, high strain values are observed in the normal parts of the heart. In contrast to the normal myocardium, ischemic myocardium or scarred cardiac segments do not contract as well, causing heterogeneous deformation and abnormally low strain values.[22] In addition, tethering effects of segments adjacent to area of myocardial infarction also cause an abnormal deformation pattern.[23,24] Thus, quantitative strain measurement can be used to detect regional myocardial dysfunction in patients with ischemic heart disease, cardiomyopathies, hypertension, and valvular disease.[25] Furthermore, strain analysis has been explored to evaluate heterogeneity of myocardial contractile function in patients with dilated cardiomyopathy. Three-dimensional color contour maps based on strain values using MRI accurately visualize heterogeneous contraction in patients with dilated cardiomyopathy.[5] In other words, in the field of cardiology, strain measurement should be "uniformly high" throughout the myocardium and reduced or heterogeneous strain values imply underlying myocardial dysfunction by various diseases.[26]

In the current study, we attempted to introduce strain measurement to 4D dynamic-ventilation CT during free breathing. As strain values express deformation of targeted structures, we expected that two different types of deformation must have existed in the lung: normal deformation of the lung due to inhalation/exhalation and abnormal regional deformation caused by heterogeneous ventilation due to COPD (emphysema and airway disease). Normal deformation of the lung would appear at lung areas with large respiratory movements, such as the lung bottom adjacent to the diaphragm and the dorsal part of the lung in the supine position (Figure 3). In contrast, abnormal deformation may be observed throughout the lung without any specific locations, because this abnormal deformation is caused by heterogeneous ventilation or partial air-trapping due to emphysema and airway disease of COPD (Figure 4). To distinguish these two different deformation patterns, we adjusted measured strain values by the degree of expiration in this study. The changes in MLD between the first and the second to fifth respiratory frames indicate the magnitude of exhalation during the expiratory phase. Even if large deformation occurs by deep (sufficient) expiration in a relatively healthy subject, the high strain values are adjusted by large changes in MLD. In contrast, the value of strain itself may be intermediate in patients with severe COPD without large expiratory movements, but the adjusted strain value may be quite large because of small changes in MLD (insufficient expiration) due to limited airflow. Using this method, we successfully extracted "abnormal" deformation of the lung, which was expressed as the adjusted strain value, and this should be closely associated with heterogeneous lung movements.

The mechanical properties of the lung tissue are mainly determined by collagen and elastic fibers, demonstrating viscoelastic behavior during deflation and inflation.[15] Normally, the stresses under constant ventilation are homogeneously transmitted throughout the entire lung.[27] However, in COPD patients, in addition to loss of pulmonary elastic recoil, heterogeneous distribution of pulmonary emphysema and abnormalities of thoracic structures (such as narrowed/collapsed airways and the flattened diaphragm) must result in asynchronous transmission of physical stress in the lung during ventilation, which causes heterogeneous pulmonary movement. Although heterogeneity or asynchrony of lung/airway motion has been reported in COPD patients,[17–20] this is the first study to quantitatively assess abnormal deformation in the entire scanned lung using strain measurement.

Interestingly, in the current study, adjusted strain was negatively correlated with FEV_1, FEV_1/FVC, MMFR, and PEF. Although the strength of the correlations was intermediate, these correlations suggest that pulmonary motion heterogeneity may be caused by various patterns, such as proximal airway disease, small airway disease, and lung parenchymal abnormalities. Thus, it should be possible to expand strain measurement by dynamic-ventilation CT to other lung/airway diseases, such as asthma, cystic fibrosis, or even diffuse lung disease, which have not been a target of quantitative motion analysis of the lung and airways. Currently, several different approaches have been described using novel CT techniques to measure respiratory changes in lung volume and the emphysema index. These new approaches, including our approach of dynamic-ventilation CT, should generate new information on the pathophysiology of various lung diseases.[28]

There were several limitations of the present study. First, a limited number of subjects were enrolled. These preliminary results should be reproduced with a larger cohort. Second, MLD and adjusted strain were calculated from part of the lung on 4D dynamic-ventilation CT due to the limited scan length in the *Z*-axis ($\leq$160 mm). Thus, selection bias of the lung location would have influenced the strain measurements. Third, the adjusted strain measurements were extracted from the expiratory phase only. As it is known that CT indices at the expiratory phase show higher correlations than at the inspiratory phase,[29] we focused on the expiratory phase only. However, strain measurements during inspiration may provide additional insight into pulmonary physiology, and these measurements shown be performed in future studies. Fourth, several patients enrolled in the current study had resectable thoracic neoplasms. Although no patient had a large mass invading the chest wall or proximal airways, the presence of thoracic tumor may have influenced the strain measurement. Fifth, other coexisting diseases caused by smoking, such as chronic bronchitis or slight interstitial changes, may have influenced the strain measurement. Ideally, healthy subjects without a smoking history should have been enrolled as a control group to assess the normal respiratory deformation of the lung.

In conclusion, strain analysis using 4D dynamic-ventilation CT is feasible to quantify the abnormal deformation of lung motion in patients with COPD. This technique can be expanded to various lung and airways diseases, in a manner that is similar to cardiac imaging.

Acknowledgments

The authors greatly thank Mr Shun Muramatsu (Ohara General Hospital) for his great help in scanning patients. The authors also thank Dr Shinsuke Tsukagoshi (Canon Medical Systems) and Mr Yasuhiro Kondo (Ziosoft) for their technical support. The ACTIve Study Group currently consists of the following institutions: Ohara General Hospital, Fukushima City, Fukushima, Japan (Kotaro Sakuma, MD, Hiroshi Moriya, MD, PhD); Saitama International Medical Center, Saitama Medical University, Hidaka, Saitama, Japan (Fumikazu Sakai, MD, PhD); Kanagawa Cardiovascular and Respiratory Center, Yokohama, Kanagawa, Japan (Tae Iwasawa, MD, PhD); Shiga University of Medical Science, Otsu, Shiga, Japan (Yukihiro Nagatani, MD, Norihisa Nitta, MD, Kiyoshi Murata, MD); Osaka University, Suita, Osaka, Japan (Masahiro Yanagawa, MD, PhD, Osamu Honda, MD, PhD, Noriyuki Tomiyama, MD, PhD); Osaka Medical College, Takatsuki, Osaka, Japan (Mitsuhiro Koyama, MD, PhD); Tenri Hospital, Tenri, Nara, Japan (Yuko Nishimoto, MD, Satoshi Noma, MD, PhD); Kobe University, Kobe, Hyogo, Japan (Yoshiharu Ohno, MD, PhD); University of Occupational and Environmental Health, Kitakyushu, Fukuoka, Japan (Takatoshi Aoki, MD, PhD); University of the Ryukyus, Nishihara, Okinawa, Japan (Tsuneo Yamashiro, MD, Maho Tsubakimoto, MD, PhD, Yanyan Xu, MD, Sadayuki Murayama, MD, PhD). University of the Ryukyus, Ohara General Hospital, and Shiga University of Medical Science receive a research grant from Canon Medical Systems (formerly Toshiba Medical Systems). University of the Ryukyus also receives a research grant from Ziosoft. Xu Y receives a scholarship (Sasagawa scholarship) from the Japan China Medical Association. Yamashiro T received a research grant from the Japan Society for the Promotion of Science (Kakenhi-16K19837).

Disclosure

The authors report no conflicts of interest in this work.

References

1. Pedrizzetti G, Sengupta S, Caracciolo G, et al. Three-dimensional principal strain analysis for characterizing subclinical changes in left ventricular function. *J Am Soc Echocardiogr*. 2014;27(10):1041–1050.
2. Mor-Avi V, Lang RM, Badano LP, et al. Current and evolving echocardiographic techniques for the quantitative evaluation of cardiac mechanics: ASE/EAE consensus statement on methodology and indications endorsed by the Japanese Society of Echocardiography. *J Am Soc Echocardiogr*. 2011;24(3):277–313.
3. Stefani L, De Luca A, Toncelli L, Pedrizzetti G, Galanti G. 3D strain helps relating LV function to LV and structure in athletes. *Cardiovasc Ultrasound*. 2014;12(1):33.
4. Tanabe Y, Kido T, Kurata A, et al. Three-dimensional maximum principal strain using cardiac computed tomography for identification of myocardial infarction. *Eur Radiol*. 2017;27(4):1667–1675.
5. Joseph S, Moazami N, Cupps BP, et al. Magnetic resonance imaging-based multiparametric systolic strain analysis and regional contractile heterogeneity in patients with dilated cardiomyopathy. *J Heart Lung Transplant*. 2009;28(4):388–394.
6. McComb C, Carrick D, McClure JD, et al. Assessment of the relationships between myocardial contractility and infarct tissue revealed by serial magnetic resonance imaging in patients with acute myocardial infarction. *Int J Cardiovasc Imaging*. 2015;31(6):1201–1209.
7. Buckert D, Tibi R, Cieslik M, et al. Myocardial strain characteristics and outcomes after transcatheter aortic valve replacement. *Cardiol J*. 2018;25(2):203–212.
8. Di Franco A, Kim J, Rodriguez-Diego S, et al. Multiplanar strain quantification for assessment of right ventricular dysfunction and non-ischemic fibrosis among patients with ischemic mitral regurgitation. *PLoS One*. 2017;12(9):e0185657.
9. Helle-Valle TM, Yu WC, Fernandes VR, Rosen BD, Lima JA. Usefulness of radial strain mapping by multidetector computer tomography to quantify regional myocardial function in patients with healed myocardial infarction. *Am J Cardiol*. 2010;106(4):483–491.
10. Miyagi H, Nagata M, Kitagawa K, et al. Quantitative assessment of myocardial strain with displacement encoding with stimulated echoes MRI in patients with coronary artery disease. *Int J Cardiovasc Imaging*. 2013;29(8):1779–1786.
11. Maret E, Liehl M, Brudin L, Todt T, Edvardsen T, Engvall JE. Phase analysis detects heterogeneity of myocardial deformation on cine MRI. *Scand Cardiovasc J*. 2015;49(3):149–158.
12. Simpson RM, Keegan J, Firmin DN. MR assessment of regional myocardial mechanics. *J Magn Reson Imaging*. 2013;37(3):576–599.
13. Jiang K, Yu X. Quantification of regional myocardial wall motion by cardiovascular magnetic resonance. *Quant Imaging Med Surg*. 2014;4(5):345–357.
14. Lai-Fook SJ. Lung parenchyma described as a prestressed compressible material. *J Biomech*. 1977;10(5–6):357–365.
15. Faffe DS, Zin WA. Lung parenchymal mechanics in health and disease. *Physiol Rev*. 2009;89(3):759–775.
16. Sciurba FC, Rogers RM, Keenan RJ, et al. Improvement in pulmonary function and elastic recoil after lung-reduction surgery for diffuse emphysema. *N Engl J Med*. 1996;334(17):1095–1099.
17. Stahr CS, Samarage CR, Donnelley M, et al. Quantification of heterogeneity in lung disease with image-based pulmonary function testing. *Sci Rep*. 2016;6(1):29438.
18. Estrada L, Torres A, Sarlabous L, et al. Estimation of bilateral asynchrony between diaphragm mechanomyographic signals in patients with chronic obstructive pulmonary disease. *Conf Proc IEEE Eng Med Biol Soc*. 2014;2014:3813–3816.
19. Yamashiro T, Moriya H, Tsubakimoto M, Matsuoka S, Murayama S. Continuous quantitative measurement of the proximal airway dimensions and lung density on four-dimensional dynamic-ventilation CT in smokers. *Int J Chron Obstruct Pulmon Dis*. 2016;11(1):755–764.
20. Yamashiro T, Moriya H, Matsuoka S, et al. Asynchrony in respiratory movements between the pulmonary lobes in patients with COPD: continuous measurement of lung density by 4-dimensional dynamic-ventilation CT. *Int J Chron Obstruct Pulmon Dis*. 2017;12(1):2101–2109.
21. Vestbo J, Hurd SS, Agustí AG, et al. Global strategy for the diagnosis, management, and prevention of chronic obstructive pulmonary disease: GOLD executive summary. *Am J Respir Crit Care Med*. 2013;187(4):347–365.
22. Haugaa KH, Smedsrud MK, Steen T, et al. Mechanical dispersion assessed by myocardial strain in patients after myocardial infarction for risk prediction of ventricular arrhythmia. *JACC Cardiovasc Imaging*. 2010;3(3):247–256.
23. Edvardsen T, Gerber BL, Garot J, Bluemke DA, Lima JA, Smiseth OA. Quantitative assessment of intrinsic regional myocardial deformation by Doppler strain rate echocardiography in humans: validation against three-dimensional tagged magnetic resonance imaging. *Circulation*. 2002;106(1):50–56.
24. Force T, Kemper A, Perkins L, Gilfoil M, Cohen C, Parisi AF. Overestimation of infarct size by quantitative two-dimensional echocardiography: the role of tethering and of analytic procedures. *Circulation*. 1986;73(6):1360–1368.
25. Jeung MY, Germain P, Croisille P, El ghannudi S, Roy C, Gangi A. Myocardial tagging with MR imaging: overview of normal and pathologic findings. *Radiographics*. 2012;32(5):1381–1398.
26. Nagao M, Yamasaki Y, Yonezawa M, et al. Geometrical characteristics of left ventricular dyssynchrony in advanced heart failure. Myocardial strain analysis by tagged MRI. *Int Heart J*. 2014;55(6):512–518.
27. Cai J, Altes TA, Miller GW, et al. MR grid-tagging using hyperpolarized helium-3 for regional quantitative assessment of pulmonary biomechanics and ventilation. *Magn Reson Med*. 2007;58(2):373–380.
28. Ley-Zaporozhan J, Ley S, Mews J, Weinheimer O, Kandel S, Rogalla P. Changes of emphysema parameters over the respiratory cycle during free breathing: preliminary results using respiratory gated 4D-CT. *COPD*. 2017;14(6):597–602.
29. Yamashiro T, Matsuoka S, Bartholmai BJ, et al. Collapsibility of lung volume by paired inspiratory and expiratory CT scans: correlations with lung function and mean lung density. *Acad Radiol*. 2010;17(4):489–495.

International Journal of COPD Dovepress

Publish your work in this journal

The International Journal of COPD is an international, peer-reviewed journal of therapeutics and pharmacology focusing on concise rapid reporting of clinical studies and reviews in COPD. Special focus is given to the pathophysiological processes underlying the disease, intervention programs, patient focused education, and self management protocols. This journal is indexed on PubMed Central, MedLine and CAS. The manuscript management system is completely online and includes a very quick and fair peer-review system, which is all easy to use. Visit http://www.dovepress.com/testimonials.php to read real quotes from published authors.

Submit your manuscript here: http://www.dovepress.com/international-journal-of-chronic-obstructive-pulmonary-disease-journal

Original Investigation

Correlation Between Intravoxel Incoherent Motion and Dynamic Contrast-Enhanced Magnetic Resonance Imaging Parameters in Rectal Cancer

Hongliang Sun, MD, Yanyan Xu, MD, Qiaoyu Xu, MD, Jianghui Duan, MD, Haibo Zhang, MD,
Tongxi Liu, MD, Lu Li, MD, Queenie Chan, PhD, Sheng Xie, MD, Wu Wang, MD

Rationale and Objectives: This study aimed to determine the correlation between intravoxel incoherent motion (IVIM) and multiphase dynamic contrast-enhanced magnetic resonance imaging (DCE-MRI) quantitative parameters in patients with rectal cancer.

Materials and Methods: Ninety-seven patients with rectal cancer were included in this study. All pelvic MRI examinations were performed in a 3.0 T MR unit, including diffusion-weighted imaging with 16 *b* values, DCE-MRI with two different flip angles (5° and 10°, respectively), and T1-fast field echo sequences as the reference. The IVIM perfusion-related parameters (*f*, perfusion fraction; D^*, pseudo-diffusion coefficient; $f{\cdot}D^*$, the multiplication of the two parameters) were calculated by biexponential analysis. Quantitative DCE-MRI parameters were transfer constant (K^{trans}) between blood plasma and extravascular extracellular space), K_{ep} (rate between extravascular extracellular space and blood plasma), V_e (extravascular volume fraction), V_p (plasma volume fraction), and area under the gadolinium concentration curve. Interobserver agreements were evaluated using the intraclass correlation coefficient and Bland−Altman analysis. A *p* value <0.05 indicated a statistically significant difference.

Results: The study included 75 males and 22 females with a median age of 58.8 years (range, 26−85years). Interobserver reproducibility for IVIM perfusion-related parameters and DCE-MRI quantitative parameters was good to excellent (intraclass correlation coefficient = 0.8618−0.9181, intraclass correlation coefficient = 0.7826−0.9088, respectively). Moderate correlations were found between $f{\cdot}D^*$ and K^{trans} ($r = 0.533$; $p < 0.001$), and relatively weak correlations between D^* and K^{trans} ($r = 0.389$; $p < 0.001$), D^* and V_p ($r = 0.442$; $p < 0.001$), $f{\cdot}D^*$ and V_p ($r = 0.466$; $p < 0.001$), and *f* and V_p ($r = -0.234$; $p = 0.021$).

Abbreviations

D	Diffusion coefficient
D*	Pseudo-diffusion coefficient
DCE-MRI	dynamic contrast-enhanced magnetic resonance imaging
DWI	Diffusion-weighted imaging
f	Perfusion fraction
FFE	fast field echo
IVIM	Intravoxel incoherent motion
K^{trans}	transfer constant between blood plasma and extravascular extracellular space

Acad Radiol 2018; ■:1−7

Reprint requests: No.
Grant Support: This work was supported by grants from Beijing Municipal Science & Technology Commission (No. Z181100001718099), the National Natural Science Foundation of China (No. 81501469) and the Health Industry Special Scientific Research Project of National Health and Family Planning Commission of the People's Republic of China (No. 201402019).

From the Department of Radiology, China-Japan Friendship Hospital, No.2 Yinghua East Street, Chaoyang District, Beijing 100029, China (H.S., Y.X., Q.X., J.D., H.Z., T.L., L.L., S.X., W.W.); Philips Healthcare, Shatin, New Territories, Hong Kong, China (Q.C.). Received May 22, 2018; revised August 24, 2018; accepted August 24, 2018. **Address correspondence to:** H.S. e-mail: stentorsun@gmail.com

© 2018 The Association of University Radiologists. Published by Elsevier Inc. All rights reserved.

https://doi.org/10.1016/j.acra.2018.08.012

Downloaded for Anonymous User (n/a) at Faculty of Medicine & Affiliated Hospital from ClinicalKey.jp by Elsevier on January 28, 2019.
For personal use only. No other uses without permission. Copyright ©2019. Elsevier Inc. All rights reserved.

K_{ep}
rate between EES and blood plasma

ROI
Region of interest

TE
Echo time

TR
Repetition time

TSE
Turbo spin echo

V_e
extravascular volume fraction

V_p
plasma volume fraction

Conclusion: IVIM perfusion-related parameters, especially $f{\cdot}D^*$, demonstrated moderate correlations with DCE-MRI quantitative parameters in rectal cancer.

Key Words: Rectal cancer; intravoxel incoherent motion; dynamic contrast-enhanced; magnetic resonance imaging.

© 2018 The Association of University Radiologists. Published by Elsevier Inc. All rights reserved.

INTRODUCTION

Tumor angiogenesis plays a vital role in tumor growth and progressively invasion, and evaluation of tumor angiogenesis activity is quite helpful for diagnosis, prognostic evaluation, and therapeutic monitoring of rectal cancer (1–2). T1-weighted dynamic contrast-enhanced magnetic resonance imaging (DCE-MRI) is a well-established technique used to map quantitative perfusion and permeability parameters, which indirectly reflect tumor microcirculation. It has been proved that perfusion parameters of DCE-MRI correlated with tumor angiogenesis and molecular markers in rectal cancer (3–7). Previous clinical studies (8–10) also demonstrated the potential value of DCE-MRI in monitoring treatment response of rectal cancer to neoadjuvant chemoradiation. However, DCE-MRI could not provide perfusion information without the injection of intravenous contrast media, which was a dilemma, particularly in patients with renal insufficiency or individuals with severe allergies to intravenous gadolinium-based contrast media.

Intravoxel incoherent motion diffusion-weighted imaging (IVIM-DWI) (11) is another attractive functional MRI technique that provides parameters reflecting tissue perfusion without intravenous contrast injection. IVIM-DWI consists of a series of diffusion-weighted acquisitions with a wide range of *b* values, subsequently, allowing for simultaneous acquisition of both microcirculatory and diffusivity information. Furthermore, Le Bihan and Turner (12,13) provided the equations that linked perfusion-related IVIM parameters and conventional perfusion parameters in the brain, stating that theoretical relationships existed between f and blood volume, $D^\star$ and mean transit time, and flow-related parameters and blood flow. Therefore, IVIM perfusion-related parameters were assumed to be theoretically associated with DCE-MRI parameters. If perfusion information of rectal cancer can be evaluated using IVIM-DWI, then IVIM-DWI may possibly serve as a surrogate for DCE-MRI to some degree, eventually bringing down the need for contrast agent injection.

Although the potential ability of IVIM-DWI parameters in probing tumor microcirculation is fascinating, no clear relationships between perfusion-related IVIM parameters and DCE-MRI quantitative parameters in rectal cancers have been reported.

Therefore, this study aimed to evaluate the relationship between perfusion-related IVIM parameters and DCE-MRI quantitative parameters in patients with rectal cancer, and to explore the possibility of noninvasively evaluating tumor perfusion using DWI in the future.

MATERIALS AND METHOD

Patients

This retrospective study was approved by the ethics committee of the hospital, and written informed consent was obtained in all cases.

Totally, 152 consecutive patients with biopsy-proven rectal cancers, waiting to undergo initial staging investigations, were recruited. After imaging examinations (including MRI), although surgery was performed in all patients, the other therapy procedures including chemoradiation therapy were individually tailored.

However, patients who met any of the following criteria were excluded from the late evaluation: (1) prior rectal surgery (rectal cancer resection [n = 2], polypectomy [n = 1], anal fistulectomy [n=1], and rectal prolapse surgery [n=1]); (2) pre-examination chemoradiation therapy ($n = 20$) or unidentified herbal medicine therapy ($n = 7$); (3) poor image quality (heavy intestinal peristalsis or heavy susceptibility artifacts [$n = 5$], too small lesion [diameter <5 mm], or difficult to identify on images [n=6]); and (4) mucinous adenocarcinoma ($n = 12$). Finally, 97 patients (75 men and 22 women; mean age, 58.8 years; age range, 26–85 years) were enrolled in the final analysis. Selected patient and tumor characteristics are shown in Table 1.

MRI Examination

Patients had low-residue diet before examination and fasted on the day of examination. Intramuscular injection of 10 mg

Downloaded for Anonymous User (n/a) at Faculty of Medicine & Affiliated Hospital from ClinicalKey.jp by Elsevier on January 28, 2019.
For personal use only. No other uses without permission. Copyright ©2019. Elsevier Inc. All rights reserved.

TABLE 1. Patient and Tumor Characteristics

Characteristic	No.
Patient number	97
Age (year)	
Mean (range)	58.8 (26−85)
Sex (M/F)	75/22
Tumor length (cm)	4.06 ± 1.75
Radiologic T stage	
T1−2	30 (30.93%)
T3	55 (56.70%)
T4	12 (12.37%)
Tumor location (distance from the anal verge)	
Upper (>10 cm)	15 (15.46%)
Middle (5−10 cm)	40 (41.24%)
Lower (<5 cm)	42 (43.30%)

anisodamine hydrochloride was given to each patient to inhibit intestinal peristalsis. The patients had to lie on the table without moving to minimize the possible motion artifacts or deformation introduced during the examination.

Pelvic MRI scanning was implemented on a 3T whole-body scanner (Ingenia, Philips Medical Systems, Best, the Netherlands) with a gradient strength 45 mT/m and a gradient switching rate 200 mT/(m·ms), using a 16-channel anterior torso dS coil and a 16-channel posterior table dS coil. 2D Sagittal and coronal T2-weighted turbo spin echo sequences were performed with the following parameters: repetition time (TR) 4347 ms, echo time (TE) 102 ms, Echo-train length 21, field of view (FOV) 24 × 24 cm^2, slice thickness 4 mm with 0.4-mm gap, acquisition matrix 336 × 246, and number of signals averaged (NSA) 1. A 2D oblique axial T2-weighted turbo spin echo sequence was planned perpendicularly to the tumor axis using the following parameters: TR 4522 ms, TE 102 ms, FOV 18 × 18 cm^2, slice thickness 3.5 mm with 0.35-mm gap, and acquisition matrix 300 × 296.

Oblique axial IVIM−MRI scan was performed using a single-shot echo-planar imaging pulse sequence in free breathing with the following parameters: TE/TR 76/4000 ms, FOV 40 × 32 cm^2, slice thickness 6 mm with 0.6-mm gap, acquisition matrix 160 × 102, echo-planar imaging (EPI) factor 35, bandwidth 3113.1, number of slices 20, fat saturation technique SPectral Attenuated Inversion Recovery and 16 *b* values (0, 10, 20, 30, 40, 60, 80, 100, 150, 200, 400, 800, 1000, 1200, 1500, and 2000 s/mm^2). When *b* values were 0, 10, 20, 30, 40, 60, 80, 100, 150, 200, 400 s/mm^2, the NSA was 1. When *b* value was 800 s/mm^2, the NSA was 2.When *b* values were 1000, 1200, 1500, and 2000 s/mm^2, the NSA was 3. The scan time of single IVIM was 5 minutes.

DCE-MRI (40 dynamic phases) used a 3D fast field echo sequence with fat suppression on the oblique axial plane (the same as IVIM−MRI sequence). Two precontrast T1-fast field echo sequences with different flip angles (5° and 10°, respectively) were set as references to calculate the baseline T1 relaxation time per pixel (baseline T1 map). The two reference series were identical to the DCE sequences in terms of, for example, FOV, orientation, resolution, slice thickness, and number of slices. Scan parameters of DCE-MRI were as follows: TR/TE 1.63/3.3 ms; flip angle 15°; acquisition matrix 252 × 222; FOV 304 × 362 mm^2; slice thickness 1.5 mm; and number of slices 70; the temporal resolution 2 seconds. The total scan time of DCE-MRI (40 dynamic phases) was approximately 4.8 minutes.

A gadolinium-based agent gadopentetate dimeglumine (Magnevist; Bayer Healthcare, Berlin, Germany) was intravenously injected at a flow rate of 2.5 ml/s and at a dose of 0.2 ml/kg of body weight, followed by a 20-ml saline flush with a high-pressure injector.

Image Analysis

The IVIM perfusion-related parameters (*f*, perfusion fraction; $D^\star$, pseudo-diffusion coefficient) and the flow-related parameter ($f \cdot D^\star$) were calculated using the biexponential model described by Le Bihan et al. (11,12) as follows:

$$S_b/S_0 = (1-f)\exp(-bD) + f\exp(-bD^*)$$

where S_b is the signal intensity in the pixel with diffusion gradient, S_0 is the signal intensity in the pixel without diffusion gradient, *D* is the true diffusion as reflected by pure molecular diffusion, *f* is the fractional perfusion related to microcirculation, and $D^\star$ is the pseudo-diffusion coefficient related to perfusion. The raw data of diffusion-weighted images were transferred to an EWS4.1 workstation and analyzed using in-house software (IDL6.3 software, Colorado).

Quantitative DCE-MRI parameters were K^{trans} (transfer constant between blood plasma and extravascular extracellular space [EES]), K_{ep} (rate between EES and blood plasma), V_{e} (extravascular volume fraction), V_{p} (plasma volume fraction), and AUC (area under the gadolinium concentration curve). The pharmacokinetic calculation was done on a pixel-by-pixel basis using a two-compartment model. The calculation was based on the extended Tofts model (14) as follows:

$$C(t) = V_P C_a(t) + K^{trans} e^{-tK_{ep}} * C_a(t)$$

where *C*(*t*) is the contrast concentration in tissue and $C_a(t)$ is the arterial input function. DCE-MRI data were transferred to an advantage workstation using T1 permeability software (Intellispace portal workstation, Philips Medical Systems).

K^{trans} and DWI images ($b = 1000$ s/mm^2) were used as references to determine the lesion areas on corresponding IVIM and DCE maps (Fig 1).

Regions of interest (ROIs) were manually drawn to cover the entire tumor area slice by slice, avoiding the inclusion of intestinal gas, liquid, and anatomical structures. Necrotic and large cystic areas by visual view were excluded from ROI. An ROI of the lesion was manually drawn on the basis of the DWI images ($b = 1000$ s/mm^2), and the values of *f* and

Downloaded for Anonymous User (n/a) at Faculty of Medicine & Affiliated Hospital from ClinicalKey.jp by Elsevier on January 28, 2019.
For personal use only. No other uses without permission. Copyright ©2019. Elsevier Inc. All rights reserved.

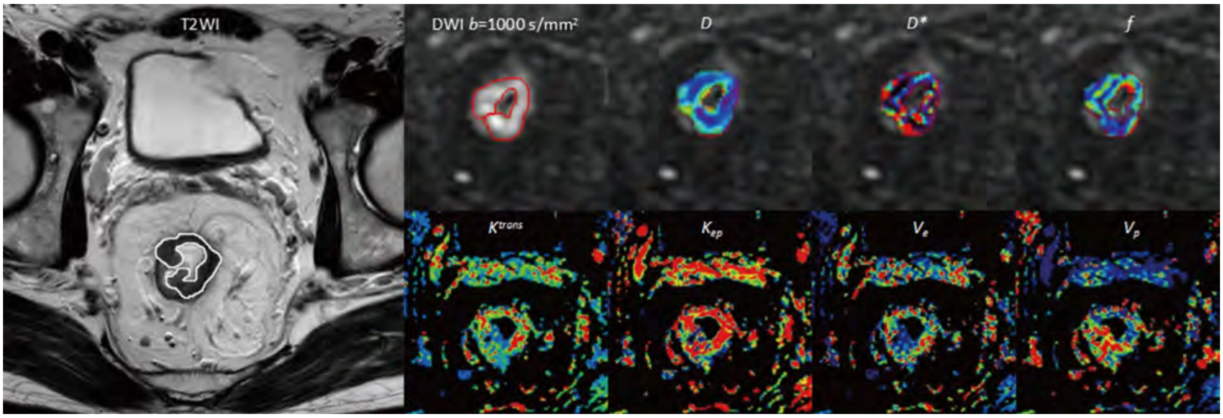

Figure 1. Images in a 53-year-old man with moderately differentiated rectal cancer. The border of the lesion on the T2WI image was manually drawn. The top row small images: DWI (b = 1000 s/mm^2) and IVIM-DWI parameter images (*D, D**, and *f*); the bottom row small images: corresponding DCE-MRI quantitative parameter images (K^{trans}, K_{ep}, V_e, and V_p). DCE-MRI, dynamic contrast-enhanced magnetic resonance imaging; DWI, Diffusion-weighted imaging; IVIM-DWI; intravoxel incoherent motion diffusion-weighted imaging.

$D^\star$were obtained automatically for measuring the IVIM parameters. For DCE-MRI measurements, an arterial input function obtained from the iliac artery was applied for modeling procedure. Then, the following maps were obtained automatically: K^{trans}, K_{ep}, V_e, V_p, and AUC. Eventually, an ROI of the lesion was manually drawn on the basis of the K^{trans} map, and the corresponding values of K^{trans}, K_{ep}, V_e, V_p, and AUC were obtained automatically.

Two experienced radiologists (10 and 6 years, respectively, in gastrointestinal imaging) placed the ROIs and analyzed all the IVIM and DCE-MRI images independently. The data generated by the two observers were used to calculate interobserver reliability.

Statistical Analysis

All analyses were performed using statistical software SPSS17.0 (SPSS 17.0 for Windows, SPSS, Illinois). Normality testing was performed using the Shapiro−Wilk test and homogeneity-of-variance testing using the Levene test. Continuous variables were expressed as mean ± standard deviation or median ± interquartile range. Correlations between f and all quantitative DCE-MRI parameters were analyzed using Pearson's or Spearman's correlation coefficients, respectively. $D^\star$ and $f{\cdot}D^\star$ were also similarly analyzed. Interobserver reliability. was evaluated using the intraclass correlation coefficient (ICC) and Bland−Altman analysis. Correlation coefficient $|r|$ of 0−0.5, 05−0.8, and >0.8 was considered as poor, moderate, and high correlations, respectively. A p value <0.05 was considered to indicate a statistically significant difference.

RESULTS

Interobserver Reliability

The measurement consistency between two observers was evaluated by ICC and Bland−Altman analysis (Table 2). ICC and Bland−Altman bias values for IVIM and DCE-MRI quantitative parameters indicated good to excellent interobserver reliability. (ICC_{IVIM}, 0.8618−0.9181, ICC_{DCE}, 0.7826−0.9088; $Bias_{IVIM}$, 0.5%−2.8%, $Bias_{DCE}$, −10.4%−5.3%).

TABLE 2. Interobserver Reliability in Assessing IVIM and DCE-MRI Parameters

Parameters	ICC (95% CI)	Bland−Altman Bias (95% CI), %
f	0.9181 (0.8643−0.9554)	0.5 (−39.7 to 40.7)
D^*	0.8618 (0.8334−0.8843)	2.8 (−49.7 to 55.3)
$f{\cdot}D^*$	0.8817 (0.8540−0.9306)	2.3 (−53.6 to 58.2)
K^{trans}	0.9088 (0.8344−0.9655)	5.1 (−55.2 to 65.4)
K_{ep}	0.8774 (0.8221−0.9163)	5.3 (−62.3 to 72.9)
V_e	0.7826 (0.6749−0.8547)	−10.4 (−140.6 to 119.8)
V_p	0.9021 (0.8571−0.9335)	−1.6 (−52.2 to 49.0)
AUC	0.8445 (0.8181−0.8825)	−2.9 (−33.8 to 28.0)

AUC, area under the gadolinium concentration curve; D^*, pseudo-diffusion coefficient; DCE-MRI, dynamic contrast-enhanced magnetic resonance imaging; f, perfusion fraction; $f{\cdot}D^*$, the multiplication of the two parameters; ICC, intraclass correlation coefficient; IVIM, intravoxel incoherent motion; K_{ep}, rate between EES and blood plasma; K^{trans}, transfer constant between blood plasma and extravascular extracellular space; V_e, extravascular volume fraction; $V_{p,}$ plasma volume fraction; 95% CI, 95% confidence interval.

Downloaded for Anonymous User (n/a) at Faculty of Medicine & Affiliated Hospital from ClinicalKey.jp by Elsevier on January 28, 2019.
For personal use only. No other uses without permission. Copyright ©2019. Elsevier Inc. All rights reserved.

Tissue Perfusion Parameters

The IVIM perfusion parameters were as follows: $f = (17.02 \pm 8.37)\%$, $D^\star = (15.83 \pm 55.56) \times 10^{-3}$ mm²/s, $f{\cdot}D^\star = (2.04 \pm 5.69) \times 10^{-3}$ mm²/s.

The DCE-MRI quantitative parameters were as follows: $K^{trans} = (2.00 \pm 4.20)$ min^{-1}, $K_{ep} = (0.99 \pm 0.87)$ min^{-1}, $V_e = 1.76 \pm 3.61$, $V_e = 0.49 \pm 0.88$, and AUC = 46.96 ± 21.29.

Correlations Between Parameters of IVIM and DCE-MRI

Moderate correlations were found between $f{\cdot}D^\star$ and K^{trans} ($r = 0.533$; $p < 0.001$), and relatively weak correlation between $D^\star$ and K^{trans} ($r = 0.389$; $p < 0.001$), $D^\star$ and V_p ($r = 0.442$; $p < 0.001$), $f{\cdot}D^\star$ and V_p ($r = 0.466$; $p < 0.001$), and f and V_p ($r = -0.234$; $p = 0.021$; Table 3).

DISCUSSION

The present study investigated the correlations between IVIM perfusion-related parameters and quantitative DCE-MRI perfusion metrics in rectal cancer to evaluate the ability of IVIM-DWI to measure tumor perfusion. The results showed that $f{\cdot}D^\star$ was moderately related to K^{trans}, and relatively weak correlations were also found between $D^\star$ and K^{trans} ($r = 0.389$), $D^\star$ and V_p ($r = 0.442$), $f{\cdot}D^\star$ and V_p ($r = 0.466$), and f and V_p ($r = -0.234$). The findings supported the aforementioned hypothesis that potential relationships existed between IVIM and DCE-MRI perfusion parameters to some degree.

$f{\cdot}D^\star$ allowed the estimation of relative perfusion or blood flow in the tumor microcirculation (13), which was thought to depend on the interplay among the microvascular anatomy, vascular permeability, and blood flow dynamics. In contrast, K^{trans} was defined as transfer constant between blood plasma and EES, reflecting vascular permeability when contrast uptake was limited by vascular endothelial leakiness (15,16). Furthermore, K^{trans} was possibly related to tumor angiogenesis, and higher mean K^{trans} value was observed in epidermal growth factor receptor-positive rectal cancer (3). Therefore, the moderate correlation between $f{\cdot}D^\star$ and K^{trans} in this study suggested that $f{\cdot}D^\star$ was associated with vascular permeability and blood flow in rectal cancer. Similar results were reported in studies on non–small-cell lung cancer, head and neck squamous cell cancer, breast lesions, and cervical cancers (17–21).

TABLE 3. Correlation Coefficient Between IVIM Perfusion-Related Parameters and Perfusion Measurements From DCE-MRI

Variables	*f*		*f·D**		*D**	
	r	*p*	*R*	*p*	*r*	*p*
K^{trans}	0.068	0.506	0.533	<0.001	0.389	<0.001
K_{ep}	0.144	0.768	−0.077	0.452	−0.093	0.641
V_e	0.094	0.358	−0.130	0.658	−0.166	0.773
V_p	−0.234	0.021	0.466	<0.001	0.442	<0.001
AUC	−0.140	0.771	−0.110	0.838	−0.120	0.845

AUC, area under the gadolinium concentration curve; *D**, pseudodiffusion coefficient; DCE-MRI, dynamic contrast-enhanced magnetic resonance imaging; *f*, perfusion fraction; *f·D**, the multiplication of the two parameters; ICC, intraclass correlation coefficient, IVIM, intravoxel incoherent motion; K_{ep}, rate between EES and blood plasma; K^{trans}, transfer constant between blood plasma and extravascular extracellular space; V_e, extravascular volume fraction; V_p, plasma volume fraction.

The f value was a measure of the fractional volume of capillary blood flow in each voxel, while $D^\star$ was reported to be proportional to blood velocity and mean capillary segment length (11), which were heterogeneous in the tortuous tumor vasculature. Thus, f and $D^\star$ indirectly reflected the increased immature vessels and capillary permeability. Furthermore, in an animal study of human colorectal cancer (HT29) implanted mice model, f and $D^\star$ were significantly associated with the tumor microvessel density, which was considered as a surrogate marker for angiogenesis (22). Moreover, delivery of the tracer to the tissues was still dependent on intravascular flow even with the use of diffusible tracers (12,13). Thus, a relationship between perfusion parameters quantified by DWI and tracer kinetic methods could plausibly be deduced (13).

However, the aforementioned relationship is still controversial, as evident from the published studies (17–21, 23–26). In the present study, relatively weak correlations were observed between f, $D^\star$, and DCE-MRI parameters, especially f and V_p ($r = -0.234$). Possible reasons for the discrepancy reported in some studies (26,27) and the present study were as follows: (1) the fast component of f and $D^\star$ measured by DWI might comprise more than one physiologic process in some organs (eg, glandular secretion, ductal flow, and cerebrospinal fluid flow) (28–30); (2) the evolution time of DWI sequence for significant water exchange was limited and thus the signal could be interpreted as separate intra- and extravascular compartments, with the parameters f and $D^\star$ referring to the intravascular compartments. In contrast, DCE-MRI tracked contrast continuously over much longer periods (several minutes) and thus necessarily involved intravascular, extravascular, and exchange dynamics. Thus, the parameters of the DCE-MRI model reflected not only the microvascular volume or flow but also some composite encompassing total tracer transit (24); (3) signal intensity would be affected by different b-value selection, especially low b value (≤ 200 s/mm²) (31–32); and (4) non-negligible heterogeneity within an individual tumor (17). Further studies and a more standardized approach to data collection (IVIM-DWI or DCE-MRI sequence) and analysis are needed to verify the conflicting results published in the literature.

In addition, careful consideration should also be given to the interobserver reliability of IVIM and DCE-MRI parameters. Compared to other parameters, relatively larger range of 95% confidence interval limits of agreement in V_e has been

Downloaded for Anonymous User (n/a) at Faculty of Medicine & Affiliated Hospital from ClinicalKey.jp by Elsevier on January 28, 2019.
For personal use only. No other uses without permission. Copyright ©2019. Elsevier Inc. All rights reserved.

observed in this study. V_e is one of the perfusion parameters derived from DCE-MRI data, reflecting the situation in EES, however, it was less consistent (21). The following factors may contribute to large variability in V_e. One factor is tumor angiogenesis, abnormal vessels have been heterogeneously distributed, and the vascular space and EES could be variable (3,4). Furthermore, the high ratio of advanced cancer in subjects (69.07% rectal cancer $\geq$T3 stage) may intensify the variability in the study. Another possible factor is that V_e can vary with edema around the lesion (33). Therefore, V_e may be less reliable and needs to be further studied.

This study had several limitations. First, only patients with pathologically proven rectal adenocarcinoma were included and evaluated in this study. Second, the optimal *b*-value selection for rectal cancer was not assessed. Different *b*-value selection methods affected the IVIM parameter estimates, especially *f* (34,35). The clinical tolerance and IVIM characterization both were taken into consideration. Further, 16 *b* values were used in this study, and half of them were less than 200 s/mm^2. Third, other analysis methods for IVIM estimation, such as nonnegative least squares fitting, were not introduced (36). Fourth, the perfusion parameters derived from IVIM and DCE-MRI were not correlated with the histopathological results (such as the microvascular density). However, the purpose of the present study was not to identify the correlation between MR parameters and histopathology, but the relationship between the MR parameters derived using different techniques.

In conclusion, IVIM-DWI could be performed without the administration of exogenous contrast medium, making it a safer and more convenient method for patients, especially for individuals with renal insufficiency. Furthermore, the present study implied that IVIM perfusion-related parameters, especially $f \cdot D^\star$, demonstrated moderate correlations with quantitative perfusion parameters derived from DCE-MRI in rectal cancer. Thus, the rectal IVIM-DWI analysis can provide both diffusion and perfusion information, which has a potential value in evaluating treatment response, differentiating cancer recurrence from radiofibrosis in patients with rectal cancer without exogenous contrast agent.

REFERENCES

1. Folkman J. What is the evidence that tumors are angiogenesis dependent? J Natl Cancer Inst 1990; 82:4–6.
2. Choi HJ, Hyun MS, Jung GJ, et al. Tumor angiogenesis as a prognostic predictor in colorectal carcinoma with special reference to mode of metastasis and recurrence. Oncology 1998; 55:575–581.
3. Yeo DM, Oh SN, Jung CK, et al. Correlation of dynamic contrast-enhanced MRI perfusion parameters with angiogenesis and biologic aggressiveness of rectal cancer: preliminary results. J Magn Reson Imaging 2015; 41:474–480.
4. Yao WW, Zhang H, Ding B, et al. Rectal cancer: 3D dynamic contrast-enhanced MRI; correlation with microvascular density and clinicopathological features. Radiol Med 2012; 116:366–374.
5. Tuncbilek N, Karakas HM, Altaner S. Dynamic MRI in indirect estimation of microvessel density, histologic grade, and prognosis in colorectal adenocarcinomas. Abdom Imaging 2004; 29:166–172.
6. de Lussanet QG, Backes WH, Griffioen AW, et al. Dynamic contrast-enhanced magnetic resonance imaging of radiation therapy-induced microcirculation changes in rectal cancer. Int J Radiat Oncol Biol Phys 2005; 63:1309–1315.
7. Zhang XM, Yu D, Zhang HL, et al. 3D dynamic contrast-enhanced MRI of rectal carcinoma at 3T: correlation with microvascular density and vascular endothelial growth factor markers of tumor angiogenesis. J Magn Reson Imaging 2008; 27:1309–1316.
8. Lim JS, Kim D, Baek SE, et al. Perfusion MRI for the prediction of treatment response after preoperative chemoradiotherapy in locally advanced rectal cancer. Eur Radiol 2012; 22:1693–1700.
9. Intven M, Reerink O, Philippens ME. Dynamic contrast enhanced MR imaging for rectal cancer response assessment after neo-adjuvant chemoradiation. J Magn Reson Imaging 2015; 41:1646–1653.
10. Martens MH, Subhani S, Heijnen LA, et al. Can perfusion MRI predict response to preoperative treatment in rectal cancer? Radiother Oncol 2015; 114:218–223.
11. Le Bihan D, Breton E, Lallemand D, et al. Separation of diffusion and perfusion in intravoxel incoherent motion MR imaging. Radiology 1988; 168:497–505.
12. Le Bihan D, Breton E, Lallemand D, et al. MR imaging of intravoxel incoherent motions: application to diffusion and perfusion in neurologic disorders. Radiology. 1986; 161:401–407.
13. Le Bihan D, Turner R. The capillary network: a link between IVIM and classical perfusion. Magn Reson Med 1992; 27:171–178.
14. Tofts PS, Brix G, Buckley DL, et al. Estimating kinetic parameters from dynamic contrast-enhanced T(1)-weighted MRI of a diffusable tracer: standardized quantities and symbols. J Magn Reson Imaging 1999; 10:223–232.
15. Zahra MA, Hollingsworth KG, Sala E, et al. Dynamic contrast-enhanced MRI as a predictor of tumour response to radiotherapy. Lancet Oncol 2007; 8:63–74.
16. Barnes SL, Whisenant JG, Loveless ME, Yankeelov TE. Practical dynamic contrast enhanced MRI in small animal models of cancer: data acquisition, data analysis, and interpretation. Pharmaceutics 2012; 4:442–478.
17. Shi C, Liu D, Xiao Z, et al. Monitoring tumor response to antivascular therapy using non-contrast intravoxel incoherent motion diffusion-weighted MRI. Cancer Res 2017; 77:3491–3501.
18. Fujima N, Yoshida D, Sakashita T, et al. Intravoxel incoherent motion diffusion-weighted imaging in head and neck squamous cell carcinoma: assessment of perfusion-related parameters compared to dynamic contrast-enhanced MRI. Magn Reson Imaging 2014; 32:1206–1213.
19. Lee EY, Hui ES, Chan KK, et al. Relationship between intravoxel incoherent motion diffusion-weightedMRI and dynamiccontrast-enhanced MRI in tissue perfusion of cervical cancers. J Magn Reson Imaging 2015; 42:454–459.
20. Kim JH, Kim CK, Park BK, et al. Dynamic contrast-enhanced 3-T MR imaging in cervical cancer before and after concurrent chemoradiotherapy. Eur Radiol 2012; 22:2533–2539.
21. Liu C, Wang K, Chan Q, et al. Intravoxel incoherent motion MR imaging for breast lesions: comparison and correlation with pharmacokinetic evaluation from dynamic contrast-enhanced MR imaging. Eur Radiol 2016; 26:3888–3898.
22. Lee HJ, Rha SY, Chung YE, et al. Tumor perfusion-related parameter of diffusion-weighted magnetic resonance imaging: correlation with histological microvessel density. Magn Reson Med 2014; 71:1554–1558.
23. Suo S, Lin N, Wang H, et al. Intravoxel incoherent motion diffusion-weighted MR imaging of breast cancer at 3.0 tesla: comparison of different curve-fitting methods. J Magn Reson Imaging 2015; 42:362–370.
24. Patel J, Sigmund EE, Rusinek H, et al. Diagnosis of cirrhosis with intravoxel incoherent motion diffusion MRI and dynamic contrast-enhanced MRI alone and in combination: preliminary experience. J Magn Reson Imaging 2010; 31:589–600.
25. Xu XQ, Choi YJ, Sung YS, et al. Intravoxel Incoherent motion MR imaging in the head and neck: correlation with dynamic contrast-enhanced MR imaging and diffusion-weighted imaging. Korean J Radiol 2016; 17:641–649.
26. Marzi S, Stefanetti L, Sperati F, et al. Relationship between diffusion parameters derived from intravoxel incoherent motion MRI and perfusion measured by dynamic contrast-enhanced MRI of soft tissue tumors. NMR Biomed 2016; 29:6–14.
27. Guo Z, Zhang Q, Li X, et al. Intravoxel incoherent motion diffusion weighted MR imaging for monitoring the instantly therapeutic efficacy of radiofrequency ablation in rabbit VX2 tumors without evident links between conventional perfusion weighted images. PLoS One 2015; 10:e0127964.

Downloaded for Anonymous User (n/a) at Faculty of Medicine & Affiliated Hospital from ClinicalKey.jp by Elsevier on January 28, 2019.
For personal use only. No other uses without permission. Copyright ©2019. Elsevier Inc. All rights reserved.

28. Kwong KK, McKinstry RC, Chien D, et al. CSF-suppressed quantitative single-shot diffusion imaging. Magn Reson Med 1991; 21:157–163.
29. Zhang L, Murata Y, Ishida R, et al. Functional evaluation with intravoxel incoherent motion echo-planar MRI in irradiated salivary glands: a correlative study with salivary gland scintigraphy. J Magn Reson Imaging 2001; 14:223–239.
30. Thoeny HC, De Keyzer F, Oyen RH, et al. Diffusion-weighted MR imaging of kidneys in healthy volunteers and patients with parenchymal diseases: initial experience. Radiology 2005; 235:911–917.
31. Iima M, Reynaud O, Tsurugizawa T, et al. Characterization of glioma microcirculation and tissue features using intravoxel incoherent motion magnetic resonance imaging in a rat brain model. Invest Radiol 2014; 49:485–490.
32. Liu C, Liang C, Liu Z, et al.. Intravoxel incoherent motion (IVIM) in evaluation of breast lesions: comparison with conventional DWI. Eur J Radiol 2013; 82:e782–e789.
33. Tofts PS. Modeling tracer kinetics in dynamic Gd-DTPA MR imaging. J Magn Reson Imaging 1997; 7:91–101.
34. Lemke A, Stieltjes B, Schad LR, et al. Toward an optimal distribution of b values for intravoxel incoherent motion imaging. Magn Reson Imaging 2011; 29:766–776.
35. Zhang JL, Sigmund EE, Rusinek H, et al. Optimization of b-value sampling for diffusion-weighted imaging of the kidney. Magn Reson Med 2012; 67:89–97.
36. Keil VC, Mädler B, Gielen GH, et al. Intravoxel incoherent motion MRI in the brain: impact of the fitting model on perfusion fraction and lesion differentiability. J Magn Reson Imaging 2017; 46:1187–1199.

Downloaded for Anonymous User (n/a) at Faculty of Medicine & Affiliated Hospital from ClinicalKey.jp by Elsevier on January 28, 2019.
For personal use only. No other uses without permission. Copyright ©2019. Elsevier Inc. All rights reserved.

Observational Study

Medicine®

OPEN

Relationship between CT activity score with lung function and the serum angiotensin converting enzyme in pulmonary sarcoidosis on chest HRCT

Jianghui Duan, MD[a], Yanyan Xu, MD[a], Haixu Zhu, MD[b], Haibo Zhang, MD[a], Shilong Sun, BS[a], Hongliang Sun, MD[a,*], Wu Wang, MD[a], Sheng Xie, MD[a]

Abstract

To address the reliability of CT activity score (CTAS) and investigate the relationships between CTAS, lung function changes after treatment and the serum angiotensin-converting enzyme (SACE) levels.

Fifty-seven sarcoidosis patients underwent chest high-resolution CT (HRCT) and spirometry, as well as SACE examination, were retrospectively analyzed. Follow-up spirometry in each patient was obtained about 6 months after the initial spirometry. The correlations between CTAS and pulmonary function changes were evaluated by Spearman correlation analysis. According to SACE status, patients were divided into normal and high level 2 subgroups. Comparisons of pulmonary function parameters, HRCT abnormalities extent scores between SACE normal and high 2 subgroups were performed with the Mann–Whitney *U* test or Independent samples *t* test.

CTAS demonstrated significant correlations with lung function changes (Δ%VC: $\rho = 0.543$, $P < .001$; $\Delta FEV_{1.0}/FVC$: $\rho = 0.417$, $P = .001$; Δ%TLC: $\rho = 0.309$, $P = .019$). In addition, worse initial lung function, larger changes of lung function, and higher extent scores of HRCT were observed in SACE high-level subgroup.

The findings of this study suggest that CTAS of initial HRCT is a promising index for disease activity in pulmonary sarcoidosis to some degree. Prospective studies with large cohort designed to address further verification are warranted before wide clinical practice.

Abbreviations: %TLC = total lung capacity as percent of the predicted value, %VC = vital capacity as percent of the predicted value, CTAS = CT activity score, EBUS-TBNA = endobronchial ultrasound-guided transbronchial needle aspiration, $FEV_{1.0}$ = forced expiratory volume in the first second, FVC = forced vital capacity, GGO = ground-glass opacity, HRCT = high-resolution CT, HU = Hounsfield units, IQR = interquartile range, IST = interlobular septal thickening, SACE = serum angiotensin-converting enzyme, TBLB = transbronchial lung biopsy, WASOG = World Association of Sarcoidosis and Other Granulomatous Disorders.

Keywords: disease activity, high-resolution computed tomography, lung function, sarcoidosis, serum angiotensin converting enzyme

1. Introduction

Sarcoidosis is a multisystem granulomatous disorder with unclear etiology and unpredictable course.[1–3] The clinical course and the prognosis are related to the symptoms at onset and to extent of disease, ranging from an acute self-limited process to progressive fibrosis of the lung or other organs.[4–8] In sarcoidosis treatment, the search for disease activity marker that associates with organ function (i.e., pulmonary function) is ongoing.[9–25] Respiratory tract involvement is evaluated by regular clinical examinations, chest X-ray, and pulmonary function testing (spirometry). The most encouraging indicator for disease activity in clinical trial was pulmonary function testing, which showed the correlation with pulmonary PET outcomes.[13–15]

Additionally, the serum angiotensin-converting enzyme (SACE) has been the most frequently used laboratory test in sarcoidosis. Some studies have shown that SACE is produced by the alveolar macrophages in the sarcoid granuloma, and SACE level reflects the total sarcoidosis granuloma burden.[1,2] SACE level is commonly elevated and may correlate with disease activity.[20–23]

To date, high-resolution computed tomography (HRCT) has been a routine item for airway or interstitial involvement diseases. Various studies have demonstrated that HRCT is superior to conventional radiography in detecting nodules, early fibrosis, and parenchymal distortion.[6,9–12,15–19] Some HRCT features have the potential to discriminate between reversible disease (active inflammation) and irreversible disease (fibrosis).[9]

Editor: Eleonore Fröhlich.

This work has received funding from Beijing Municipal Science and Technology Commission No. Z181100001718099, the National Natural Science Foundation of China (81501469), and the Health Industry Special Scientific Research Project of National Health and Family Planning Commission of the People's Republic of China (201402019).

The authors have no conflicts of interest to disclose.

[a] Department of Radiology, China-Japan Friendship Hospital, Beijing, [b] Department of Radiology, The People's Hospital of Xinjiang Uyghur Autonomous Region, Urumqi, China.

[*] Correspondence: Hongliang Sun, Department of Radiology, China-Japan Friendship Hospital, Beijing 100029, China (e-mail: stentorsun@gmail.com).

Copyright © 2018 the Author(s). Published by Wolters Kluwer Health, Inc. This is an open access article distributed under the Creative Commons Attribution-NoDerivatives License 4.0, which allows for redistribution, commercial and non-commercial, as long as it is passed along unchanged and in whole, with credit to the author.

Medicine (2018) 97:36(e12205)

Received: 25 September 2017 / Accepted: 13 August 2018

http://dx.doi.org/10.1097/MD.0000000000012205

Furthermore, HRCT abnormalities appeared to be useful in evaluating parameters of disease severity and lung functional impairment.[9–12,16,17,20,25] However, the results of the correlation between HRCT scores and disease activity and/or lung function appeared to be conflicting for variable HRCT scoring systems. To achieve a valid, reliable evaluation of lung abnormalities, a standard quantitative estimation of radiological abnormalities is necessary.

Currently, the HRCT scoring system proposed by Benamore et al[25]-CT activity score (CTAS) takes the extent of radiological abnormalities in pulmonary parenchyma into account, showing significant correlation with forced vital capacity (FVC) response to treatment. In addition, extent scores 4 radiological features (ground-glass opacity [GGO], interlobular septal thickening [IST], nodularity and consolidation) enrolled in CTAS correlated with at least one of the surrogates of disease activity, suggesting the validation of the relationship of CTAS to disease activity in sarcoidosis.

However, given that the limited patients were followed up in Benamore et al[25] study, the relationship between CTAS and the changes of lung function after treatment will benefit from further verification with a larger cohort. In addition, whether the extent scores of CT abnormalities mentioned above would be different in patients with different SACE status, in other words, the relationship between CT features and serum marker-ACE was still debated. Therefore, the aims of the article were to address the reliability of CTAS and investigate the relationship between CTAS and lung function changes, aiming to provide a more reliable reference for assessment of disease activity; and to compare CTAS in patients with different SACE status, exploring the potential relationship between CTAS and SACE.

2. Materials and methods

2.1. Subjects

The Institutional Review Board granted approval for our retrospective study, waiving informed consent because of its retrospective nature. This retrospective study included 57 patients with newly diagnosed pulmonary sarcoidosis between December 2010 and September 2016. Inclusion criteria in the study: the initial laboratory test and spirometry were obtained within a 2-week interval before or after the HRCT; patients without corticosteroids therapy or comorbidity before HRCT examination. To assess pulmonary function changes that have occurred over time, follow-up spirometry in each patient was obtained about 6 months after the initial spirometry.

The 57 patients included 16 males and 41 females, 27 to 66 years of age (mean age 49 ± 10 years). Of these patients,11 were ex-smoker/current smoker and 46 were nonsmoker. The diagnosis was confirmed by histology examination of lymph nodes including 16 (28.1%) transbronchial lung biopsy (TBLB), 18 (31.6%) endobronchial ultrasound-guided transbronchial needle aspiration (EBUS-TBNA), 8 (14.0%) thoracoscope, and 7 (12.3%) mediastinal biopsy. Two patients (3.5%) initially presented with a classic Löfgren's syndrome (fever, erythema nodosum, arthralgias, and bilateral hilar lymphadenopathy) without biopsy. For the other 6 patients (10.5%) without histological evidence, clinical features and bronchoalveolar fluid analysis consistent with the WASOG guidelines[26] confirmed the final diagnosis. All the patients received systemic corticosteroids therapy after HRCT examination, but the dose and treatment duration were adjusted according to clinical presentation. None of them have received immunosuppressive therapy during the 6 months.

2.2. HRCT technique and image analysis

HRCT scans were performed on either a 16-slice (Toshiba Aquilion), 320-slice (Toshiba Aquilion One) or a 256-slice CT scanner (Philips Brilliance iCT). All scans were acquired using the high-resolution technique. Images were acquired in the supine position after end-inspiration and extended from the lung apices to the costophrenic angles by using the following parameters: section thickness, 5 mm; section intervals, 5 mm; pitch, 0.75; rotation time, 330 ms; tube voltage, 120 kV; tube current, 200 mA; thin collimation 0.75 mm; reconstruction matrix, 512 × 512. From raw data, 1-mm-thick section images were reconstructed at 1-mm intervals by using a high-spatial-frequency algorithm (B60S). All CT scans were obtained with window settings that were appropriate for lung parenchyma (window width, 1300 Hounsfield units [HU]; level, −450 HU) and mediastinum (window width, 400 HU; level, 40 HU). All data were analyzed on the postprocessing workstation EBW4.52 (Extended Brilliant Workshop 4.52, Philips Healthcare Systems).

The CT images were assessed in totally random order by 2 radiologists (with 6 years and 10 years of experience in chest CT imaging, respectively) without reference to the clinical or laboratory test results. Sarcoidosis-related HRCT abnormalities (including GGO (Fig. 1A), IST, nodule (Fig. 1B), conglomeration, consolidation (Fig. 1C), intrathoracic lymphadenopathy, fibrosis (Fig. 1D)] were scored for the presence, character, and extent follow the criteria defined in the previous study.[25] Specifically, the sum of the scores for GGO, IST, nodularity and consolidation was defined as the CT activity score or CTAS and recorded. In addition, the pleural effusion and the fibrosis were also recorded without enrolling in CTAS scoring system. The fibrosis was defined as the presence of any honeycombing, reticulation, traction bronchiectasis or intralobular linear opacities with or without architectural distortion or lobar volume loss (Tables 1 and 2).

Each lung was divided into 3 zones on HRCT as follows: the upper zone above the carina in the cranio-caudal plane; the lower zone below the inferior pulmonary veins in the cranio-caudal plane; the middle zone between the upper and lower zones.

The extent of CT abnormalities was estimated visually in each aforementioned zone and measured by quartiles (25%) for GGO and consolidation, number of IST (</=5 or > 5) per zone, number of nodules per zone (0–25/26–50/ > 50), 2.5 cm intervals of short-axis diameter for conglomeration.[25] In addition, the sub-1 mm nodules were considered GGO since indistinguishability between innumerable sub-1 mm and GGO with current HRCT resolution.

2.3. SACE examination

SACE examination was performed with 3 mL venous blood on fasting state in the morning, all specimen were sent to our clinical laboratory by immunoturbidimetry (reagent kit were provided by Beijing Strong Biotechnologies, Inc. The instrument was adopted by BECKMAN COULTER AU5800 type automatic biochemical analyzer, America). The normal range of the SACE level was 17 U/mL to 55 U/mL in our institution, and the upper limit of normal of the SACE level is above 55 U/mL.

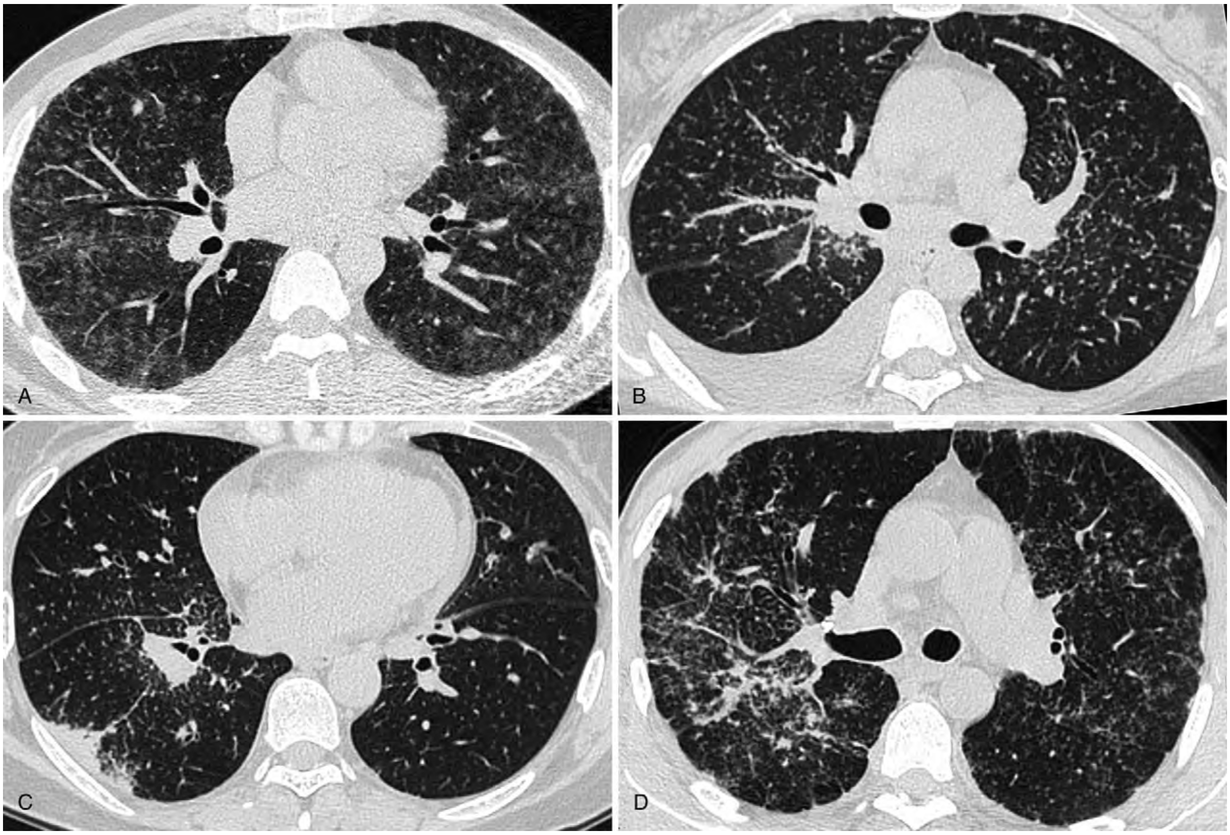

Figure 1. A, HRCT obtained at the level of right lower bronchus displayed bilateral diffuse ground-glass opacities in a 41-year-old male patient. Note the right hilar lymphadenopathy. The SACE level was 60.1 U/mL. B, HRCT showed micronodules with a perivascular distribution and thickening of bronchovascular bundles accompanied with right pleural effusion in a 43-year female patient. The SACE value was 68.1 U/mL. C, HRCT demonstrated consolidation in subpleural region, multiple micronodules clustered interlobar fissures and centrilobular interstitium of right lower lobe in a 50-year-old female patient, enlarged right hilar lymph nodes were also seen, the SACE level was 28.3 U/mL. D, HRCT depicted right bronchovascular bundles distortion in a 48-year male patient, a usual finding of pulmonary fibrosis. Note the bilateral irregular thickening of the pleura (pseudoplaque) and multiple miliary nodules. The SACE value was 33.7 U/mL. HRCT = high-resolution CT, SACE = serum angiotensin converting enzyme.

2.4. Pulmonary function test

All subjects performed spirometry, including vital capacity as the percent of the predicted value (%VC), forced expiratory volume in the first second ($FEV_{1.0}$), forced vital capacity (FVC), and total lung capacity as the percent of the predicted value (%TLC). The initial spirometry was performed within 2 weeks before or after HRCT examination, and the second spirometry was performed with a 6-month interval. The initial spirometric values (Table 3) and the changes between the twice spirometric results were both recorded.

Table 1

Definition of terms for abnormalities on HRCT.

Terms	Definition
Ground glass opacity	Increased lung attenuation, with preserved bronchial and vascular margins; nodules < 1 mm
Consolidation	Obviously increased pulmonary parenchymal attenuation with obscured vessels and airway walls
Internal septal thickening	Thickening of the septa between lobules (smooth or nodular)
Conglomeration	A large opacity > 3 cm surrounding and encompassing hilar bronchi and vessels

2.5. Statistical analysis

All data were expressed as mean ± standard deviation (SD) or median± interquartile range (IQR). The correlations between pulmonary function changes, SACE values, and CT activity score (CTAS), between SACE values and pulmonary function changes were evaluated by Spearman correlation analysis or Pearson

Table 2

Scoring system for abnormalities on HRCT.

Abnormalities	Score for extent
GGO (or nodules < 1 mm)	One zone 1–25% =1 point; one zone 26–50%=2 point; one zone 51–75%=3 point; one zone 76–100%=4 point
Consolidation	One zone 1–25%=1 point; 1 zone 26–50%=2 point; 1 zone 51–75%=3 point; 1 zone 76–100%=4 point
Interlobular septal thickening (IST)	One zone, up to 5=1 point; 1 zone >5=2 point
Nodules 1 mm or greater	One zone 1–25 nodules=1 point; 1 zone 26–50 nodules=2 point; 1 zone >50 nodules=3 point;
Conglomeration	Yes =1 point; no =0 point; each 2.5 cm dimension (right or left) =1
Lymphadenopathy	Yes =1 point; no =0 point.

Table 3

Clinical characteristics of 57 subjects.

Factors	Mean±SD	Range
Gender (male: female)	(16:41)	–
Age, y	48.75±10.30	27–66
Smoking status (ex-/current smoker: nonsmoker)	(11:46)	–
SACE, U/mL	63.20±3.45	11.70–137.10
%VC	98.74±15.15	55.20–129.70
FEV$_{1.0}$/FVC, %	74.18±9.88	50.31–99.56
%TLC	88.65±12.86	52–116

%TLC = total lung capacity as percent of the predicted value, %VC = vital capacity as percent of the predicted value, FEV$_{1.0}$ = forced expiratory volume in the first second, FVC = forced vital capacity, SACE = serum angiotensin converting enzyme, SD = standard deviation.

correlation analysis. According to SACE status, patients were divided into normal and high level 2 subgroups. Comparisons of pulmonary function parameters, HRCT abnormalities extent scores between SACE normal, and high 2 subgroups were performed using Mann–Whitney *U* test or Independent samples *t* test. Concordance rates and kappa values were calculated to show the reliability of calculating HRCT features and CTAS between observers. All statistical analyses were performed using a statistical software package (SPSS 17.0 for Windows, SPSS, Chicago, IL). A *P* values $<.05$ was considered to be significant.

3. Results

The concordance rates and kappa values were 91.2% to 95.4% and 0.85 to 0.91 for different HRCT features and CTAS. Clinical characteristics of subjects are summarized in Table 3. Extent scores for HRCT abnormalities are listed in Table 4. In addition, 4 patients (7.02%) presented with pleural effusion, 14 (24.56%) patients showed evidence of pulmonary fibrosis.

3.1. Correlations between pulmonary function changes, SACE and HRCT abnormality extent score

Following the scoring criterion for disease activity suggested by Benamore et al,[25] the sum score of GGO, IST, consolidation, and nodularity is termed CTAS. Correlations between pulmonary function changes, SACE, and CTAS are summarized in Table 5. Pulmonary function changes and SACE both demonstrated significant correlations with CTAS.

Table 4

HRCT abnormalities and extent score.

Abnormalities	N (percentage)	Median±IQR	Range
GGO	44 (77.19%)	3±4.5	0–24
IST	9 (15.79%)	0±0	0–12
Nodule	39 (68.42%)	2±3	0–18
Consolidation	18 (31.58%)	0±1.5	0–8
Conglomeration	12 (21.05%)	0±0	0–4
Intrathoracic lymphadenopathy	57 (100%)	1±0	1–1
Total score		7±8	1–36
CTAS		6±8	0–35

CTAS = the CT activity score, defined as the sum of the scores for GGO, IST, nodule and consolidation, GGO = ground glass opacity, HRCT = high-resolution computed tomography, IQR = interquartile range, IST = interlobular septal thickening.

Table 5

Correlation between pulmonary function changes, SACE values, and CT activity score (CTAS).

	Correlation to CTAS	
Variables	Coefficient (ρ)	*P* value
Δ%VC	0.543	<.001
ΔFEV$_{1.0}$/FVC	0.417	.001
Δ%TLC	0.309	.019
SACE	0.435	.001

%TLC = total lung capacity as percent of the predicted value, %VC = vital capacity as percent of the predicted value, Δ = the value change after six months, FEV$_{1.0}$ = forced expiratory volume in the first second, FVC = forced vital capacity, SACE = serum angiotensin converting enzyme.

We also have evaluated the relationships between pulmonary function changes, SACE values, and total score of the HRCT features (excluding fibrosis), and have observed similar results to CTAS's (Δ%VC: ρ= 0.509, $P<.001$; ΔFEV$_{1.0}$/FVC:ρ= 0.382, $P=.003$; Δ%TLC: ρ= 0.327, $P=.013$; SACE: ρ= 0.440, $P=.001$).

In addition, the SACE value showed significant correlations with pulmonary function changes (Δ%VC: ρ= 0.413, $P=.001$; ΔFEV$_{1.0}$/FVC:ρ= 0.317, $P=.016$; Δ%TLC:ρ= 0.439, $P=.001$).

3.2. Pulmonary function parameters, HRCT scores between different SACE status

The values of pulmonary function parameters and HRCT scores in patients with different SACE status were described in Table 6. Worse initial lung function, larger changes of %TLC values, and higher HRCT scores were observed in SACE high-level subgroup.

4. Discussion

In the present study, CTAS demonstrated the significant correlations with lung function changes (Δ%VC: ρ= 0.543, $P<.001$; ΔFEV$_{1.0}$/FVC:ρ= 0.417, $P=.001$; Δ%TLC: ρ= 0.309, $P=.019$). Interestingly, similar outcomes were observed in the total score of HRCT abnormalities. The results suggest that

Table 6

Comparisons of pulmonary function parameters, HRCT abnormalities scores between different SACE status.

	SACE status		
	Normal level (n = 32)	High level (n = 25)	*P* value
Initial pulmonary function			
%VC	104.62±9.21	91.20±17.91	.001
FEV$_{1.0}$/FVC (%)	78.95±7.03	68.07±9.74	<.001
%TLC	94.13±9.14	81.63±13.67	<.001
Pulmonary function changes			
Δ%VC	0.60±6.63	2.60±13.05	.096
ΔFEV$_{1.0}$/FVC (%)	1.93±7.86	2.00±9.33	.317
Δ%TLC	0.90±3.28	2.30±7.90	.037
HRCT score			
Total score	7±3.75	11±11	<.001
CTAS	5±3.5	10±12	<.001

Note: data were expressed as median± interquartile range (IQR).

%TLC = total lung capacity as percent of the predicted value, %VC = vital capacity as percent of the predicted value, Δ = the value change after six months, CTAS = the CT activity score, FEV$_{1.0}$ = forced expiratory volume in the first second, FVC = forced vital capacity, HRCT = high-resolution computed tomography, SACE = serum angiotensin converting enzyme.

CTAS is useful in evaluating disease activity in sarcoidosis. In addition, higher extent scores of HRCT and larger changes of lung function were also observed in SACE high-level subgroup, which further supported the aforementioned outcome to some degree.

Chest HRCT is an important modality to identify chest involvement of sarcoidosis. It has been demonstrated that 15% of symptomatic patients have normal chest X-ray but abnormal findings on CT scans.[27] The correlation between HRCT abnormalities and impaired lung function at rest has been well estimated in previous studies.[9–12,16,17,20,25] Thus far, most of the previous studies have been focused on the disease severity (not activity) on HRCT, and its relationship with lung function impairment. The HRCT features of pulmonary sarcoidosis could be divided into reversible and irreversible ones,[6,7,9] in other words, "reversible" feature could be improved after treatment over time, while "irreversible" ones would be unchangeable with or without treatment. GGO, IST and nodular has been proved to be potentially reversible changes in sarcoidosis.[9] Furthermore, HRCT features including GGO, IST, nodular, and consolidation have been demonstrated the significant correlation with lung function,[11,16,19] although the sample size and, more importantly, the scoring system were different. Therefore, it is reasonable to predict that the disease activity scoring system CTAS involving of GGO, IST, nodular, and consolidation associated with lung function changes after treatment in this study.

The increased level of SACE is thought to be secondary to increased expression by the epithelioid cells present in the granulomas.[28] One study showed that SACE was produced by the alveolar macrophages in the sarcoid granuloma, and SACE levels reflected the secreted total granuloma burden.[1,2] Many studies have confirmed that SACE levels can reflect the activity of the disease,[3,21–24] furthermore, it has been reported that the baseline and serial SACE levels correlate with lung function improvement during methotrexate therapy in sarcoidosis patients.[21] Therefore, SACE could be supposed to be an index for disease activity in some degree.

Although it was quite difficult to speculate about the intrinsic reason that underlay this observation, pathologic correlation factors may lead to the correlation between morphology score and SACE in sarcoidosis. First of all, the high percent of GGO (77.19%) and nodular (68.42%) were observed in the lung parenchyma. More recently, studies have shown that ground-glass opacities actually pointed to numerous granulomas along the interlobular fissures and septa and within the centrilobular interstitium surrounding arterioles and bronchioles.[20] They demonstrated as ground-glass opacities, because of beyond the resolution of HRCT.[3,4,29,30] In addition, ground-glass opacities also represented centrilobular interstitial disease in some cases.[23,30] Also, thickened bronchovascular bundles and the surrounding micronodules on HRCT, pathologically corresponded to granulomas surrounding the connective tissue sheath of bronchovascular bundles, which caused bronchovascular bundles nodular or irregular thickening.[4] Whether granulomas stand in the peribronchial interstitium or centrilobular interstitium, these 2 signs are representative of accumulation of granuloma in the lung. Nodules located in bronchovascular bundles distribute more widespread than that located in subpleural regions, the interlobular septa, centrilobular interstitium, and parts of subpleural nodules represent intrapulmonary lymph nodes.[31] Second, 100% lymphadenopathy presented in this study, although it was not enrolled in the CTAS. The bilateral hilar lymph node enlargement also undoubtedly added the total granuloma burden, although the corresponding influence on SACE may be variable in individuals. Together, these factors may explain the significant correlation between CTAS and SACE.

Our study has the following clinical significances. First, CTAS has potential clinical value to judge the disease activity of patients with sarcoidosis. CTAS showed the significant correlations with lung function and the SACE in pulmonary sarcoidosis. Second, we can indirectly judge treatment response and determine the clinical outcome with HRCT features. Finally, based on CTAS and SACE, pulmonary function and improvement after treatment might be predicted in some degree.

Our study has some limitations that need to be addressed. First, the number of cases is limited, and the study is a retrospective study. Studies with larger patients are needed to reduce selective bias. Second, considering the limited subjects, the potential effects of smoking on HRCT appearance, function test, and SACE level were not analyzed; this is a monocentric study focusing on the scoring system proposed by Benamore et al[25] without comparison with other scoring systems on HRCT. Third, in this study 100% intrathoracic lymphadenopathy was observed, similar as in Benamore et al[25] study. However, for the subjects without intrathoracic lymphadenopathy, the CTAS scoring system still needs to be discussed. Finally, it is necessary to follow up patients and to make a dynamic longitudinal study between HRCT activity score and clinical parameters (including pulmonary function, serum ACE) in order to reflect the outcome of the disease.

5. Conclusion

In conclusion, our results suggest that CTAS involving of GGO, IST, nodular and consolidation on HRCT could be a promising index for disease activity; CTAS demonstrated significant correlations both with lung function changes after treatment and SACE; subjects with high SACE prefer to behave higher CTAS on HRCT and worse initial lung function to some degree. Prospective studies with a large cohort designed to address further verification are warranted before wide clinical practice.

Author contributions

Conceptualization: Jianghui Duan, Hongliang Sun, Wu Wang.
Data curation: Jianghui Duan, Yanyan Xu, Haixu Zhu, Haibo Zhang, Shilong Sun, Hongliang Sun.
Formal analysis: Jianghui Duan, Yanyan Xu, Haibo Zhang, Hongliang Sun.
Funding acquisition: Hongliang Sun, Wu Wang.
Investigation: Hongliang Sun.
Methodology: Yanyan Xu, Hongliang Sun.
Project administration: Hongliang Sun, Sheng Xie.
Resources: Jianghui Duan, Haibo Zhang, Sheng Xie.
Software: Jianghui Duan, Haixu Zhu.
Supervision: Wu Wang.
Writing – original draft: Jianghui Duan, Yanyan Xu.
Writing – review & editing: Yanyan Xu, Haixu Zhu, Hongliang Sun, Wu Wang, Sheng Xie.

References

[1] Rosen Y. Pathology of sarcoidosis. Semin Respir Crit Care Med 2007;28:36–52.
[2] Sheffield EA. Pathology of sarcoidosis. Clin Chest Med 1997;18: 741–54.

[3] Wessendorf TE, Bonella F, Costabel U. Diagnosis of sarcoidosis. Clin Rev Allergy Immunol 2015;49:54–62.

[4] Little BP. Sarcoidosis: overview of pulmonary manifestations and imaging. Semin Roentgenol 2015;50:52–64.

[5] Koyama T, Ueda H, Togashi K, et al. Radiologic manifestations of sarcoidosis in various organs. Radiographics 2004;24:87–104.

[6] Criado E, Sánchez M, Ramírez J, et al. Pulmonary sarcoidosis: typical and atypical manifestations at high-resolution CT with pathologic correlation. Radiographics 2010;30:1567–86.

[7] Nishimura K, Itoh H, Kitaichi M, et al. Pulmonary sarcoidosis: correlation of CT and histopathologic findings. Radiology 1993;189: 105–9. Erratum in: *Radiology* 1994;190:907.

[8] Reich JM. Mortality of intrathoracic sarcoidosis in referral vs population-based settings: influence of stage, ethnicity, and corticosteroid therapy. Chest 2002;121:32–9.

[9] Murdoch J, Müller NL. Pulmonary sarcoidosis: changes on follow-up CT examination. AJR Am J Roentgenol 1992;159:473–7.

[10] Oberstein A, von Zitzewitz H, Schweden F, et al. Non invasive evaluation of the inflammatory activity in sarcoidosis with high-resolution computed tomography. Sarcoidosis Vasc Diffuse Lung Dis 1997;14:65–72.

[11] Drent M, De Vries J, Lenters M, et al. Sarcoidosis: assessment of disease severity using HRCT. Eur Radiol 2003;13:2462–71.

[12] Akira M, Kozuka T, Inoue Y, et al. Long-term follow-up CT scan evaluation in patients with pulmonary sarcoidosis. Chest 2005;127: 185–91.

[13] Keijsers RG, Verzijlbergen EJ, van den Bosch JM, et al. 18F-FDG PET as a predictor of pulmonary function in sarcoidosis. Sarcoidosis Vasc Diffuse Lung Dis 2011;28:123–9.

[14] Mostard RL, Vöö S, van Kroonenburgh MJ, et al. Inflammatory activity assessment by F18 FDG-PET/CT in persistent symptomatic sarcoidosis. Respir Med 2011;105:1917–24.

[15] Mostard RL, Verschakelen JA, van Kroonenburgh MJ, et al. Severity of pulmonary involvement and (18)F-FDG PET activity in sarcoidosis. Respir Med 2013;107:439–47.

[16] Sileo C, Epaud R, Mahloul M, et al. Sarcoidosis in children: HRCT findings and correlation with pulmonary function tests. Pediatr Pulmonol 2014;49:1223–33.

[17] Polverosi R, Russo R, Coran A, et al. Typical and atypical pattern of pulmonary sarcoidosis at high-resolution CT: relation to clinical evolution and therapeutic procedures. Radiol Med 2014;119:384–92.

[18] Keijsers RG, van den Heuvel DA, Grutters JC. Imaging the inflammatory activity of sarcoidosis. Eur Respir J 2013;41:743–51.

[19] Remy-Jardin M, Giraud F, Remy J, et al. Pulmonary sarcoidosis: role of CT in the evaluation of disease activity and functional impairment and in prognosis assessment. Radiology 1994;191:675–80.

[20] Ors F, Gumus S, Aydogan M, et al. HRCT findings of pulmonary sarcoidosis; relation to pulmonary function tests. Multidiscip Respir Med 2013;8:8.

[21] Vorselaars AD, van Moorsel CH, Zanen P, et al. ACE and sIL-2R correlate with lung function improvement in sarcoidosis during methotrexate therapy. Respir Med 2015;109:279–85.

[22] Popević S, Šumarac Z, Jovanović D, et al. Verifying sarcoidosis activity: chitotriosidase versus ace in sarcoidosis— case-control study. J Med Biochem 2016;35:390–400.

[23] Mathur RS, Kurdikar VL, Shah JR. Serum angiotensin converting enzyme in the diagnosis of pulmonary sarcoidosis. J Assoc Physicians India 1990;38:474–5.

[24] Sainani GS, Mahbubani V, Trikannad V. Serum angiotensin converting enzyme activity in sarcoidosis and pulmonary tuberculosis. J Assoc Physicians India 1996;44:29–30.

[25] Benamore R, Kendrick YR, Repapi E, et al. CTAS: a CT score to quantify disease activity in pulmonary sarcoidosis. Thorax 2016;71: 1161–3.

[26] Statement on sarcoidosisJoint Statement of the American Thoracic Society (ATS), the European Respiratory Society (ERS) and the World Association of Sarcoidosis and Other Granulomatous Disorders (WASOG) adopted by the ATS Board of Directors and by the ERS Executive Committee, February 1999. Am J Respir Crit Care Med 1999; 160:736–55.

[27] Epler GR, McLoud TC, Gaensler EA, et al. Normal chest roentgenograms in chronic diffuse infiltrative lung disease. N Engl J Med 1978; 298:934–9.

[28] Silverstein E, Pertschuk LP, Friedland J. Immunofluorescent localization of angiotensin converting enzyme in epithelioid and giant cells of sarcoidosis granulomas. Proc Natl Acad Sci U S A 1979;76:6646–8.

[29] Nakatsu M, Hatabu H, Morikawa K, et al. Large coalescent parenchymal nodules in pulmonary sarcoidosis: "sarcoid galaxy" sign. AJR Am J Roentgenol 2002;178:1389–93.

[30] Marchiori E, Zanetti G, Barreto MM, et al. Atypical distribution of small nodules on high resolution CT studies: patterns and differentials. Respir Med 2011;105:1263–7.

[31] Koo HJ, Chae EJ, Kim JE, et al. Presence of macronodules in thoracic sarcoidosis: prevalence and computed tomographic findings. Clin Radiol 2015;70:815–21.

European Radiology (2018) 28:3059–3065
https://doi.org/10.1007/s00330-018-5329-y

GASTROINTESTINAL

Could IVIM and ADC help in predicting the KRAS status in patients with rectal cancer?

Yanyan Xu[1] · Qiaoyu Xu[1] · Hongliang Sun[1] · Tongxi Liu[1] · Kaining Shi[2] · Wu Wang[1]

Received: 5 December 2017 / Revised: 8 January 2018 / Accepted: 12 January 2018 / Published online: 15 February 2018
© European Society of Radiology 2018

Abstract

Purpose To evaluate the diagnostic potential of DW-MRI relative parameters for differentiation of rectal cancers with different Kirsten rat sarcoma viral oncogene homologue (KRAS) mutation status.

Methods Fifty-one patients with rectal cancer underwent diffusion-weighted MR imaging with eight b values. ADCs (including Max-ADC, Min-ADC and Mean-ADC) and IVIM parameters (*D*, pure diffusion; *f*, perfusion fraction; *D**, pseudodiffusion coefficient) were respectively calculated by mono- and bi-exponential analysis. Patients were stratified into two groups: KRAS wild type and mutant. The DW-MRI-derived parameters between the KRAS wild-type group and KRAS mutant group were compared using the Mann-Whitney U test. Receiver-operating characteristic (ROC) analysis of discrimination between KRAS wild-type and KRAS mutant rectal cancer was performed for the DW-MRI-derived parameters.

Results Max-ADC, Mean-ADC and *D* values were significantly lower in the KRAS mutant group than in the KRAS wild-type group, whereas a higher *D** value was demonstrated in the KRAS mutant group. According to the ROC curve, Mean-ADC and *D** values showed moderate diagnostic significance with the AUC values of 0.756 and 0.710, respectively. The cut-off values for Mean-ADC and *D** were $1.43 \times 10^{-3} mm^2/s$ and $26.58 \times 10^{-3} mm^2/s$, respectively.

Conclusion Rectal cancers had distinctive diffusion/perfusion characteristics in different KRAS mutation statuses. The DW-MRI-derived parameters, specifically Mean-ADC and *D**, show a moderate diagnostic significance for KRAS status.

Key Points

- *Rectal cancers with different KRAS mutation statuses demonstrated distinctive diffusion/perfusion characteristics.*
- *Max-ADC, Mean-ADC and D values were lower in the KRAS mutant group.*
- *A higher D* value was demonstrated in the KRAS mutant group.*
- *IVIM-DW MRI may potentially help preoperative KRAS mutant status prediction.*

Keywords Rectal cancer · Magnetic resonance imaging · Diffusion · Perfusion · Mutation

Abbreviations

ADC	Apparent diffusion coefficient
CRC	Colorectal cancer
D	Diffusion coefficient
D*	Pseudo-diffusion coefficient
DWI	Diffusion-weighted imaging
EGFR	Epidermal growth factor receptor
f	Perfusion fraction
IVIM	Intravoxel incoherent motion
KRAS	Kirsten rat sarcoma viral oncogene homologue
MRI	Magnetic resonance imaging
NCCN	National Comprehensive Cancer Network
ROI	Region of interest
ROC	Receiver-operating characteristic
TE	Echo time
TR	Repetition time
TSE	Turbo spin echo

Introduction

Rectal cancer, which accounts for 30-35% [1] of all colorectal cancer (CRC) cases, is distinctive from the rest of the colon, and local recurrence is a major problem for clinical

---

✉ Hongliang Sun
stentorsun@gmail.com

[1] Department of Radiology, China-Japan Friendship Hospital, No.2 Yinghua East Street, Chaoyang District, Beijing 100029, China

[2] Philips Healthcare, Beijing 100600, China

management. Currently, it is considered that CRC occurs as a result of the accumulation of both mutations and epigenetic alterations in several key genes [2]. Kirsten rat sarcoma viral oncogene homologue (KRAS) is one of those key genes, and its mutations were observed in approximately 35-40% of CRCs [3, 4]. Generally, metastatic CRCs with KRAS mutations tended to be resistant to anti-EGFR (epidermal growth factor receptor) monoclonal antibody-targeted therapy [5, 6]. It has been explicitly pointed out in the National Comprehensive Cancer Network (NCCN) clinical practice guidelines [5, 6] that the KRAS mutation is a highly specific negative biomarker for benefitting from anti-EGFR monoclonal antibody-targeted therapy. In general, postoperative pathology specimens are required for KRAS mutation status testing; however, patients with more advanced rectal cancer may not be treated surgically to obtain specimens for testing. Therefore, further effort is desirable for the development of a relatively simple and noninvasive method that can be helpful for the differentiation of KRAS mutations and then assisting in selecting the most suitable adjuvant therapeutic methods.

Much work has been focused on the MR functional imaging, such as diffusion-weighted magnetic resonance imaging (DW-MRI), providing objective and quantitative parameters [ADCs (including Max-ADC, Min-ADC and Mean-ADC) and IVIM parameters (*D*, pure diffusion; *f*, perfusion fraction; *D**, pseudodiffusion coefficient)] in vivo. Currently, most interest is focussed on developing the role of various DW-MRI-derived parameters in tumour characterisation, predicting tumour aggressiveness or monitoring treatment response [7–9]. DW-MRI has rarely been investigated in genomic expression. As we know, most of the tumour's aggressive bio-behaviour can be considered the result of interior genetic regulation, so we assume that rectal cancers with different KRAS genetic phenotypes might present with variable DW-MRI characteristics. To date, the DW-MRI relative parameter characteristics in rectal cancers with different KRAS mutation statuses are unknown. Thus, the aim of this retrospective study was to detect if the DW-MRI-derived parameters can predict the genotype of rectal cancer (KRAS mutant/wild type).

Materials and Methods

Patients and tissue samples

This retrospective study was approved by the institutional review board of the hospital, and waived the requirement for written informed consent. Between August 2013 and December 2014, 109 patients with biopsy-proven rectal adenocarcinoma underwent pelvic MR examination (including multi-*b* value DW-MRI sequences). Exclusion criteria were: (1) previous rectal surgery ($n = 3$); (2) pre-examination neoadjuvant chemoradiotherapy or unidentified herbal medicine therapy for the rectal lesion ($n = 25$); (3) heavy intestinal peristalsis artefacts ($n = 4$); (4) small lesions (< 5mm) hard to identify on images ($n = 3$); (5) without KRAS testing ($n = 12$); (6) mucinous adenocarcinoma ($n = 11$). Finally, 51 patients were enrolled in this study. The relevant detailed clinical data are illustrated in Table 1. Surgical pathology results of all patients were analysed by a pathologist with 6 years' experience in gastrointestinal pathological diagnosis. Genomic DNA was extracted from formalin-fixed paraffin-embedded (FFPE) tissue using the QLAamp DNA FFPE Tissue kit (Qiagen), and KRAS mutations were examined by the amplification refractory mutation system (ARMS) method. According to the test results, patients were stratified into two groups: KRAS wild type and mutant, and the patients with KRAS mutation were further divided into codon 12 and codon 13 subgroups based on different mutation locations. From the analysis of the surgical specimens, 38 patients had the *KRAS* wild type and 13 patients had the KRAS mutation including eight codon 12 mutations(G12A, G12C, G12S, G12V) and five codon 13 mutations (G13A).

Patient preparation and imaging protocol

The patients were on a low-residue diet before the MRI examination and were asked to fast on the day of the examination. An intramuscular injection of 10 mg anisodamine hydrochloride was given to each patient to prevent intestine peristalsis 10 min prior to the MR examination. Pelvis MR scanning was performed on a 3-T whole-body scanner (Ingenia, Philips Medical Systems) with a gradient strength of 45mT/m and a gradient switching rate of 200mT/m/ms, using a 16-channel anterior torso dS coil and a 16-channel posterior table dS coil.

The 2D sagittal and oblique coronal T2W (parallel to long axis of the tumour) Turbo spin echo (TSE) sequences were performed with the following parameters: repetition time (TR), 3761 ms; echo time (TE), 110 ms; field of view (FOV), 24 × 24 cm; slice thickness, 3 mm with 0.3-mm gap;

Table 1 Basic clinical information of rectal cancers ($n = 51$)

Factors	Numbers/values
Patient age (years)*	61.3 ± 13.6
Gender *n* (%)	
Male	29 (57.7%; 29/51)
Female	22 (42.3%; 22/51)
KRAS status	
Wild type	38 (74.5%; 38/51)
Mutant codon 12	8(15.7%; 8/51)
Mutant codon 13	5(9.8%; 5/51)

Note. * Data are means ± standard deviation slice number, 24 acquisition matrix, 336 × 252; number of sample (signals) averaged (NSA) 1; an oblique axial T2W-high resolution sequence was planned perpendicularly to the tumour axis in the sagittal view: TR 3865 ms, TE 100 ms, FOV 14 × 14 cm, slice thickness 3 mm with 0.3-mm gap, slice number 20, acquisition matrix 232 × 228.

An oblique axial multi-b value DW-MRI sequence perpendicular to the tumoral axis in sagittal view was performed with the parallel acquisition technique (sensitivity encoding, SENSE) using a single-shot echo-planar imaging (SE-EPI) pulse sequence with free breathing using the following parameters: TE/TR 76/6000 ms, FOV 20 × 30 cm, slice thickness 5 mm with 0.2-mm gap, slice number 24, acquisition matrix 80 × 144, NSA 6 and eight b values (0, 25, 50, 75, 150, 400, 800 and 1000s/mm^2). Frequency selection plus the inversion recovery fat-suppression technique (spectral attenuated inversion recovery) was adopted in the DWI sequence. The scan time for the DWI sequence was about 6 min 30 s.

Image processing and analysis

The raw data of multi-b value DW images were transferred to a workstation (Extended Workspace 4.1; Philips Healthcare Systems) and analysed with in-house software (IDL6.3 software). The ADC was obtained by using all b values (0-1000s/mm^2) fitted to the following equation:

$$S_b/S_o = \exp(-bADC) \tag{1}$$

where S_b is the signal intensity at a given b value and S_0 is the signal intensity observed in the absence of a diffusion gradient. In the bi-exponential model, the IVIM parameters were calculated by the following equation [10]:

$$S_b/S_o = (1-f)(-bD) + f\exp\left(-bD^*\right) \tag{2}$$

where S_b is the signal intensity in the pixel with the diffusion gradient, S_0 is the signal intensity in the pixel without a diffusion gradient, D is the true diffusion as reflected by pure molecular diffusion, f is the fractional perfusion related to microcirculation, and D^* is the pseudodiffusion coefficient related to perfusion.

Conventional T2WI and DWI (b = 1000s/mm^2) images were used as references to determine lesion areas on corresponding DWI colour-coded maps. Regions of interest (ROIs) were manually drawn covering the entire tumour area on all continuous slices (T2WI, DWI images; Fig. 1a-b), avoiding the inclusion of intestinal gas, liquid and anatomical structures by one radiologist (H.S., 10 years' experience in gastrointestinal imaging). Macroscopic necrosis, if any, would be excluded. The DW-MRI-derivedparameter values (ADCs, D, f, D^*; Fig. 1c-f)for each tumour were calculated by the pixel-by-pixel fitting method and expressed as mean values of all pixels within the all ROIs. Inter-observer reliability of DW-MRI derived-parameters (ADC, D, f and D^*) used in this study were proved to be good to excellent, as reported in a previous study with the same observers (the intraclass correlation coefficient, abbreviated ICC, ranged from 0.7444 to 0.9106) [11]. Furthermore, volumetric analysis demonstrated better-interobserver reproducibility when compared with single-section ROI analysis [12]. Accordingly, in the present study, volumetric measurement by a single radiologist was regarded as sufficient.

Statistical Analysis

All analyses were performed with JMP 12.0 statistical software (SAS Institute). Continuous variables were expressed as the mean ± standard deviation. Comparisons of continuous variables, including DW-MRI parameters of rectal cancers with the codon 12 subgroup versus codon 13 subgroup, were made using the Mann-Whitney test. Then, receiver-operating characteristic (ROC) analysis was performed to evaluate the diagnostic performance of the DW-MRI-derived parameters (ADCs, D, f, D^* values) for KRAS status. The areas under the ROC curve (AUC) were calculated: an AUC value < 0.50 indicated poor diagnostic accuracy; an AUC value of 0.51-0.70, fair diagnostic accuracy; an AUC value of 0.71-0.90, moderate diagnostic accuracy; an AUC value > 0.91, high diagnostic accuracy. The cut-off values with the largest Youden index [(sensitivity + specificity) - 1] were calculated from the ROC curves. The final KRAS testing results were used as the standard. For all the analyses mentioned above, $p < 0.05$ was considered statistically significant.

Results

DW-MRI-derived parameters in the KRAS wild-type and mutant groups

Values of DW-MRI-derived parameters (Max-ADC, Min-ADC, Mean-ADC, D, f, D^*) of the *KRAS* wild-type and mutant groups are described in Table 2. Regarding the differentiation of the KRAS mutant group from the KRAS wild-type group, the values of Max-ADC, Mean-ADC and D in the mutant group were significantly lower than those in the wild-type group ($p = 0.04$, $p = 0.01$ and $p = 0.03$, respectively), while a higher D^* value was demonstrated in the mutant group ($p = 0.03$). However, no significant differences were demonstrated in the values of Min-ADC and f between the two groups ($p = 0.27$ and $p = 0.29$, respectively).

In addition, the values of DW-MRI-derived parameters between the codon 12 and codon 13 subgroups showed no statistical differences (Max-ADC: $z = 0.66$, $p = 0.51$; Min-ADC: $z = 0.29$, $p = 0.77$; Mean-ADC: $z = 0.52$, $p = 0.61$; D: $z = 0.51$, $p = 0.61$; f :$z = 0.22$, $p = 0.83$; D^*: $z = 0.66$, $p = 0.51$).

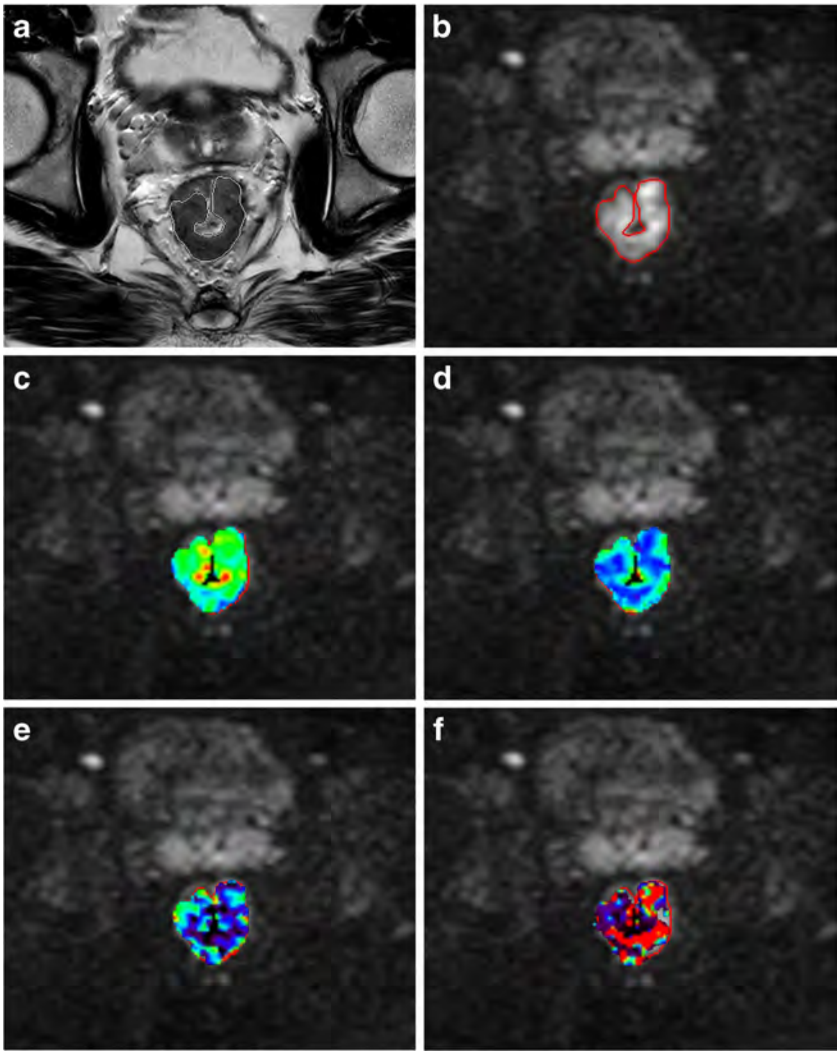

Fig. 1 Images of 46-year-old male patient with rectal cancer. **a** Oblique axial T2W-high resolution sequence planned perpendicularly to the bowel with tumour; outline indicates tumour region. **b** Diffusion-weighted image (DWI) obtained at b of 1000s/mm^2; outline indicates tumour region. **c**-**f**: D: parametric maps (ADC, D, f and D*, respectively) fused with relevant DWIs

Predictive significance of DW-MRI-derived parameters for KRAS mutation status

In the ROC analysis for the differentiation between the *KRAS* wild-type and mutant group, AUC values of Max-ADC, Min-ADC, Mean-ADC, *D*, *f* and *D** were 0.695, 0.604, 0.756, 0.701, 0.599 and 0.710, respectively. These findings suggested that Mean-ADC and *D** showed moderate diagnostic significance for KRAS mutation in rectal cancer, while the diagnostic values of Max-ADC, Min-ADC, *D* and *f* showed fair diagnostic accuracy. According to the ROC curve (Fig. 2a), the cut-off value for Mean-ADC was 1.43 × 10^{-3}mm^2/s. The Mean-ADC value for the KRAS mutant group was lower than the cut-off value and that for the KRAS wild-type group was greater than the cut-off value, with an accuracy rate of 78.43%, sensitivity of 69.23% and specificity of 81.58%. The cut-off value for *D** was 26.58 × 10^{-3}mm^2/s. The *D** value for the KRAS mutant group was higher than the cut-off value and

Table 2 Rectal cancer DW-MRI relative parameters in different KRAS statuses

DW-MRI -derived parameters	*KRAS* mutant (*n* = 13)	*KRAS* wild type (*n* = 38)	*z*	*p*
Max-ADC (×10^{-3}mm^2/s)	2.08 ± 0.49	2.35 ± 0.42	2.08	0.04
Min-ADC (×10^{-3}mm^2/s)	0.71 ± 0.32	0.74 ± 0.18	1.10	0.27
Mean-ADC (×10^{-3}mm^2/s)	1.26 ± 0.36	1.43 ± 0.22	2.72	0.01
D (×10^{-3}mm^2/s)	0.94 ± 0.27	1.13 ± 0.33	2.14	0.03
f (%)	19.47 ± 12.25	16.78 ± 14.04	-1.05	0.29
*D** (×10^{-3}mm^2/s)	70.77 ± 67.77	32.98 ± 43.74	2.22	0.03

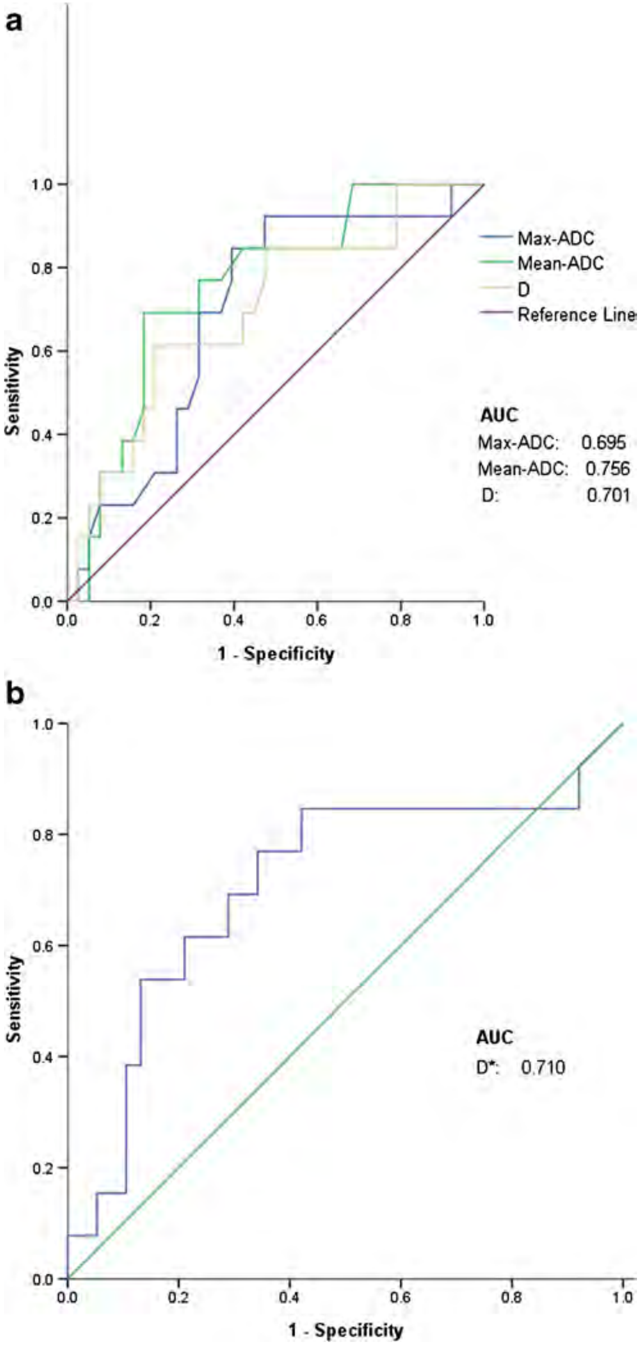

Fig. 2 Receiver-operating characteristic curves for Max-ADC, Mean-ADC, D (**a**) and D* (**b**) in distinguishing KRAS mutant rectal cancers from wild-type ones

that for the KRAS wild-type group was lower than the cut-off value, with an accuracy rate of 68.62%, sensitivity of 76.92% and specificity of 65.79% (Fig. 2b).

Discussion

In the present study, lower Max-ADC, Mean-ADC, *D* and higher *D** values were observed in rectal cancers with the KRAS mutant than in those with the wild type. According to the ROC analysis, Mean-ADC and *D** values showed moderate diagnostic significance for the KRAS mutant status with the AUC values of 0.756 and 0.710, respectively. Theoretically, ADC integrates the effects of both diffusion (D) and perfusion (D*), reflecting the total diffusion in tissues. However, ADC is mainly a diffusion-related parameter rather than a perfusion-related parameter at high b values (> 200 s/mm^2). As the diffusion coefficient level is mainly decided by the ratio of the intra- and extracellular space in tissue [10], both ADC and D are generally considered to be negatively correlated with the cellularity and positively correlated with necrosis and cystic changes in tissue [13, 14]. According to IVIM theory [10], D* (pseudo-diffusion coefficient) is associated with perfusion with the equation stating that $D^* = (l \cdot v)/6$, where l means the length of the voxel capillary and v is the average velocity of blood in the capillary [15]. Thus, lower Max-ADC, Mean-ADC and *D* and higher *D** values observed in the KRAS mutant group in the present study may suggest a relatively tight tumour cell structure and hypervascularity in the tumour.

It has been reported that the DW-MRI-derived parameters have clinical value in characterising tumour biological behaviour [9] and predicting tumour prognosis [12]. The values of ADC and *D* tended to decrease with higher T stages, and f and D* were independent predictors for T staging [16, 17]. In addition, diffusion-related IVIM-based parameters (D and ADC) have been helpful to predict the treatment response to CRT for locally advanced cancers and nasopharyngeal carcinoma [13, 18].

Mutations of the KRAS oncogene result in the constitutive activation of the G-protein signal transduction pathway, associating with diffuse proliferation and decreased apoptosis [19, 20]. However, to date, there are no consistent results about the associations between KRAS mutations and CRC prognosis. Shigenori et al. [21] reported that CRC with KRAS mutations were associated with poor prognosis. Similar results were also observed in the Kirsten Ras Colorectal Cancer Collaborative Group Study II (RASCAL II) on more than 3000 patients with CRCs, particularly in patients with higher stage [22]. Conversely, negative results were reported by Roth et al. [23]. In our results, the relationship between DW-MRI-derived parameters and KRAS mutant status indirectly confirmed the potential relationship between KRAS mutation and prognosis in rectal cancer.

The KRAS oncogene is one of the important effectors in EGFR signalling pathways, located in chromosome 12 p12. 1 and ultimately controlling processes such as cell growth and survival [24]. The incidence of KRAS mutation in the present study is 25.5%, slightly lower than that in previous studies [3, 4]. This is possibly due to several factors including the limited study sample size and only patients with rectal cancer being enrolled in study. Up to 90% of activating KRAS mutations were detected in codons 12 and 13 [24]. In our study, there were eight codon 12 mutations and five codon 13 mutations. It is intriguing that specific KRAS mutations may be heterogeneous in their phenotype. For example, Bazanet et al, [25] found that KRAS codon 12 mutations were associated with a mucinous phenotype of CRC as well as more aggressive tumour behaviour with greater metastatic potential [26]. However, the values of DW-MRI-derived parameters between the codon 12 and codon 13 subgroup showed no statistical differences. Considering the limited sample size and multiple alternative genetic pathways in CRC [27], further analysis needs to be performed with much larger patients cohort.

The present study has a number of limitations. First, there were a limited number of patients with rectal cancer in the study; thus, preliminary results by using a relatively small sample size were provided. Second, it is a retrospective study, so unintended selective bias may exist. Third, the f values were not T2 corrected and thus may be impacted by the T2 relaxation times of blood and tissues. Fourth, only KRAS status was investigated in the present study; other mutations in key genes [28], such as APC, CTNNB1 and BRAF, and the potential crosstalk among these mutations were not involved. A meta-analysis showed that patients with CRCs harbouring the BRAF mutation may not benefit from treatment with anti-EGFR antibodies, and the BRAF mutation is an adverse prognostic biomarker for the survival of patients with metastatic CRC [29]. Therefore, further BRAF testing should be recommended for rectal cancers with wild-type KRAS, which is beyond the scope of the current study.

In conclusion, the DW-MRI-derived parameters, specifically Mean-ADC and D^*, showed moderate diagnostic performance in differentiating rectal cancers with different KRAS mutant statuses from wild type in rectal cancer, suggesting potential for predicting the genotype of rectal cancer (KRAS mutant/wild type).

Funding This work was supported by grants from the National Natural Science Foundation of China (no. 81501469) and the Health Industry Special Scientific Research Project of the National Health and Family Planning Commission of the People's Republic of China (no. 201402019).

Compliance with ethical standards

Guarantor The scientific guarantor of this publication is Dr. Hongliang Sun.

Conflict of interest The authors of this manuscript declare no relationships with any companies, whose products or services may be related to the subject matter of the article.

Statistics and biometry One of the authors has significant statistical expertise.

No complex statistical methods were necessary for this paper.

Informed consent Written informed consent was waived in this study.

Ethical approval Institutional Review Board approval was obtained.

Methodology
- retrospective
- observational
- performed at one institution

References

1. Weizt J, Koch M, Debus J, Höhler T, Galle PR, Büchler MW (2005) Colorectal cancer. Lancet 365:153–165
2. Migliore L, Migheli F, Spisni R, Coppedè F (2011) Genetics, cytogenetics, and epigenetics of colorectal cancer. J Biomed Biotechnol. 2011:792362
3. Brand TM, Wheeler DL (2012) KRAS mutant colorectal tumors: past and present. Small GTPases 3:34–39
4. Wang HL, Lopategui J, Amin MB, Patterson SD (2010) KRAS mutation testing in human cancers: The pathologist's role in the era of personalized medicine. Adv Anat Pathol 17:23–32
5. NCCN Clinical Practice Guidelines in Oncology: Colon Cancer (2016)-NCCN Evidence Blocks. National Comprehensive Cancer Network Web site. http://www.nccn.org/professionals/physician_gls/pdf/colon.pdf. Published February 8, 2016.
6. NCCN Clinical Practice Guidelines in Oncology: Rectal Cancer (2016)\ National Comprehensive Cancer Network Web site. http://www.nccn.org/professionals/physician_gls/pdf/rectal.pdf. Published November 4, 2015.
7. Bae H, Yoshida S, Matsuoka Y et al (2014) Apparent diffusion coefficient value as a biomarker reflecting morphological and biological features of prostate cancer. Int Urol Nephrol 46:555–561
8. Higano S, Yun X, Kumabe T et al (2006) Malignant astrocytic tumors: clinical importance of apparent diffusion coefficient in prediction of grade and prognosis. Radiology 241:839–846
9. Curvo-Semedo L, Lambregts DM, Maas M, Beets GL, Caseiro-Alves F, Beets-Tan RG (2012) Diffusion-weighted MRI in rectal cancer: apparent diffusion coefficient as a potential noninvasive marker of tumor aggressiveness. J Magn Reson Imaging 35:1365–1371
10. Le Bihan D, Breton E, Lallemand D, Aubin ML, Vignaud J, Laval-Jeantet M (1988) Separation of diffusion and perfusion in intravoxel incoherent motion MR imaging. Radiology 168:497–505
11. Sun H, Xu Y, Xu Q et al (2017) Rectal cancer: Short-term reproducibility of intravoxel incoherent motion parameters in 3.0T magnetic resonance imaging. Medicine (Baltimore) 96:e6866
12. Nougaret S, Vargas HA, Lakhman Y et al (2016) Intravoxel incoherent motion-derived histogram metrics for assessment of response after combined chemotherapy and radiation therapy in rectal cancer: initial experience and comparison between single-section and volumetric analyses. Radiology 280:446–454
13. Xiao-ping Y, Jing H, Fei-ping L et al (2016) Intravoxel incoherent motion MRI for predicting early response to induction chemotherapy and chemoradiotherapy in patients with nasopharyngeal carcinoma. J Magn Reson Imaging 43:1179–1190
14. Jenkinson MD, du Plessis DG, Smith TS, Brodbelt AR, Joyce KA, Walker C (2010) Cellularity and apparent diffusion coefficient in oligodendroglial tumours characterized by genotype. J Neuro oncol 96:385–392
15. Guiu B, Petit JM, Capitan V et al (2012) Intravoxel incoherent motion diffusion-weighted imaging in nonalcoholic fatty liver disease: a 3.0-T MR study. Radiology 265:96–103

16. Sun Y, Tong T, Cai S, Bi R, Xin C, Gu Y (2014) Apparent Diffusion Coefficient (ADC) Value: a potential imaging biomarker that reflects the biological features of rectal cancer. Plos One 9:e109371
17. Lai V, Li X, Lee VH et al (2014) Nasopharyngeal carcinoma: comparison of diffusion and perfusion characteristics between different tumour stages using intravoxel incoherent motion MR imaging. Eur Radiol 24:176–183
18. Jung SH, Heo SH, Kim JW et al (2012) Predicting response to neoadjuvant chemoradiation therapy in locally advanced rectal cancer: diffusion-weighted 3 Tesla MR imaging. J Magn Reson Imaging 35:110–116
19. Ward RL, Todd AV, Santiago F, O'Connor T, Hawkins NJ (1997) Activation of the K-ras oncogene in colorectal neoplasms is associated with decreased apoptosis. Cancer 79:1106–1113
20. Kobayashi M, Watanabe H, Ajioka Y, Honma T, Asakura H (1996) Effect of K-ras mutation on morphogenesis of colorectal adenomas and early cancers: relationship to distribution of proliferating cells. Hum Pathol 27:1042–1049
21. Shigenori K, Miho K, Shuhei T et al (2015) Prognostic value of KRAS and BRAF mutations in curatively resected colorectal cancer. World J Gastroenterol 21:1275–1283
22. Andreyev HJ, Norman AR, Cunningham D et al (2001) Kirsten ras mutations in patients with colorectal cancer: the 'RASCAL II' study. Br J Cancer 85:692–696
23. Roth AD, Tejpar S, Delorenzi M et al (2010) Prognostic role of KRAS and BRAF in stage II and III resected colon cancer: results of the translational study on the PETACC-3, EORTC 40993, SAKK 60-00 trial. J Clin Oncol 28:466–474
24. Downward J (2003) Targeting RAS signaling pathways in the cancer therapy. Nat Rev Cancer 3:11–322
25. Bazan V, Agnese V, Corsale S et al (2005) Specific TP53 and/ or K-ras mutations as independent predictors of clinical outcome in sporadic colorectal adenocarcinomas: results of 5-year Gruppo Oncologico dell'Italia Meridionale (GOIM) prospective study. Ann Oncol 16:iv50–iv55
26. Li W, Qiu T, Zhi W et al (2015) Colorectal carcinomas with KRAS codon 12 mutation are associated with more advanced tumor stages. BMC Cancer 15:340
27. Smith G, Carey FA, Beattie J et al (2002) Proc Natl Acad Sci USA 99:9433–9438. Mutations in APC, Kirsten-ras, and p53—alternative genetic pathways to colorectal cancer
28. Coppedè F, Lopomo A, Spisni R, Migliore L (2014) Genetic and epigenetic biomarkers for diagnosis, prognosis and treatment of colorectal cancer. World J Gastroenterol 20:943–956
29. Xu Q, Xu AT, Zhu MM, Tong JL, Xu XT, Ran ZH (2013) Predictive and prognostic roles of BRAF mutation in patients with metastatic colorectal cancer treated with anti-epidermal growth factor receptor monoclonal antibodies: a meta-analysis. J Dig Dis 14: 409–416

Quantitative Intravoxel Incoherent Motion Parameters Derived From Whole-Tumor Volume for Assessing Pathological Complete Response to Neoadjuvant Chemotherapy in Locally Advanced Rectal Cancer

Qiaoyu Xu, MD,[1] Yanyan Xu, MD,[1] Hongliang Sun, MD,[1]* Queenie Chan, PhD,[2]
Kaining Shi, PhD,[3] Aiping Song, MD,[4] and Wu Wang, MD, PhD[1]

Background: Many locally advanced rectal cancer (LARC) patients can benefit from neoadjuvant chemotherapy (NACT), with some achieving a pathological complete response (pCR). However, there is limited research reporting on the value of intravoxel incoherent motion (IVIM) in monitoring pCR in patients with LARC.
Purpose: To identify whether IVIM parameters derived from whole-tumor volume (WTV) before and after NACT could accurately assess pCR in patients with LARC.
Study Type: Prospective patient control study.
Population: Fifty-one patients with LARC before and after NACT, prior to surgery.
Field Strength/Sequence: IVIM-diffusion imaging at 3T.
Assessment: Apparent diffusion coefficient (ADC), slow diffusion coefficient (D), fast diffusion coefficient (D*), and perfusion-related diffusion fraction (*f*) values were obtained on diffusion-weighted magnetic resonance images (DW-MRI) using WTV methods and calculated using a biexponential model before and after NACT.
Statistical Tests: DWI-derived ADC and IVIM-derived parameters and their percentage changes (ΔADC%, ΔD%, ΔD*%, and Δ*f*%) were compared using independent-samples *t*-test and Mann–Whitney *U*-test between the pCR and non-pCR groups. The diagnostic performance of IVIM parameters and their percentage changes were evaluated using receiver operating characteristic curves.
Results: Compared with the non-pCR group, the pCR group exhibited significantly lower pre-ADC_{mean} ($P = 0.003$) and pre-D values ($P = 0.024$), and significantly higher post-*f* ($P = 0.002$), $\Delta ADC_{mean}\%$ ($P = 0.002$), ΔD% ($P = 0.001$), and Δ*f*% values ($P = 0.017$). Receiver operating characteristic curves showed that the pre-D value had the best specificity (95.12%) and accuracy (86.27%) in predicting the pCR status, and ΔD% had the highest area under the curve (0.832) in assessing the pCR response to NACT.
Data Conclusions: The IVIM-derived D value is a promising tool in predicting the pCR status before therapy. The percentage changes in D values after therapy may help assess the pCR status prior to surgery.
Level of Evidence: 2
Technical Efficacy: Stage 2

J. MAGN. RESON. IMAGING 2018;48:248–258.

Colorectal cancer is the third most commonly diagnosed cancer in men and the second most commonly diagnosed cancer in women worldwide.[1] Approximately one-third of colorectal cancer is located in the rectum, and

View this article online at wileyonlinelibrary.com. DOI: 10.1002/jmri.25931

Received Oct 24, 2017, Accepted for publication Dec 7, 2017

*Address reprint requests to: H.S., Department of Radiology, China-Japan Friendship Hospital, No. 2 Yinghua East Street, Chaoyang District, Beijing 100029, China. E-mail: stentorsun@gmail.com

From the [1]Department of Radiology, China-Japan Friendship Hospital, Beijing, China; [2]Philips Healthcare, Shatin, New Territories, Hong Kong, China; [3]Philips Healthcare, Beijing, China; and [4]Department of Pathology, China-Japan Friendship Hospital, Beijing, China

© 2017 International Society for Magnetic Resonance in Medicine

a fair number of patients are in the locally advanced stage at initial diagnosis. Neoadjuvant chemotherapy (NACT) has been widely applied in treating locally advanced rectal cancer (LARC) for effectively decreasing local recurrence after total mesorectal excision (TME).[2] Most of the patients can benefit substantially from NACT. After neoadjuvant treatment, approximately 10–30% of LARC patients may achieve a pathological complete response (pCR), which is defined as the absence of viable tumor cells after full pathologic examination of the resected specimen.[3–6] For these patients, surgical resection may not lead to an increase in overall and disease-free survival, but may result in extensive comorbidities, such as sexual, urinary, and bowel dysfunction, and even mortality.[7–10] On the contrary, other patients who have a lesser degree of response to therapy may also benefit from early prediction because they can be prevented from ineffectively toxic therapy and alerted for a timely therapeutic regimen. Recently, a paradigm of "nonoperative" or "watch-and-wait" strategy has been proposed for patients with LARC who have a good response to adjuvant therapy.[10–13] However, there is still a lack of an accurate diagnosis method to predict and identify complete responders without relying on the pathological examination of surgical specimens.[14,15] Thus, reliable noninvasive diagnostic tools are needed.

Although conventional morphologic magnetic resonance imaging (MRI) can accurately evaluate local invasiveness of the rectal tumor and lymph node metastasis in pretherapeutic patients, restaging after therapy is still challenging.[14,16,17] The difficulty in distinguishing residual tumor from posttherapeutic fibrosis and edema can potentially lead to overstaging.[18] Diffusion-weighted imaging (DWI) may be helpful in solving this problem. Apparent diffusion coefficient (ADC), the quantitative parameter of DWI, has been used as an imaging marker to evaluate rectal tumor response to therapy.[2] Several recent studies demonstrated the potential of ADC in distinguishing pCR from non-pCR, but the results remained inconsistent.[2,19–26] This is possibly because the ADC value could reflect the rate of diffusion in cellular tissues but failed to distinguish the perfusion effects from true tissue diffusion, thereby introducing the signal attenuation of imaging.[27,28] Intravoxel incoherent motion (IVIM) model, which could estimate tissue perfusion and diffusion components individually using multi-b-values, was introduced to overcome this limitation.[27,29] It was used in predicting the treatment response of nasopharyngeal carcinoma. The IVIM-derived D values exhibited a higher diagnostic performance compared with ADC values.[30]

Furthermore, most of the previous studies used a single section of tumor to represent the whole tumor, such as contouring tumor or placing regions of interest (ROIs) on one representative section of tumor.[21,31,32] However, considering tumor's heterogeneity, the researchers are subjective in choosing the measurement section, which may result in the measured deviation. Recently, Nougaret et al[33] used whole-tumor volume (WTV) analyses in assessing the response to chemotherapy and radiation therapy in rectal cancer. They demonstrated better interobserver reproducibility compared with single-section ROI analysis.[33] The WTV analysis method was adopted in the present study for minimizing subjectivity of drawing ROIs on tumors among different observers and obtaining more reliable results. IVIM parameters derived from WTV analysis were not used in assessing the response to NACT therapy in LARC. Therefore, this study aimed to evaluate the utility of IVIM parameters by using WTV analysis in assessing the pCR response to NACT.

Materials and Methods

Patients

This prospective study was approved by the Institutional Review Board of our hospital, and written informed consent was obtained from all patients. A 3Tesla MRI scanner was used for pelvic MRI examination of 179 patients with pathologically proven rectal adenocarcinoma between March 2015 and March 2017. The inclusion criteria were: 1) histologically confirmed rectal adenocarcinoma; 2) LARC (stage IIIA and above) at pre-NACT MRI; 3) pre- and post-NACT MRI, including DWI sequences with 16 b values; 4) neoadjuvant chemotherapy; and 5) surgical resection. A total of 128 patients were excluded for the following reasons: i) lack of NACT treatment ($n = 88$); ii) heavy susceptibility artifact or lack of DWI sequences with 16 b values ($n = 6$); iii) lack of pre- or post-NACT MRI ($n = 15$); or iv) mucinous adenocarcinoma or signet-ring cell carcinoma ($n = 19$). Thus, 51 patients (mean age, 60.2 years; range, 35–79 years), including 41 men (mean age, 60.1 years; range, 35–79 years) and 10 women (mean age, 60.8 years; range, 42–79 years) were enrolled in this study.

The median time intervals were as follows: 94 days (range, 30–202 days) between pre-NACT MRI and surgery; 82 days (range, 28–182 days) between pre- and post-NACT MRI imaging; and 6 days (range, 0–72 days) between post-NACT MRI and surgery. The median time interval between the completion of NACT and surgery was 37 days (range, 5–105 days).

The NACT regimens consisted of oxaliplatin, 5-fluorouracil, and calcium folinate once every 2 weeks. All patients were treated with two to four cycles according to their treatment response and physical situation. The patients in this study did not receive radiation therapy.

MRI

On the day of examination, the patients were asked to fast and were intramuscularly injected with 10 mg anisodamine hydrochloride to prevent intestinal peristalsis 10 minutes before MRI. Pre- and post-NACT MRI was performed on a 3T whole-body scanner (Ingenia, Philips Medical Systems, Best, the Netherlands) with a gradient strength of 45 mT/m and a gradient switching rate of 200 mT/m/ms, using a 16-channel anterior torso dS coil and a 16-channel posterior table dS coil. T_2-weighted (T_2W) imaging was performed in the oblique axial, coronal, and sagittal planes, and 2D sagittal T_2W turbo spin echo (TSE) sequences were

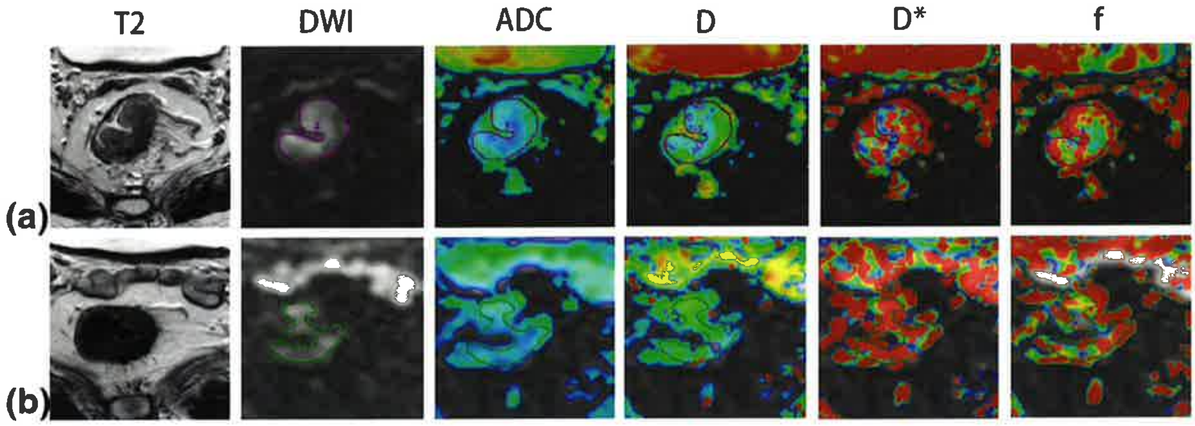

FIGURE 1: A 61-year-old man with LARC from the pCR group (TRG 4). Images in row A are T_2, DWI, ADC, D, D*, and f maps before NACT. The ADC, D, D*, and f values were $0.840 \times 10^{-3}mm^2/s$, $0.804 \times 10^{-3}mm^2/s$, $9.321 \times 10^{-3}mm^2/s$, and 0.319, respectively. Images in row B are T_2, DWI, ADC, D, D*, and f maps after NACT. The ADC, D, D*, and f values were $1.270 \times 10^{-3}mm^2/s$, $1.094 \times 10^{-3}mm^2/s$, $7.460 \times 10^{-3}mm^2/s$, and 0.362, respectively.

obtained using the following parameters: repetition time (TR), 4203 msec; echo time (TE), 102 msec; field of view (FOV), 24 × 24 cm^2; slice thickness, 4 mm with a 0.4-mm gap; acquisition matrix, 336 × 246; and NSA, 3. Coronal T_2W TSE sequences were obtained using the following parameters: TR, 4515 msec; TE, 110 msec; FOV, 24 × 24 cm^2; slice thickness, 3 mm with a 0.3-mm gap; acquisition matrix, 336 × 253;and NSA, 3. 2D axial T_2W TSE sequences were obtained perpendicular to the tumoral axis using the sagittal plane[34]: TR, 5191 msec; TE, 102 msec; FOV, 18 × 18 cm^2; slice thickness, 3.5 mm with a 0.35-mm gap; acquisition matrix, 200 × 296; and NSA, 3.

The DWI pulse sequence was obtained in the same orientation as oblique axial T_2W imaging by using a single-shot echo-planar imaging pulse sequence using the following parameters: echo time / repetition time (TE/TR), 76/4000 msec; field of view (FOV), 40 × 32 cm^2; slice thickness, 6 mm with a 0.6-mm gap; acquisition matrix, 160 × 104; pixel size, 2.5 × 3.12 mm^2; NSA, 3; and 16 b values (0, 10, 20, 30, 40, 60, 80, 100, 150, 200, 400, 800, 1000, 1200, 1500, and 2000 s/mm^2). The frequency selection plus inversion recovery fat-suppression technique (spectral attenuated inversion recovery) was used in the DWI sequence. The scan time for DWI sequence was about 5 minutes.

Image Analysis

Conventional scan sequences were used for radiological diagnosis by morphological evaluation of parameters, such as the depth of invasion and lymph node involvement.

MatLab (MathWorks, Natick, MA) was used to analyze the raw data from diffusion-weighted images. The ADC was obtained using b values fitted to a monoexponential model, whereas IVIM parameters were calculated with a biexponential model using 16 b values (0–2000 s/mm^2) described by Le Bihan et al.[29]

$$Sb/S0=(1-f)x\exp^{(-bD)}+fxep^{(-bD*)}$$

where Sb is the signal intensity in the pixel with diffusion gradient b; $S0$ is the mean signal intensity in the pixel without diffusion gradient; D (given in units of $\times\ 10^{-3}mm^2/s$) is the diffusion coefficient of slow or nonperfusion-related diffusion, which represents true molecular diffusion; D^* (given in units of $\times\ 10^{-3}mm^2/s$) is the diffusion coefficient of fast or perfusion-related diffusion; and f (given as a percentage) is the perfusion-related diffusion fraction, which represents fractional volume occupied in the voxel by flowing spins.

For each patient, ROIs were manually drawn to contour the border of the rectal cancers on each slice (DWI images, $b = 800$ s/mm^2) of tumor with reference to the T_2W image before and after NACT, avoiding the inclusion of intestinal gas, liquid, and necrotic regions (those showing fluid-like signal characteristics) by two experienced radiologists (10 years and 6 years in gastrointestinal imaging) blinded to the histopathology results (Figs. 1 and 2). All the parameters were measured twice 2 weeks later by one of the radiologists. When no residual tumor was seen on the post-NACT images obtained with the DWI pulse sequence, tracings were placed on the rectal wall at the prior tumor site.

Percentage changes in ADC, D, D^*, and f were calculated as follows:

$$\Delta ADC\% = (postADC - preADC)/preADC \times 100$$
$$\Delta D\% = (postD - preD)/preD \times 100$$
$$\Delta D^*\% = (postD^* - preD^*)/preD^* \times 100$$
$$\Delta f\% = (postf - pref)/pref \times 100$$

where preADC, postADC, pre$D$, post$D$, preD^*, postD^*, pre$f$, and post$f$ refer to ADC, D, D^*, and f values before and after NACT, respectively.

Surgical Resection and Histopathological Examination

All patients underwent TME. One experienced gastrointestinal pathologist (9 years of experience) assessed the surgical resection specimens according to the TNM staging system of the 7th edition of the American Joint Committee on Cancer.[35] The degree of tumor differentiation was categorized as highly, moderately, and poorly differentiated according to the WHO classification system.[36] The tumor response to NACT was evaluated according to tumor regression grade (TRG) system proposed by Dworak et al.[37]

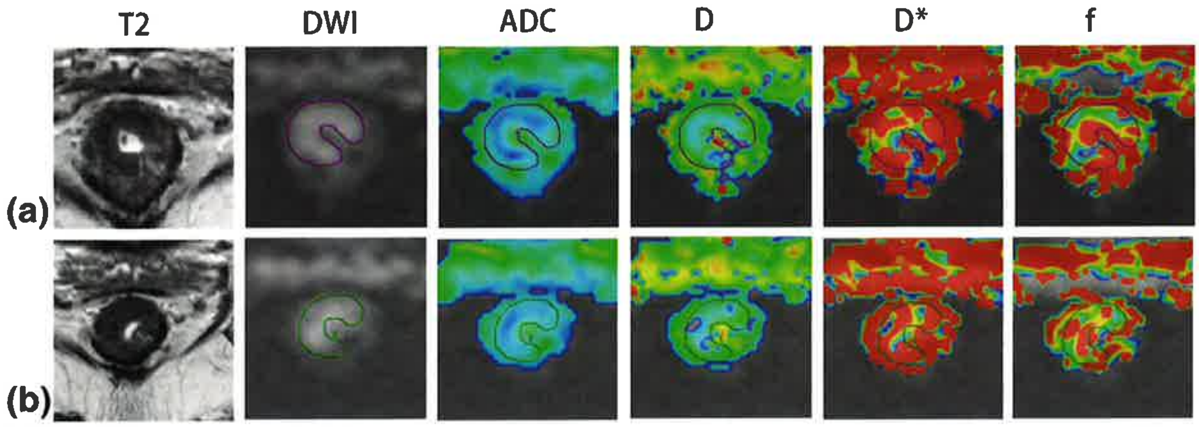

FIGURE 2: A 75-year-old man with LARC from the non-pCR group (TRG 2). Images in row A are T_2, DWI, ADC, D, D*, and f maps before NACT. The ADC, D, D*, and f values were 1.140×10^{-3}mm^2/s, 0.811×10^{-3}mm^2/s, 11.384×10^{-3}mm^2/s, and 0.320, respectively. Images in row B are T_2, DWI, ADC, D, D*, and f maps after NACT. The ADC, D, D*, and f values were 1.180×10^{-3}mm^2/s, 0.852×10^{-3}mm^2/s, 10.539×10^{-3}mm^2/s, and 0.313, respectively.

Patients with TRG grades 0–3 were put into the no-pCR group, whereas patients with TRG 4 were put into the pCR group.

Statistical Analysis

The one-sample Kolmogorov–Smirnov test was first used to analyze continuous variables for normality. Continuous variables were expressed as mean ± standard deviation (normal distribution) or median ± interquartile range (abnormal distribution). The intraclass correlation coefficient (ICC) was calculated to evaluate intra- and interobserver reproducibility. ICC values smaller than 0.4 indicated poor reproducibility, values ranging from 0.4 to 0.59 indicated fair reproducibility, values ranging from 0.6 to 0.74 indicated good reproducibility, and values above 0.75 indicated excellent reproducibility. Independent-samples *t*-test and Mann–Whitney *U*-test were employed to estimate the differences in continuous variables between pCR and non-pCR groups. The paired *t*-test was used to compare the parameters between pre-NACT and post-NACT. The diagnostic accuracy of indicators (pre-ADC_{mean}, pre-D, post-f, ΔADC_{mean}%, ΔD%, and Δ*f*%) was evaluated in terms of sensitivity, specificity, positive predictive value (PPV), negative predictive value (NPV), and area under the receiver operating characteristic (ROC) curve (AUC). A two-tailed test pattern was used in all statistical analyses with the level of statistical significance determined as $P < 0.05$. All statistical calculations were performed using SPSS (17.0 for Windows, SPSS, Chicago, IL).

Results

Clinical Characteristics

This study was performed on 51 patients with rectal cancer, including 41 men (80.4%) and 10 women (19.6%) who conformed to the selection criteria. Ten patients (pCR rate, 19.6%) had pCR to NACT, and 41 patients had no pCR to NACT. Table 1 summarizes the clinicopathological characteristics of the patients.

Parameters Before and After NACT

The ADC_{min} ($P = 0.020$), ADC_{mean} ($P = 0.001$), and D ($P < 0.001$) values were significantly higher after NACT, *f* ($P = 0.004$) values were significantly lower after NACT, whereas ADC_{max} and D* values did not significantly change ($P = 0.563$ and 0.451, respectively) in the pCR group. In non-pCR group, only ADC_{min} values ($P = 0.004$) were significantly higher after NACT, whereas ADC_{max}, ADC_{mean}, D, D*, and *f* values did not significantly change after NACT ($P = 0.242$, 0.205, 0.266, 0.269, and 0.309, respectively) (Table 2, Fig. 3).

Comparison of Parameters Between pCR and Non-pCR groups

The values of pre-ADC_{mean} and pre-D in the pCR group were much lower than that in the non-pCR group ($P = 0.003$ and 0.024, respectively), whereas no significant differences were found in the values of pre-ADC_{min}, pre-ADC_{max}, pre-D*, and pre-*f* ($P = 0.569$, 0.245, 0.687, and 0.448, respectively). Significant differences in post-*f* values were found ($P = 0.002$), whereas no significant differences in other post-NACT parameters were found, including post-ADC_{min}, post-ADC_{mean}, post-ADC_{max}, post-D, and post-D* ($P = 0.151$, 0.217, 0.499, 0.063, and 0.831, respectively). The values of ΔADC_{mean}%, ΔD%, and Δ*f*% were significantly higher in the pCR group than in the non-pCR group ($P = 0.002$, 0.001, and 0.017, respectively); however, no significant difference in the values of ΔADC_{min}%, ΔADC_{max}%, and ΔD*% was observed ($P = 0.155$, 0.868, and 0.618, respectively) (Table 3, Figs. (3 and 4)).

Diagnostic Performance for Assessing pCR

The diagnostic performance of ADC and IVIM-derived parameters were evaluated using the ROC curves to assess a pCR. Pre-ADC_{mean}, pre-D, post-*f*, ΔADC_{mean}%, ΔD%, and Δ*f*% located in the area under the curve were 0.802, 0.732, 0.812, 0.761, 0.832, and 0.746, respectively (Fig. 5). The optimal cutoff value for accurately identifying patients

TABLE 1. Baseline and Demographic Data of 51 Patients

Characteristic	Value
Age (year)	
Male	60.1 (35–79)
Female	60.8 (42–79)
All	60.2 (35–79)
Sex (%)	
Male	41 (80.4%)
Female	10 (19.6%)
Distance of the primary tumor from the anal verge	
0–5.0cm	20 (39.2%)
5.1–10.0cm	27 (52.9%)
10.1–15.0cm	4 (7.8%)
Post-NACT pathologic T(ypT) classification	
ypT0	10 (19.6%)
ypT1	2 (3.9%)
ypT2	14 (27.5)
ypT3	25 (49.0%)
ypT4	0 (0%)
Post-NACT pathologic N (ypN) classification	
ypN0	39 (76.5%)
ypN1	10 (19.6%)
ypN2	2 (3.9%)
Tumoral regression grade	
Grade 4	10 (19.6%)
Grade 3	5 (9.8%)
Grade 2	17 (33.3%)
Grade 1	16 (31.4%)
Grade 0	2 (3.9%)
Post-NACT pathological differentiation	
High	5 (12.2%)
Moderate	31 (75.6%)
Poor	5 (12.2%)

Continuous data are expressed as means, with ranges in parentheses. Categorical data are expressed as numbers of patients, with percentages in parentheses.

TABLE 2. ADC and IVIM Parameters Before and After NACT

Parameters	Before NACT	After NACT	*P*
ADC_{max}			
pCR	1.59 ± 0.46	1.48 ± 0.23	0.563
non-pCR	1.75 ± 0.42	1.63 ± 0.50	0.242
ADC_{min}			
pCR	0.44 ± 0.21	0.75 ± 0.29	0.020
non-pCR	0.50 ± 0.21	0.66 ± 0.28	0.004
ADC_{mean}			
pCR	0.80 ± 0.18	1.10 ± 0.09	0.001
non-pCR	0.99 ± 0.18	1.05 ± 0.26	0.205
D			
pCR	0.63 ± 0.10	0.82 ± 0.14	<0.001
non-pCR	0.71 ± 0.08	0.74 ± 0.16	0.266
D*			
pCR	9.59 ± 0.84	9.10 ± 1.62	0.451
non-pCR	9.31 ± 1.35	8.98 ± 2.09	0.269
f(%)			
pCR	31.34 ± 1.80	34.64 ± 3.75	0.004
non-pCR	30.69 ± 3.22	29.70 ± 5.95	0.309

Data are presented as mean ± standard deviation; ADC, apparent diffusion coefficient; D, slow diffusion coefficient; D*, fast diffusion coefficient; and *f*, perfusion-related diffusion fraction; ADC, D, and D* value = $\times 10^{-3} mm^2/s$.

with pCR was $0.89 \times 10^{-3} mm^2/s$ for pre-ADC_{mean} (80% sensitivity, 73.17% specificity, 42.11% PPV, 93.75% NPV, and 74.51% accuracy), $0.58 \times 10^{-3} mm^2/s$ for pre-D (50% sensitivity, 95.12% specificity, 71.43% PPV, 88.64% NPV, and 86.27% accuracy), 33.25% for post-*f* (80% sensitivity, 78.05% specificity, 47.06% PPV, 94.12% NPV, and 78.43% accuracy), 18% for ΔADC_{mean}% (90% sensitivity, 65.85% specificity, 39.13% PPV, 96.43% NPV, and 70.59% accuracy), 23.35% for ΔD% (80% sensitivity, 80.49% specificity, 50% PPV, 94.29% NPV, and 80.39% accuracy), –5.31% for Δ*f*% (100% sensitivity, 51.22% specificity, 33.33% PPV, 100% NPV, and 60.78% accuracy) (Table 4).

Intra- and Interobserver Repeatability of the Parameters Derived from WTV

No significant intra- and interobserver differences were found in the parameters (D, D*, and *f*) derived from WTV. All parameters showed excellent reproducibility (Table 5).

Discussion

The present study demonstrated that the pCR group had significantly lower ADC and D values before NACT compared with the non-pCR group, which might help clinicians predict the pCR to NACT in LARC. The percentage changes in ADC, D, and *f* values before and after NACT were significantly higher in the pCR group, suggesting that ADC, D, and *f* values

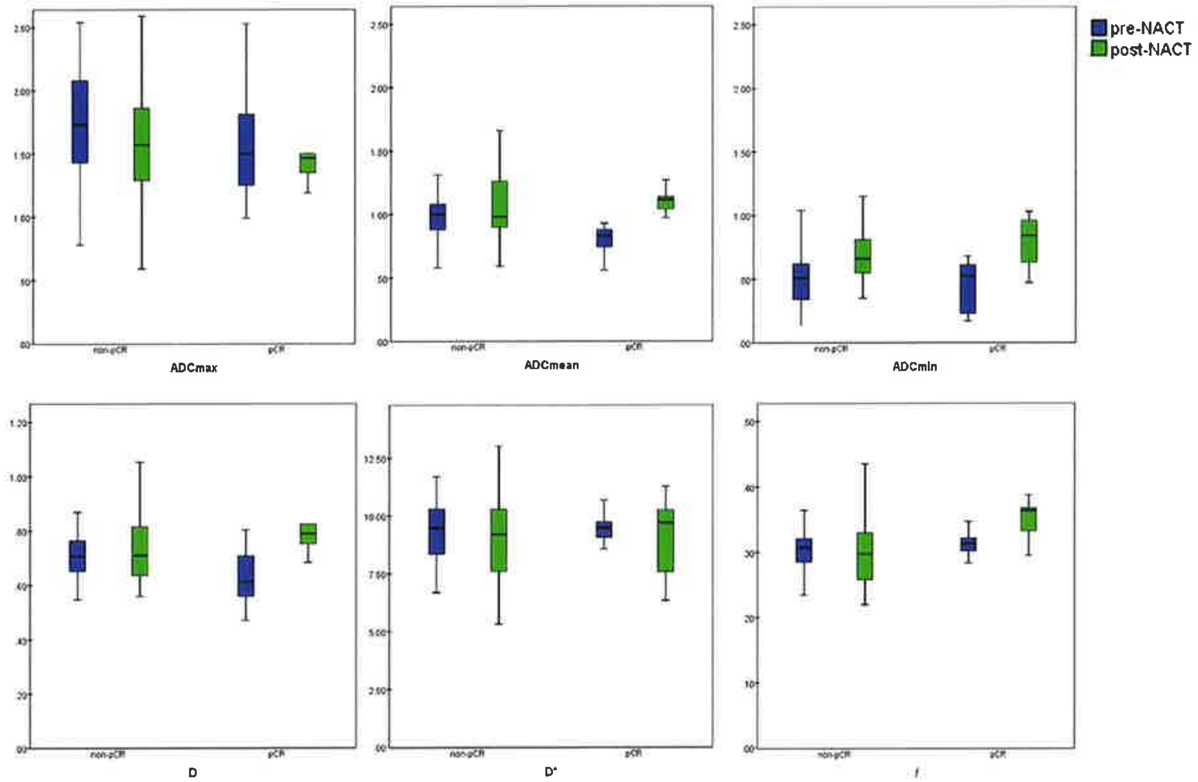

FIGURE 3: Box-and-whisker plots of ADC and IVIM parameters before and after NACT in non-pCR and pCR groups.

might be useful in assessing the pCR response before surgery. In addition, the percentage changes in D values before and after NACT showed the highest diagnostic performance, and D values before therapy showed the best specificity and accuracy among all parameters. The WTV measurement showed excellent reproducibility.

Preoperative pelvic radiation therapy could result in long-term bowel and sexual functional changes.[38] Moreover, Schrag et al demonstrated that adding radiation therapy to neoadjuvant chemotherapy could not improve treatment outcomes, but delayed administration of optimal chemotherapy.[39] Therefore, patients in this study did not receive radiation therapy. Early prediction of rectal tumor response to therapy can help clinicians choose the optimal treatment regimen, and finding a tool to predict pCR before therapy and assessing it accurately after therapy is important. However, assessing the tumor residual and nodal statuses after therapy was usually limited because the morphologic imaging of tumor was similar to fibrous replacement of the tumor tissues.[18] DWI-derived ADC values were regarded as a reasonable imaging biomarker, which could quantitatively measure random diffusion of water molecules in biologic tissues. The increase in ADC values was related to decreased cellular density and increased interstitial space, which was useful when evaluating the malignancy of the tumor and monitoring the tumor response to treatment.[22,25,40,41] However, this technique did not consider the influence of microcirculation perfusion. Therefore, it could not accurately reflect the diffusion characteristics. IVIM DW-MRI could distinguish perfusion information from diffusion using a biexponential model and multi-b-value sampling. Hence, the true molecular diffusion and microcirculation perfusion could be obtained simultaneously.[27,29] This notion was supported by the results of the present study that IVIM-derived D values were significantly lower than DWI-derived ADC values both before and after NACT, which were also consistent with previous findings in various tumor and organs.[42–44]

Furthermore, the ADC and D values were found to be significantly lower before the start of therapy in the pCR group compared with the non-pCR group. Similarly, Lambrecht et al showed that the low ADC values before therapy were significantly associated with the pCR status.[26] Perhaps the necrotic area in the tumor could decrease the movement of water molecules and also inhibit the delivery of therapy due to lack of vascularization. Conversely, several studies reported that pretreatment ADC[21–24] and D values[31,32] were not associated with the pCR status. These differences might be because of the variations in the MRI technique and the difference in measurement methodology such as ROI selection.

In addition, this study found that pre-ADC and pre-D values significantly increased in the pCR group compared with

TABLE 3. Comparison of ADC and IVIM Parameters Before and After NACT Between pCR and Non-pCR Groups

	Parameters	PCR ($n = 10$)	Non-pCR ($n = 41$)	P
Pre-NACT	ADC_{max}	1.59 ± 0.46	1.75 ± 0.42	0.245
	ADC_{min}	0.44 ± 0.21	0.50 ± 0.21	0.569
	ADC_{mean}	0.80 ± 0.18	0.99 ± 0.18	0.003
	D	0.63 ± 0.10	0.71 ± 0.08	0.024
	D*	9.59 ± 0.84	9.31 ± 1.35	0.687
	f(%)	31.34 ± 1.80	30.69 ± 3.22	0.448
Post-NACT	ADC_{max}	1.48 ± 0.23	1.63 ± 0.50	0.499
	ADC_{min}	0.75 ± 0.29	0.66 ± 0.28	0.151
	ADC_{mean}	1.10 ± 0.09	1.05 ± 0.26	0.217
	D	0.82 ± 0.14	0.74 ± 0.16	0.063
	D*	9.10 ± 1.62	8.98 ± 2.09	0.831
	f(%)	34.64 ± 3.75	29.70 ± 5.95	0.002
*Δ(%)	ADC_{max}	−9.21 ± 45.37	−7.813 ± 40.12	0.868
	ADC_{min}	91.50 ± 138.22	47.76 ± 114.72	0.155
	ADC_{mean}	42.49 ± 33.63	−1.18 ± 47.15	0.002
	D	36.23 ± 24.30	−0.08 ± 31.65	0.001
	D*	−4.61 ± 33.03	−1.85 ± 24.65	0.618
	f	11.77 ± 12.73	−5.63 ± 28.60	0.017

Data are presented as mean ± standard deviation or median ± interquartile range (*); ADC, apparent diffusion coefficient; D, slow diffusion coefficient; D*, fast diffusion coefficient; and f, perfusion-related diffusion fraction; ADC, D, and D* value = $\times 10^{-3} mm^2/s$; $\Delta(\%) = (post\gamma - pre\gamma)/ pre\gamma \times 100$; ($\gamma = ADC_{max}$, ADC_{min}, ADC_{mean}, D, D*, or f).

post-ADC and post-D values. It was different from several previous studies that obtained increased ADC values in the pCR and non-pCR groups.[21,31] Furthermore, several studies showed that posttreatment ADC[22,32] and D[31] values could help distinguish pCR from non-pCR in patients with LARC. However, several other studies did not demonstrate this utility.[23,24] In this study, post-ADC and post-D values were not found to be significantly different between the two groups. However, the percentage changes in ADC and D before and after NACT were significantly higher in the pCR group than in the non-pCR group. This suggested that these two groups of patients had different sensitivities to NACT. Cytotoxic chemotherapy could more effectively eradicate tumor cells, which was reflected in an increase in ADC and D values.

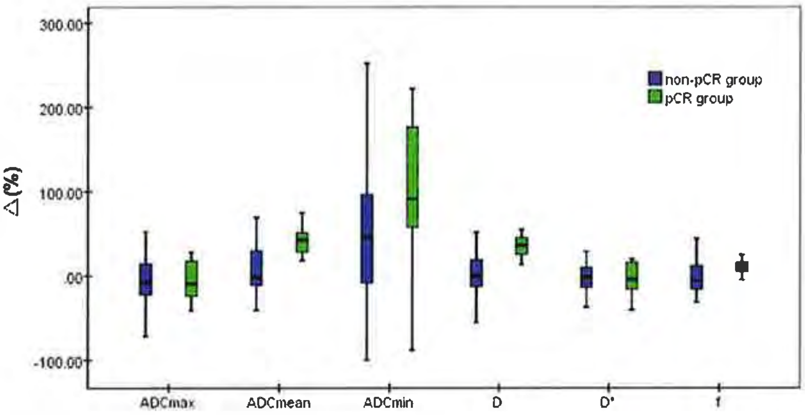

FIGURE 4: The percentage changes of ADC and IVIM parameters before and after NACT in non-pCR and pCR groups.

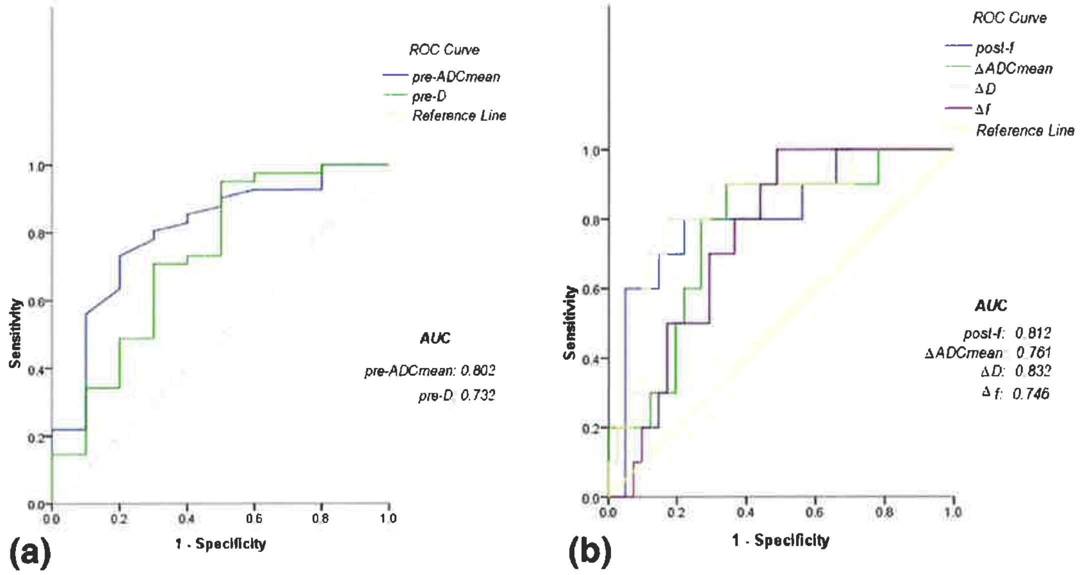

FIGURE 5: (a) ROC curve analysis of pre-ADC$_{mean}$ and pre-D values for predicting pCR. (b) ROC curve analysis of post-f, ΔADC$_{mean}$, ΔD, and Δf values for assessing pCR.

However, the results of the present study and prior studies might be different because the investigators used various methods of placing ROIs in rectal tumor when evaluating the parameters on DW-MRI. Contouring lesions on a representative section of rectal tumor was the most common and convenient method. However, the distribution of signal intensity in rectal cancer was heterogeneous, and a single section of tumor may not represent the information on tumor heterogeneity.[19–22,45,46] Moreover, the selection of section and the position of ROIs highly depended on the subjective judgment of different observers. Thus, its accuracy was limited. Recently, Nougaret et al indicated that the WTV analysis of IVIM-derived parameters had better reproducibility than single-section ROI analysis when assessing the treatment response in patients with LARC.[33] Additionally, Goh et al suggested that WTV analysis might improve the assessment of tumor by capturing inherent intratumoral heterogeneity better.[47] The WTV analysis was adopted in the present study for minimizing sampling bias and obtaining more reliable results. The ADC$_{mean}$ values were significantly different from both ADC$_{min}$ ($P < 0.001$) and ADC$_{max}$ ($P < 0.001$) values, further proving heterogeneity in the tumor. Moreover, the data showed that WTV analysis had excellent reproducibility, which was consistent with the findings of previous studies.[33] The present study showed that the pre-D values had the highest specificity and accuracy when predicting the pCR response and ΔD% had the highest AUC when assessing the pCR status after therapy. This suggested that IVIM-derived D values were significantly associated with pCR.

TABLE 4. Diagnostic Performance of ADC and IVIM Parameters Obtained Using Whole-Tumor Volume Analysis to pCR Response After NACT

Parameters	Sensitivity (%)	Specificity (%)	PPV (%)	NPV (%)	Accuracy (%)	AUC (95%CI)	Cutoff value
Pre-ADC$_{mean}$ ($\times 10^{-3}$mm^2/s)	80	73.17	42.11	93.75	74.51	0.802 (0.646–0.959)	0.89
Pre-D ($\times 10^{-3}$mm^2/s)	50	95.12	71.43	88.64	86.27	0.732 (0.538–0.926)	0.58
Post-*f* (%)	80	78.05	47.06	94.12	78.43	0.812 (0.658–0.966)	33.25
ΔADC$_{mean}$ (%)	90	65.85	39.13	96.43	70.59	0.761 (0.604–0.918)	18.00
ΔD (%)	80	80.49	50	94.29	80.39	0.832 (0.690–0.973)	23.35
Δ*f* (%)	100	51.22	33.33	100	60.78	0.746 (0.611–0.881)	-5.31

TABLE 5. Intra- and Interobserver Agreement for Whole-Tumor Volume Measurement

	Parameters	Intraobserver	Interobserver
Pre-NACT	ADC_{max}	0.8282	0.7593
	ADC_{min}	0.8812	0.8489
	ADC_{mean}	0.9786	0.9763
	D	0.9507	0.9433
	D*	0.9841	0.9774
	f	0.9660	0.9603
Post-NACT	ADC_{max}	0.7939	0.7550
	ADC_{min}	0.8017	0.7538
	ADC_{mean}	0.8807	0.8633
	D	0.9863	0.9836
	D*	0.9657	0.7949
	f	0.9582	0.9669

In addition, the results of f values in assessing the treatment response were variable across different studies. Lu et al found that pre-f values were significantly higher in the pCR group of rectal cancer,[31] whereas other studies found that f values were not useful in assessing the treatment response in rectal tumor.[32,33] These conflicting results might be due to the fact that f values represented the signal intensity ratio of blood capillaries and tumor tissues, which were both affected by the T_2 contribution.[48,49] After treatment, the T_2 values of tumor tended to increase, leading to an underestimation of the increase in f values.[49] In the present study, post-f values and its percentage changes significantly increased after NACT in the pCR group, whereas no significant changes were found in the non-pCR group. However, the vascular damage and the influence of inflammation and edema were complex, limiting the utility of f values.[50] Therefore, although f values showed the highest sensitivity (100%) in the present study, the results still should be interpreted with caution.

The present study demonstrated that IVIM-derived D* values were useless in predicting or identifying pCR response. Similarly, Zhu et al did not find a significant difference in D* values between the two groups.[32] Moreover, Yu et al proved that IVIM-derived diffusion parameters might be more helpful than IVIM-derived perfusion parameters in patients with nasopharyngeal carcinoma.[30] However, Lu et al reported higher pre-D* in the pCR group of rectal cancer. These conflicting results were possibly due to the poor reproducibility of D* values,[32,33] which was also proved in the present study showing that the interobserver agreement of D* values after NACT was lower than that of other parameters. This might also result from the relatively high sensitivity of D* values to noise.[51]

The present study had several limitations. First, the sample size was relatively small and confined to a single center, resulting in selection bias. Second, different timepoints of therapy were not taken into account. Further studies could monitor the parameters after every cycle of chemotherapy to obtain more information in predicting or assessing pCR. Third, the results were not compared with the dynamic contrast material-enhanced acquisition parameters, which could quantitatively assess tumor microcirculation after therapy directly. Fourth, in our study we excluded rectal mucinous adenocarcinoma, which is seen as abundant extracellular mucin exceeding 50% of the tumor stroma.[52] However, the diffusion and perfusion characteristics of mucinous adenocarcinoma in DWI-derived images were different from typical rectal adenocarcinoma[53] and accumulating evidence indicates that the prognosis of mucinous adenocarcinoma is poorer than nonmucinous adenocarcinoma.[54,55] Finally, the IVIM model required sufficient b values, but too many b values would increase the scan time. Therefore, the proper number and interval of b values need to be explored.

In conclusion, this study suggested that IVIM-derived D values before therapy might be a promising tool for predicting pCR, and the percentage changes in D values after therapy had the best diagnostic performance of pCR response. These results still need be proved by conducting larger, multicenter, prospective studies. Furthermore, the WTV analysis showed excellent reproducibility, which can be applied in further studies for obtaining reliable results.

Conflict of Interest

Queenie Chan and Kaining Shi are employees of Philips Healthcare but they had no control over inclusion of any data or information that might have presented a conflict of interest. There are no actual or potential conflicts of interest to declare in relation to this article. The other authors have nothing to disclose.

Acknowledgment

Contract grant sponsor: National Natural Science Foundation of China; contract grant number: 81501469; Contract grant sponsor: Health Industry Special Scientific Research Project of National Health and Family Planning Commission of the People's Republic of China; contract grant number: 201402019

References

1. Torre LA, Bray F, Siegel RL, Ferlay J, Lortet-Tieulent J, Jemal A. Global cancer statistics, 2012. CA Cancer J Clin 2015;65:87–108.

2. Hötker AM, Garcia-Aguilar J, Gollub MJ. Multiparametric MRI of rectal cancer in the assessment of response to therapy. Dis Colon Rectum 2014;57:790–799.

3. Yeo S, Kim DY, Kim TH, et al. Pathologic complete response of primary tumor following preoperative chemoradiotherapy for locally advanced rectal cancer. Ann Surg 2010;252:998–1004.

4. Wallin U, Rothenberger D, Lowry A, Luepker R, Mellgren A. CEA — A predictor for pathologic complete response after neoadjuvant therapy for rectal cancer. Dis Colon Rectum 2013;56:859–868.

5. Habrgama A, Perez R, Nadalin W, et al. Long-term results of preoperative chemoradiation for distal rectal cancer correlation between final stage and survival. J Gastrointest Surg 2005;9:90–101.

6. Wheeler JMD, Dodds E, Warren BF, et al. Preoperative chemoradiotherapy and total mesorectal excision surgery for locally advanced rectal cancer: correlation with rectal cancer regression grade. Dis Colon Rectum 2004;47:2025–2031.

7. Pozo ME. Watch and wait approach to rectal cancer: A review. World J Gastrointest Surg 2015;7:306.

8. Kim M, Kim ES, Yeo S. Definitive high-dose radiotherapy with concurrent chemotherapy for locally advanced rectal cancer. Medicine 2016; 95:e5059.

9. Camilleri-Brennan J, Steele RJ. Objective assessment of morbidity and quality of life after surgery for low rectal cancer. Colorectal Dis 2002;4:61–66.

10. Habr-Gama A, Perez RO, Nadalin W, et al. Operative versus nonoperative treatment for stage 0 distal rectal cancer following chemoradiation therapy. Ann Surg 2004;240:711–718

11. Beets GL, Figueiredo NL, Habr-Gama A, van de Velde CJH. A new paradigm for rectal cancer: Organ preservation. Eur J Surg Oncol 2015;41:1562–1564.

12. Habr-Gama A, Perez RO, São Julião GP, Proscurshim I, Gama-Rodrigues J. Nonoperative approaches to rectal cancer: a critical evaluation. Semin Radiat Oncol 2011;21:234–239.

13. Maas M, Beets-Tan RG, Lambregts DM, et al. Wait-and-see policy for clinical complete responders after chemoradiation for rectal cancer. J Clin Oncol 2011;29:4633–4640.

14. Habr-Gama A, Gama-Rodrigues J, São Julião GP, et al. Local recurrence after complete clinical response and watch and wait in rectal cancer after neoadjuvant chemoradiation: impact of salvage therapy on local disease control. Int J Radiat Oncol Biol Phys 2014;88:822–828.

15. Habrgama A, Perez R, Proscurshim I, et al. Patterns of failure and survival for nonoperative treatment of stage c0 distal rectal cancer following neoadjuvant chemoradiation therapy. J Gastrointest Surg 2006;10:1319–1329.

16. Suppiah A, Hunter IA, Cowley J, et al. Magnetic resonance imaging accuracy in assessing tumour down-staging following chemoradiation in rectal cancer. Colorectal Dis 2009;11:249–253.

17. van der Paardt MP, Zagers MB, Beets-Tan RG, Stoker J, Bipat S. Patients who undergo preoperative chemoradiotherapy for locally advanced rectal cancer restaged by using diagnostic MR imaging: a systematic review and meta-analysis. Radiology 2013;269:101–112.

18. Beets-Tan RG, Beets GL, Vliegen RF, et al. Accuracy of magnetic resonance imaging in prediction of tumour-free resection margin in rectal cancer surgery. Lancet 2001;357:497–504.

19. Choi MH, Oh SN, Rha SE, et al. Diffusion-weighted imaging: Apparent diffusion coefficient histogram analysis for detecting pathologic complete response to chemoradiotherapy in locally advanced rectal cancer. J Magn Reson Imaging 2016;44:212–220.

20. Kim SH, Lee JM, Hong SH, et al. Locally advanced rectal cancer: added value of diffusion-weighted MR imaging in the evaluation of tumor response to neoadjuvant chemo- and radiation therapy. Radiology 2009;253:116–125.

21. Hu F, Tang W, Sun Y, et al. The value of diffusion kurtosis imaging in assessing pathological complete response to neoadjuvant chemoradiation therapy in rectal cancer: a comparison with conventional diffusion-weighted imaging. Oncotarget 2017 [Epub ahead of print].

22. Kim SH, Lee JY, Lee JM, Han JK, Choi BI. Apparent diffusion coefficient for evaluating tumour response to neoadjuvant chemoradiation therapy for locally advanced rectal cancer. Eur Radiol 2011;21:987–995.

23. Engin G, Sharifov R, Gural Z, et al. Can diffusion-weighted MRI determine complete responders after neoadjuvant chemoradiation for locally advanced rectal cancer? Diagn Interv Radiol 2012:574–581.

24. Curvo-Semedo L, Lambregts DM, Maas M, et al. Rectal cancer: assessment of complete response to preoperative combined radiation therapy with chemotherapy—conventional MR volumetry versus diffusion-weighted MR imaging. Radiology 2011;260:734–743.

25. Ha HI, Kim AY, Yu CS, Park SH, Ha HK. Locally advanced rectal cancer: diffusion-weighted MR tumour volumetry and the apparent diffusion coefficient for evaluating complete remission after preoperative chemoradiation therapy. Eur Radiol 2013;23:3345–3353.

26. Lambrecht M, Vandecaveye V, De Keyzer F, et al. Value of diffusion-weighted magnetic resonance imaging for prediction and early assessment of response to neoadjuvant radiochemotherapy in rectal cancer: preliminary results. Int J Radiat Oncol Biol Phys 2012;82:863–870.

27. Iima M, Le Bihan D. Clinical intravoxel incoherent motion and diffusion MR imaging: past, present, and future. Radiology 2016;278:13–32.

28. Buijsen J, van Stiphout RG, Menheere PPCA, Lammering G, Lambin P. Blood biomarkers are helpful in the prediction of response to chemoradiation in rectal cancer: A prospective, hypothesis driven study on patients with locally advanced rectal cancer. Radiother Oncol 2014;111:237–242.

29. Le Bihan D, Breton E, Lallemand D, Aubin ML, Vignaud J, Laval-Jeantet M. Separation of diffusion and perfusion in intravoxel incoherent motion MR imaging. Radiology 1988;168:497–505.

30. Xiao-ping Y, Jing H, Fei-ping L, et al. Intravoxel incoherent motion MRI for predicting early response to induction chemotherapy and chemoradiotherapy in patients with nasopharyngeal carcinoma. J Magn Reson Imaging 2016;43:1179–1190.

31. Lu W, Jing H, Ju-Mei Z, et al. Intravoxel incoherent motion diffusion-weighted imaging for discriminating the pathological response to neoadjuvant chemoradiotherapy in locally advanced rectal cancer. Sci Rep-UK 2017;7.

32. Zhu H, Zhang X, Zhou X, et al. Assessment of pathological complete response to preoperative chemoradiotherapy by means of multiple mathematical models of diffusion-weighted MRI in locally advanced rectal cancer: A prospective single-center study. J Magn Reson Imaging 2017;46:175–183.

33. Nougaret S, Vargas HA, Lakhman Y, et al. Intravoxel incoherent motion-derived histogram metrics for assessment of response after combined chemotherapy and radiation therapy in rectal cancer: initial experience and comparison between single-section and volumetric analyses. Radiology 2016;280:446–454.

34. Brown G, Richards CJ, Newcombe RG, et al. Rectal carcinoma: thin-section MR imaging for staging in 28 patients. Radiology 1999;211: 215–222.

35. Edge SB, Compton CC. The American Joint Committee on Cancer: The 7th Edition of the AJCC Cancer Staging Manual and the Future of TNM. Ann Surg Oncol 2010;17:1471–1474.

36. World Health Organization Classification of Tumours of the Digestive System. Lyon: International Agency for Research on Cancer (IARC). 2010. p 134–146.

37. Dworak O, Keilholz L, Hoffmann A. Pathological features of rectal cancer after preoperative radiochemotherapy. Int J Colorectal Dis 1997; 12:19–23.

38. Bruheim K, Guren MG, Skovlund E, et al. Late side effects and quality of life after radiotherapy for rectal cancer. Int J Radiat Oncol Biol Phys 2010;76:1005–1011.

39. Schrag D, Weiser MR, Goodman KA, et al. Neoadjuvant chemotherapy without routine use of radiation therapy for patients with locally advanced rectal cancer: a pilot trial. J Clin Oncol 2014;32:513–518.

40. Genovesi D, Filippone A, Ausili Cèfaro G, et al. Diffusion-weighted magnetic resonance for prediction of response after neoadjuvant chemoradiation therapy for locally advanced rectal cancer: Preliminary results of a monoinstitutional prospective study. Eur J Surg Oncol 2013;39:1071–1078.

41. Jung SH, Heo SH, Kim JW, et al. Predicting response to neoadjuvant chemoradiation therapy in locally advanced rectal cancer: Diffusion-weighted 3 Tesla MR imaging. J Magn Reson Imaging 2012;35:110–116.

42. Woo S, Lee JM, Yoon JH, Joo I, Han JK, Choi BI. Intravoxel incoherent motion diffusion-weighted MR imaging of hepatocellular carcinoma: correlation with enhancement degree and histologic grade. Radiology 2014;270:758–767.

43. Joo I, Lee JM, Yoon JH, Jang JJ, Han JK, Choi BI. Nonalcoholic fatty liver disease: intravoxel incoherent motion diffusion-weighted MR imaging—An experimental study in a rabbit model. Radiology 2013: 122506.

44. Andreou A, Koh DM, Collins DJ, et al. Measurement reproducibility of perfusion fraction and pseudodiffusion coefficient derived by intravoxel incoherent motion diffusion-weighted MR imaging in normal liver and metastases. Eur Radiol 2013;23:428–434.

45. Lambregts DMJ, Vandecaveye V, Barbaro B, et al. Diffusion-weighted MRI for selection of complete responders after chemoradiation for locally advanced rectal cancer: a multicenter study. Ann Surg Oncol 2011;18:2224–2231.

46. Park MJ, Kim SH, Lee SJ, Jang KM, Rhim H. Locally advanced rectal cancer: added value of diffusion-weighted MR imaging for predicting tumor clearance of the mesorectal fascia after neoadjuvant chemotherapy and radiation therapy. Radiology 2011;260:771–780.

47. Goh V, Halligan S, Gharpuray A, Wellsted D, Sundin J, Bartram CI. Quantitative assessment of colorectal cancer tumor vascular parameters by using perfusion CT: influence of tumor region of interest. Radiology 2008;247:726–732.

48. Guiu B, Petit JM, Capitan V, et al. Intravoxel incoherent motion diffusion-weighted imaging in nonalcoholic fatty liver disease: a 3.0-T MR study. Radiology 2012;265:96–103.

49. Lemke A, Laun FB, Simon D, Stieltjes B, Schad LR. An in vivo verification of the intravoxel incoherent motion effect in diffusion-weighted imaging of the abdomen. Magn Reson Med 2010;64:1580–1585.

50. Hauser T, Essig M, Jensen A, et al. Characterization and therapy monitoring of head and neck carcinomas using diffusion-imaging-based intravoxel incoherent motion parameters—preliminary results. Neuroradiology 2013;55:527–536.

51. Mazaheri Y, Afaq A, Rowe DB, Lu Y, Shukla-Dave A, Grover J. Diffusion-weighted magnetic resonance imaging of the prostate: improved robustness with stretched exponential modeling. J Comput Assist Tomogr 2012;36:695–703.

52. Hanski C. Is mucinous carcinoma of the colorectum a distinct genetic entity? Br J Cancer 1995;72:1350–1356.

53. Çolakoglu Er H, Erden A. Mean ADC values discriminate rectal mucinous carcinomafrom rectal nonmucinous adenocarcinoma. Turk J Med Sci 2017;47:1520–1525.

54. Park JS, Huh JW, Park YA, et al. Prognostic comparison between mucinous and nonmucinous adenocarcinoma in colorectal cancer. Medicine 2015;94:e658.

55. Yu SKT, Chand M, Tait DM, Brown G. Magnetic resonance imaging defined mucinous rectal carcinoma is an independent imaging biomarker for poor prognosis and poor response to preoperative chemoradiotherapy. Eur J Cancer 2014;50:920–927.

Downloaded from www.ajronline.org by Tufts University on 02/18/18 from IP address 130.64.11.153. Copyright ARRS. For personal use only; all rights reserved

Intravoxel Incoherent Motion MRI of Rectal Cancer: Correlation of Diffusion and Perfusion Characteristics With Prognostic Tumor Markers

Hongliang Sun[1]
Yanyan Xu[1]
Aiping Song[2]
Kaining Shi[3]
Wu Wang[1]

OBJECTIVE. The objective of our study was to evaluate the intravoxel incoherent motion (IVIM)–DWI derived parameters and their relationships with tumor prognostic markers using 3-T MRI in patients with rectal cancer.

SUBJECTS AND METHODS. Fifty-two patients with histopathologically proven rectal cancer who underwent preoperative pelvic MRI were prospectively enrolled in this study. Diffusion and perfusion parameters including the apparent diffusion coefficient (ADC), pure diffusion coefficient, perfusion fraction, and pseudodiffusion coefficient derived from IVIM-DWI were independently measured by two radiologists. Comparisons of IVIM-DWI–derived parameters in patients with different tumor prognostic markers were made using the independent-samples *t* test, ANOVA, and Mann-Whitney *U* test. The correlations between IVIM-DWI–derived parameters and tumor grade and tumor stage were further evaluated using Spearman correlation analysis. Interobserver agreement was evaluated using the intraclass correlation coefficient (ICC).

RESULTS. Excellent interobserver reproducibility was obtained for the IVIM-DWI–derived parameters (range of ICCs with 95% limits of agreement = 0.9309–0.9948, which is narrow). ADC, pseudodiffusion coefficient, and perfusion fraction tended to rise with greater tumor differentiation ($r = 0.520$, $p < 0.001$; $r = 0.447$, $p = 0.001$; $r = 0.354$, $p = 0.010$, respectively). The pure diffusion coefficient and pseudodiffusion coefficient showed a trend of decreasing with increasing tumor stages ($r = 0.479$, $p < 0.001$; $r = 0.517$, $p < 0.001$). The group of patients with extramural vascular invasion (EMVI) showed lower pseudodiffusion coefficient values than the group of patients with no EMVI ($p < 0.05$).

CONCLUSION. IVIM-DWI–derived parameters in patients with rectal cancer, especially the pseudodiffusion coefficient, are associated with tumor grade and tumor stage and show statistically significant differences between subjects with EMVI and those without EMVI. IVIM-DWI–derived parameters would be helpful in predicting tumor aggressiveness and prognosis.

Keywords: DWI, intravoxel incoherent motion, MRI, rectal cancer, tumor grading

doi.org/10.2214/AJR.17.18342

Received April 4, 2017; accepted after revision August 25, 2017.

Supported by grants 81501469 from the National Natural Science Foundation of China and 201402019 from the Health Industry Special Scientific Research Project of National Health and Family Planning Commission of the People's Republic of China.

The employment status of K. Shi at Philips Healthcare did not influence the data in this study.

[1]Department of Radiology, China-Japan Friendship Hospital, No. 2 Yinghua E St, Chaoyang District, Beijing 100029, China. Address correspondence to H. Sun (stentorsun@gmail.com).

[2]Department of Pathology, China-Japan Friendship Hospital, Beijing, China.

[3]Philips Healthcare MR Research Institution, Beijing, China.

WEB
This is a web exclusive article.

AJR 2018; 210:W1–W9

0361–803X/18/2104–W1

© American Roentgen Ray Society

Colorectal cancer (CRC) is a malignant tumor with a high morbidity and mortality. There were 1.4 million new cases worldwide in 2012 and approximately 0.7 million patients died of CRC in 2012 [1]. Rectal cancer accounts for approximately 30–35% of CRCs [1, 2]. The prognosis of patients with rectal cancer is closely related to tumor pathologic grade and stage. Higher tumor grade and advanced stage predict poor prognosis [3, 4]. In addition, the clinical treatment also depends on rectal cancer stage. Patients with advanced-stage rectal cancer often require preoperative chemotherapy or chemoradiotherapy [5–7]. Clinical studies have confirmed that neoadjuvant chemoradiation therapy is effective for downstaging disease and reducing the rate of local recurrence [7, 8]. Therefore, preoperative staging and grading have important clinical significance in the management of rectal cancer.

Tumor markers, such as carcinoembryonic antigen (CEA) and cancer antigen 19-9 (CA19-9) [9, 10], and relevant imaging indicators based on MRI, such as involvement of the circumferential resection margin (CRM) [11, 12] and the presence of extramural vascular invasion (EMVI) [13–15], are also correlated with prognosis. Previous studies have shown that the probability of metastasis within 1 year is 3.7 times higher in rectal cancer patients with MRI-detected EMVI than in those with no EMVI detected on MRI [14].

Downloaded from www.ajronline.org by Tufts University on 02/18/18 from IP address 130.64.11.153. Copyright ARRS. For personal use only; all rights reserved

It has been reported that tumor shape is associated with differentiation of colorectal adenocarcinoma and that the extramural depth of tumor invasion is related to prognostic factors (including tumor differentiation grade) [16–18]; thus, we hypothesized that the range of bowel circumferential invasion might be associated with tumor grade as a prognostic factor. However, the reference standard of tumor grading and staging is evaluation of postoperative pathologic specimens, whereas MRI indicators are relatively subjective with large interobserver variations [19, 20]; therefore, noninvasive quantitative preoperative evaluation methods are needed.

The DWI sequence has been gradually incorporated into the routine MRI protocol because of its proven advantages in tumor detection, tumor characterization, and monitoring of treatment response [21–27]. The apparent diffusion coefficient (ADC) has been proved to be a potential prognostic factor [22–26]. Intravoxel incoherent motion (IVIM) is based on a biexponential mathematic model with multiple b values, noninvasively measuring both the diffusion of free water molecules and the perfusion caused by microcirculation in vivo. The main parameters derived from the biexponential model are the pure diffusion coefficient, the perfusion fraction, and the pseudodiffusion coefficient [28]. Promising results have been reported in the relationship between IVIM parameters and histologic grade and tumor stage of various tumors [29–33]. However, in rectal cancer, research focusing on the relationships between IVIM parameters and clinicopathologic factors is rare [34, 35]. The only study in the literature that we found was by Surov et al. [35]. In that work, a negative relationship between IVIM parameters and tumor differentiation grade was reported. However, considering various factors, such as inconsistent IVIM protocol settings (especially b values), a limited number of subjects, and the use of different built-in analysis software programs by different vendors, further study of the relationship between IVIM parameters and the clinicopathologic factors of rectal cancer is needed. Therefore, the purpose of our study was to investigate the relationship between IVIM-DWI–derived parameters and clinicopathologic prognostic indicators in patients with rectal cancer to evaluate the feasibility of IVIM-DWI as a quantitative method for assessing tumor aggressiveness and predicting prognosis.

Subjects and Methods

Participants

This prospective study was approved by the institutional review board of China-Japan Friendship Hospital, and written informed consent was obtained from all patients. Between August 2013 and August 2014, 118 consecutive patients with rectal cancer confirmed by endoscopic biopsy and with complete clinical data underwent 3-T MRI. The exclusion criteria were as follows: preoperative neoadjuvant chemoradiotherapy ($n = 40$); an interval between surgery and MRI of more than 4 weeks ($n = 15$); non–rectal adenocarcinoma confirmed by postoperative pathologic results (i.e., neuroendocrine tumor [$n = 4$]); poor image quality (i.e., heavy intestinal peristalsis artifacts [$n = 5$]); and the lesion was too small (diameter < 5 mm) or was too difficult to identify on DW images ($n = 2$). A total of 52 patients were involved in the final analysis (Fig. 1). The clinical data of the 52 patients are listed in Table 1. The median interval between the primary staging MRI examination and surgery was 16 days (range, 7–27 days).

Patient Preparation and Imaging Protocol

Patients had a low-residue diet before the MRI examination and fasted on the day of the examination. Intramuscular injection of 10 mg of anisodamine hydrochloride was given to each patient approximately 10 minutes before MRI examination in the injection room to inhibit intestinal peristalsis.

Pelvic MRI scanning was performed on a 3-T whole-body scanner (Ingenia, Philips Healthcare) with a gradient strength of 45 mT/m and a gradient slew rate of 200 mT/m/ms using a 16-channel anterior torso coil and a 16-channel posterior table coil. Two-dimensional sagittal and coronal T2-weighted turbo spin-echo (TSE) sequences were performed using the following parameters: TR/TE, 3761/110; FOV, 24 × 24 cm; slice thickness, 3 mm with a 0.3-mm gap; acquisition matrix, 336 × 252; and number of signals averaged (NSA), 3. A 2D axial T2-weighted TSE sequence was performed perpendicular to the long axis of the rectum at the level of the tumor using the following parameters: TR/TE, 3865/100; FOV, 14 × 14 cm; slice thickness, 3 mm with a 0.3-mm gap; and acquisition matrix, 232 × 228.

Axial IVIM scanning was performed perpendicular to the lesion in the same direction as the axial TSE T2-weighted series using a single-shot DWI sequence with the following parameters: TR/TE, 6000/76; FOV, 20 × 30 cm; slice thickness, 4 mm with a 0.4-mm gap; acquisition matrix, 80 × 144; NSA, 6; and eight b values (0, 25, 50, 75, 150, 400, 800, and 1000 s/mm^2). The scanning time of IVIM was approximately 6 minutes 30 seconds.

Image Analysis and Postprocessing

DW images were postprocessed on a workstation (Extended Workspace 4.1, Philips Healthcare) and analyzed using in-house software (IDL, version 6.3, IDL Software) [36]. The ADC was obtained using b values (0–1000 s/mm^2) fitted to the monoexponential model. The IVIM parameters—that is, the diffusion coefficient (D), perfusion fraction (f), and pseudodiffusion coefficient (D^*)—were derived from the curve fit of the following equation [28]:

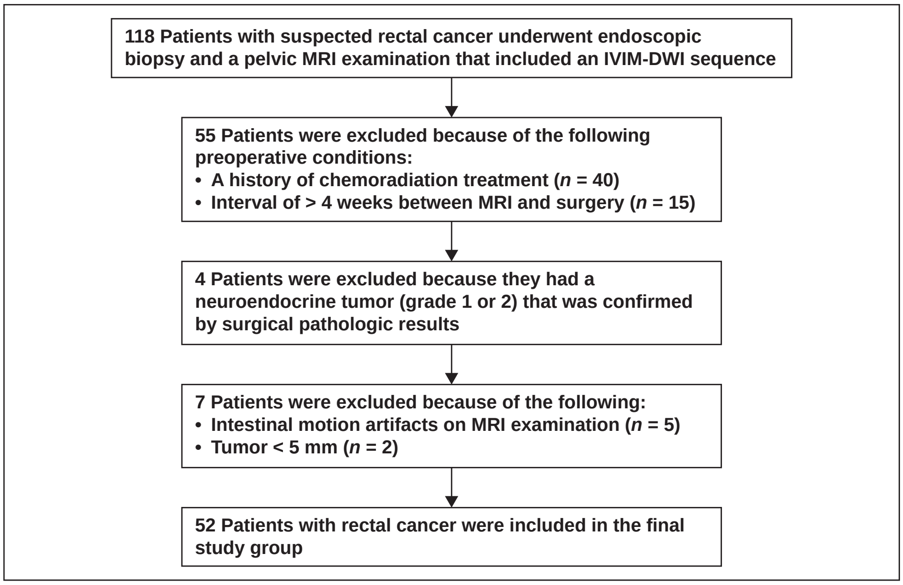
118 Patients with suspected rectal cancer underwent endoscopic biopsy and a pelvic MRI examination that included an IVIM-DWI sequence
55 Patients were excluded because of the following preoperative conditions:
• A history of chemoradiation treatment (n = 40)
• Interval of > 4 weeks between MRI and surgery (n = 15)
4 Patients were excluded because they had a neuroendocrine tumor (grade 1 or 2) that was confirmed by surgical pathologic results
7 Patients were excluded because of the following:
• Intestinal motion artifacts on MRI examination (n = 5)
• Tumor < 5 mm (n = 2)
52 Patients with rectal cancer were included in the final study group

Fig. 1—Flowchart shows subject selection process and exclusion criteria. IVIM = intravoxel incoherent motion.

Downloaded from www.ajronline.org by Tufts University on 02/18/18 from IP address 130.64.11.153. Copyright ARRS. For personal use only; all rights reserved

TABLE 1: Clinicopathologic Factors of 52 Patients With Rectal Cancer

Factors	Value
Age (y), mean ± SD	59.5 ± 13.7
Sex, no. (%) of patients	
Male	30 (57.7)
Female	22 (42.3)
Lesion length (cm), mean ± SD	4.9 ± 1.5
Location[a], no. (%) of patients	
Upper (> 10 cm)	12 (23.1)
Middle (5–10 cm)	25 (48.1)
Lower (< 5 cm)	15 (28.8)
Tumor grade, no. (%) of patients	
Well differentiated	14 (26.9)
Moderately differentiated	22 (42.3)
Poorly differentiated	16 (30.8)
Tumor stage, no. (%) of patients	
Stage I	17 (32.7)
Stage II	19 (36.5)
Stage III	11 (21.2)
Stage IV	5 (9.6)
Surgical procedure, no. (%) of patients	
Dixon surgery	35 (67.3)
Miles operation	13 (25.0)
Hartmann surgery	4 (7.7)

[a] Location is the distance from the inferior part of the tumor to the anal verge.

$$S_b / S_0 = (1 - f) \exp(-bD) + f \exp(-bD^*),$$

where S_b is the signal intensity at a given b value, S_0 is the signal intensity for a b value of 0 s/mm^2, and b is the b value. Two experienced radiologists (10 and 8 years' experience in gastrointestinal imaging) who were blinded to the histologic results independently drew the ROI manually on all consecutive tumor slices of the DW images (b value = 1000 s/mm^2). Once the polygonal ROI was drawn along the border of the high-signal-intensity area comprising the tumor to cover the entire tumor area on images obtained with a b value of 1000 s/mm^2, the position of the ROI was automatically placed on IVIM parametric maps. All ROIs were carefully defined not to involve necrosis by referring to T2-weighted imaging. The parameters of the ROIs on all slices (mean, 11 ± 3 slices; range, 5–20 slices) were averaged across all pixels in the ROIs (Fig. 2).

The imaging indicators were CRM, EMVI, and bowel circumferential invasion [37]. A positive CRM was defined as a tumor or suspicious lymph node lying within 1 mm of the mesorectal fascia. EMVI was considered positive if a suspicious tumor with intermediate signal intensity within the vessels was located beyond the muscularis propria in the mesorectal fat. Bowel circumferential invasion was assessed in the short axial plane; for this assessment, the bowel was divided into quarters: C1 indicated that the invasion was ≤ 1/4 of the bowel circumference; C2, > 1/4 and ≤ 1/2 of the bowel circumference; C3, > 1/2 and ≤ 3/4 of the bowel circumference; and C4, > 3/4 of the bowel circumference. Two gastrointestinal radiologists who were blinded to the patients' clinical and pathologic information independently reviewed the MRI studies for the status of CRM, EMVI, and bowel circumferential invasion. Discrepancies were resolved at a third analysis session during which a decision was reached by consensus of the two radiologists.

Pathology Evaluation

Surgical pathology results of all patients were analyzed by a pathologist with 6 years' experience in gastrointestinal pathologic diagnosis. Specimens were prepared into 5-mm slices. Then, the pathologic type, tumor differentiation (well differentiated, moderately differentiated, or poorly dif-

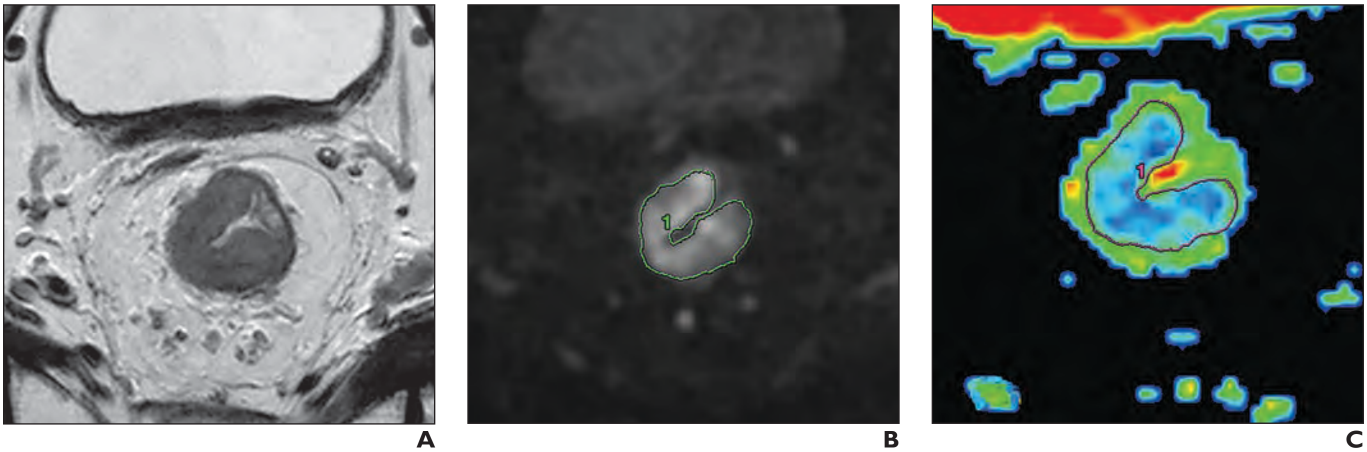

Fig. 2—67-year-old man with newly diagnosed poorly differentiated rectal cancer (stage II; location, middle).
A, Axial T2-weighted image.
B, DW image obtained using b value of 1000 s/mm^2 shows ROI (1, *green outline*) of tumor.
C, Pure diffusion color map shows ROI (1, *outline*) of tumor.

(Fig. 2 continues on next page)

Downloaded from www.ajronline.org by Tufts University on 02/18/18 from IP address 130.64.11.153. Copyright ARRS. For personal use only; all rights reserved

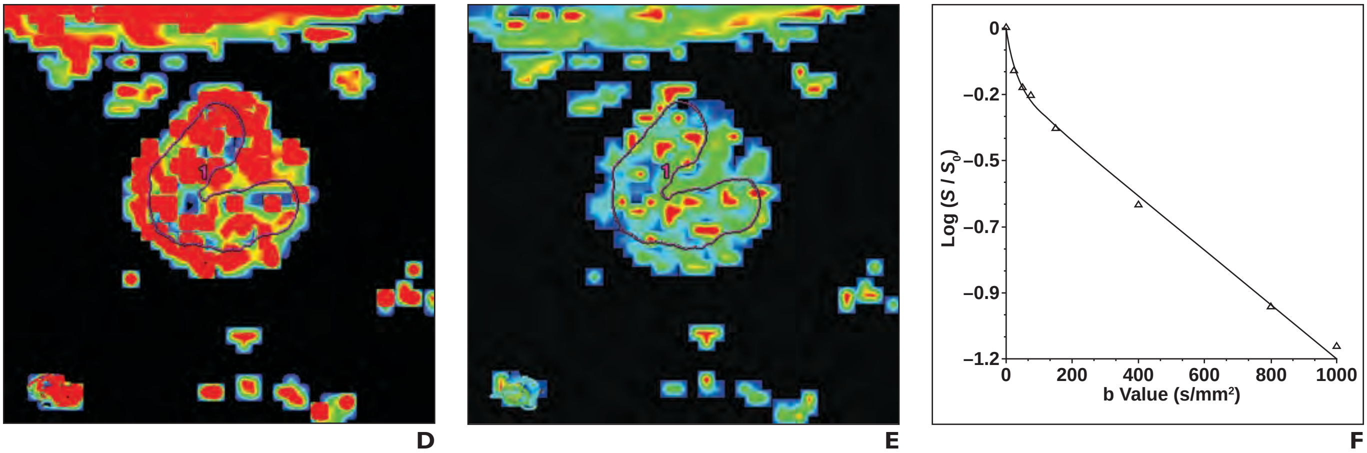

Fig. 2 (continued)—67-year-old man with newly diagnosed poorly differentiated rectal cancer (stage II; location, middle).
D, Pseudodiffusion coefficient color map shows ROI (1, *outline*) of tumor.
E, Perfusion fraction color map shows ROI (1, *outline*) of tumor.
F, Analysis curve based on biexponential model; *x*-axis shows b values, and *y*-axis shows logarithm of relative signal intensities, where S is signal intensity and S_0 is signal intensity for b value of 0 s/mm^2.

ferentiated), tumor stage (according to the 7th edition of the American Joint Committee on Cancer [AJCC] TNM staging system) [38], and the presence of lymph node metastases were evaluated.

Clinical Indicators

Clinical indicators including the plasma levels of CEA and CA19-9 before surgery were recorded. A CEA value of ≥ 5 ng/mL and a CA19-9 value of ≥ 27 U/mL were considered elevated.

Statistical Analysis

Statistical analysis was performed using statistical software (SPSS, version 17.0 for Microsoft Windows, IBM). The reproducibility of IVIM-MRI–derived parameters between different observers was evaluated using intraclass correlation coefficients (ICCs) and Bland-Altman limits of agreement. ICC values less than 0.40 were taken to indicate poor reproducibility, whereas those ranging from 0.40 to 0.59 were considered to indicate fair reproducibility, those ranging from 0.60 to 0.74 to indicate good reproducibility, and those 0.75 or greater to indicate excellent reproducibility. ANOVA analysis was used to compare IVIM-MRI–derived parameters among the various tumor grades, AJCC tumor stages, and bowel circumferential invasion levels (i.e., C1–C4). The relationships between IVIM parameters and pathology results (tumor differentiation degrees and AJCC tumor stages) and bowel circumferential invasion were evaluated through Spearman correlation analysis. Considering the limited number of subjects with stage IV tumors, patients with stage IV tumors and those with stage III tumors were merged to become one group to be analyzed using the ANOVA and Spearman correlation analysis. Independent-samples *t* test and Mann-Whitney *U* test were conducted to test the differences between groups with positive and negative findings for lymph node metastases, normal and elevated CEA values, normal and elevated CA19-9 values, positive and negative CRM, and positive and negative findings for EMVI. A $p < 0.05$ was considered statistically significant.

Results

Interobserver Agreement

Excellent interobserver agreement was obtained for the IVIM-MRI–derived parameters ADC, pure diffusion coefficient, perfusion fraction, and pseudodiffusion coefficient, with ICC values ranging from 0.9309–0.9767, 0.9844–0.9948, 0.9437–0.9811, and 0.9571–0.9857, respectively. According to Bland-Altman plots, the interobserver 95% limits of consistency of the IVIM-MRI–derived parameters (ADC, pure diffusion coefficient, perfusion fraction, and pseudodiffusion coefficient) were –8.9% to 9.0%, –11.7% to 9.7%, –14.1% to 11.5%, and –16.7% to 17.8%, respectively.

Correlation Between Intravoxel Incoherent Motion DWI Parameters and Tumor Grades

Fourteen cases of well-differentiated, 22 cases of moderately differentiated, and 16 cases of poorly differentiated tumors were confirmed by the pathology results. IVIM-MRI–derived parameters tended to rise with higher degree of tumor differentiation (Table 2). The ADC, pseudodiffusion coefficient, and perfusion fraction exhibited statistically significant differences ($p < 0.01$, $p < 0.05$, $p < 0.01$, respectively) among different tumor grades and were moderately correlated ($r = 0.520$, $p < 0.001$; $r = 0.447$, $p = 0.001$; and $r = 0.354$, $p = 0.010$, respectively) with tumor grades. The post hoc analysis in ANOVA was

TABLE 2: Intravoxel Incoherent Motion (IVIM) DWI–Derived Parameters of Rectal Cancers by Tumor Grade

	Tumor Grade			
IVIM-DWI Parameters	Well Differentiated	Moderately Differentiated	Poorly Differentiated	*p*
ADC (× 10^{-3} mm^2/s)	0.65 ± 0.09	0.57 ± 0.07	0.54 ± 0.10	< 0.01
Pure diffusion coefficient (× 10^{-3} mm^2/s)	0.79 ± 0.45	0.75 ± 0.30	0.74 ± 0.39	0.92
Perfusion fraction (%)	32.54 ± 6.91	25.83 ± 5.90	23.67 ± 5.69	< 0.01
Pseudodiffusion coefficient (× 10^{-3} mm^2/s)	91.89 ± 32.35	73.05 ± 20.55	67.40 ± 26.53	< 0.05

Note—Data are shown as mean ± SD. ADC = apparent diffusion coefficient.

Downloaded from www.ajronline.org by Tufts University on 02/18/18 from IP address 130.64.11.153. Copyright ARRS. For personal use only; all rights reserved

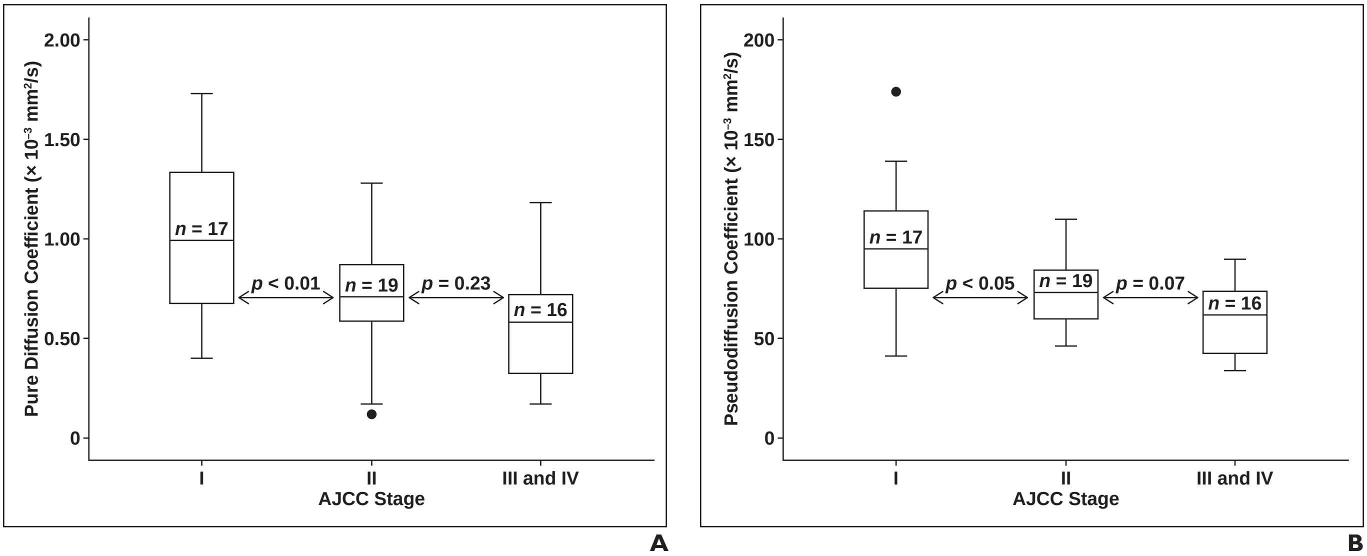

Fig. 3—Box plots.
A and **B**, Box plots of pure diffusion coefficients (**A**) and pseudodiffusion coefficients (**B**) in different tumor stages according to 7th edition of the American Joint Committee on Cancer (AJCC) TNM staging system [38]. Top and bottom of boxes are first and third quartiles, respectively. Length of box represents interquartile range within which 50% of values were located. Midline within box represents median value. Cross lines above and below mark maximum and minimum values, respectively. Data points (●) outside box are outliers and are smaller than lower quartile minus 1.5 times interquartile range or larger than upper quartile plus 1.5 times interquartile range.

selected to evaluate the differences between subgroups of tumor grade. We found that the ADC value of well-differentiated tumors was higher than that of moderately differentiated ($p < 0.05$) and poorly differentiated ($p < 0.05$) tumors, and similar differences between tumor grades were observed for the pseudodiffusion coefficient values (well differentiated vs moderately differentiated, $p < 0.05$; well differentiated vs poorly differentiated, $p < 0.05$) and perfusion fraction values (well differentiated vs moderately differentiated, $p < 0.01$; well differentiated vs poorly differentiated, $p < 0.001$). However, no significant differences in these parameters were seen between moderately differentiated tumors and poorly differentiated tumors ($p = 0.28$ for ADC, $p = 0.51$ for pseudodiffusion coefficient, and $p = 0.29$ for perfusion fraction).

Correlation Between Intravoxel Incoherent Motion MRI–Derived Parameters and the Presence of Lymph Node Metastases

Lymph node metastases were present in 16 of the 52 patients. Patients with metastases had lower values than patients without metastases for the following parameters: ADC (mean, 0.56 ± 0.07 vs 0.59 ± 0.10 × 10^{-3} mm^2/s), pure diffusion coefficient (0.56 ± 0.29 vs 0.85 ± 0.36 × 10^{-3} mm^2/s), perfusion fraction (24.35% ± 7.16% vs 28.14% ± 6.65%), and pseudodiffusion coefficient values (59.06 ± 16.44 vs 84.08 ± 27.74 × 10^{-3} mm^2/s). Significant differences were observed in the pure diffusion coefficient ($p < 0.01$) and pseudodiffusion coefficient ($p < 0.01$).

Correlation Between Intravoxel Incoherent Motion MRI–Derived Parameters and Tumor Stage

Seventeen cases of stage I, 19 cases of stage II, 11 cases of stage III, and five cases of stage IV tumors were confirmed according to the seventh edition of AJCC tumor staging system [38].

The pure diffusion coefficient and pseudodiffusion coefficient showed statistically significant differences among different stages ($p < 0.01$; $p < 0.001$) and were moderately correlated ($r = 0.479$; $r = 0.517$) with different stages. The post hoc analysis using ANOVA was selected to determine the differences between subgroups of tumor stage. We found that the pure diffusion coefficient of stage I tumors was higher than that of stage II tumors ($p < 0.01$) and stage III and IV tumors ($p < 0.01$), but the pure diffusion coefficients showed no significant difference between the latter two subgroups ($p = 0.23$) (Fig. 3A). Similar differences were observed in pseudodiffusion coefficient (stage I vs stage II, $p < 0.05$; stage I vs stages III and IV, $p < 0.05$; stage II vs stages III and IV, $p = 0.07$) between subgroups of tumor stage (Fig. 3B). However, ADC and perfusion fraction values showed no statistically significant differences among the subgroups of tumor stages ($p = 0.33$; $p = 0.26$).

Correlation Between Intravoxel Incoherent Motion MRI–Derived Parameters and Carcinoembryonic Antigen and Cancer Antigen 19-9 Values

There was no statistically significant difference in IVIM-MRI–derived parameters between patients with a normal CEA value ($n = 35$) and those with a high CEA value ($n = 17$), or between patients with a normal CA19-9 value ($n = 41$) and those with a high CA19-9 value ($n = 11$). However, the ADC, pure diffusion coefficient, perfusion fraction, and pseudodiffusion coefficient tended to be lower in patients with a high CEA value and those with a high CA19-9 value than in patients with normal values (Table 3).

Correlation of Intravoxel Incoherent Motion MRI–Derived Parameters With Circumferential Resection Margin, Extramural Vascular Invasion, and Circumferential Involvement

There was no statistically significant difference in IVIM-MRI–derived parameters between groups with positive and negative CRM: ADC, 0.58 ± 0.10 versus 0.59 ± 0.07 × 10^{-3} mm^2/s; pure diffusion coefficient, 0.74 ± 0.38 versus 0.77 ± 0.37 × 10^{-3} mm^2/s; perfusion fraction, 27.71% ± 6.94% versus 25.15% ± 6.91%; and pseudodiffusion coefficient, 74.63 ± 24.66 versus 80.71 ± 33.42 × 10^{-3} mm^2/s. The pseudodiffusion coefficient value of patients with positive EMVI was lower than that in patients with no EMVI ($p <$

Downloaded from www.ajronline.org by Tufts University on 02/18/18 from IP address 130.64.11.153. Copyright ARRS. For personal use only; all rights reserved

TABLE 3: Intravoxel Incoherent Motion (IVIM) DWI–Derived Parameters of Rectal Cancers by Preoperative Plasma Carcinoembryonic Antigen (CEA) Level and Cancer Antigen 19-9 (CA19-9) Level

IVIM-DWI Parameters	High CEA Value (n = 17)	Normal CEA Value (n = 35)	p	High CA19-9 Value (n = 11)	Normal CA19-9 Value (n = 41)	p
ADC (× 10^{-3} mm^2/s)	0.56 ± 0.06	0.59 ± 0.11	0.31	0.58 ± 0.03	0.58 ± 0.11	0.78
Pure diffusion coefficient (× 10^{-3} mm^2/s)	0.67 ± 0.31	0.80 ± 0.39	0.22	0.63 ± 0.29	0.80 ± 0.38	0.18
Perfusion fraction (%)	24.46 ± 5.80	28.19 ± 7.23	0.07	25.00 ± 7.55	27.50 ± 6.80	0.54
Pseudodiffusion coefficient (× 10^{-3} mm^2/s)	71.59 ± 21.56	78.71 ± 29.66	0.38	71.90 ± 21.54	77.59 ± 78.73	0.55

Note—Data are shown as mean ± SD. A CEA value of ≥ 5 ng/mL was considered to be high, and a CA19-9 value of ≥ 27 U/mL was considered to be high. ADC = apparent diffusion coefficient.

0.05). There was no statistically significant difference between the patients with EMVI and the patients with no EMVI for the following parameters: ADC (0.57 ± 0.08 vs 0.59 ± 0.10 ×10^{-3} mm^2/s), pure diffusion coefficient (0.75 ± 0.36 vs 0.79 ± 0.40×10^{-3} mm^2/s), and perfusion fraction (27.26% ± 7.28% vs 26.27% ± 6.29%). Patients with C1 involvement (n = 2) were grouped with patients with C2 involvement (n = 16) because of the limited number of patients with C1 involvement. There was no statistically significant difference in IVIM-MRI–derived parameters between patients with different levels of bowel circumferential invasion (Table 4).

Discussion

IVIM theory suggests that the signal intensity of DWI comes not only from the diffusion of free water in the intercellular space but also from the perfusion of the blood capillary network. The diffusion component has a larger weighting factor when a higher b value is used. Sun et al. [22] reported that the ADC value in single-exponential DWI performed with a b value of 800 s/mm^2 is about 1.20–1.53 × 10^{-3} mm^2/s for rectal adenocarcinoma. Curvo-Semedo et al. [24] reported that the ADC value of rectal tubular adenocarcinoma derived for the single-exponential model with b values of 0, 500, and 1000 s/mm^2 is about 0.98–1.32 × 10^{-3} mm^2/s. To eliminate the influence of perfusion, Ha et al. [23] used a combination of b values (i.e., 150 and 1000 s/mm^2) to calculate the ADC in their work and got an ADC value of 0.43–0.63 × 10^{-3} mm^2/s. These previous studies have indicated that the ADC value in the single-exponential DWI model varies with different b value settings and that ADC values are not consistent between studies because equipment from different vendors was used [22–26]. The ADC value decreases with higher b values because of the lower perfusion-weighted factor. IVIM theory using the biexponential DWI model not only has the ability to provide the perfusion fraction and pseudodiffusion coefficient as parameters that reflect perfusion but also can provide the pure diffusion coefficient as a parameter of the pure diffusion of free water [28].

Although few applications of IVIM-DWI in patients with rectal cancer have been published in the literature to our knowledge, the ADC value derived from the single-exponential model has already been applied to the grading of rectal cancer with mixed results [22, 24, 25]. No statistically significant difference was observed by Elmi et al. [26], although nonzero b values were used to calcu-

TABLE 4: Intravoxel Incoherent Motion DWI–Derived Parameters of Rectal Cancers by the Status of the Circumferential Resection Margin (CRM), Presence of Extramural Vascular Invasion (EMVI), and Extent of Bowel Circumferential Involvement

Imaging Indicators	ADC (× 10^{-3} mm^2/s)	p	Pure Diffusion Coefficient (× 10^{-3} mm^2/s)	p	Perfusion Fraction (%)	p	Pseudodiffusion Coefficient (× 10^{-3} mm^2/s)	p
CRM[a]		0.81		0.77		0.47		0.23
Positive (n = 15)	0.58 ± 0.10		0.74 ± 0.38		27.71 ± 6.94		74.63 ± 24.66	
Negative (n = 37)	0.59 ± 0.07		0.77 ± 0.37		25.15 ± 6.91		80.71 ± 33.42	
EMVI[b]		0.58		0.69		0.65		< 0.05
Positive (n = 17)	0.57 ± 0.08		0.75 ± 0.36		27.26 ± 7.28		70.72 ± 25.86	
Negative (n = 35)	0.59 ± 0.10		0.79 ± 0.40		26.27 ± 6.29		90.35 ± 26.39	
Bowel circumferential involvement[c]		0.24		0.63		0.89		0.49
C1 and C2 (n = 18)[d]	0.61 ± 0.08		0.83 ± 0.38		27.87 ± 7.50		83.55 ± 29.37	
C3 (n = 21)	0.56 ± 0.11		0.65 ± 0.37		26.99 ± 6.94		66.23 ± 22.31	
C4 (n = 13)	0.59 ± 0.09		0.84 ± 0.32		25.71 ± 6.59		82.85 ± 28.39	

Note—Data are shown as mean ± SD. ADC = apparent diffusion coefficient.

[a] A positive CRM was defined as a tumor or suspicious lymph node lying within 1 mm of the mesorectal fascia.

[b] EMVI was considered positive if a suspicious tumor with intermediate signal intensity within the vessels was located beyond the muscularis propria in the mesorectal fat.

[c] C1 indicated that the invasion was ≤ 1/4 of the bowel circumference; C2, > 1/4 and ≤ 1/2 of the bowel circumference; C3, > 1/2 and ≤ 3/4 of the bowel circumference; and C4, > 3/4 of the bowel circumference.

[d] Patients with C1 involvement (n = 2) were grouped with patients with C2 involvement (n = 16) because of the limited number of patients with C1 involvement.

Downloaded from www.ajronline.org by Tufts University on 02/18/18 from IP address 130.64.11.153. Copyright ARRS. For personal use only; all rights reserved

late the ADC in another study [30]. That result may have been caused by the mixing of data from different scanners and different b values. Curvo-Semedo et al. [24] have reported that the ADC is lower with less differentiated rectal tumors ($p = 0.025$), and the same trend was evident in the study by Sun et al. [22] but with no statistically significant difference. In our study, the perfusion-related parameters perfusion fraction and pseudodiffusion coefficient showed statistically significant differences between tumor differentiation groups ($F = 8.503$, $p = 0.001$; $F = 3.635$, $p = 0.034$) and showed some correlation among differentiation groups ($r = 0.447$, $p = 0.001$; $r = 0.354$, $p = 0.010$). Although the pure diffusion coefficient also showed a decreasing trend along with poorer differentiation, there was no statistically significant difference between tumor differentiation groups. These findings confirming that there is no significant difference in water diffusion between tumor differentiation groups are consistent with previous work [39]. A previously reported positive correlation can be explained by the effect of a low b value setting on perfusion [40].

In the current study, the pseudodiffusion coefficient and perfusion fraction increased with greater tumor differentiation. According to IVIM theory [28], the pseudodiffusion coefficient (D^*) is related to perfusion according to the following equation:

$$D^* = (l \times v) / 6,$$

where l means the length of the capillary segment and v is the average velocity of blood in the capillary [41]. According to Le Bihan et al. [28], the perfusion fraction is the partial volume of the whole capillary vascular fraction, and Duong and Kim [40] further suggested that the component of the arterial blood played a more vital role than the venous component for the parameter perfusion fraction at low b values. Thus, the correlation between perfusion-related parameters and tumor differentiation may indicate that the capillary vascular network is relatively well developed in well-differentiated tumors. This result is consistent with previous findings using perfusion CT [42–44]. In poorly differentiated tumors, the tumor cells grow very fast, leading to poor structure of lumenized vessels, which results in less perfusion of the microcirculation. This phenomenon is reflected in lower perfusion-related parameters, such as the pseudodiffusion coefficient and perfusion fraction, in poorly differentiated tumors. Recent studies have shown some correlation among the pseudodiffusion coefficient, perfusion fraction, and microvessel density in CRC tumors, confirming that IVIM parameters may provide important information for assessing tumor grade and other biologic features in patients with CRC [34, 35]. The TE—that is, the time between giving the radiofrequency pulse and the peak of the echo signal—is a factor that can affect the value of the perfusion fraction [45]. However, this effect would not have any impact on our conclusions because the same TE was used in every patient in our study.

Many studies have focused on the staging of rectal cancer using DWI. Curvo-Semedo et al. [24] reported that there was no correlation between the average ADC value of tumors and T stages or CEA values. On the other hand, Sun et al. [22] observed that ADC values decreased with higher tumor stages. In our study, ADC results showed a similar trend. However, our results also showed that there were statistically significant differences between different stages in both the pure diffusion and pseudodiffusion coefficient values, both of which were negatively correlated with the stages. In addition, the pure diffusion and pseudodiffusion coefficient values of tumors were lower in patients with lymph node metastases than in those without metastases, and similar findings, using ADC values, have been reported not only in rectal cancer [46], but also in nasopharyngeal carcinoma [33]. These results suggest that tumors with lower ADC, pure diffusion, and pseudodiffusion coefficient values might exhibit more aggressive biologic behavior.

The tumor marker level is one of the most important factors affecting prognosis [9, 10]. Although no statistically significant difference in DWI-derived parameters between patients with and those without increased CEA and CA19-9 levels was found in this study, all of the these parameters showed a decreasing trend with the rise of CEA and CA19-9 levels. EMVI is an important imaging marker for surgery, because it can indicate that the tumor has broken through the muscularis propria [13–15, 17, 37]. In this study, the pseudodiffusion coefficient was lower in patients with positive EMVI than in those with no EMVI. These results are consistent with other tumor staging data, which also showed that tumors of an advanced stage had lower pseudodiffusion coefficient values. Further research is needed to evaluate the prognostic value of IVIM-DWI parameters compared with existing tumor markers and other imaging indicators.

Our study had some limitations. One limitation is the selection bias that may have been caused by the fact that patients were limited to those who would undergo surgery without a history of radiation or chemotherapy. Another limitation is the small sample size, especially for some groups. This may be the reason that only a trend has been seen in several correlation analyses, without statistically significant differences. Further work with a larger sample size may reveal more statistically significant results. Third, considering the limited signal-to-noise ratio in DW images, a different slice thickness and gap were adopted for axial T2-weighted images and IVIM sequences. This difference in settings may result in a lack of direct comparison between the two sequences and may limit identification of areas of necrosis slice by slice. Moreover, tumor necrosis would be better observed on contrast-enhanced T1-weighted imaging [47, 48], which was not included in this study, than on T2-weighted imaging. Finally, the way in which the ROIs are drawn is critical in IVIM-DWI because of the huge variations in the parameters [49]: A single small ROI may highlight the extrema, whereas a large ROI can reduce the variation by averaging. The whole-tumor consecutive slices were chosen in this work to balance the representation and variation. Only the biexponential model was used in this work because its feasibility has already been tested widely. The ideal image-processing methodology to describe lesion heterogeneity, such as parameter histogram descriptors, should be explored in future studies.

In conclusion, IVIM parameters showed a decreasing trend with increasing tumor stages and grades in rectal cancer and could possibly provide useful information about diffusion and perfusion, which can be helpful in predicting tumor aggressiveness and prognosis.

References

1. Torre LA, Bray F, Siegel RL, Ferlay J, Lortet-Tieulent J, Jemal A. Global cancer statistics, 2012. *CA Cancer J Clin* 2015; 65:87–108
2. Brenner H, Kloor M, Pox CP. Colorectal cancer. *Lancet* 2014; 383:1490–1502
3. Bown EJ, Lloyd GM, Boyle KM, Miller AS. Rectal cancer: prognostic indicators of long-term outcome in patients considered for surgery. *Int J Colorectal Dis* 2014; 29:147–155
4. Wibe A, Law WL, Fazio V, Delaney CP. Tailored

Downloaded from www.ajronline.org by Tufts University on 02/18/18 from IP address 130.64.11.153. Copyright ARRS. For personal use only; all rights reserved

rectal cancer treatment: a time for implementing contemporary prognostic factors? *Colorectal Dis* 2013; 15:1333–1342

5. Sebag-Montefiore D, Stephens RJ, Steele R, et al. Preoperative radiotherapy versus selective postoperative chemoradiotherapy in patients with rectal cancer (MRC CR07 and NCIC-CTG C016): a multicentre, randomised trial. *Lancet* 2009; 373:811–820
6. Sauer R, Becker H, Hohenberger W, et al. Preoperative versus postoperative chemoradiotherapy for rectal cancer. *N Engl J Med* 2004; 351:1731–1740
7. Sauer R, Liersch T, Merkel S, et al. Preoperative versus postoperative chemoradiotherapy for locally advanced rectal cancer: results of the German CAO/ARO/AIO-94 randomized phase III trial after a median follow-up of 11 years. *J Clin Oncol* 2012; 30:1926–1933
8. Vecchio FM, Valentini V, Minsky BD, et al. The relationship of pathologic tumor regression grade (TRG) and outcomes after preoperative therapy in rectal cancer. *Int J Radiat Oncol Biol Phys* 2005; 62:752–760
9. Lee JH, Kim SH, Jang HS, et al. Preoperative elevation of carcinoembryonic antigen predicts poor tumor response and frequent distant recurrence for patients with rectal cancer who receive preoperative chemoradiotherapy and total mesorectal excision: a multi-institutional analysis in an Asian population. *Int J Colorectal Dis* 2013; 28:511–517
10. Vukobrat-Bijedic Z, Husic-Selimovic A, Sofic A, et al. Cancer antigens (CEA and CA 19-9) as markers of advanced stage of colorectal carcinoma. *Med Arch* 2013; 67:397–401
11. Park JS, Huh JW, Park YA, et al. A circumferential resection margin of 1 mm is a negative prognostic factor in rectal cancer patients with and without neoadjuvant chemoradiotherapy. *Dis Colon Rectum* 2014; 57:933–940
12. Nikberg M, Kindler C, Chabok A, Letocha H, Shetye J, Smedh K. Circumferential resection margin as a prognostic marker in the modern multidisciplinary management of rectal cancer. *Dis Colon Rectum* 2015; 58:275–282
13. Courtney ED, West NJ, Kaur C, et al. Extramural vascular invasion is an adverse prognostic indicator of survival in patients with colorectal cancer. *Colorectal Dis* 2009; 11:150–156
14. Bugg WG, Andreou AK, Biswas D, Toms AP, Williams SM. The prognostic significance of MRI-detected extramural venous invasion in rectal carcinoma. *Clin Radiol* 2014; 69:619–623
15. Sohn B, Lim JS, Kim H, et al. MRI-detected extramural vascular invasion is an independent prognostic factor for synchronous metastasis in patients with rectal cancer. *Eur Radiol* 2015; 25:1347–1355
16. Kim JE, Lee JM, Baek JH, et al. Differentiation of poorly differentiated colorectal adenocarcinomas from well- or moderately differentiated colorectal adenocarcinomas at contrast-enhanced multidetector CT. *Abdom Imaging* 2015; 40:1–10
17. Tong T, Yao Z, Xu L, et al. Extramural depth of tumor invasion at thin-section MR in rectal cancer: associating with prognostic factors and ADC value. *J Magn Reson Imaging* 2014; 40:738–744
18. Cho SH, Kim SH, Bae JH, et al. Prognostic stratification by extramural depth of tumor invasion of primary rectal cancer based on the Radiological Society of North America proposal. *AJR* 2014; 202:1238–1244
19. de Jong EA, ten Berge JC, Dwarkasing RS, Rijkers AP, van Eijck CH. The accuracy of MRI, endorectal ultrasonography, and computed tomography in predicting the response of locally advanced rectal cancer after preoperative therapy: a metaanalysis. *Surgery* 2016; 159:688–699
20. Tsai C, Hague C, Xiong W, et al. Evaluation of endorectal ultrasound (ERUS) and MRI for prediction of circumferential resection margin (CRM) for rectal cancer. *Am J Surg* 2017; 213:936–942
21. Koh DM, Collins DJ. Diffusion-weighted MRI in the body: applications and challenges in oncology. *AJR* 2007; 188:1622–1635
22. Sun Y, Tong T, Cai S, Bi R, Xin C, Gu Y. Apparent diffusion coefficient (ADC) value: a potential imaging biomarker that reflects the biological features of rectal cancer. *PLoS One* 2014; 9:e109371
23. Ha HI, Kim AY, Yu CS, Park SH, Ha HK. Locally advanced rectal cancer: diffusion-weighted MR tumour volumetry and the apparent diffusion coefficient for evaluating complete remission after preoperative chemoradiation therapy. *Eur Radiol* 2013; 23:3345–3353
24. Curvo-Semedo L, Lambregts DM, Maas M, Beets GL, Caseiro-Alves F, Beets-Tan RG. Diffusion-weighted MRI in rectal cancer: apparent diffusion coefficient as a potential noninvasive marker of tumor aggressiveness. *J Magn Reson Imaging* 2012; 35:1365–1371
25. Akashi M, Nakahusa Y, Yakabe T, et al. Assessment of aggressiveness of rectal cancer using 3-T MRI: correlation between the apparent diffusion coefficient as a potential imaging biomarker and histologic prognostic factors. *Acta Radiol* 2014; 55:524–531
26. Elmi A, Hedgire SS, Covarrubias D, Abtahi SM, Hahn PF, Harisinghani M. Apparent diffusion coefficient as a non-invasive predictor of treatment response and recurrence in locally advanced rectal cancer. *Clin Radiol* 2013; 68:e524–e531
27. Nougaret S, Vargas HA, Lakhman Y, et al. Intravoxel incoherent motion-derived histogram metrics for assessment of response after combined chemotherapy and radiation therapy in rectal cancer: initial experience and comparison between single-section and volumetric analyses. *Radiology* 2016; 280:446–454
28. Le Bihan D, Breton E, Lallemand D, Aubin ML, Vignaud J, Laval-Jeantet M. Separation of diffusion and perfusion in intravoxel incoherent motion MR imaging. *Radiology* 1988; 168:497–505
29. Hu YC, Yan LF, Wu L, et al. Intravoxel incoherent motion diffusion-weighted MR imaging of gliomas: efficacy in preoperative grading. *Sci Rep* 2014; 4:7208
30. Hwang EJ, Lee JM, Yoon JH, et al. Intravoxel incoherent motion diffusion-weighted imaging of pancreatic neuroendocrine tumors: prediction of the histologic grade using pure diffusion coefficient and tumor size. *Invest Radiol* 2014; 49:396–402
31. Kuru TH, Roethke MC, Stieltjes B, et al. Intravoxel incoherent motion (IVIM) diffusion imaging in prostate cancer: what does it add? *J Comput Assist Tomogr* 2014; 38:558–564
32. Woo S, Lee JM, Yoon JH, Joo I, Han JK, Choi BI. Intravoxel incoherent motion diffusion-weighted MR imaging of hepatocellular carcinoma: correlation with enhancement degree and histologic grade. *Radiology* 2014; 270:758–767
33. Lai V, Li X, Lee VH, et al. Nasopharyngeal carcinoma: comparison of diffusion and perfusion characteristics between different tumour stages using intravoxel incoherent motion MR imaging. *Eur Radiol* 2014; 24:176–183
34. Lee HJ, Rha SY, Chung YE, et al. Tumor perfusion-related parameter of diffusion-weighted magnetic resonance imaging: correlation with histological microvessel density. *Magn Reson Med* 2014; 71:1554–1558
35. Surov A, Meyer HJ, Höhn AK, et al. Correlations between intravoxel incoherent motion (IVIM) parameters and histological findings in rectal cancer: preliminary results. *Oncotarget* 2017; 8:21,974–21,983
36. Sun H, Xu Y, Xu Q, Shi K, Wang W. Rectal cancer: short-term reproducibility of intravoxel incoherent motion parameters in 3.0T magnetic resonance imaging. *Medicine (Baltimore)* 2017; 96:e6866
37. Nougaret S, Reinhold C, Mikhael HW, Rouanet P, Bibeau F, Brown G. The use of MR imaging in treatment planning for patients with rectal carcinoma: have you checked the “DISTANCE”? *Radiology* 2013; 268:330–344
38. Edge SB, Compton CC. The American Joint Committee on Cancer: the 7th edition of the AJCC cancer staging manual and the future of TNM. *Ann Surg Oncol* 2010; 17:1471–1474
39. Attenberger UI, Pilz LR, Morelli JN, et al. Multiparametric MRI of rectal cancer: do quantitative functional MR measurements correlate with radiologic and pathologic tumor stages? *Eur J Radiol* 2014; 83:1036–1043
40. Duong TQ, Kim SG. In vivo MR measurements of regional arterial and venous blood volume fractions in intact rat brain. *Magn Reson Med* 2000; 43:393–402
41. Guiu B, Petit JM, Capitan V, et al. Intravoxel inco-

Downloaded from www.ajronline.org by Tufts University on 02/18/18 from IP address 130.64.11.153. Copyright ARRS. For personal use only; all rights reserved

herent motion diffusion-weighted imaging in nonalcoholic fatty liver disease: a 3.0-T MR study. *Radiology* 2012; 265:96–103

42. Hayano K, Shuto K, Koda K, Yanagawa N, Okazumi S, Matsubara H. Quantitative measurement of blood flow using perfusion CT for assessing clinicopathologic features and prognosis in patients with rectal cancer. *Dis Colon Rectum* 2009; 52:1624–1629
43. Goh V, Halligan S, Wellsted DM, Bartram CI. Can perfusion CT assessment of primary colorectal adenocarcinoma blood flow at staging predict for subsequent metastatic disease? A pilot study. *Eur Radiol* 2009; 19:79–89
44. Sun H, Xu Y, Yang Q, Wang W. Assessment of tumor grade and angiogenesis in colorectal cancer: whole-volume perfusion CT. *Acad Radiol* 2014; 21:750–757
45. Lemke A, Laun FB, Simon D, Stieltjes B, Schad LR. An in vivo verification of the intravoxel incoherent motion effect in diffusion-weighted imaging of the abdomen. *Magn Reson Med* 2010; 64:1580–1585
46. Mizukami Y, Ueda S, Mizumoto A, et al. Diffusion-weighted magnetic resonance imaging for detecting lymph node metastasis of rectal cancer. *World J Surg* 2011; 35:895–899
47. Boss A, Martirosian P, Schraml C, et al. Morphological, contrast-enhanced and spin labeling perfusion imaging for monitoring of relapse after RF ablation of renal cell carcinomas. *Eur Radiol* 2006; 16:1226–1236
48. Breen MS, Lazebnik RS, Fitzmaurice M, Nour SG, Lewin JS, Wilson DL. Radiofrequency thermal ablation: correlation of hyperacute MR lesion images with tissue response. *J Magn Reson Imaging* 2004; 20:475–486
49. Andreou A, Koh DM, Collins DJ, et al. Measurement reproducibility of perfusion fraction and pseudodiffusion coefficient derived by intravoxel incoherent motion diffusion-weighted MR imaging in normal liver and metastases. *Eur Radiol* 2013; 23:428–434

协和医生访学日本，同样拼命工作的日本医生，待遇和我们有何不同?

海外访学 **好医生** 2018-10-01

好医生国际教育
专业 / 高效 / 低费 / 高质
出国访学 医路无忧

> 2017年4月有幸获得笹川奨学金资助，到日本冲绳“琉球大学医学研究科放射线诊断治疗学讲座”研修一年。

日本印象初体验

在来日本之前，我对冲绳的印象就只局限于“日本最南端的旅游城市”，另外因为历史上琉球王国的存在，对于这里有种莫名的好奇。

日本冲绳

冲绳包括许多离岛，与日本的本岛隔海相望，飞机行程大概两个半小时（羽田机场到那霸机场）。冲绳区域的公共交通远没有日本本岛便捷，出租车又超级贵，所以主要的交通工具其实是小汽车（私家车）。

冲绳单轨电车

我下了飞机，坐了一段单轨电车（モノレール）到达市中心之后，已经将近晚上十点，附近并没有直达琉球大学的公交车，山城先生把我安排到一家酒店住宿，等第二天让科里的椿本先生开车接我。

琉球大学附属医院所见所感

别有特色的"懇親会"

琉球大学附属医院紧挨着琉大医学部，与琉球大学校本部稍微有点距离。琉大附属医院病床床位大概是600，和国内的医学院校附属医院相比，规模并不是很大，但只此一家，别无分号。

琉大的医学生大五开始下临床实习，大六中期就选择自己中意的科室。也许因为医学生数目不是很多，各个科室对于实习轮转学生都十分重视。我所在的放射科医局会给实习的学生订餐，会一对一给学生讲解报告的书写以及疾病诊断问题。

琉球大学附属医院

此外为了让更多的学生能够选择本科室，大概**每年七月开始陆续举办各种“懇親会”，宣传介绍本科室。**当然只有“懇親会”这种官方宣传是不够的。这时候本科室去年新入职的“前辈们”，就成了亲善大使，会和这些大六的后辈们有着各种形式私下小聚会（费用医局给予报销），解答后辈的疑问，介绍科室优势，尽可能的为科室招揽新人。总之，**整体感觉医学生很抢手。**

对于入职新人，科室也是很大胆的委以重任。每年的“懇親会、忘年会”等都是由前一年入职的新人筹备。事无巨细，从海报，聚会安排【一般分为聚餐会（19:00-21:00），饮酒会（21:00-23:00）以及唱K三场（23:00以后）】，聚会地点预订，每个聚会时段人数变动的统计，甚至聚会地点转移Taxi预订都是由他们安排。所以新人们其实压力都很大，但正是这种方式，强而有力地将新人融入到科室集体中。

自我介绍是一种礼仪

到了琉大放射科之后，第一个感受，自我介绍很重要。第一天到放射科医局的时候，就发现在医局通知栏那个位置，贴着之前我和村山教授在会议上的合影，上面标注着我的名字以及我要来琉大的日期。

村山教授先带着我在全科上下转了一圈，紧接着就是各种场合的自我介绍，包括本科室每周例会，和别的医院一起举办的学术会议，以及年末的琉球放射年会。也正是这样，一次次正式场合的自我介绍，让我对自己的存在，莫名有了一种底气，不再畏惧人前说话。也许会有人说，因为你是外国人所以会这样。其实并不是，来科室轮转实习的学生、进修医生、新调来的医生，**大家都要在这样正式的场合一次次做自我介绍。对于日本人来说，好像这就是一项基本的礼仪。**

日本医院的仪式感

因为我的到来，科室的大BOSS村山教授办了一个欢迎会，聚餐的地方还特意选择了一个中华料理店（说来好笑，这是一个大阪人，在东京学艺，到冲绳开了一家中华料理店）。

来这边没多久，科室的奈々絵先生要去美国进修，同时岡田先生升迁到日本大学任教授，科室为两人举办了送别会（或者叫壮行会），壮行会上村山教授发言并送礼物。除了值班老师外，放射科几乎全员参加。

岡田先生（右一）的壮行会

从左至右依次是：椿本先生，村山教授，我，岡田先生

新年放假前（日本是按照阳历进行算，12月底到一月初，有1周的样子），在放射科休息室（医院内），几乎所有技师，大夫以及护士都集聚一起，搞了一个简单的年终聚会。教授和技师长简单总结一年工作，并和大家一起举杯，祝福大家新年快乐。年假结束，在相同的地方，大家又一起举杯迎接新一年的开始。

琉球大學医学部附属病院 忘年会

像这样无论是一个人的到来和离去，还是一年的开始和结束，日本人都会满怀真诚，认真对待。也许多年以后记不得中间的情节，但是在某个特别的节点，大家一

起欢笑，一起祝福，一起举杯的场景总会让人不自主想起，分外留恋。**用稍微郑重的方式，好好开始认真告别，感恩相遇，这是身边的日本人用行动告诉我的生活方式。**

拼命工作，放开玩

日本人工作很拼命，但是玩的时候也很放得开。
周一到周围五午餐时间（一个小时），会有读文献学习或者病例讨论。**中午不休息，边吃饭边学习，好像是种常态。**在国内一直是“中午不睡，下午崩溃”的我，刚到这边的时候，完全无法适应，全靠咖啡提神，后来好久才调整过来。日本国内年初到年末有各种大大小小的会议，不过这边的老师基本都有自己的研究方向，一般只挑选自己领域的会议参加。倒是教授会忙一些，他被邀请做各种大会的座长、发言人，经常出差。

我的带教山城先生，典型对工作“热衷”的人，一年365天几乎无休。聚会11点结束后，依然要去医局。黄金周大家放假，他坐飞机去南美开放射学年会。医局有个不是笑话的笑话，有人问：山城先生在干嘛？（不分时候），答：山城先生在写论文。如此调侃山城先生是工作狂。

话说自己还闹了一个笑话，日本开学术会议最后一般都会有个“情报交流会”，我最开始以为是属于学术交流会，穿的很正式，兴冲冲地跑去参加，后来发现其实就是聚餐，不过是自助餐形式，你可以边吃饭边和身边人搭讪。当然如果这时候你有看到心仪崇拜的教授或者老师，这是个绝佳的套磁机会。

但是无论平时多严肃的老师，到了聚会活动的时候好像都会换一个样子。**健谈，拼酒，甚至是乐器演奏，随手就来。**K歌一唱就到后半宿，然后东倒西歪的坐上计程车回家（真心为冲绳良好的治安点赞）。当然拼酒并不是男人的特权，这边医局的有两三位女老师酒量也是好的惊人，到了飲み会，豪饮的做派丝毫不输给男同事。**也许平时太一本正经，玩的时候又如此放得开，反差实在太有冲击力。**

放射科的日常点滴

第四点感触比较深的，与琉大附院放射科老师工作相关。

这边社区的基础医疗做的很好，重病疑难病才会被转送到琉大附院，所以和国内相比，这边放射科医生的临床工作量真算的上轻松。另外，周一到周五5个工作日中，有1.5天算是他们的个人的科研时间，由自己安排，因而他们相对有更多时间专心做科研方面的工作。

放射诊断、治疗、介入以及核医学都属于放射线科，每周三有疑难病例的集体讨论（包括上面各个方面的），放射科医师基本都会参加。讨论结束后，如果近期需要外出开会发言的老师，会将PPT提前试讲一下，然后由大家一起挑问题。经过这么集体的“审核”后，才会拿到外面讲演。

此外，在日本国内学会上发表的内容，日本老师更注重的是经验总结以及知识的传

承，而不是研究领域新技术相关探索性研究。这边老师带教都很耐心，无论是对实习学生还是新入职的后辈，一步步的讲解，直到你明白为止。我的带教老师山城先生平时不苟言笑，很是严肃，简直是移动的冰山，但只要是专业上的问题请教他，他会很耐心讲解，不会因为有其他事情要做就敷衍了事，在他看来这是他工作的一部分。

> PS. 有一次还认真地纠正了我的英文发音半天，感觉超级囧。他在美国波士顿进修过两年，英文比较纯正。

日中笹川医学奨学金制度
第39期研究者歓迎式典

39期笹川奨学金研修生合影

除此以外，其他的日本老师和staff给予了我很多帮助，感觉自己一直被温暖地“守护着”，经常被他们的小细节感动到。跟着椿本先生去超市大采购，跟随與儀先生参加与美国驻军医生的联谊Party，和城间女士观看首里城祭り并且吃到最地道的冲绳料理，一点一滴他们给予了我最大的善意和帮助。

当繁忙的工作按下暂停键

这次来日本的研修，就像给繁忙的临床工作按了一下暂停键。从有些疲懒的舒适区跳到了一个完全陌生环境里，从最初到手忙脚乱到后面的渐渐习惯，自己多多少少会受到周围日本老师的影响，也在潜移默化接受他们的一些理念。

无论是日本还是中国，医生都不是一个轻松的行业。虽然医疗制度不同，从业环境也有差异，但从周围日本老师身上，依然能够汲取适合自己的正能量，希望借此可以更顺畅的走好下面的路。

投稿来源：中日友好医院放射科 徐妍妍

后记

国外医疗有很多值得我们借鉴学习的地方，医院只有依赖高素质、高质量专业技术人才，才能综合提升医院核心竞争力和可持续发展潜力，最终造福患者。医生个人也只有抓住机遇不断突破自我，才能拥有更广阔职业发展空间。

好医生国际教育专注于**医疗教育18年**，依托长年积累的优势资源，帮助无数医生拿到海外名校的访学邀请函，在**美国、英国、德国、日本**等医疗水平先进的国家有**众多成功案例**。好医生为助力医生的梦想而感到自豪。如果您也有一颗勇于攀登的心，请**点击下方“阅读原文”，开启访学之行！**

往期回顾

案例 | 5年工作经验的住院医，2周斩获哈佛医学院offer

案例 | 主治医师是如何收到牛津大学访学邀请函的？

热点 | 见证德国医院300多台手术，我明白了中国医疗为何摆脱不了“成长壁垒”

日中笹川医学奨学金制度第 40 期＜共同研究コース＞研究者

2019.3.31 現在

氏　名	共同研究機関（中国）	共同研究機関（日本）		共同研究者
	研究テーマ		研究期間	
黄 紅蘭	吉林大学基礎医学院病原生物学・教授	筑波大学大学院医学医療系循環器内科学		青沼 和隆 教授
	心筋自己抗原に対するトレランスの破綻がもたらす心筋炎の慢性化機能の解明		6 か月	
陳 小東	四川省腫瘍医院胃腸外科・副主任医師	国立がん研究センター東病院胃外科		木下 敬弘 科長
	Laparoscopic transhiatal approach for esophagogastric junction (EGJ) cancer		6 か月	
何 海萍	昆明理工大学附属医院（雲南省第一人民医院）血液内科・副教授	東京大学医科学研究所附属病院セルプロセッシング・輸血部		長村 登紀子 部長・准教授
	A study of the influence of Triptolide on the biological activity of umbilical cord derived mesenchymal stromal cells		6 か月	
殷　猛	上海交通大学医学院附属上海児童医学中心心胸外科・副主任医師	東京医科歯科大学生体材料工学研究所		岸田 晶夫 教授
	脱細胞化生体組織の医療応用に関する基礎研究		6 か月	
敖　強	中国医科大学公共基礎学院組織工程学教研室・教授	帝京大学医学部脳神経外科		松野　彰 主任教授
	Synergistic effects of sequential expression of miRNA-222 and miRNA-338 on repair of injured peripheral nerve through two different lentivirus vector systems		6 か月	
鄭 志剛	広西壮族自治区疾病予防控制中心エイズ病防控所・副所長	国立感染症研究所エイズ研究センター		俣野 哲朗 センター長
	A Bayesian hierarchical-based back calculation model for estimating HIV testing and incidence rate in Guangxi province. Southern China		6 か月	
蒋 小華	上海市東方医院（同済大学附属東方医院）胃腸外科・主任医師	がん研究会有明病院消化器センター胃外科		比企 直樹 部長
	Comparison of anastomotic complications after laparoscopic total gastrectomy with esophagojejunostomy using circular stapler versus linear stapler		3 か月	
朴 紅梅	延辺大学附属医院呼吸内科・科主任/主任医師	横浜市立大学大学院医学研究科呼吸器病学		金子 猛 主任教授
	肺癌患者に対する免疫チェックポイント阻害剤耐性のメカニズム		6 か月	
呉　琳	中国医科大学附属口腔医院修復科・教授	神奈川歯科大学全身管理医歯学		玉置 勝司 教授
	The Relationship between Temporomandibular Disorders and Psychological Factors		4 か月	
金 京春	延辺大学附属医院血液内科・主任医師/教授	金沢大学医学系免疫学		華山 力成 教授
	貪食細胞による免疫疾患の発症機序およびエクソソームの役割		6 か月	
王 宇輝	北京大学基礎医学院心血管研究所基因治療研究室　・副研究員	山梨大学大学院総合研究部分子病理学講座		範　江林 教授
	The pathogenesis and pathologic characteristics of coronary atherosclerosis and coronary heart disease in several knockout hamster models		6 か月	
張 暁昀	黒龍江省中医薬科学院内分泌科・教授/主任医師	京都大学大学院医学研究科糖尿病・内分泌・栄養内科学		稲垣 暢也 教授
	Effects of medium-chain fatty acid triglyceride (MCT) on incretin secretion		6 か月	
呉　伙	安徽医科大学第一附属医院胃腸外科・副教授	京都大学大学院医学研究科腫瘍生物学		小川 誠司 教授
	Sanger sequencing and next generation sequencing			
李 南方	新疆ウイグル自治区人民医院・副院長	京都大学大学院総合生存学館（思想館）		趙　亮 准教授
	The project of artificial intelligence for secondary hypertension screening		6 か月	
徐　雯	哈爾浜医科大学基礎医学院免疫学教研室・教授	大阪大学免疫学フロンティア研究センター		坂口 志文 副拠点長・教授
	The research of prevention effects and the mechanism of antigen specific inducible regulatory T cells on experimental autoimmune encephalomyelitis		6 か月	

呉　江	第四軍医大学口腔医院口腔修復科・副教授/主治医師	広島大学大学院医歯薬保健学研究科生体材料学	加藤 功一 教授
	Fabrication of novel nanoparticles and its release character	5か月	
程 為平	黒龍江中医薬大学附属第一医院鍼灸二科・教授	県立広島大学保健福祉学部理学療法学科	原田 俊英 教授
	A comparative analysis of cognitive impairment in elderly in China and Japan	6か月	
楊 立群	遼寧省計画生育科学研究院薬物研究室・副研究員	九州大学工学研究院応用化学部門	片山 佳樹 教授
	Biodegradable oral delivery system based on butyrate-functionalized PTMC particles for inflammatory bowel disease therapy	6か月	
胡 英華	黒龍江省労働衛生職業病研究院（黒竜江省第二医院道理院区）中毒科・主任医師	産業医科大学産業生態科学研究所	河井 一明 教授
	A accurate measurement of oxidative DNA damage in inflammatory model rat	3か月	
孟 召偉	天津医科大学総医院核医学科・主任医師	長崎大学原爆後障害医療研究所	光武 範吏 准教授
	Genetic mutation for ^{131}I refractory papillary thyroid cancer	3か月	

日中笹川医学奨学金制度第40期＜学位取得コース＞研究者

2019.3.31現在

氏　名	所　属　機　関	受 け 入 れ 機 関	指導責任者
	研究テーマ	学位取得方法	
鄭 衛青	南昌市疾病預防控制中心・検験技師	帯広畜産大学原虫病研究センター	玄 学南 教授・センター長
	中国におけるマダニ媒介感染症の疫学調査と有効な駆除法の開発	論文博士	
劉　珏	復旦大学附属華山医院北院・康復治療師	筑波大学大学院人間総合科学研究科	大藏 倫博 准教授
	地域在住高齢者におけるフレイルと交通事故発生率およびリスクとの関連	課程博士	
孫 長博	中国医科大学附属第一医院・住院医師	東京大学大学院医学系研究科呼吸器外科学	中島 淳 教授
	肺がんに対する免疫療法の研究	課程博士	
田　東	川北医学院附属医院・医師	東京大学大学院医学系研究科呼吸器外科学	中島 淳 教授
	肺移植に関する実験的・臨床的研究	課程博士	
張 春東	中国医科大学附属第四医院・医師	東京大学大学院医学系研究科消化管外科学・乳腺内分泌外科学	瀬戸 泰之 教授
	腫瘍の位置と組み合わせた幽門輪から腫瘍の遠位端までの長さは胃の遠位部に沿ったリンパ節転移の強力な決定因子である	課程博士	
唐 春花	大坪医院(第三軍医大学附属第三医院)・主治医師	慶應義塾大学医学部内科学教室(神経内科)	中原　仁 教授
	家族性片麻痺性頭痛２型モデルマウスを用いた片頭痛病態の解明	論文博士	
張　順	上海市東方医院(同済大学附属東方医院)・主治医師	順天堂大学大学院医学研究科 消化器・低侵襲外科学	福永 哲 教授
	The Relationship between p21 and Carboxylesterase 2 Expression in human Colorectal Cancer Cells	論文博士	
許 文成	湖北省中医院・主管薬師	東京薬科大学薬学部臨床薬理学教室	平野 俊彦 教授
	ヒト末梢血リンパ球に対する生薬成分の効果	論文博士	
李 弘揚	天津中医薬大学・修士	金沢大学附属病院漢方医学科	小川 恵子 臨床教授・ 特任准教授
	画像解析技術を用いた人体における漢方薬の評価	課程博士	
徐 妍妍	中日友好医院・住院医師	琉球大学大学院医学研究科放射線診断治療学	村山 貞之 教授
	超多列CT, 超高精細CT等を用いた胸部疾患の研究	論文博士	